Structural Studies of Biofuel Components

by

Katrina Anne Warrack

Supervisor: Dr Joseph A. Hriljac

A thesis submitted to The University of Birmingham for

the degree of Doctor of Philosophy

The School of Chemistry

College of Engineering and Physical Sciences

University of Birmingham

April 2017

UNIVERSITY OF BIRMINGHAM

University of Birmingham Research Archive

e-theses repository

Abstract

The main aim of this project is to find, solve and characterise polymorphs of methyl stearate and methyl palmitate, which are the two major compounds that have prevented the widespread use of biodiesel. Biodiesel is traditionally derived from biomass containing high percentages of triglycerides, which are converted into fatty acid methyl esters (FAMEs). High melting point saturated FAMEs produce the same poor low temperature flow properties experienced with petroleum diesel.

For many years additives have been designed for petroleum diesel to reduce the cold flow problems; however these are not structurally selective for FAMEs. The most common compounds in biodiesel which cause cold flow problems are methyl stearate and methyl palmitate; therefore accurate crystal structures for all polymorphs that may crystallise in the fuel should be found, to design additives which are structurally selective for these compounds.

Throughout this thesis powder x-ray and neutron diffraction were used in conjunction with Gaussian dipole calculations, to characterise the polymorphs of methyl stearate and methyl palmitate and their interactions with 5 straight chain *n*-alkanes. Variable temperature and solvents were used to mimic the conditions that might be experienced in the fuel tank of a car.

Acknowledgements

List of Abbreviations

12:0 – Lauric Acid

14:0 – Myristic Acid

16:0 – Palmitic acid

18:0 – Stearic acid

18:1 – Oleic acid

18:2 – Linoleic acid

18:3 – Linolenic acid

20:0 – Arachidic acid

20:1 – Gondoic acid

22:0 – Behendic acid

22:1 – Erucic acid

AM1 – Austin Model 1

B3LYP – Becke three term correlation functional Lee, Yang and Parr

C – Base-Centred

CFI – Cold Flow Improver

CFPP – Cold Filter Plugging Point

CIF – Crystallographic Information File

CP – Cloud Point

CPD – Cloud Point Depressants

D-1 – High Grade Petroleum Diesel or Jet Fuel

D-2 – Standard Transportation Diesel Fuel

DFT – Density Functional Theory

DM – Direct Method

DST – Direct Space Techniques

ES-*Aa* – Ethyl Stearate 1968 structure

EVA – Ethylene Vinyl Acetate

F – Face-Centred

FAMEs - Fatty Acid Methyl Esters

FFT – Fast Fourier Transform

FWHM – Full Width at Half Maximum

HF – Hartree-Fock

HRPD – High Resolution Powder Diffraction

I – Body-Centred

KLP – Known Lattice Parameters

KS – Known Structures

LTFT – Low Temperature Filterability Test

MP-*C*2 – Methyl Palmitate *C*2 structure

MP-*Pnab* – Methyl Palmitate *Pnab* structure

MS-*A*2/*a* – Methyl Stearate 1960 structure

MS-*C*2 – Methyl Stearate *C*2 structure

MS-*Cc* – Methyl Stearate *Cc* structure

MS-*C*2/*c* – Methyl Stearate I19 structure

MS-*Pnab* – Methyl Stearate 1970 structure

NMR – Nuclear Magnetic Resonance

P – Primitive

PM – Patterson Method

PM3 – Parametric Model Number 3

PP – Pour Point

PPD – Pour Point Depressants

PSD – Position Sensitive Detector

PS-*Pa* – Propyl Stearate 1968 structure

PXRD – Powder X-Ray Diffraction

R – Rhombohedral

RAL – Rutherford Appleton Laboratory

TOF – Time of Flight

UFF – Universal Force Field

U.S.A. – United States of America

WAFI – Wax Antisettling Flow Improvers

WCM – Wax Crystalline Modifiers

wt% – Weight Percentage

XRD – X-Ray Diffraction

Contents

List of Figures

List of Tables

List of Equations

Triglyceride + ROH $\rightleftharpoons$ Diglyceride + ROOCR$_1$ **Equation 1.1**

Diglyceride + ROH $\rightleftharpoons$ Monoglyceride + ROOCR$_2$ **Equation 1.2**

Monoglyceride + ROH $\rightleftharpoons$ Glycerol + ROOCR$_3$ **Equation 1.3**

$$n \cdot \lambda = 2d\sin\theta$$ **Equation 2.1 - Bragg's law**

$$\lambda = \left(\frac{h^2}{2mE}\right)^{\frac{1}{2}} = \frac{9.04}{E^{\frac{1}{2}}}$$ **Equation 2.2**

$$\lambda = \frac{0.003955}{v} = \frac{0.003955 \cdot T}{L}$$ **Equation 2.3**

$$t_{hkl} = 505.55685 \cdot L \cdot d_{hkl} \sin\theta$$ **Equation 2.4**

$$|F_{hkl}|^2 \propto I_{hkl}$$ **Equation 2.5**

$$F_{hkl} = \sum_{j=1}^{atoms} f_{(j)} exp[2\pi \cdot i(hx+ky+lz)]$$ **Equation 2.6**

$$\rho_{xyz} = \frac{1}{V}\sum |F_{hkl}| exp[-2\pi i(hx+ky+lz)-\alpha_{hkl}]$$ **Equation 2.7**

$$S_y = \sum_{i=1}^{n} w_i (y_i - y_{ci})^2$$ **Equation 2.8 - Residual**

$$y_{ci} = s \sum_K L_K |F_K{}^2| \emptyset_i (2\theta_i - 2\theta_K) P_K A - y_{bi}$$

Equation 2.9 - Intensities

$$R_{wp} = \left\{ \frac{\sum_i w_i [y_i - y_{ci}]^2}{\sum_i w_i [y_i]^2} \right\}^{\frac{1}{2}}$$

Equation 2.10 - R_{wp}

$$R_p = \frac{\sum |y_i - y_{ci}|}{\sum y_i}$$

Equation 2.11 - R_p

$$R_{exp} = \left\{ \frac{(N - P)}{\sum_i^N w_i y_i{}^2} \right\}^{\frac{1}{2}}$$

Equation 2.12 - R_{exp}

$$GOF = \chi = \frac{R_{wp}}{R_{exp}}$$

Equation 2.13 - χ

$$\text{Thermal expansion coefficient} = \frac{\Delta L}{L_0 \cdot \Delta T}$$

Equation 3.1

1. Chapter 1 - Introduction

1.1 Introduction to biodiesel

Finding a secure and reliable renewable source of energy is of major concern with conventional fossil fuel resources decreasing every day[1,2]. Furthermore with greenhouse gas emissions and climate change on the increase, a new sustainable energy source must be more environmentally friendly than current energy sources[2,3]. As petroleum resources are decreasing and limited to certain regions of the world, a renewable alternative is required [2].

The current alternative to petroleum diesel is termed biodiesel which is renewable (produced through biological processes rather than the geological processes that are used in the formation of fossil fuels), environmentally friendly due to its low toxicity and rapid biodegradability, and is safer to handle and store due to its higher flash point[2,4,5]. Biodiesel at present is usually blended with petroleum diesel as a fuel extender; when blended in ratios of up to 20% it significantly reduces exhaust emissions of hydrocarbons, carbon monoxide, sulphur dioxide, polycyclic aromatic hydrocarbons and particulate matter[4-6]. Biodiesel does, however, increase nitrogen oxide emissions by around 5% when blended with petroleum diesel, but this may decrease in the future with new exhaust emission technologies[7,8].

1.1.1 Formation and Composition of Biodiesel

Biodiesel is traditionally derived from vegetable oils, animal fats or algal lipids that are mostly composed of triglycerides[1,8,9]. Through transesterification with a monohydric alcohol, typically methanol or ethanol, and in the presence of a catalyst, usually potassium hydroxide or sodium hydroxide, long straight chain fatty acid alkyl esters are yielded, with the by-product of the reaction being glycerol as shown in Figure 1.1[1,2,8,10].
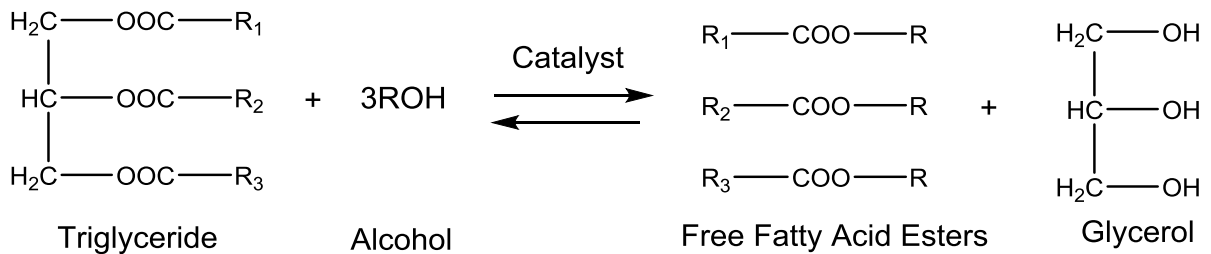
Figure 1.1 Transesterification of triglyceride with alcohol. R_1, R_2, R_3 = Fatty acid tailgroup. R = Alkyl group.

The catalyst is used to split the triglyceride oil molecules stepwise from triglycerides, to diglycerides, to monoglycerides, and then finally to glycerol in three reversible steps; whilst the now free fatty acids undergo transesterification with the alcohol, to form the fatty acid alkyl esters as shown in Equations 1.1 to 1.3 below[11,12].

$$\text{Triglyceride} + \text{ROH} \rightleftharpoons \text{Diglyceride} + \text{ROOCR}_1 \qquad \textbf{Equation 1.1}$$

$$\text{Diglyceride} + \text{ROH} \rightleftharpoons \text{Monoglyceride} + \text{ROOCR}_2 \qquad \textbf{Equation 1.2}$$

$$\text{Monoglyceride} + \text{ROH} \rightleftharpoons \text{Glycerol} + \text{ROOCR}_3 \qquad \textbf{Equation 1.3}$$
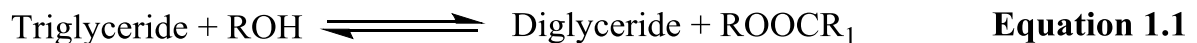
As the transesterification reaction is usually carried out with methanol the resulting fatty esters are usually termed fatty acid methyl esters (FAMEs)[3,4,13]. Biodiesel is composed of a mixture of fatty acid esters, with the transesterification reaction of the oil or fat yielding a fatty acid ester profile identical to that of the parent oil or fat [1,8]. A wide variety of oils and fats have been reported in the literature with the possibility of regional development in biodiesel production; however the most dominant feedstocks currently being used are soybean oil in the United States of America (U.S.A.), rapeseed / canola oil in Europe, and palm oil in southeast Asia[3,8,12].

Whilst these and other oils can contain a wide composition of different fatty acids, which can vary dramatically depending on the parent oil, there are five acids which tend to dominate the composition[14]. A fatty acid naming abbreviation is used consisting of two numbers[3]. The first number corresponds to the number of carbons in the fatty acid chain and the second to the number of carbon-carbon double bonds[3]. The fatty acids which dominate the composition are: saturated acids palmitic acid (16:0) and stearic acid (18:0), monounsaturated oleic acid (18:1), di-unsaturated linoleic acid (18:2) and tri-unsaturated linolenic acid (18:3)[3,8,15].

As can be seen from Table 1.1, containing typical fatty acid composition profiles for a few common oils used in biodiesel, biodiesel produced from the transesterification of triglycerides is almost entirely composed of even-numbered fatty acid chains[3]. This is in contrast to renewable diesel which is produced from the same triglyceride feedstock, but by catalytic hydroprocessing produces hydrocarbons with no glycerol by-product, and doesn't require an alcohol[3]. Renewable diesel contains large amounts of odd-numbered fatty acid chains, even if produced from the same

3

feedstocks as biodiesel, due to one carbon being removed in the manufacturing

hydroprocessing step[3].

Table 1.1 Fatty acid composition profiles (wt%) from oils typically used in biodiesel.

Fatty Acid & Abbrev.	Palm[16]	Soybean[16]	Rapeseed[16]	Canola[17]	Sunflower[17]
Lauric 12:0	0.5				
Myristic 14:0	1.6				
Palmitic 16:0	49.8	11.7	5.2	4.58	5.79
Stearic 18:0	2.9	3.97	1.4	2.01	5.68
Oleic 18:1	38.8	21.27	66.0	60.00	20.43
Linoleic 18:2	6.6	53.7	18.9	21.66	66.02
Linolenic 18:3		8.12	5.6	7.92	
Arachidic 20:0		1.23	1.9	0.78	0.58
Gondoic 20:1				1.52	
Behenic 22:0			1.0	0.33	1.01
Erucic 22:1				0.79	
Total Saturated fatty acid composition (wt%)	54.8	16.9	9.5	7.70	13.06
Total Unsaturated fatty acid composition (wt%)	45.4	83.09	90.5	91.89	86.45

1.1.2 Production and Costing Implications of Biodiesel

Global non-renewable petroleum consumption is greatly increasing every year

as the world's energy consumption increases. In 2007 there were 806 million cars

and small trucks on the roads, but by 2030 this may increase to 1.3 billion and to 2

billion by 2050[18,19]. As biofuels have the potential to replace conventional energy

resources, create sustainable energy for the world, and reduce the emissions of air

pollutants including greenhouse gases, research into biofuels is an important direction focused into turning biomass effectively into biofuels such as bioethanol, biobutanol, biohydrogen and biodiesel[20,21]. Biofuels are currently catogerised into three generations with 95% of biodiesel currently being sourced from first generation biomass[22,23].

First generation biofuels are souced from agriculural edible crop oils such as soybean, sunflower, and rapeseed; however these oils impact food security increasing both the price of food and fuel derived from edible oils grown on agricultural land[23-25]. Expansion of oil crop land used for biodiesel has also caused deforestation and destruction of ecosystems in countries such as Malaysia, Indonesia and Brazil, along with increasing the competition between food and fuel markets[22].

Second generation fuels are dervied from non-edible oils such as jatropha oil, waste edible cooking oils and animal fats from industry which do not affect food security[21,23,25]. Whilst second generation biofuels are more favourable, sustainability may be an issue, with non-edible oils often still grown on land which could be used for food crops. Furthermore the feasibility of collecting and purifying waste oils and fats from many companies to produce enough biofuel is not ideal[23].

The most promising options are third generation biofuel sources which come from microalgae, containing large quatities of carbohydrates, proteins, pigments and lipids[23,26]. Microalgae can be grown on non-arable land, and do not require freshwater, therefore not competing with land that would otherwise be suitable for food production[26]. Microalgae also have a much faster growth rate, as they can

double their biomass within 24 hours but this can be as little as 3.5 hours during exponential growth periods, with dry biomass containing 20-50% of oil by weight[27].

Microalgae also need a lot less space in which to be cultivated, with between 1 and 3% of land used for growing crops in the U.S.A. needed to produce 50% of the transport fuels required by the U.S.A.(as of 2007)[27]. Whilst microalgae production is both rich in oil (lipids) and other useful materials, and quick to grow, it is currently more expensive to produce due to light, carbon dioxide, water and nutrients containing nitrogen, phosphorus and iron being required[27]. To prevent water shortages, sea water can be used for certain strains of microalgae, along with commercial fertilisers containing nitrates and phosphates, or waste water high in nutrients. Carbon dioxide needs to be fed continually during daylight hours, therefore microalgae production can be a useful carbon dioxide trap, to use up waste gases produced from power plants and industry, that would otherwise be released into the atmosphere[27]. Microalgae does however need to grow in an environment with a small temperature variation[25]. Whilst biofuels produced from microalgae are currently more costly than that of first and second generation feedstocks, it is the only feedstock that has the potential to displace the need for petroleum resources completely, with production available all year round. With the correct funding, implementation and research into genetic and metabolic engineering (light/wavelength exposure, algae strain, media and the cultivation method), the production of low cost microalgae biomass is viable[25,27].

1.2 Important Properties of Biodiesel

There are several physical and chemical properties of a biodiesel, or rather the fatty acid alkyl esters, which are important to consider when assessing whether it is a suitable alternative to petroleum diesel.

Cetane numbers are used as an indicator of ignition quality within diesel engines, with the larger the number the shorter the delay between the injection of the fuel into the cylinders, and the ignition of the engine[1,28]. Hexadecane, a long straight chain hydrocarbon, is assigned the high quality standard cetane number of 100; with a highly branched compound 2,2,4,4,6,8,8-heptamethylnonane, the low quality standard, and a cetane number of 15[1,28]. If the cetane number is too high, combustion can occur before the fuel and air is mixed together properly, causing smoke and incomplete combustion of the fuel[28]. However, if the cetane number for the fuel is too low, incomplete combustion will occur due to higher air temperatures, slower engine warm-up and misfiring[28]. The cetane number minimum for biodiesel is 47 or 51, so the common FAMEs methyl stearate and methyl palmitate with cetane numbers of 101 and 85.9, respectively, are well above current regulations[28,29]. Whilst the individual numbers of saturated methyl esters are good, when combined within the actual fatty acid profile of the oil or fat, the values tend to decrease. This is due to large percentages of unsaturated esters with lower cetane numbers: they are however, generally above the industry regulations which require higher numbers for biodiesel than petroleum diesel[28]. This therefore is one of the reasons why derivatives of triglycerides are suitable alternatives to petroleum diesel[28]. The carbon chain length, the degree of branching and the degree of unsaturation heavily

influence the cetane number[28]. Cetane numbers decrease with shorter carbon chain lengths, aswell as increasing unsaturation and branching in the hydrocarbon chain[28]. The gross heat of combustion is another property which verifies the suitability of fatty acid esters, as esters with chain lengths of around 18 have similar values to that of hexadecane[1,28].

Iodine values are often used to assess the degree of unsaturation, and therefore the oxidative stability of oils, fats and waxes[28]. It is "measured in g iodine/100 g of sample when formally adding iodine to the double bonds"[28]. The more iodine which is attached to the double bonds, the higher the iodine value and the more susceptible the sample is to oxidation due to a higher degree of unsaturation present in the sample [28]. As shown in Table 1.1 the percentage of unsaturated fatty acids tends to be above 80% which can lead to poor oxidative stability and high iodine values of biodiesel fuels[8,30]. This can cause problems on extended storage of the fuel, and ultimately leads to all biodiesel fuels requiring antioxidants[8].

The main reason why oils and fats have to undergo transesterification is due to their viscosity, as the viscosity of biodiesel fatty esters is an order of magnitude lower than that of the parent oil or fat[8]. High viscosity values can lead to poor atomisation, and deposits building up in the engine[28]. Viscosity increases with chain length and with increasing degree of saturation; whilst trans double bond configurations in unsaturated esters have higher viscosity values than cis configurations[28].

In blends of petroleum diesel with ratios as little as 2% biodiesel, biodiesel has been found to restore lubricity to petroleum diesel, which is lost during the desulfurization process[1,6,7].

The above physical and chemical properties, along with cold temperature properties which shall be discussed below, are mostly determined from the compositional profile of FAMEs and the structures of the individual fatty acid esters[3,29,31].

1.3 Cold Flow properties of Petroleum Diesel Fuel

Conventional petroleum diesel fuels which are composed of mid-range cracking products termed `middle distillates` (aromatics, paraffins, cycloparaffins, and olefins) that boil between 180 - 340°C, are susceptible to poor start-up performance when ambient temperatures fall[14,28,32]. As the temperature begins to fall over a long period of time, for example overnight, high molecular weight paraffins, C_{18}-C_{30} n-alkanes, start to nucleate and form wax crystals[28,32]. The wax crystals that form are suspended within a solution of smaller n-alkanes, olefins and aromatic compounds, and generally have one of three distinct crystal structures which grow and agglomerate into large platelet lamellae that can block fuel filters[28,32-34]. This leads to the starvation of fuel to the engine and subsequent engine failure[28,32]. The three crystal groups which the n-alkanes (C_nH_{2n+2}) in the solid state fall into are: triclinic [12<n(even)<26], monoclinic [28<n(even)<36], and orthorhombic [n(even)≥36 and n(odd)][34].

There are four cold-temperature values/performance tests that are important to be determined for both petroleum diesel and biodiesel fuels to assess their low temperature properties. These are the cloud point (CP), the pour point (PP), the low-temperature filterability test (LTFT), and the cold-filter plugging point (CFPP). The CP is the temperature at which the crystals first become visible and are seen as a

cloudy/hazy suspension in the fuel[28]. The lowest temperature before which the crystal formation and agglomeration stops the free pouring of the fuel is known as the PP[1,28]. The two industry standard tests which are used as operability tests for the fuel, are known as the LTFT (used in North America), and the CFPP (used outside of North America)[1].

Many different additives have been developed over the years to try and control the crystallisation of the waxes and improve the cold weather properties of petroleum diesel[28,32]. The first additives to be developed in the 1950s were pour point depressants (PPD) which inhibit crystal growth and reduce agglomeration, rather than affecting the nucleation or crystal morphology[28]. The most common PPDs used (shown in Figure 1.2) are based on ethylene vinyl acetate (EVA) copolymers and polyalkylacrylates such as poly(methyl methacrylate), which either adsorb onto or cocrystallise with the *n*-alkanes once nucleation has commenced[13,35]. The polymers usually contain both polar and non-polar moietes; with the non-polar moiety interacting with long alkyl chains, and the polar moiety disrupting the wax crystal growth[36]. The cocrystallisation of the PPD and the paraffins causes modifications to the crystal growth of the wax, due to steric hindrance of the polymer backbone which keeps wax crystals apart, preventing formation of a three-dimentional network structure, and promoting small needle shaped crystals to form[35,37]. They don't, however, greatly affect the CP of the diesel fuel, as crystalline nuclei are required to form before the additive can be activated[35].
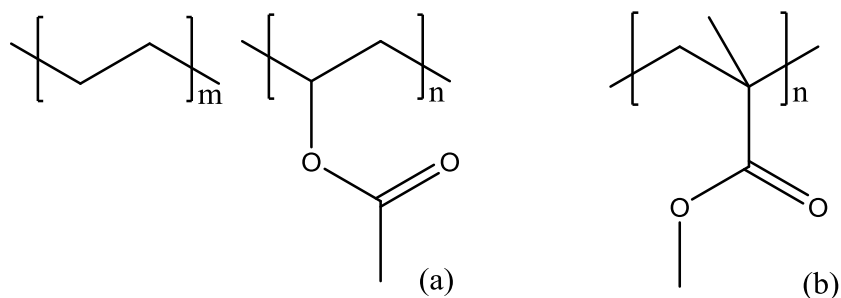
Figure 1.2 Molecular structures of common PPDs (a) EVA copolymers, and (b) poly(methyl methacrylate).

Wax crystalline modifiers (WCM) are another type of additive which have been developed to influence one or more parts of the crystallisation process, nucleation, growth or agglomeration[28]. The aim of these additives is to promote the formation of smaller needle-shaped crystals so they form a more permeable cake layer on the fuel filter[28,32]. This allows some fuel to flow, before the crystals can melt once warm excess fuel is recycled back into the fuel tank[28,32]. WCM additives are categorised into three types. CFPP improvers (which are the same as PPDs) can reduce the CFPP and PP by up to 20°C but not the CP[28]. Cloud point depressants (CPD) are low-molecular weight comb-shaped copolymers that are designed to adsorb the paraffin molecules to compete with the normal nucleation and stay soluble below the CP, due to the soluble backbone of the polymer[28]. Wax antisettling flow improvers (WAFI) are similar to CPD in that they cocrystallise with the nuclei, however WAFI impart a dispersive effect causing only very small crystals to form by attaching highly polar functional groups containing heteroatoms, such as nitrogen, oxygen, sulphur or phosphorus[28,38].

1.4 Cold Flow properties of Biodiesel Fuels

Like conventional petroleum diesel, biodiesel also has poor low-temperature flow properties when ambient temperatures fall overnight during cold weather, which can restrict its use in moderate climates[4,7]. As temperatures drop towards 0°C, high melting point long chain saturated FAMEs (C_{16}-C_{18}) begin to nucleate and crystallise in the fuel[4,7]. Analogous to the long chain paraffin molecules that cause low temperature problems in petroleum diesel, saturated FAMEs also crystallise rapidly in the *yz* direction forming platelet-like lamellae[7,35]. They then stack on top of each other as they agglomerate and block the fuel filters, as growth in the *x* direction is limited due to weak intermolecular forces between the platelets[7,35]. The CP of neat biodiesel tends to be significantly higher than that of petroleum diesel, which can be explained by the melting points of the individual components[33]. The melting points of saturated esters of methyl palmitate and methyl stearate are 29.6°C and 38.7°C respectively; whilst unsaturated methyl esters of methyl oleate, linoleate and linolenate have much lower melting points of -19.7°C, -39°C and -45.0°C respectively[39]. Therefore biodiesel derived from oils or fats with compositions containing higher percentages of saturated FAMEs, are more likely to have poor cold flow properties and higher CPs[4,40].

1.5 Current methods of Improving Cold Flow Properties of Biodiesel Fuels

There are several methods that offer possibilities of improving the cold flow properties of biodiesel which are as follows: (i) blending with petroleum diesel; (ii) treating the biodiesel with existing cold flow improver (CFI) additives designed for

petroleum diesel; (iii) developing new additives for biodiesel; (iv) transesterification of the oils and fats with alcohols other than methanol with longer or branched chains; and (v) crystallisation fractionation (winterisation)[28].

Blending petroleum diesel D-2 (standard transportation fuel) with higher grade D-1 petroleum diesel or jet fuel can often be used to improve the cold weather properties, as D-1 has better cold flow properties, however it does have lower viscosity, energy and power outputs therefore increasing fuel consumption[28]. As both D-1 and D-2 fuels have lower viscosities and better CP, PP, CFPP, LTFT values, blending with biodiesel will improve the cold flow properties of biodiesel, and to a greater extent with D-1 than D-2[33].

As a wide range of CFI additives have been developed over the years for petroleum diesel, various commercial additives have been studied with biodiesel[28]. Additives are also preferred over blending with D-1 or jet fuel as they don't have reduced power/energy output, increased fuel consumption side effects and don't use up valuable petroleum resources[28]. In a study by Dunn et al[35], petroleum diesel CFI additives have shown the ability to reduce the PP by up to 20°C for blends with up to 30% soybean derived biodiesel. The results of the study suggest that the ability of these additives to reduce the PP by a significant amount, must mean that the growth and agglomeration of the wax crystals in biodiesel are similar to those that form in petroleum diesel[28,35]. Whilst these additives can significantly reduce the PP and CFPP, the CP was not really affected which suggests that those studied are CFPP improver additives, which is what most diesel manufacturers use currently[28].

Whilst cold flow improver additives designed for petroleum diesel do work to some extent, both with neat and blended biodiesel, the degree of structural selectivity

can greatly affect the outcome[28]. As noted the study showed a decrease in the PP and CFPP but not in the CP or LTFT, which suggests that the additive was restricted by structural selectivity, as the nucleation and crystal growth mechanisms were not altered to a great extent[28]. PPDs have the lowest structural selectivity, whilst CFPP additives promote smaller crystal formation and are more selective than PPDs, that only decrease the PP[28]. Additives with the highest structural selectivity that promote formation of even smaller crystals are CPD and WAFI additives[28]. The greatest chance of improving the cold flow properties of biodiesel with additives, is to design compounds with high structural selectivity towards high melting point alkyl esters[28]. The additives should modify nucleation and crystal growth, similar to that of CPDs and decrease the CP of the biodiesel[28].

Transesterification using alcohols other than methanol with medium (C_3-C_8) or branched alkyl chains, is another possibility to improving the cold flow properties by reducing the CP[1,7,8,13,28]. Increasing the chain length or branching in the alkyl alcohol headgroup, disrupts the spacing between the individual molecules in the crystal structure, causing rotational disorder in the hydrocarbon tailgroup[13,28]. The result of the disorder in the crystal structure is a reduction in the melting point for headgroups up to *n*-butyl with stearate and palmitate esters; however headgroups larger than *n*-butyl begin to increase the melting point again[13,28,41]. Heat of combustion and cetane numbers are not detrimentally affected by the increase in headgroup size; however branching in the hydrocarbon tailgroup decreases the cetane number[13,28]. Whilst cold weather properties can be improved significantly using longer or branched chain alkyl alcohols, they are more expensive than methanol which is traditionally used[28].

Due to the large differences between the melting points of saturated and unsaturated FAMEs, crystallisation fractionation or winterisation could be a useful technique in improving the cold flow properties of biodiesel[1,5,28,31,42]. The objective of crystallisation fractionation is separation of high melting point components such as methyl palmitate and methyl stearate from the bulk oil esters through a series of cooling cycles[1,5,28,31]. The two stages of fractionation are: (1) selective nucleation and crystal growth under slow agitation and controlled cooling; and (2) filtration and separation of resulting liquid and solid fractions[28,42]. There are two common fractionation processes that could be employed to biodiesel; dry fractionation and solvent fractionation[5,28]. Dry fractionation is crystallisation from the melt without dilution in solvent, and is the cheapest and simplest form of separation of the high and low melting point fatty acid derivatives[5,28,43]. Solvent fractionation involves the use of an organic solvent to aid fractionation, reducing viscosity, crystallisation time and ease of separation. This, however, is more expensive and the end product may contain residual solvent[28,43]. Whilst the cold flow properties of the fractionated product may have been vastly improved, due to the reduction of high melting point saturated esters, the removal of these compounds leads to the reduction of the cetane number and other combustion related properties, and also a reduction in the oxidative stability due to a large increase in the percentage of unsaturated compounds[31].

1.6 Crystal Structures of Compounds of Diesel and Biodiesel

As additives are a popular way to improve the cold flow properties of biodiesel, knowing the crystal structures of the esters that form is crucial in designing suitable compounds for this task. Esters of saturated palmitic acid and stearic acid are the most common compounds that crystallise out and cause cold flow problems[7,28,31,33]. There are no published structures of palmitic acid esters; however there are two structures for both methyl stearate and ethyl stearate, and one of propyl stearate with the lattice parameters shown in Table 1.2[44-48].

Table 1.2 Lattice parameters of published structures of alkyl stearate esters[44-48].

Name & Year Published	Unit cell & Space Group	a	b	c	α	β	γ	Z
Methyl Stearate 1960[45]	Monoclinic A2/a	5.61 Å	7.33 Å	106.6 Å	90°	116°	90°	8
Methyl Stearate 1970[46]	Orthorhombic Pnab	5.61 Å	7.35 Å	95.15 Å	90°	90°	90°	8
Ethyl Stearate 1965[47]	Monoclinic Ia	5.59 Å	7.40 Å	57.1 Å	90°	118°	90°	4
Ethyl Stearate 1968[44]	Monoclinic Aa	5.59 Å	7.40 Å	55.0 Å	90°	113.5°	90°	4
Propyl Stearate 1968[48]	Monoclinic Pa	5.59 Å	7.39 Å	30.0 Å	90°	119.2°	90°	2

Both crystal structures of methyl stearate were obtained by crystallisation from carbon disulphide at -14°C; whist the ethyl stearate 1968 structure was obtained by crystallisation from glacial acetic acid at room temperature; and the propyl stearate crystals were obtained from crystallisation in ethanol at room temperature[44-46,48,49].

Schematic diagrams of the stearate structures are shown in Figure 1.3 comparing them to paraffin *n*-alkanes found in diesel. Figure 1.3(a) shows the paraffin molecules stacked side by side, with weak intermolecular interactions between the ends of the hydrocarbon chains, resulting in slow crystal formation in the *x*- direction, and rapid growth in the *yz*- direction forming flat platelet lamellae[28]. Crystalline fully ordered thermodynamically stable even-straight-chain paraffins n-C_mH_{2m+2} are preferentially triclinic $m \leq 24$, monoclinic $26 \leq m \leq 38$, orthorhombic $m \geq 40$, and odd-chain paraffins $11 \leq m \leq 43$ are orthorhombic[50]. Table 1.3 shows the lattice parameters of even *n*-alkanes with between 12 and 22 carbons in the molecule. These compounds are thought to be more likely to interact with the common FAMEs found in biodiesel (those that are likely to crystallise out at low temperatures) to form either cocrystals or coordinated crystals. In this range, alkanes of this size could potentially pack and form new unit cells with methyl esters due to similar chain lengths, and could interact and pack along the whole length of the methyl ester molecules, or fit in alongside just the alkane part of the methyl esters. Alkanes of this size also crystallise at similar temperatures to the methyl esters that cause cold flow problems in biodiesel, which additives were originally designed to prevent in petroleum diesel.

a) Paraffins (n-alkanes)

b) Methyl Stearate unit cell

c) Ethyl Stearate unit cell

d) Propyl Stearate unit cell
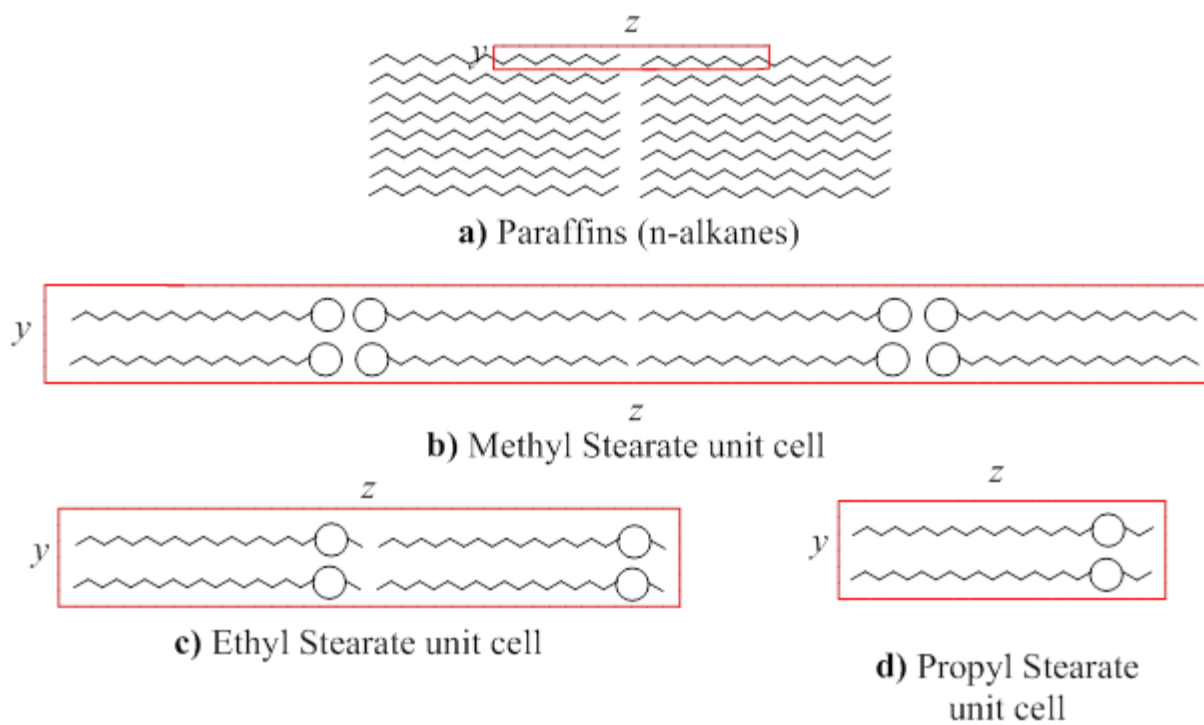
Figure 1.3 Crystal structures of a) *n*-alkanes (paraffins), b) Methyl Stearate, c) Ethyl Stearate and d) Propyl Stearate, viewed down the *x* axis at the *yz* plane, with the unit cell outlined in red.

Table 1.3 Lattice parameters of published straight chain *n*-alkane unit cells with similar sized molecular chains to methyl palmitate and methyl stearate molecules[34,51-53].

Name & Year Published	Unit cell & Space Group	*a*	*b*	*c*	*α*	*β*	*γ*	*Z*
Dodecane 1972[51]	Triclinic *P*-1	4.28 Å	4.81 Å	16.12 Å	93.3°	79.9°	106.6°	1
Tetradecane 1972[51]	Triclinic *P*-1	4.29 Å	4.82 Å	18.58 Å	93.1°	78.8°	107.0°	1
Tetradecane 1994[34]	Triclinic *P*-1	4.256 Å	4.822 Å	20.733 Å	80.733°	61.439°	72.711°	1
Hexadecane 1972[51]	Triclinic *P*-1	4.29 Å	4.81 Å	20.87 Å	91.9°	80.5°	106.9°	1
Hexadecane 1994[34]	Triclinic *P*-1	4.286 Å	4.820 Å	22.357 Å	84.570°	67.309°	72.728°	1
Octadecane 1972[53]	Triclinic *P*-1	4.285 Å	4.82 Å	24.898 Å	85.15°	67.8°	72.7°	1
Eicosane 1992[52]	Triclinic *P*-1	4.293 Å	4.84 Å	27.35 Å	85.3°	68.2°	72.6°	1
Docosane 1994[34]	Triclinic *P*-1	4.288 Å	4.828 Å	29.552 Å	86.424°	70.755°	72.199°	1

Although the polar carboxylic headgroup interactions are weak in methyl stearate structures, there is sufficient polarity for them to possess amphiphilic nature with bilayers formed and a head-to-head, tail-to-tail alignment of the molecules, which can be seen in Figure 1.3(b)[28,54]. This is in contrast to ethyl stearate structures, and those of esters with larger alkyl headgroups shown in figures 1.3(c) and 1.3(d), which form monolayered structures with head-to-tail alignment of the

molecules[28,50,54]. This is due to sufficient shielding of the ester moiety by the nonpolar chains within the headgroup[28,54].

1.7 Rotator Phases in *n*-Alkanes

Between the fully ordered crystalline phases of the straight chain *n*-alkanes mentioned in section 1.6 and their isotropic liquid phases, straight chain alkanes can exist in a series of rotator phases or plastic crystals several degrees below their melting point[55-58]. There are five reported rotator phases which are layered crystals with typically long range positional order of the molecules in three dimensions, but no long range orientational order of the molecule about their long axes[55-58]. The rotator phases can also be clasified as plastic crystals or smectics, due to their finite but weak crystalline ordering where the positional order remains, but the orientational order disappears[55-57]. More than one rotator phase can succeed another in a single system on increasing the temperature within the rotator phase region[59].

Unlike the fully ordered crystalline phases of the *n*-alkanes, which crystallise into different space groups depending on whether there are an even or odd number of carbons in the chain, there are no pronounced effects with the rotator phases[55,57]. This is due to the lack of long range rotational order which makes even and odd chain length molecules appear on average the same[55,57].

If the assumption is made that the molecules in the rotator phases are hexagonally close packed rods orientated nearly normally along the layer, then the rotator phase structures can be described by parameters such as[55]:

- Distortion of the hexagonal lattice,
- Magnitude of the tilt of the molecules,

- The direction of the molecular tilt with respect to the lattice,

- Stacking of one layer above the other.

The distortion of the hexagonal lattice can also be described as[55,57]:

- Hexagonally packed cylinders are tilted, so the lattice remains unaffected in the direction normal to the tilt, and just expanded the tilt direction by $1/\cos\theta$; and the molecules are still packed hexagonally when viewed along their long axes,

- Without tilt but the molecules are no longer effective cylindrical rods.

Rotator phase – R_I is a face centred orthorhombic phase where the molecules are untilted, but the hexagonal lattice is distorted where four (out of six) of the nearest neighboured molecules are closer than the other two[55-58]. The structure also has bilayer stacking ABA where one layer of molecules lie above the centre of a line connecting the two nearest neighbours[55-57].

Rotator phase – R_{II} is a rhombohedral phase with the molecules pointing along the layers untilted in an undistorted hexagonal lattice[55-58]. It has a trilayer ABC stacking sequence with the molecules in each layer above the centre of a triangle formed by the molecules below[55-57].

Rotator phase – R_{III} is a triclinic phase where neither the direction of the lattice distortion or the tilt direction are along symmetry directions of the base hexagonal lattice, and is similar to the $L_{\beta L}$ phase which can be found in phospholipids[55,57].

Rotator phase - R_{IV} is monoclinic and has end to end AAA molecular stacking, but the molecules are tilted between the nearest neighbours which is also found in crystal-G phases found in liquid crystals[55-57]. The distortion of the local chain-chain

packing is much weaker, however, in this phase than the distortion found in the R_I and R_V phases[55].

Rotator phase – R_V has the same layer stacking and hexagonal lattice distortion as the R_I phase but the molecular axis is also tilted in the direction between the nearest neighbours[55-57].

In chain lengths less than C_{26} the general phase sequence is liquid – R_{II} – R_I – R_V – crystal, and with chain lengths greater than C_{27} the sequence is liquid – R_{IV} – R_{III} – crystal; but regardless of what combination of rotator phases are present they always occur in the following order, liquid – R_{IV} – R_{III} – R_{II} – R_I – R_V – crystal[55-57]. The higher carbon chain length rotator phases tend to be characterised by large tilt angles and an increase in gauche bonds near the ends of the chains compared to lower carbon chain length phases on increasing temperature[55,56,58].

Rotator phases can also occur in mixtures of alkanes with the rotator phases present over an extended temperature range when compared to their single phase ranges[56,57,59].

1.8 Conclusion

Biodiesel fuels derived from the transesterification of oils and fats primarily composed of triglycerides possess the same cold flow problems that exist with conventional petroleum diesel. Improving these cold flow properties is essential before a more widespread application of biodiesel can be implemented, with higher concentrations in biodiesel blends all year round. Whilst there are many different possible methods as mentioned to improving these properties, many have disadvantages which could limit their potential success in practical applications. Each

22

potential method should be thoroughly assessed to make sure that the disadvantages don't outweigh the benefits of using the biodiesel. The most promising method which is currently used with petroleum diesel, is the use of additives to reduce the CP, PP, CFPP and LTFT by influencing one or more parts of the crystallisation process. Knowing the crystal structures of the compounds that crystallise out is essential for the optimisation of designing additives, with high structural selectivity towards high melting point saturated esters. Also the interactions between the methyl esters found in biodiesel and the hydrocarbons found in petroleum diesels could also show whether in diesel/biodiesel blends any new cocrystals or coordinated crystals may form; as they could decrease the efficiency of the additives already designed for diesel or biodiesel, if the cocrystals are preferentially formed.

1.9 Scope of the project

In this project we aim to confirm and solve the crystal structures of as bought phases of methyl palmitate and methyl stearate, along with any new polymorphs that may be formed. Temperature and solvent were used to mimic the conditions experienced in the fuel tank of a car. We aim to solve the structures of any cocrystals or coordinated crystals of methyl palmitate and methyl stearate, with different chain length hydrocarbons that may form, whilst using different solvents, variable temperature and starting stoichiometry of the cocrystal formers. From knowing these structures additives can be designed for biodiesel to improve the cold flow properties and hopefully increase the worldwide use of biodiesel all year round.

2. Chapter 2 – Experimental

2.1 Synthesis Techniques

Throughout this project various methods of crystallisation and recrystallisation were used to study the crystal structures and polymorphism of the methyl esters methyl palmitate and methyl stearate along with the straight chain hydrocarbons dodecane, tetradecane, octadecane, eicosane and docosane. Mixtures of the methyl esters individually with each hydrocarbon were also studied.

2.1.1 Solvent Recrystallisations

Solvent recrystallisation is often used as a method of purifying an impure crystalline compound into a pure one with the impurities remaining dissolved in the solvent on formation of the desired crystalline compound. Solvent recrystallisation can also be used to recrystallise a crystalline compound into a different polymorph to that of the starting crystal structure.

2.1.2 Variable Temperature Recrystallisations

The rate at which the material or solution is cooled can greatly influence what crystalline materials may form, and can be a route to forming new polymorphs. In this project, polymorphs were formed from the melt, along with solvent to recrystallise and cocrystallise mixtures of the compounds used.

2.2 Characterisation Techniques

Materials in this project were analysed using powder X-ray diffraction for crystal structure determination, and Gaussian dipole calculations to validate proposed crystal structures.

2.2.1 Fundamentals of Crystallography

Crystals are solids which contain an array of atoms in a regular arrangement with the smallest repeating arrangement of these atoms called the unit cell. A lattice is generated by stacking the unit cell via translations to show the full symmetry of the crystal structure. The unit cell can be described by the lengths a, b and c and the angles between the edges of the unit cell α, β and γ which together are referred to as lattice parameters. The relationship between these lattice parameters result in the seven crystal systems as noted in Table 2.1, and when combined with one of the lattice centrings such as primitive (P), body-centred (I) or face-centred (F) generate 14 Bravais lattice types[60]. The 14 Bravais lattice types shown in Figure 2.1 describe the lattice points, the translational symmetry of the lattice, and therefore give each Bravais lattice a distinct lattice type.

Table 2.1 The Seven Crystal Systems[60].

Crystal System	Axis System	Lattice Centrings
Cubic	$a = b = c, \alpha = \beta = \gamma = 90°$	P, I, F
Tetragonal	$a = b \neq c, \alpha = \beta = \gamma = 90°$	P, I
Hexagonal	$a = b \neq c, \alpha = \beta = 90°, \gamma = 120°$	P
Rhombohedral	$a = b = c, \alpha = \beta = \gamma \neq 90°$	R
Orthorhombic	$a \neq b \neq c, \alpha = \beta = \gamma = 90°$	P, C, I, F
Monoclinic	$a \neq b \neq c, \alpha = \gamma = 90°, \beta \neq 90°$	P, C
Triclinic	$a \neq b \neq c, \alpha \neq \beta \neq \gamma \neq 90°$	P

Simple
cubic (*P*)

Body - centred
cubic (*I*)

Face - centred
cubic(*F*)

Simple
tetragonal (*P*)

Body - centred
tetragonal (*I*)

Hexagonal (*P*)

Rhombohedral (*R*)

Simple
orthorhombic (*P*)

Body - centred
orthorhombic (*I*)

Base - centred
orthorhombic (*C*)

Face - centred
orthorhombic (*F*)

Simple
monoclinic (*P*)

Base - centred
monoclinic (*C*)

Triclinic (*P*)
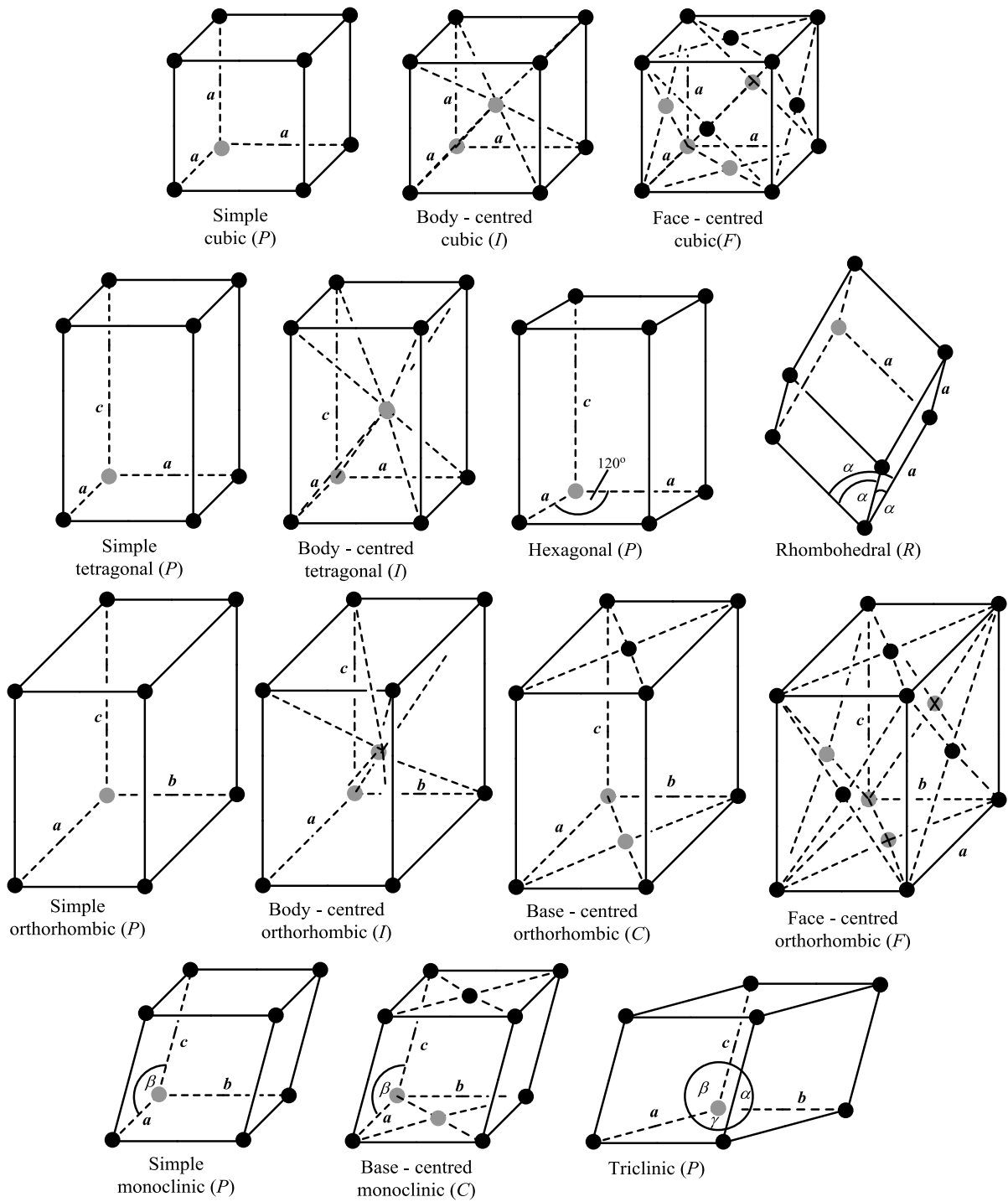
Figure 2.1 Unit cells of the 14 Bravais lattices[60].

27

Additional point and translational symmetry elements need to be considered in three dimensions. The point symmetry elements are centres of symmetry, mirror planes and inversion axes; the translational symmetry elements are glide planes and screw axes[60]. There are only 32 unique ways of combining the above symmetry elements which can repeat in three dimensions, to give 32 crystallographic point groups, and when combined with the 14 Bravais lattices give 230 unique three dimensional crystallographic patterns which are called space groups[60].

Crystallographic unit cells must contain internal symmetry corresponding to one of the 230 space groups, however they can also be described as a series of lattice planes[60]. The planes are described by the inverse of the fractional intercept of the unit cell axis a, b and c, referred to as Miller indices and labelled as (hkl). For an example the plane intercepting half way along the a-axis and not intercepting the b or c-axis is the (200) plane. A family of equivalent lattice planes which are parallel to each other, and at a fixed translational distance apart (defined as d_{hkl}), are perpendicular to the lattice planes it is describing.

2.2.2 Diffraction

When X-rays encounter a set of parallel lattices planes (such as in a crystal) which are separated by a distance d_{hkl}, and at an incident angle θ, they are scattered with the reflected X-ray angle also equal to θ[60,61] as shown in Figure 2.2. Diffracted beams occur when the X-rays interfere and reflect constructively with the parallel lattice planes, so that the difference in the path length of the X-ray beams is equal to an integer multiple of the wavelength which satisfies Bragg's law[60].

$$n \cdot \lambda = 2d\sin\theta \qquad \textbf{Equation 2.1 - Bragg's law}$$
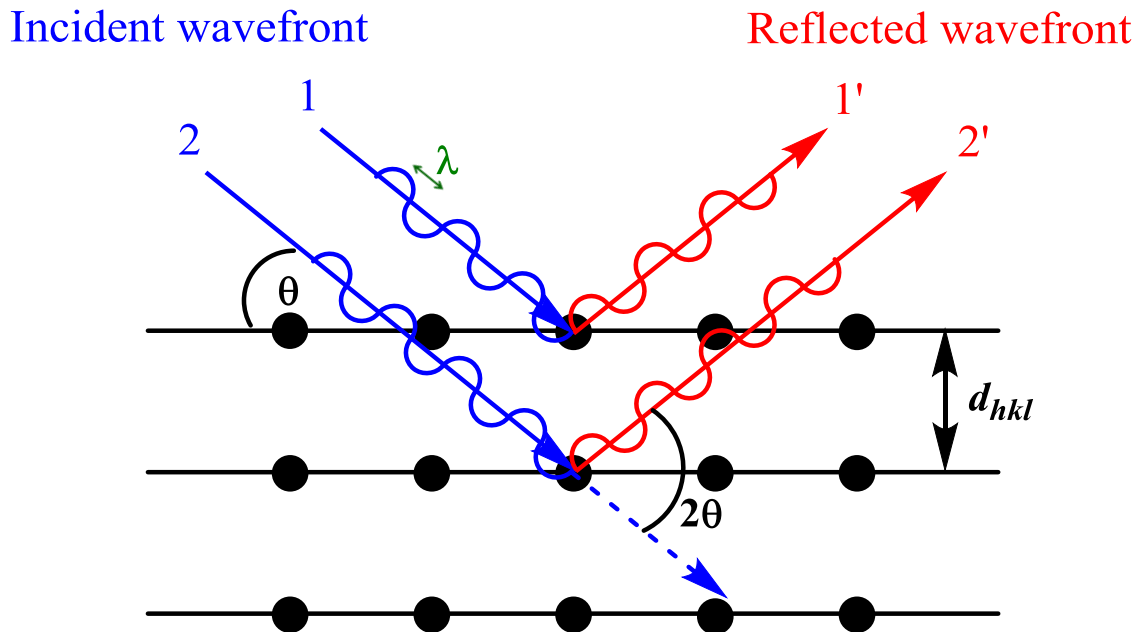
Figure 2.2 Schematic representation of Bragg's Law[60,61]**.**

When constructive interference occurs with the lattice planes, the reflected beams can be detected for each value of 2θ and will be characteristic of both 2θ and d_{hkl}. It is from this we can use diffraction of X-rays to study crystal structures with the X-rays interacting with atoms in the lattice planes.

2.2.3 X-Ray Diffraction (XRD)

X-ray diffraction allows us to understand materials on the atomic scale and gives us the ability to relate the crystal structures of materials with the physical and chemical properties which are more easily seen on the larger scale.

2.2.3.1 Generation of X-Rays

X-ray sources

In laboratory X-ray diffraction, the X-ray beam is generated within a sealed vacuum tube consisting of a tungsten filament (cathode) and a water cooled metal target (anode)[61]. The most common metal anodes used are Cu, Mo and Co, and when a potential difference of between 30 - 60 kV is generated, it accelerates electrons which bombard the metal target, and a series of cascading electronic transitions occur[61]. These electronic transitions emit characteristic electromagnetic radiation (X-ray photons), as electrons from higher atomic levels drop down to fill vacancies of inner shells[61]. For most laboratory sources a copper metal target is used which emits a principle emission line of K_α 1.54056 Å when an electron drops from the L shell to the K shell [61]. Continuous Bremsstrahlung background radiation is also produced when accelerated electrons rapidly decelerate when they are fired and collide at the metal target[60]. The sudden loss of energy is converted into electromagnetic photons called Bremsstrahlung (white) radiation[60].

Filters

X-ray diffraction requires an essentially monochromatic wavelength of radiation, therefore for a common copper source the Cu K_β radiation (when an electron drops from the M shell to the K shell) contaminates the powder pattern[61]. For each target anode material there is a chemical element which has an absorption edge which falls between the K_α and K_β [61]. The element can therefore be used as a filter to block out the K_β radiation. For example the energy of the Cu K_β X-rays (λ = 1.392 Å) have higher energy than the absorption edge of Ni K of λ = 1.488 Å;

however the Cu K_α X-rays (λ = 1.542 Å) do not have sufficient energy to excite the Ni K transition, and therefore are not completely absorbed allowing a thin Ni layer to be used as a filter[61].

Monochromators

Single crystal monochromators can also be used instead of filters to block out certain wavelengths that are not wanted in the powder pattern. Monochromators typically are made from silicon, quartz, germanium, diamond or graphite, and are set to a particular orientation that reflects only the radiation wavelength that is wanted, and satisfies Bragg's law[61]. For example a pre-sample quartz or Si (111) monochromator can eliminate Cu $K_{\alpha2}$ and K_β radiation[61]. With both pre-sample monochromators and filters there is a loss of intensity of the radiation that makes it to the sample[61].

Detectors

The most common detectors used with laboratory sources are scintillation counters, which work when a X-ray photon collides with a phosphor screen (scintillator) which then emits photons in the blue region of the visible spectrum that are then converted into voltage pulses by a photomultiplier tube[61]. The number of emitted light photons is proportional to the energy of the original X-ray photon[61]. Gas-filled position sensitive detectors (PSD) are the second type of detector that may also be used with a laboratory source, and simultaneously records the diffracted intensity at all measured angles which can greatly speed up data collection times[61]. PSD detectors contain a long anode wire, to which a high voltage is applied to both

ends. The pulse moves towards the ends of the wire, and by measuring the rate at which the pulse arrives it is possible to calculate where on the wire the pulse originated. The position of the pulse on the wire is then stored in a multi-channel analyser. As with all other gas-filled detectors a quenching gas mixture of around 10% methane / 90% argon is used to minimise dead time.

2.2.3.2 Powder X-Ray Diffraction (PXRD)

In powder X-ray diffraction the ideal sample can be considered as a polycrystalline mass of randomly orientated crystallites, which represent all possible orientations and within with each crystal will diffract independently. This results in Debye-Scherrer cones which can be seen in Figure 2.3, being recorded by the detectors and converted into a PXRD pattern which contains a series of peaks.
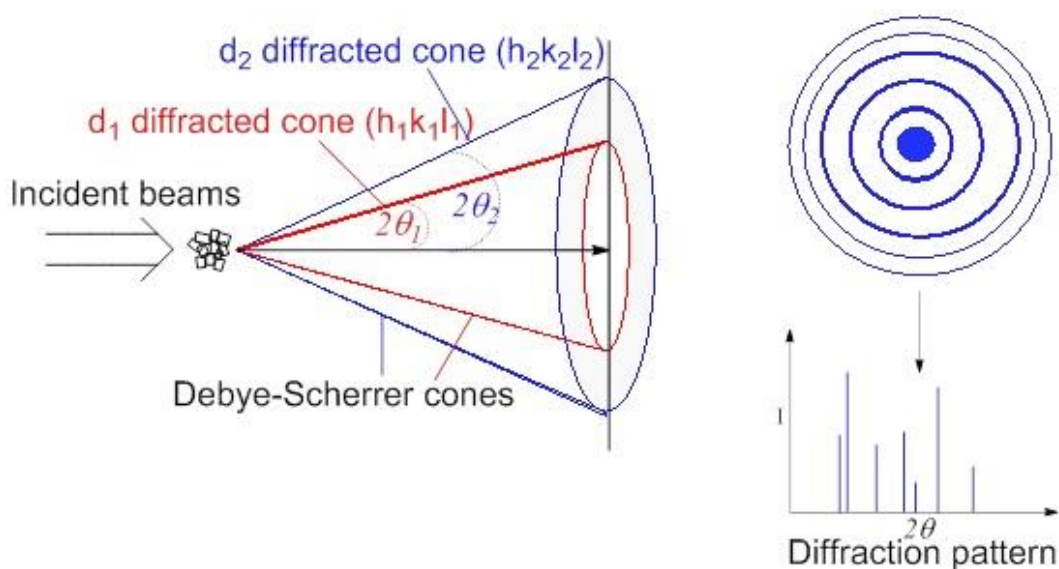
Figure 2.3 Schematic diagram of the generation of Debye-Scherrer cones.

When a powder reflects X-rays and yields a PXRD pattern, a combination of the unique set of angles (2θ) at which peaks are present, and the intensities of the peaks produces a fingerprint which can be used to identify crystal structures. PXRD patterns contain information within the peak positions, peak shape, peak intensity and non-indexed lines, which can be used to determine further information about the sample analysed.

Table 2.2 Content of a powder X-ray diffraction pattern.

Feature	Information Obtained
Background	Amorphous fraction
	Incoherent scattering
	Contribution from sample holder or sample preparation
Peak positions	Lattice parameters
	Space group
	Symmetry
	Zero point
	Sample height
	Wavelength of radiation
Non-indexed lines	Presence of a crystalline impurity
Peak intensities	Atomic positions
	Preferred orientation
	Thermal vibrations
	Amount of each phase present
Peak widths (FWHM)	Crystal size
	Crystallinity
	Strain
	Stress
	Instrument functions

2.2.3.3 PXRD Lab Diffractometers

For PXRD lab diffractometers there are two different geometries, transmission and reflection, which are shown in Figure 2.4. Providing the sample preparation is correct and the powder has a random orientation of the crystallites, then both geometry diffractometers should produce the same PXRD pattern; however both geometries have certain advantages and disadvantages depending on the sample being analysed. Transmission geometry can be preferential for a sample with low absorption, and for samples with preferred orientation or air-sensitive samples, the sample can be loaded into a capillary and the diffraction pattern can be recorded in transmission mode. Reflection geometry is beneficial for strongly absorbing samples which can be mounted on a flat surface.
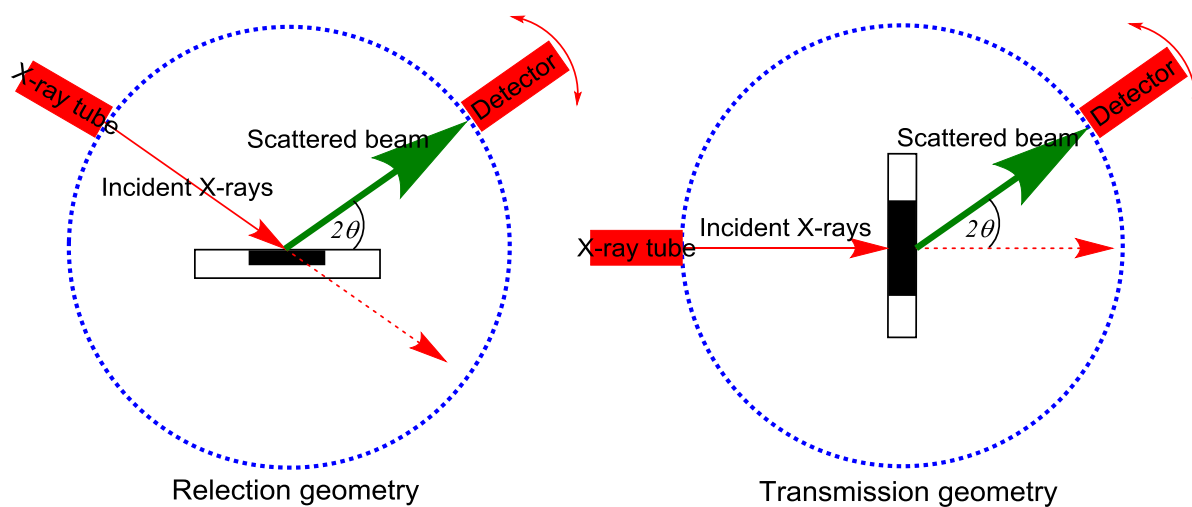
Figure 2.4 Lab Diffractometer Geometries.

In this work most of the PXRD data was collected using a Siemens D5000 diffractometer in transmission mode with capillary stage fitted. A copper X-ray source was fitted with a monochromator producing Cu K_{a1} radiation at a wavelength of 1.54056 Å. The samples were prepared by grinding in a pestle and mortar and firmly

packed into either 0.686 mm or 1.1 mm Kapton tube capillaries. The Kapton tubes give very little scattering compared to the crystalline samples and therefore do not contribute much to the background. The samples were rotated throughout data collection and the diffraction patterns were produced electronically as .raw files.

Variable temperature studies were also carried out using a Siemens D5000 with an Oxford Cryostream stage (using liquid nitrogen) fitted to carry out the cooling of the samples. Desired temperatures were programmed with a dwell time of 5 minutes before the collection started to allow for crystallisation or melting to take place. The samples which were mostly liquid at room temperature were injected and sealed in 1.0 mm special glass capillary with 0.1 mm glass walls, and were rotated during data collection.

2.2.3.4 Synchrotrons

Synchrotron radiation sources for X-ray diffraction experiments have many advantages over traditional laboratory sources, producing higher quality powder diffraction data[61]. Advantages include high intensity, high vertically collimated radiation, tuneable wavelength, a range of sample environments and a high signal to noise ratio; all of which lead to better structural solution, phase identification, quantitative analysis and rapid data collection[61].

Synchrotron radiation is created when electrons or positrons are accelerated to near the speed of light in circular vacuum tubes (storage rings), which are guided around by a range of magnets[61]. Storage rings are made up of straight sections and curved sections where the electrons are steered around by bending magnets[61]. It is in the curved sections where synchrotron radiation is emitted, and channelled off

towards experiment hutches to be used as a source of X-rays for experiments[61]. In the straight sections of the storage ring, insertion device magnets such as wigglers and undulators, are placed to oscillate the beam of electrons by producing alternating magnetic fields[61]. These insertion devices can then tailor the beam for different applications and experiments.

Synchrotron data was collected at beamline I11, Diamond Light Source, UK. Samples were firmly packed into either 0.7 mm special glass capillaries or 1.1 mm Kapton tube capillaries and sealed. The capillaries were then fixed onto magnetic holders and aligned before mounting onto a sample spinner therefore reducing preferred orientation effects. The exact wavelength was determined by running silicon standards before data collection began, and were typically around 0.83 Å.

2.2.4 Neutron diffraction

In neutron diffraction the neutron beam is scattered by the nuclei of the atoms in the sample following Bragg's law, with the intensities of the diffracted beams detected in a similar way to X-ray diffraction. Compared to X-ray diffraction in which the beam of X-rays is scattered by electrons in the sample, neutrons are scattered by the nucleus allowing for much better sensing of lighter atoms in the presence of heavier atoms. Whilst scattering is relatively strong with X-rays, neutron mass scattering is fairly weak but can still be a useful technique to use. Along with better detection of heavier atoms compared to lighter atoms, neighbouring atoms in the periodic table and even different isotopes of the same elements can have significantly different scattering cross sections, which can give rise to better differentiation. In contrast, X-ray diffraction scattering varies linearly with atomic

number so neighbouring elements in compounds may have similar X-ray diffraction data. Due to the relatively weak scattering of neutrons, large sample sizes of over 1 g are often needed, and the signal-to-noise ratio is much weaker than in X-ray diffraction resulting in much longer scan times required to gain sufficient counting statistics.

There are commonly two different ways in which neutrons are produced for neutron diffraction; the first is from a nuclear reactor and the second is from a pulsed spallation source. Neutrons produced at a nuclear reactor are commonly termed 'thermal neutrons' and typically have a wide range of energies, so to select the required wavelength a monochromator is required. The second source of neutrons is from a pulsed spallation source where neutrons are generated by bombarding a heavy metal target with energetic particles such as protons which are accelerated up to 1 GeV.

The neutron source used in this work, ISIS at the RAL (Rutherford Appleton Laboratory), generates neutrons using a spallation source by using a particle accelerator to fire a pulsed beam of protons at 0.8 GeV at a tungsten target. The polychromatic nature of the pulsed neutron beam allows for data collection to be carried out using a time of flight (TOF) method, instead of changing the angle of the detector or the energy of the neutron beam. TOF experiments use diffraction from a variety of different wavelengths due to the polychromatic nature of the beam with detectors at fixed angles and distance from the spallation source discriminating by time of arrival at the detector.

The wavelength of a neutron is related to its energy via Equation 2.2;

$$\lambda = \left(\frac{h^2}{2mE}\right)^{\frac{1}{2}} = \frac{9.04}{E^{\frac{1}{2}}} \qquad \textbf{Equation 2.2}$$

where λ is in Å, E is the energy of the neutron in meV, and the mass m is taken as 1.675×10^{-27} kg. At a pulsed spallation source the method of determining the wavelength is to measure the time of flight, t, of the neutron over a known path length, L (from the source to the sample and the subsequent scattering path to the detector). The wavelength is related to the velocity, v, of the neutron and thus substituting into Equation 2.2 gives;

$$\lambda = \frac{0.003955}{v} = \frac{0.003955 \cdot T}{L} \qquad \textbf{Equation 2.3}$$

where v is in m(μs)$^{-1}$, t in μs and L in m, which gives a linear relationship between the neutron wavelength and the time of flight. The combination of Equation 2.3 and Bragg's law (Equation 2.1) gives the following relationship (Equation 2.4) between the time of flight and the different d-spacing at fixed scattering angles in convenient units of time in μs and d-spacing in Å.

$$t_{hkl} = 505.55685 \cdot L \cdot d_{hkl} \sin\theta \qquad \textbf{Equation 2.4}$$
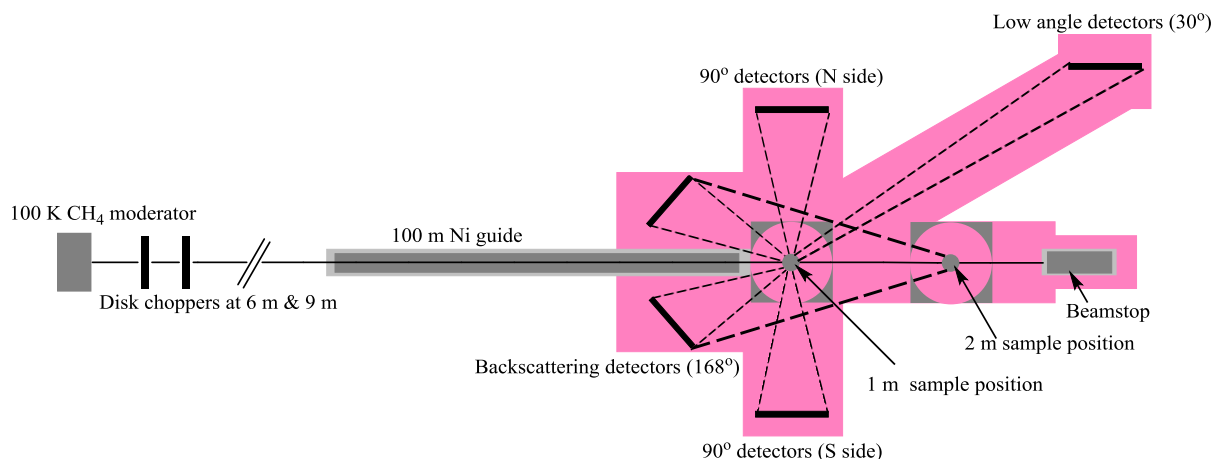
Figure 2.5 Schematic of HRPD (high resolution powder diffraction) detector configuration[62].

A schematic of HRPD, the instrument which was used in this work is shown in Figure 2.5, where the time of flight path length is 100 m from the spallation target, and there are three banks of detectors at set fixed angles of 30°, 90° and back scattering 168°.

The samples were ground and loaded into vanadium cans and cooled and heated through variable temperature experiments using liquid helium in a cryostat.

2.2.5 Indexing and Space Group Determination

The first step in solving a crystal structure from PXRD data is indexing. Indexing is the identification of lattice parameters for the unit cell. If these parameters are incorrectly determined then structure solution will fail. Whereas in single crystal diffraction the information is recorded from the reflected position in three dimensions, in PXRD the three dimensional diffraction information is lost as the diffraction information is recorded in one dimension. The aim of indexing is the reconstruction of the three dimensional reciprocal lattice information, from one dimensional data

(selected *2θ* peak positions), with the generation of possible lattice parameters and figures of merit ranking the possible unit cells the end goal. Each successfully indexed peak will be assigned a *hkl* reflection, and it is from this that the space group can be determined from the systematic absences of the *hkl* reflections.

A large number of programs are available for indexing such as CRYSFIRE[63], EXPO[64] and TOPAS[65], but in this project TOPAS[65] was used for indexing and space group determination.

2.2.6 Pawley / Le Bail Fits

Pawley and Le Bail methods are both pattern decomposition techniques of `structureless refinement` which can be used to achieve more accurate lattice parameters, zero point, peak shape and help towards space group determination. A Pawley phase fit uses the following parameters for refinement:

- Intensity of each reflection with indices *hkl*

- Unit cell metric tensor parameters

- Instrumental zero error

- Peak width parameters

- Any other peak shape parameters

Whilst many of the above parameters are the same as used in Rietveld refinement, the Rietveld method calculates the peak intensity from the structure factors *F(hkl)*, which are calculated from the parameters of the model structure. Compared to the Pawley fit method, the Le Bail method uses the above parameters apart from the individual peak intensities. The individual peak intensities are not treated as least-square parameters, and are therefore never refined which greatly

speeds up each cycle of least squares. The peak intensities with Le Bail are all initially set to an arbitrary number e.g. 1 and treated as F_{hkl}(calc). The Rietveld procedure of extracting F_{hkl}(obs) is applied and are used instead of a structural model. The correct process is iterated and fresh observed intensities are obtained.

As the intensities in both Pawley and Le Bail phase fits are not constrained by a structural model, the weighted profile *R*-factor is usually lower and better than a weighted profile *R*-factor obtained by full Rietveld refinement. Pawley or Le Bail fits may also be able to help determine which space group may be correct, if overlapping peaks hamper space group determination by visual inspection.

TOPAS[65] was used to carry out Pawley fits to refine lattice parameters and confirm space groups of the phases recorded before structure solution was attempted.

2.2.7 Structure Solution

There are several problems when trying to solve a crystal structure from PXRD data such as the uncertainty in the background determination, the possible presence of preferred orientation, and that powder data is essentially three dimensional reciprocal space, represented as one dimensional data and therefore overlapping of diffraction peaks[61].

The electron density in a unit cell can be represented by a single wave which is a combination of the magnitude and relative phase for X-rays scattered along that direction, with the mathematical representation of this wave called a structure factor. It is however only possible to measure experimentally the amplitude of the wave in a diffraction pattern which means the phase information is missing, termed the phase problem. The amplitude of the wave can be derived from the intensities in a

diffraction pattern, and the phase can be derived from knowledge of the molecular structure. The intensity of the diffraction peaks are related to the structure factors by Equation 2.5:

$$|F_{hkl}|^2 \propto I_{hkl} \qquad \textbf{Equation 2.5}$$

Structure factor for a reflection can be derived by Equation 2.6:

$$F_{hkl} = \sum_{j=1}^{atoms} f_{(j)} exp[2\pi \cdot i(hx+ky+lz)] \qquad \textbf{Equation 2.6}$$

where $f_{(j)}$ is the scattering factor of atom j.

To calculate the electron density at position xyz, a summation of contributions to point xyz of waves scattered from plane xyz, whose amplitude depends on the number of electrons in plane added with the correct phase relationship, gives Equation 2.7 which is a Fourier transform of Equation 2.6.

$$\rho_{xyz} = \frac{1}{V} \sum |F_{hkl}| exp[-2\pi i(hx+ky+lz)-\alpha_{hkl}] \qquad \textbf{Equation 2.7}$$

Where V is the volume of the unit cell, and α_{hkl} is the phase associated with the structure factor amplitude $|F_{hkl}|$.

Structure solution from PXRD data was traditionally started by extracting the intensities of individual reflections (using either Pawley or Le Bail pattern decomposition) and then either using a Patterson Method (PM) or a Direct Method (DM)[61]. A method that doesn't require pattern decomposition and extraction of reflection intensities but instead uses the whole experimental diffraction pattern is Direct Space Techniques (DST)[61]. Global optimisation algorithms are used for DST to locate atom positions, orientate and solve the structural model[61]. There are many different methods for structure solution such as Monte Carlo, simulated annealing, genetic algorithms and grid search methods; however charge flipping and simulated

annealing will be detailed below. They are fairly different methods of structure solution, with charge flipping only requiring the X-ray wavelength and the diffraction data set to start with, but simulated annealing requires a model structure or part structure to begin.

2.2.7.1 Charge Flipping

Charge flipping is an *ab initio* structure solution method similar to DM belonging to a family of dual space iterative phasing algorithms, that begin with no preliminary chemical or phase information, but just knowledge of the X-ray wavelength and a diffraction data set[66]. A diffraction experiment produces information on the magnitudes of structure factors which represent electron density in reciprocal space, and it is this that charge flipping relies on in the algorithm[67]. The basic charge flipping algorithm comprises of four steps, as shown in Figure 2.6, transforming between the dual spaces (real and reciprocal)[67]:

1. A real space modification of the electron density
2. A Fourier transform into reciprocal space
3. A reciprocal space modification of calculated structure factors
4. An inverse Fourier transform back into real space

$$\rho(\mathbf{r}) \xrightarrow{\ \ \textbf{1}\ \ } g(\mathbf{r})$$

$$FFT^{-1}\uparrow \textbf{4} \qquad\qquad \textbf{2}\downarrow FFT$$

$$F(\mathbf{h}) \xleftarrow{\ \ \textbf{3}\ \ } G(\mathbf{h})$$
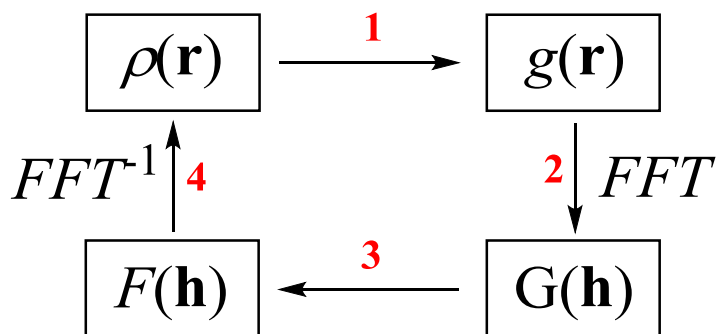
Figure 2.6 Simple Fast Fourier Transform (FFT)[67].

Where;

$\rho(\mathbf{r})$ is the electron density ($\rho_1 + \rho_2$)

$g(\mathbf{r})$ is the electron density ($\rho_1 - \rho_2$)

G($\mathbf{h}$) is the temporary structure factor

$F(\mathbf{h})$ is the structure factor constructed from calculated phases G($\mathbf{h}$)

Continuous electron density is required to be sampled with FFT at regular grid points, as the small number of pixels that have high electron density contain most of the structural information surrounded by areas of little or zero electron density[67]. There are three stages to a successful charge flipping run with:

1. Initial transient stage with around 10 cycles reaching a subspace with zero plateaus with positive peaks.

2. A stagnation period where a detailed exploration of the subspace takes place.

3. Final stable state after convergence has occurred.

The charge flipping algorithm has several advantages; simplicity of the algorithm, and the truly *ab initio* character as the use of atom types and symmetry are not used, with the electron density output represented on a grid[67]. Charge flipping can also be used when part of the structural information is known for example the

space group and symmetry, chemical composition, atom types or small connectivity of the crystal structure which can then help towards a solution of the full crystal lattice[67].

2.2.7.2 Simulated Annealing

Simulated annealing is a direct space approach where parameters are adjusted in real space rather than reciprocal space. A trial fragment or whole crystal structural model is constructed, utilising known atomic information and the possible geometric degrees of freedom. The fragment or whole structure model diffraction pattern is calculated, and compared to the observed diffraction pattern. The structural model is then adjusted in a random fashion to improve the fit between observed and calculated pattern. The change in crystal structure is then either accepted or rejected depending on limits and criteria set by the program and user, and repeated until the best agreement between the observed and calculated with the lowest energy minima is reached. The structure can then be improved by Rietveld refinement. Simulated annealing is an attempt to simulate the thermodynamic process of annealing, where materials are slowly crystallised over time, and the probability of observing one energy state over another is given by the Boltzmann distribution $\exp(\Delta E/T)$ [68]. It is an iterative numerical process where the global minimum is sought, and the search for the global minimum can be controlled by parameters such as the initial temperature, rate of temperature decrease and the relationship between temperature decrease and the amount of atom displacement that can take place[68].

TOPAS[65] was used to run simulated annealing to solve the structures of several phases detailed in this project.

2.2.8 Rietveld Refinement

Rietveld refinement[69,70] is a "whole pattern fitting" strategy to refine a calculated XRD pattern, to fit observed XRD data and obtain a more accurate crystal structure. A crystallographic model is calculated from lattice parameters, space group, atomic positions and instrumental parameters including the diffractometer wavelength[71]. Variables relating to the crystal structure and instrumental parameters can be either fixed or adjusted and refined through a least squares method to minimise the difference between the observed experimental diffraction pattern and the calculated diffraction pattern to obtain the best fit which is the residual shown in Equation 2.8[71].

$$S_y \ = \ \sum_{i=1}^{n} w_i \, (y_i - y_{ci})^2 \qquad\qquad \textbf{Equation 2.8 - Residual}$$

Where S_y is the residual, the quantity which is minimised by the refinement,

w_i the weighting factor,

y_i and y_{ci} are the observered and calculated intensities at the ith step.

The calculated intensity shown in Equation 2.9 is the sum of all Bragg reflections within the range;

$$y_{ci} \ = s \sum_{K} L_K \left| F_K{}^2 \right| \emptyset_i (2\theta_i - 2\theta_K) P_K A - y_{bi} \qquad \textbf{Equation 2.9 - Intensities}$$

Where;

s is the scale factor,

A is the absorption factor,

$\emptyset$ is the reflection profile function,

K represents the Miller indices *hkl*,

L_K is the Lorentz polarisation factor,

F_K is the structure factor,

P_K is the preferred orientation function,

Y_{bi} is the background intensity which represents the Miller indices *hkl* for a Bragg reflection at the ith step.

The mathematical and statistical agreement between the calculated and observed diffraction patterns can be evaluated by the difference profile plot of the observed and calculated patterns, but also by several functions with the most common in Equations 2.10-2.13 [69]. The weighted profile *R*-factor (R_{wp}) is defined in Equation 2.10;

$$R_{wp} = \left\{ \frac{\sum_i w_i [y_i - y_{ci}]^2}{\sum_i w_i [y_i]^2} \right\}^{\frac{1}{2}}$$ **Equation 2.10 - R_{wp}**

R-pattern (R_p) is defined in equation 2.11,

$$R_p = \frac{\sum |y_i - y_{ci}|}{\sum y_i}$$ **Equation 2.11 - R_p**

R_{exp} is the expected *R*-factor is defined in equation 2.12,

$$R_{exp} = \left\{ \frac{(N - P)}{\sum_i^N w_i y_i^2} \right\}^{\frac{1}{2}}$$ **Equation 2.12 - R_{exp}**

Where;

N is the number of observations

P is the number of parameters.

The ratio between the weighted profile *R*-factor and the expected *R*-factor (which reflects the quality of the data i.e. the counting statistics) is the goodness of fit χ shown in Equation 2.13,

$$GOF = \chi = \frac{R_{wp}}{R_{exp}} \qquad \textbf{Equation 2.13 - } \chi$$

These factors are only indicative of how well the calculated pattern fits the observed pattern in the mathematical sense, as a good fit can be achieved in local minima, but the structure may have no chemical sense. It is therefore very important to make sure that the refined structure makes chemical sense, with sensible bond lengths and bond angles. The output crystallographic information file (cif) file, which contains the space group, lattice parameters, atomic positions and fractional occupancies allows visualisation of the crystal structure. To help prevent the refinement producing crystal structures which don't make chemical sense, geometric restraints such as bond lengths and bond angles can be applied, preventing the atoms moving to unrealistic positions[69].

A large number of programs can be used to run Rietveld refinement, but in this project all refinements were run using TOPAS[65].

2.3 Computational Gaussian Dipole Calculations

The Gaussian 09[72] computer program was used to calculate dipole moments of several crystal systems in this project. This was carried out using Gaussian's molecular energy calculation which computes energy and electronic properties of the systems including dipole moments, partial charges, and bond orders of the atomic configuration without optimisation using the specified theory and basis set.

Several different theory and basis sets were used to see whether the dipole values would change or stay the same on using more complicated theories and basis sets. Theory sets and basis sets used included:

- Hartree-Fock Basic 3-21G

- Hartree-Fock Routine 6-31G(d)

- B3LYP Routine 6-31G(d)

- AM1 STO-6G

- PM3 STO-6G

The Hartree-Fock (HF) theory is an *ab initio* model which approximates that Coulombic electron – electron repulsion can be averaged and describes each electron by an orbital with the total wave function given as a product of orbitals[73]. With restricted Hartree-Fock each spatial orbital contains two electrons (one α and one β spin) and a singlet wave function type[73]. Whilst the HF theory can produce accurate results many newer approaches have been reported.

The B3LYP (Becke three-term correlation functional Lee, Yang and Parr) exchange functional, is a hybrid DFT (density functional theory) method. Whilst the HF theory derives the properties from wave functions, which are mathematical constructs and not a physical reality; DFT computational methods derive properties from the determination of the electron density[73]. B3LYP has component exchange and correlation functionals, but also has three parameters which define the hybrid functional, which specify how much exchange energy (combined with the energy from HF theory) is mixed in.

Two simpler semi empirical versions of Hartree-Fock theory which use empirical corrections to improve performance are AM1 (Austin Model 1) and PM3

(Parametric Model Number 3). Parametrised corrections are made in these methods to correct the approximate quantum mechanical model used. The calculated energies are expressed as heats of formations with the semi empirical calculations correcting thermochemical properties to 300 K, whereas Hartree-Fock and DFT do not yield all calculations at the same temperature.

A set of wave functions which describe the shape of the atomic orbitals is termed the basis set, with the level of approximation in the calculation directly related to the basis set level used. The more accurate the results the longer and more complicated the basis set is likely to be. Three basis sets were used with the simplest STO-6G then 3-21G and the most complicated 6-31G(d). STO-6G is the simplest basis set where only the minimum number of orbitals are used to contain all the electrons in the atoms and six Gaussian type orbitals used. 3-21G and 6-31G(d) are both split valence basis sets with the first number describing the number of Gaussian functions summed to describe the sp-type inner shell, the second number describes the number of Gaussian functions summed to describe the s- and p-type inner valence orbitals, and the third number describes the number of Gaussian functions summed to describe the outer valence s- and p-type orbitals. The 6-31G(d) basis set adds polarisation functions to heavy atoms and is used in many calculations of medium and large systems.

In Gaussian the visual output of dipole values are centred at the centre of mass of the calculation, with the length of the dipole moment arrow 1 Debye corresponding to 1 Angstrom pointing from positive to negative (towards excess electron density).

3. Chapter 3 – Methyl and Ethyl Stearate

3.1 Introduction

Methyl stearate, $CH_3(CH_2)_{16}C(O)OCH_3$, (Figure 3.1) is one of the five main compounds in biodiesel that cause poor cold flow properties due to rapid crystallisation of flat platelet crystals as temperatures drop towards 273 K, which can block fuel filters on start-up of a vehicle. These poor cold flow properties restrict the use of biodiesel to a fuel extender; it cannot be a complete replacement of petroleum diesel in its current form. Over the years, many additives have been designed to combat the same cold flow properties of conventional petroleum diesel, however there have been a lack of additives made which are structurally selective to the compounds which crystallise out in biodiesel. However, before these additives can be designed accurate crystal structures of the methyl esters which form, need to be solved.
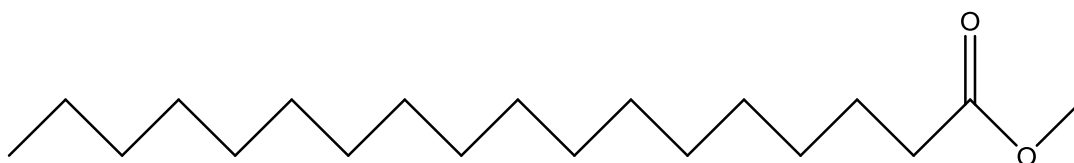
Figure 3.1 Chemical structure of Methyl Stearate.

3.1.1 Previously known structures

There are currently five known polymorphs of methyl stearate, two of which were briefly mentioned in chapter 1. Table 3.1 contains the lattice parameters of the five known structures and Figure 3.2 shows the simulated PXRD patterns.

Table 3.1 Lattice parameters of the five methyl stearate structures.

Structure code	Unit cell & space group	a (Å)	b (Å)	c (Å)	β (°)	Volume (Å³)	Z
1960[45]	Monoclinic A2/a	5.61	7.33	106.60	116.78	3920	8
1970[46]	Orthorhombic Pnab	5.613	7.354	95.147	-	3912	8
I19 (at 100 K)[74] unpublished	Monoclinic C2/c	95.24	7.09	5.54	93.22	3735	8
Slow Cooled Melt[75] unpublished	Monoclinic C2	47.960	7.400	5.603	91.153	1987.97	4
Quench Cooled Melt[76] unpublished	Monoclinic Cc	49.021	7.213	5.557	77.528	1918.33	4
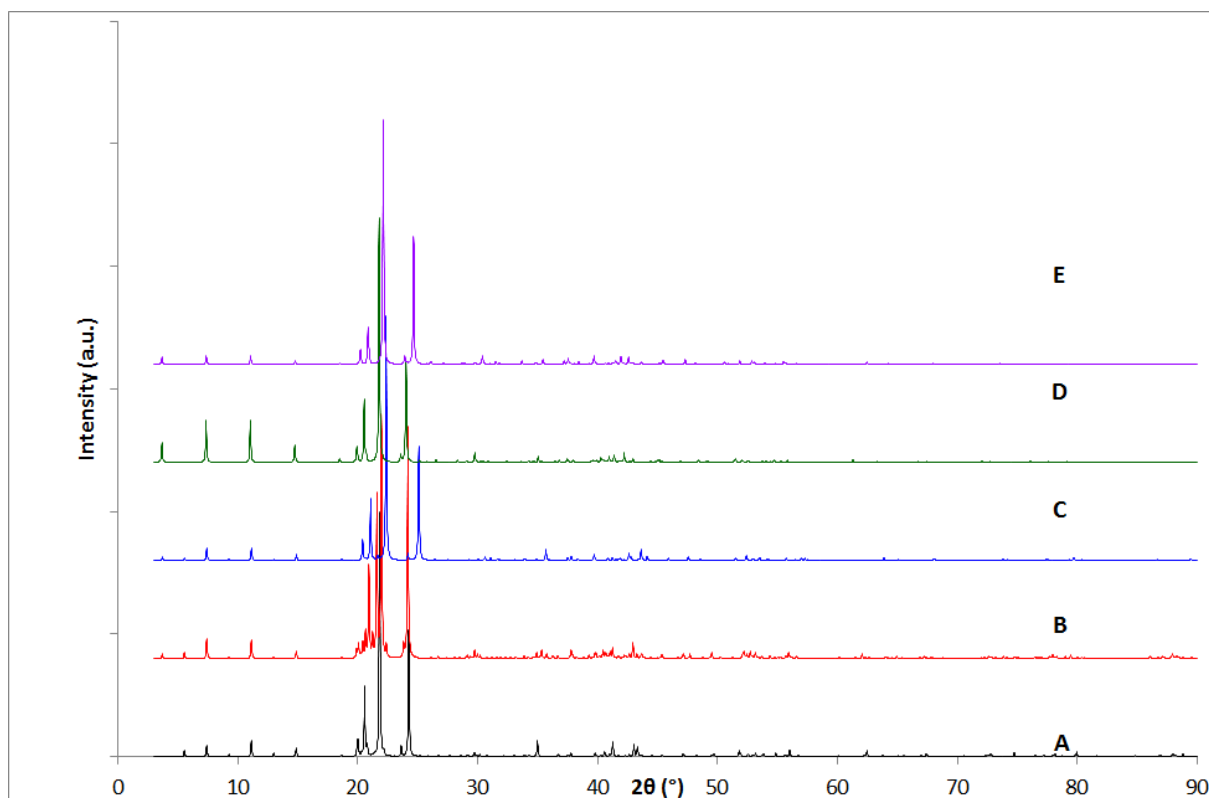
Figure 3.2 Simulated PXRD patterns of methyl stearate based on (A) the 1960 structure (room temperature)[45], (B) the 1970 structure (room temperature)[46], (C) the I19 structure (100 K), (D) the structure formed from the melt by slow cooling (233 K)[75], (E) the structure formed from the melt by quenching (193 K)[76]. λ = 1.54056 Å

Whilst the lattice parameters and the simulated PXRD patterns are fairly similar, there are subtle differences between the methyl stearate crystals structures, which will be discussed below. The 1970 orthorhombic polymorph is the only PXRD pattern which is significantly different, as all the monoclinic phases have very similar PXRD patterns; however the three structures solved from single crystals with eight molecules in the unit cell have supercell peaks at 9.2° and 13.0° 2θ which are not present in either of the two melt phases.

Methyl Stearate 1960

The methyl stearate 1960 structure (this structure will be referred to as MS-*A*2/*a*)[45] was solved from a single crystal grown from carbon disulphide between 258 K and 261 K. The structure, as shown in Figure 3.3, is a monoclinic *A*2/*a* phase and has head to head, tail to tail alignment (both within the *ac* planes and between the layers stacking along *b*). Four molecules align along the long *c* axis of unit cell, with bilayer stacking and a total of eight molecules in the unit cell.
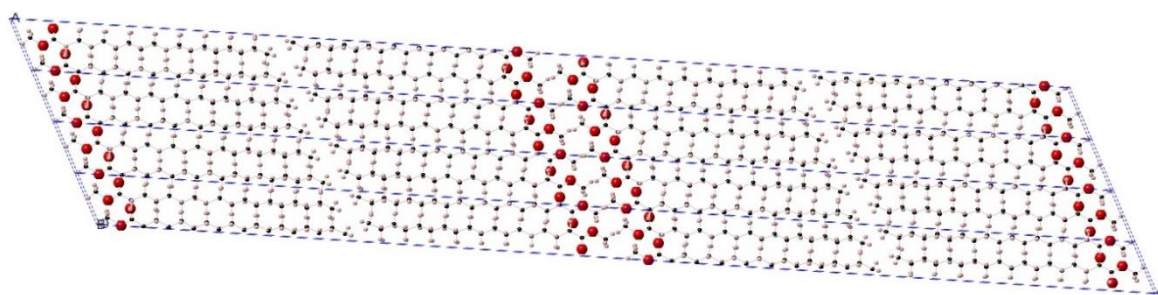
Figure 3.3 Methyl Stearate *A*2/*a* structure viewed down the *b*-axis.

Methyl Stearate 1970

The second methyl stearate polymorph is an orthorhombic *Pnab* 1970 structure (this structure will be referred to as MS-*Pnab*)[46] which has the same bilayer stacking, and eight molecules in the unit cell as the MS-*A*2/*a* structure. The single crystal that the structure was solved from was also grown from the same carbon disulphide solvent as the MS-*A*2/*a* structure. Unlike the MS-*A*2/*a* structure which has alignment of the molecules along the long axis of the unit cell, in the MS-*Pnab* structure shown in Figure 3.4 the molecules are aligned diagonally across the *ac*-plane of the unit cell.
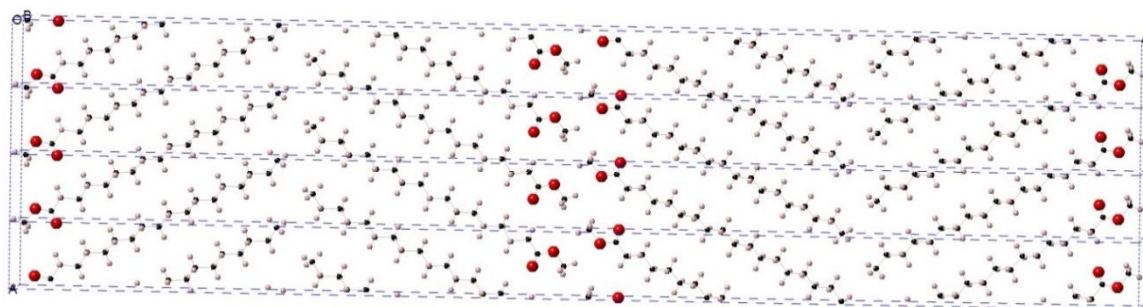
Figure 3.4 Methyl Stearate *Pnab* structure viewed down the *b*-axis.

Whilst the molecules are orientated diagonally across the unit cell there is a specific layout of the molecules which is shown in the schematic of Figure 3.5.
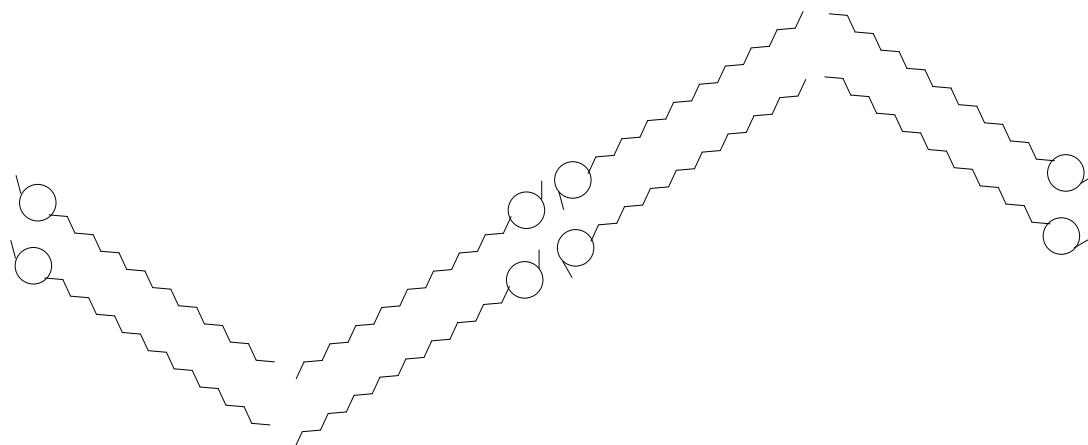
Figure 3.5 Schematic of the molecular layout of the methyl stearate *Pnab* structure.

Methyl Stearate I19

The third methyl stearate polymorph is an unpublished second monoclinic phase with a *C*2/*c* space group (this structure will be referred to as MS-*C*2/*c*). Infineum grew the single crystal from toluene in a cold room, and collected the data used to solve this polymorph at 100 K at Diamond beamline I19[74]. As with the previous two single crystal structures the head to head, tail to tail bilayer

arrangement of the molecules is kept (both within the *ac*-plane and between the

layers stacking along *b*) as shown in Figure 3.6.
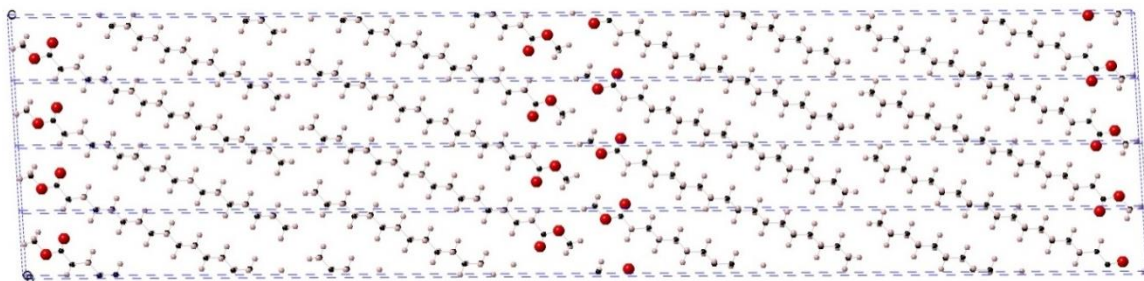
Figure 3.6 Methyl Stearate *C*2/*c* structure viewed down the *b*-axis.

As with the MS-*Pnab* structure the molecules are orientated diagonally across

the unit cell, with the schematic shown in Figure 3.7. The molecules, however, are

aligned all in a straight line as with the MS-*A*2/*a*, whereas the MS-*Pnab* has a

herringbone alignment of the molecules.
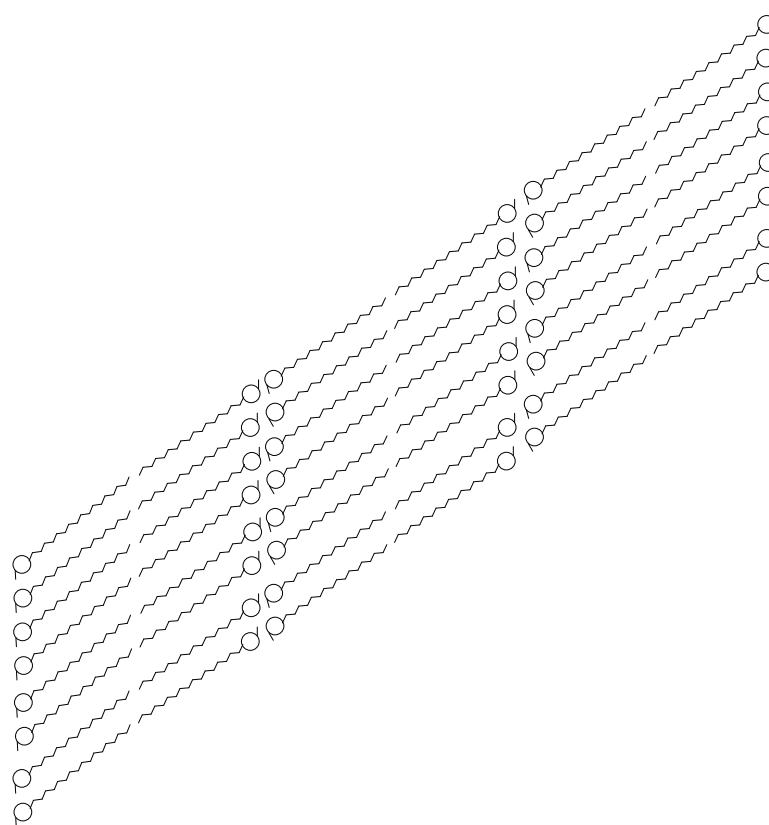
Figure 3.7 Schematic of the molecular layout of the methyl stearate *C*2/*c* structure.

Methyl Stearate Slow Cooled C2 Melt

The fourth polymorph of methyl stearate is an unpublished structure formed

from the melt in a capillary, using a cooling rate of 100 K/hr. The structure was solved

from PXRD Diamond beamline I11 data collected by Infineum by Dr Tzu-Yu Chen[75].

Unlike the three structures which were solved from single crystal data, which have a

long axis of over 95 Å and eight molecules in the unit cell; the slow cooled melt

phase (which will be referred to as MS-*C*2) has only four molecules in the unit cell,

and the long axis is about half the length. MacGillavry[46] also reported a phase from

the melt with similar unit cell parameters as this MS-*C*2, however the crystals were of

too poor quality for structural solution. As with the previous structures, the head to

head, tail to tail alignment is retained within the *ac*-layers with similar diagonal

arrangement to the MS-I19 structure as shown in Figure 3.8; however there is

alternating layering along the *b*-axis with head to tail packing as shown in Figure 3.9.
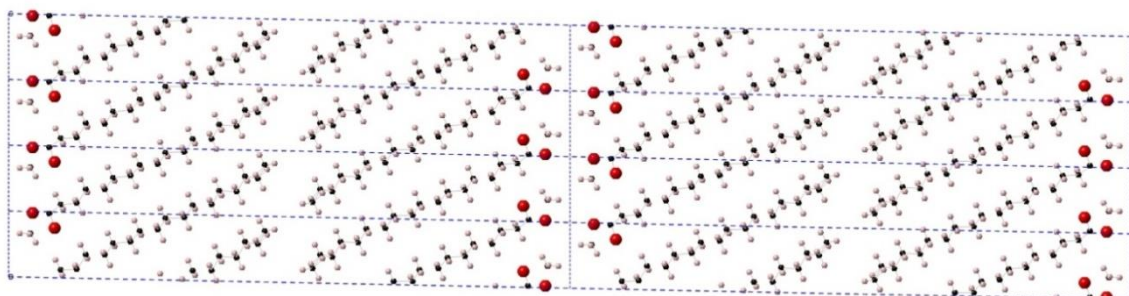
Figure 3.8 Methyl Stearate *C*2 structure viewed down the *b*-axis.
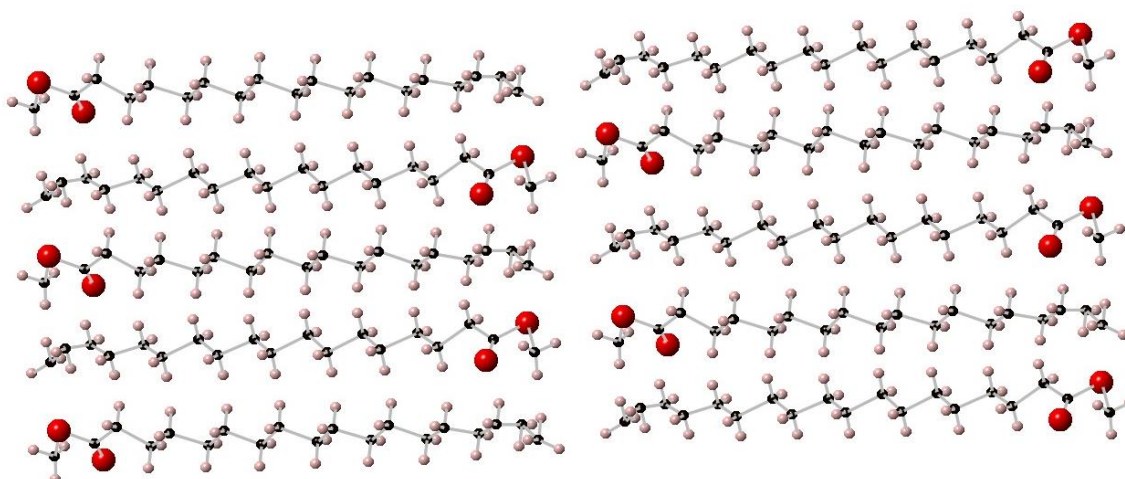
Figure 3.9 Methyl Stearate *C*2 structure viewed down the *c*-axis.

Methyl Stearate Quench Cooled Cc Melt

The fifth polymorph of methyl stearate is another unpublished form from the

melt (which will be referred to as MS-*Cc*), however this structure was quench cooled

from melted methyl stearate with liquid nitrogen. The structure was then solved from

PXRD data collected at Diamond beamline I11 by Xiaojiao Liu[76] from the University

of Edinburgh. As with the MS-*C*2 polymorph, this MS-*Cc* phase also only has four

molecules in the unit cell with the molecules lying diagonally across the *ac*-plane of
the cell, however the alignment of the molecules is slightly different.
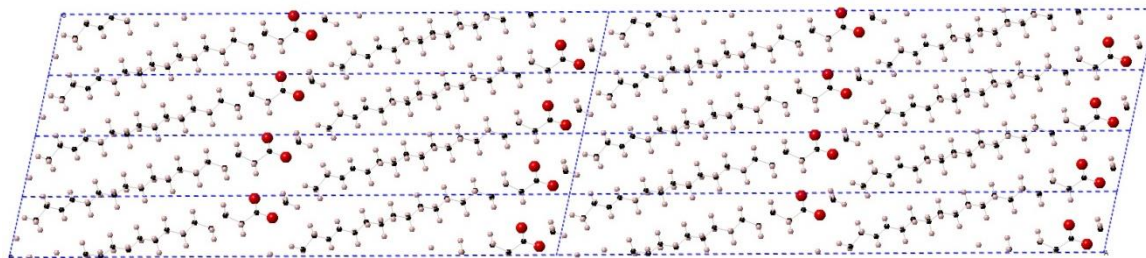
Figure 3.10 Methyl Stearate *Cc* structure viewed down the *b*-axis.

Within the *ac-layers* there is head to tail alignment of the molecules as shown in
Figure 3.10, but stacking the layers along *b* there is head to head, tail to tail
alignment as the molecules stack up, as with the single crystal structures.

Whilst many of the simulated PXRD patterns and lattice parameters are very
similar to one another, it is clear however that the structures differ in the orientation
and packing of the molecules.

3.2 Methyl Stearate as-bought

To determine the polymorph of methyl stearate as-bought, a lab PXRD scan was run and compared to the five known phases as shown in figure 3.11.

3.2.1 Methyl Stearate lab data
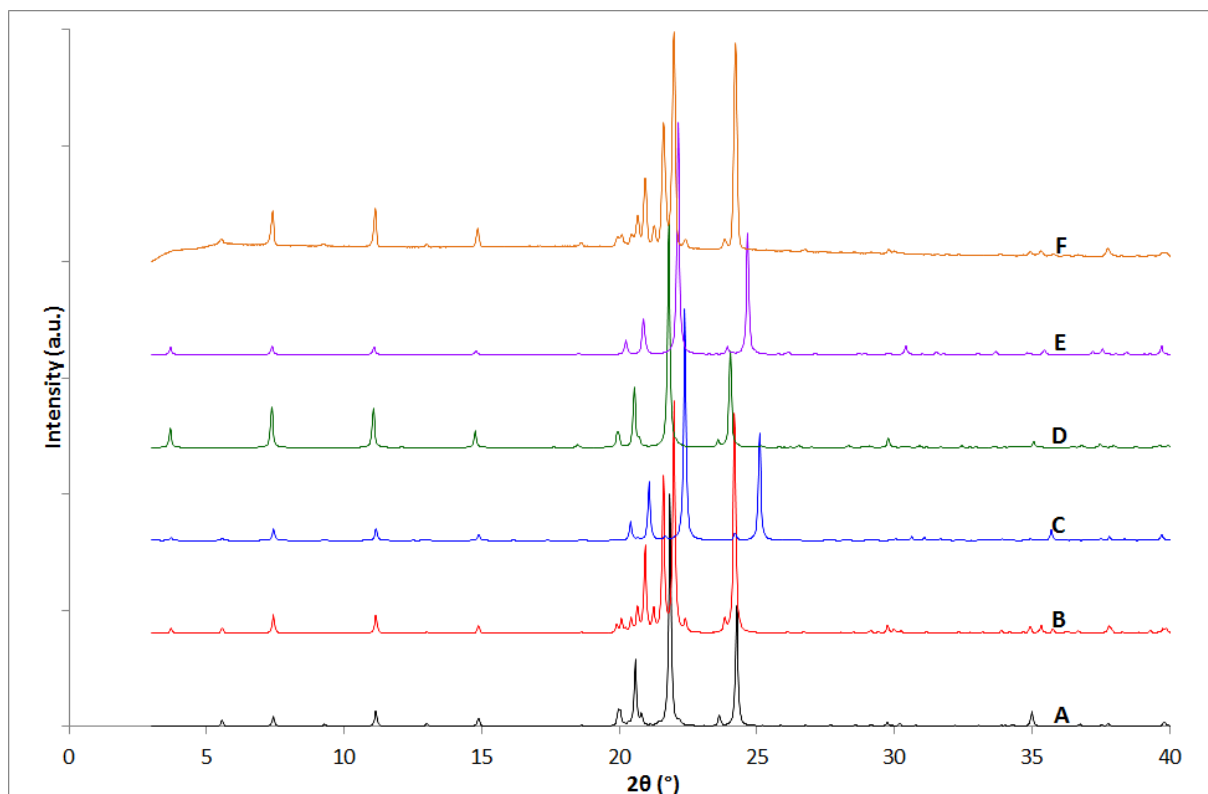
Figure 3.11 Simulated ((A) to (E)) and observed (F) PXRD patterns of methyl stearate (A) the MS-*A2/a* structure (room temperature)[45], (B) the MS-*Pnab* structure (room temperature)[46], (C) the MS-*C2/c* structure (100 K)[74], (D) the MS-*C2* structure (233 K)[75], (E) the MS-*Cc* structure (193 K)[76], (F) collected from a sample as bought. *λ* = 1.54056 Å

From visual comparison of Figure 3.11, the methyl stearate as-bought scan appears to be the same as the MS-*Pnab* phase. A Rietveld refinement was run as shown in Figure 3.12, with the refined lattice parameters shown in Table 3.2. In this refinement and all Rietveld refinements produced in this work, soft bond distance and

angle restraints (example text file for restraints shown in appendix 3.1) were used to prevent atoms being refined to unrealistic positions and, H-riding was used to keep the hydrogens in idealised positions around the molecules. Lattice parameters and atomic positions were allowed to refine along with standard TOPAS background and peak shape profiles to produce a suitable calculated pattern. A good fit between the calculated and observed profiles is shown in Figure 3.12, and the lattice parameters were refined to reasonable values for this crystal structure with small errors (atomic positions can be found in appendix 3.1.1), therefore confirming the crystal structure of the as-bought phase.
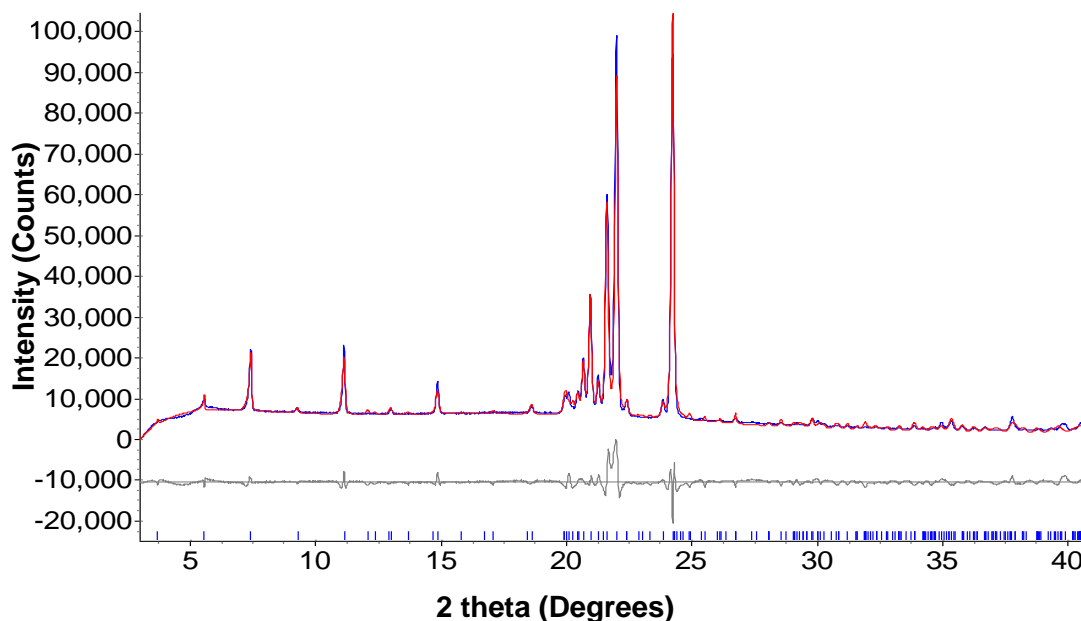
Figure 3.12 Observed (blue line) and calculated (red line) lab data profiles for the Rietveld refinement of methyl stearate as-bought using the MS-*Pnab* structure[46]. The bottom curve is the difference plot on the same intensity scale. (R_{wp} = 9.04, R_p = 6.58, χ = 5.53). The tick marks represent calculated peak positions. λ = 1.54056 Å.

61

Table 3.2 Refined lattice parameters using lab data for methyl stearate as-bought with the MS-*Pnab* structure.

Parameter	Value
Phase / Space group	MS-*Pnab* / *Pnab*
a (Å)	5.6110(4)
b (Å)	7.3409(4)
c (Å)	95.25(1)
Volume (Å^3)	3923.4(6)

3.2.2 Methyl Stearate synchrotron Diamond beamline I11 data

Methyl stearate as-bought PXRD synchrotron data was also collected at Diamond beamline I11, with a long room temperature scan and shorter scans on cooling to 100 K to get thermal expansion coefficients.
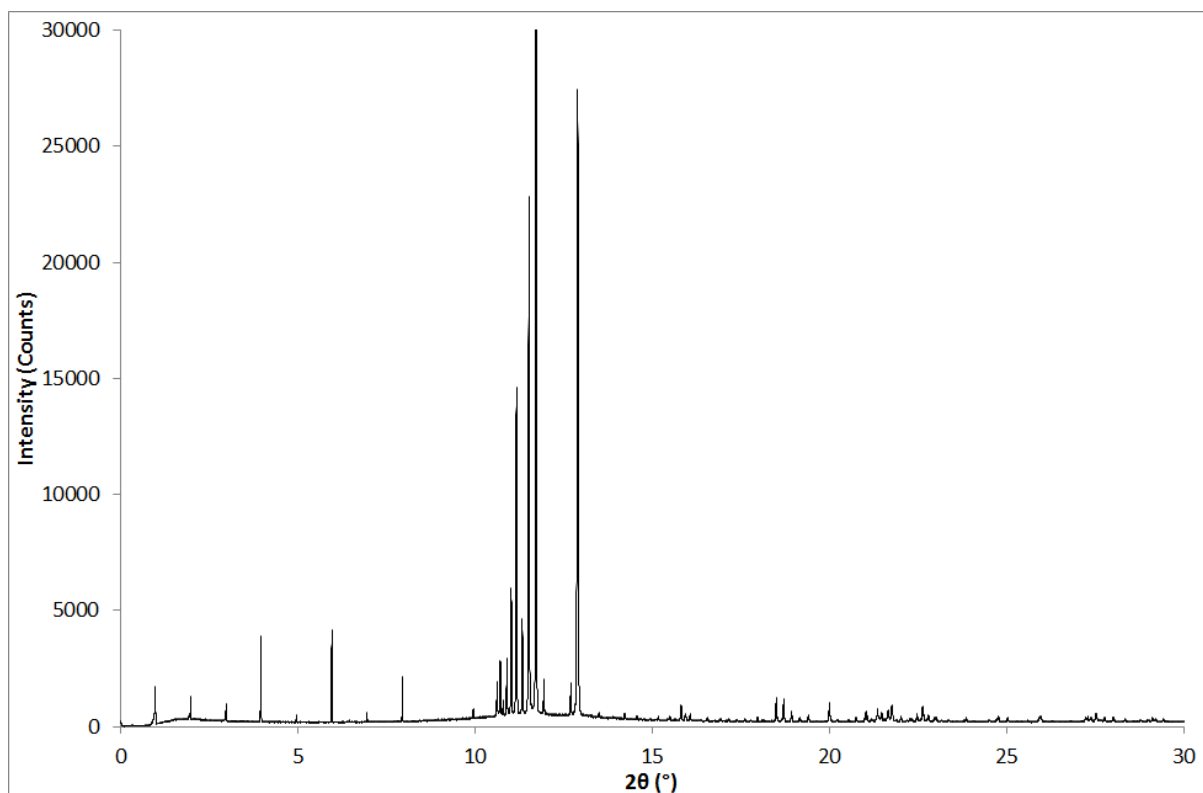
Figure 3.13 PXRD pattern of methyl stearate as-bought recorded at Diamond beamline I11 at 293 K. λ = 0.826056 Å.

Figure 3.13 shows the long scan synchrotron data set, with the Rietveld refinement with the MS-*Pnab* phase shown in Figure 3.14, the refined lattice parameters in Table 3.3 and the atomic positions in appendix 3.1.2.
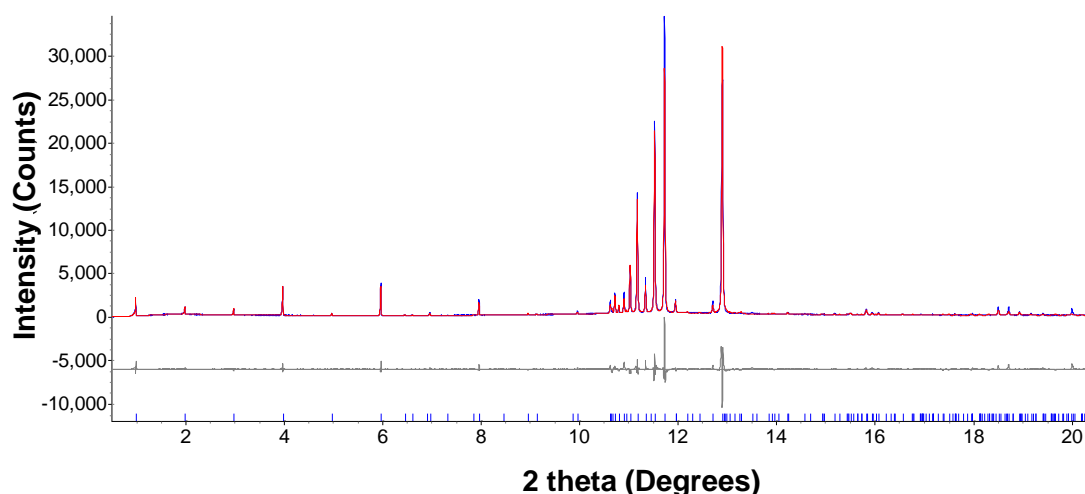
Figure 3.14 Observed (blue line) and calculated (red line) synchrotron X-ray profiles for the Rietveld refinement of methyl stearate as-bought with the MS-*Pnab* structure[46]. The bottom curve is the difference plot on the same intensity scale. (R_{wp} = 12.55, R_p = 8.87, χ = 3.42). The tick marks represent calculated peak positions. λ = 0.826056Å

Table 3.3 Refined lattice parameters using I11 data for methyl stearate as-bought with the MS-*Pnab* structure.

Parameter	Value
Phase / Space group	MS-*Pnab* / *Pnab*
a (Å)	5.6167(1)
b (Å)	7.3502(1)
c (Å)	95.162(2)
Volume (Å³)	3928.63(9)

Both the lab data and synchrotron data collected of methyl stearate as-bought confirm that the as bought phase is the same as the MS-*Pnab* phase reported by MacGillavry[46].

3.2.3 Thermal expansion coefficients

Short PXRD synchrotron data sets were collected of methyl stearate as-bought (MS-*Pnab* phase) on cooling from 300 K to 100 K at 25 K intervals as shown in Figure 3.15.
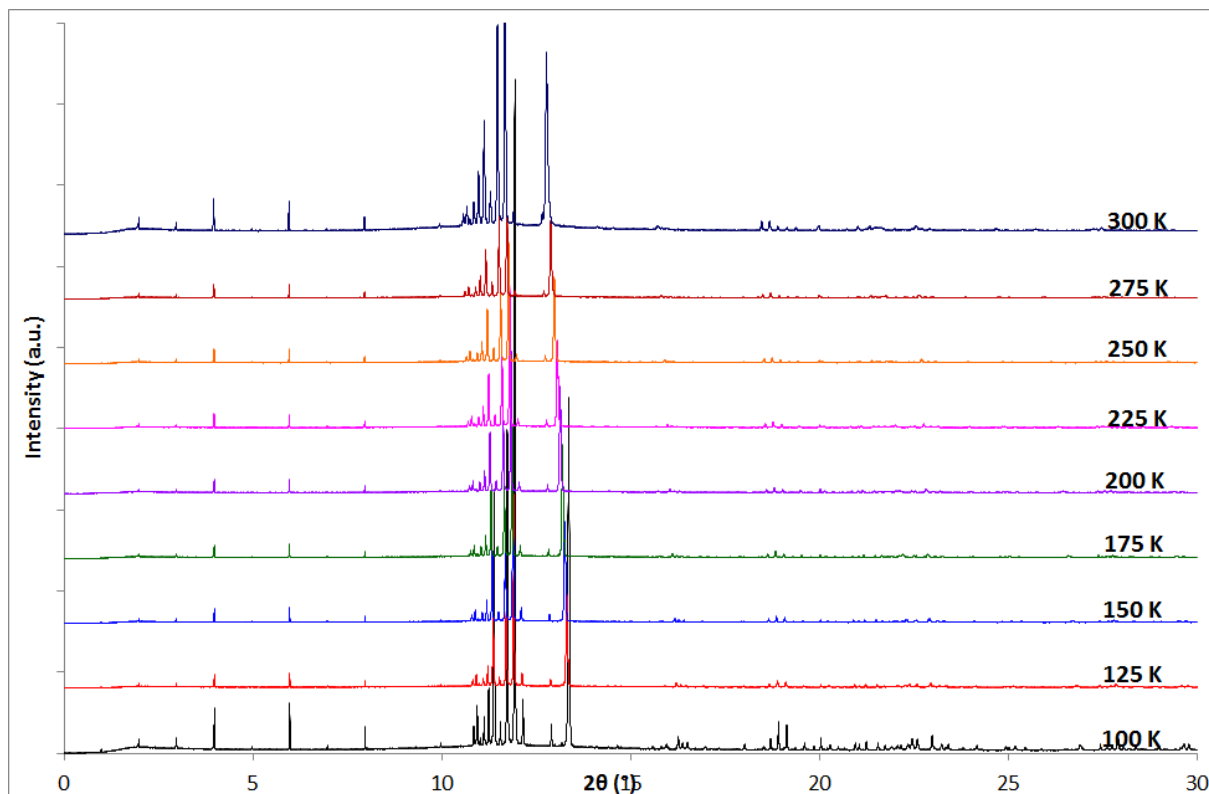
Figure 3.15 MS-*Pnab* thermal expansion scans cooling from 300 K to 100 K at 25 K intervals. *λ* = 0.826056 Å

Rietveld refinements of the scans shown in Figure 3.15 were run to determine lattice parameters to calculate thermal expansion coefficients, and can be found in appendix 3.2. Table 3.4 and Figures 3.16 – 3.19 show the refined lattice parameters on cooling, and the thermal contraction of the unit cell.

Table 3.4 Refined lattice parameters and errors for MS-*Pnab* cooling scans to 100 K.

Temperature (K)	*a* lattice parameter (Å)	*b* lattice parameter (Å)	*c* lattice parameter (Å)	Volume lattice parameter (Å³)
300	5.6236(1)	7.4172(2)	95.176(5)	3969.89(2)
275	5.6151(1)	7.3514(1)	95.114(4)	3926.2(2)
250	5.6025(1)	7.2982(1)	95.0539(4)	3886.6(2)
225	5.5922(1)	7.2512(2)	95.021(4)	3853.1(2)
200	5.5804(1)	7.2112(2)	94.951(5)	3821.0(2)
175	5.5696(1)	7.1765(1)	94.907(4)	3793.42(2)
150	5.5606(1)	7.1453(2)	94.879(5)	3769.8(2)
125	5.5517(1)	7.1193(1)	94.864(4)	3749.4(2)
100	5.5440(1)	7.0916(1)	94.863(4)	3729.7(2)
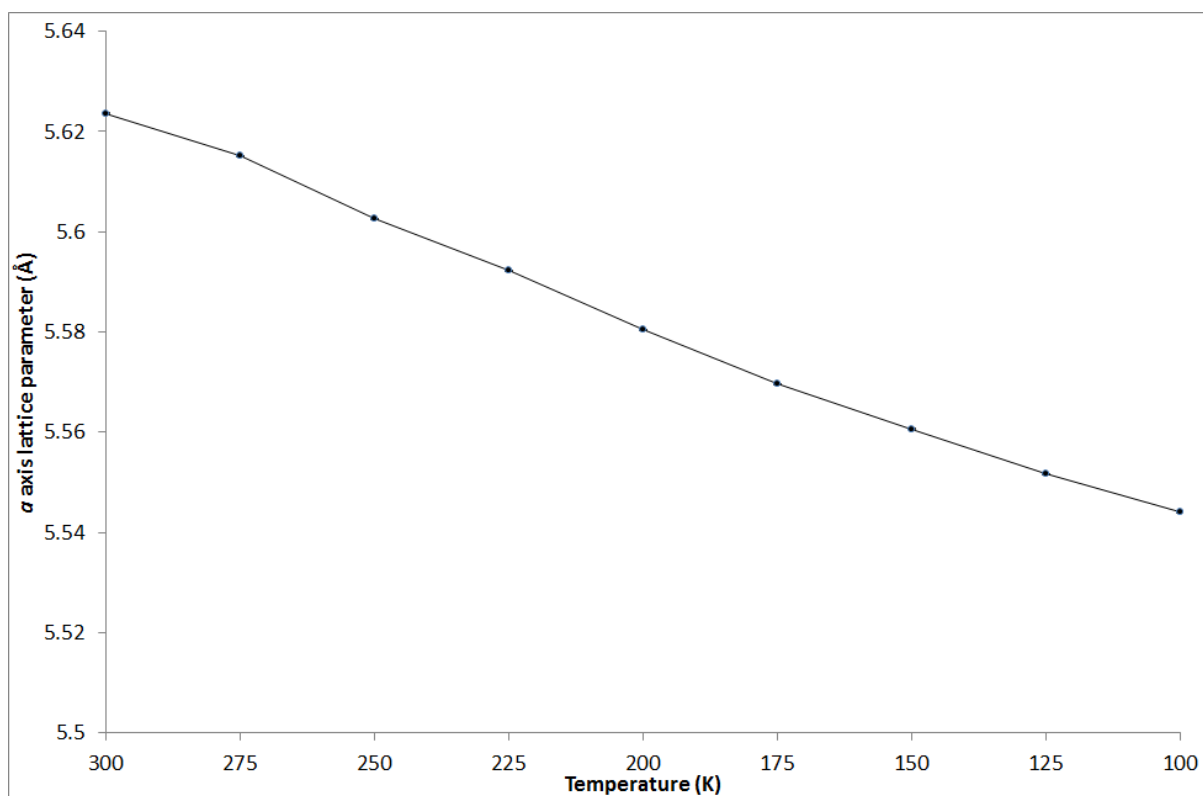
Figure 3.16 Refined *a*-axis lattice parameters for MS-*Pnab* cooling scans to 100 K. Error bars are too small to be shown.
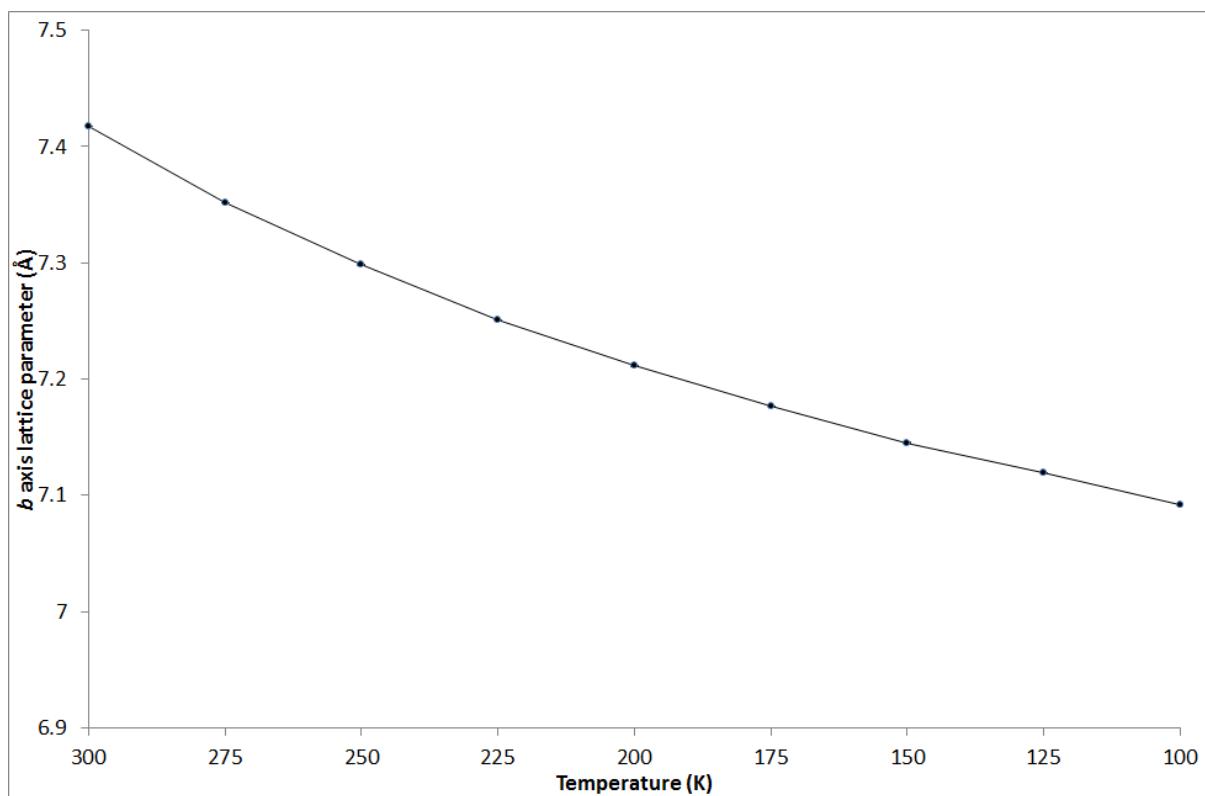
Figure 3.17 Refined *b*-axis lattice parameters for MS-*Pnab* cooling scans to 100 K. Error bars are too small to be shown.
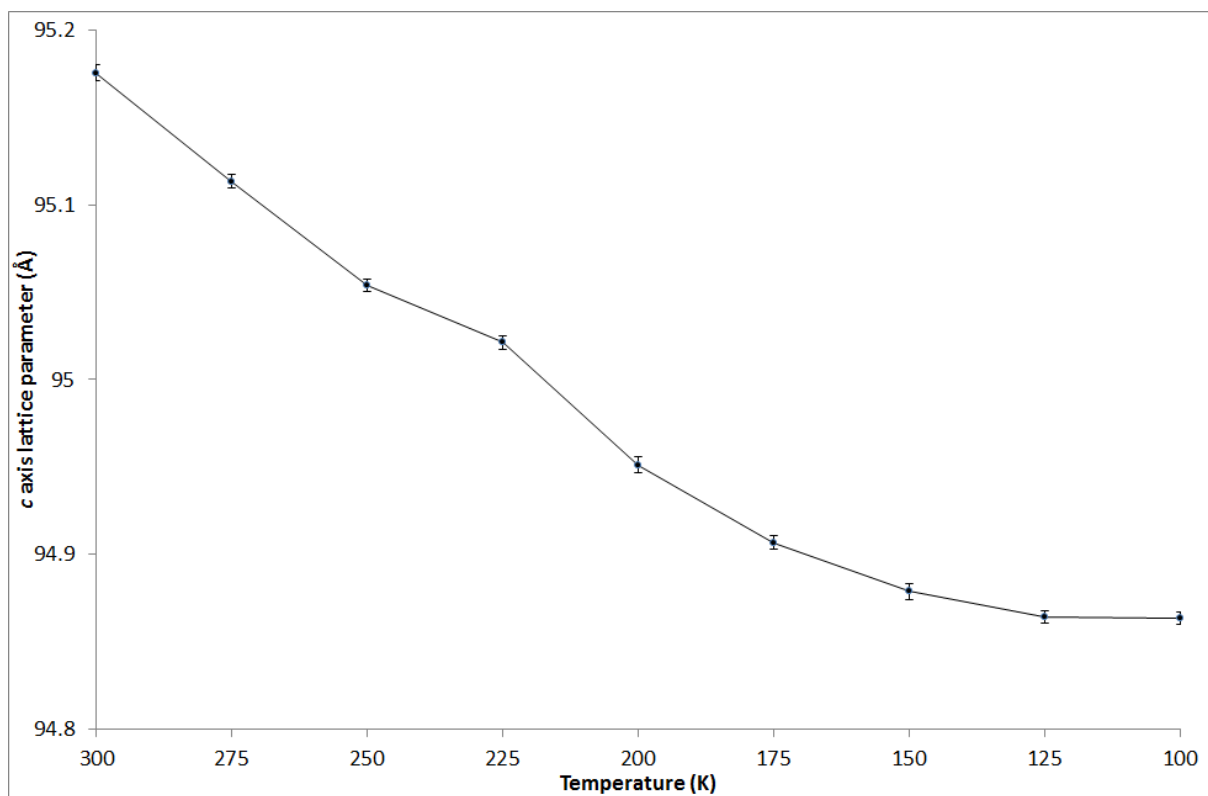
Figure 3.18 Refined *c*-axis lattice parameters for MS-*Pnab* cooling scans to 100 K.
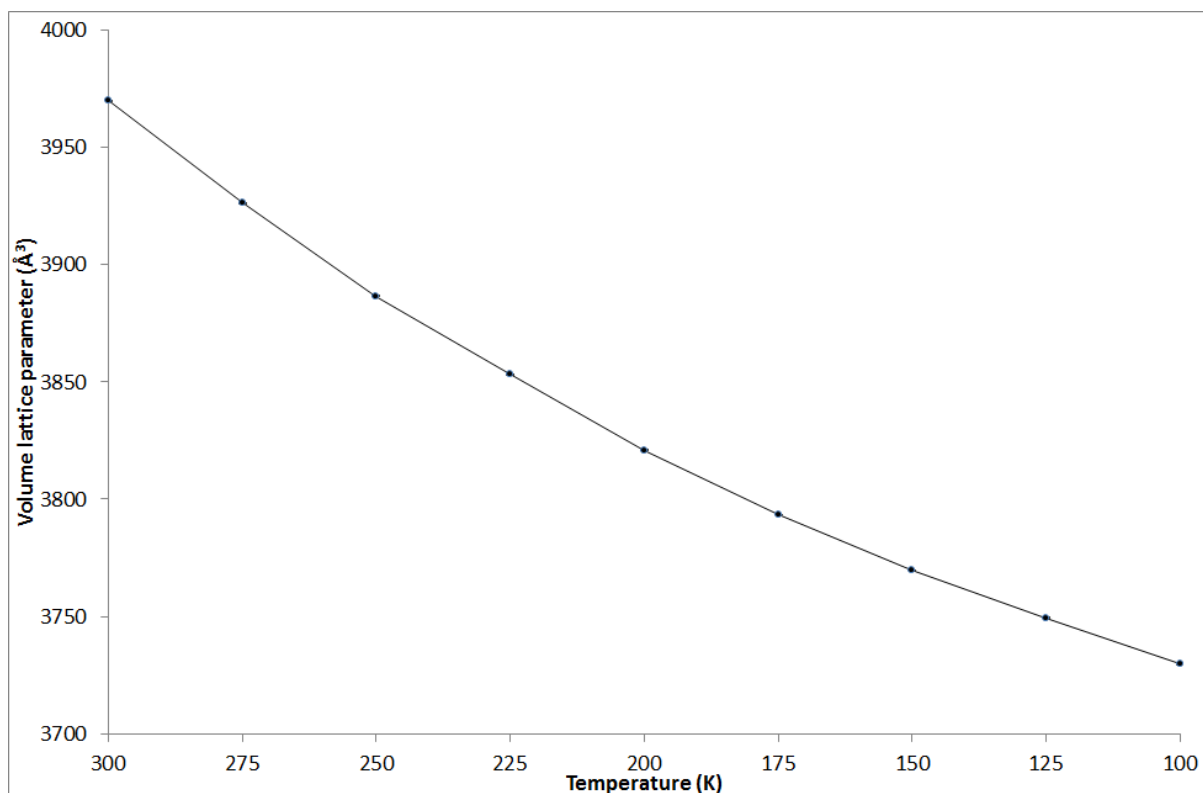
Figure 3.19 Refined unit cell volumes for MS-*Pnab* cooling scans to 100 K. Error bars too small to be shown.

From the refined lattice parameters, linear thermal expansion coefficients for the MS-*Pnab* phase were calculated as shown in Table 3.5 using Equation 3.1.

$$\text{Thermal expansion coefficient} = \frac{\Delta L}{L_0 \cdot \Delta T} \qquad \textbf{Equation 3.1}$$

Table 3.5 Calculated thermal expansion coefficients for MS-*Pnab* phase.

Lattice Parameter	Thermal Expansion Coefficient (K^{-1})
a (Å)	7.176×10^{-5}
b (Å)	2.295×10^{-4}
c (Å)	1.630×10^{-5}
Volume (Å^3)	3.221×10^{-4}

The thermal contraction of the MS-*Pnab* phase is uniform for all lattice parameters. Whilst the thermal expansion coefficients are slightly larger than those typically reported in literature with magnitude 10^{-6}, those are mostly for more rigid inorganic structures. The methyl stearate crystal structures have a lot more free space within the unit cells with less rigid crystal structures, so there is likely to be more flexibility for expansion and contraction of the unit cell, which may explain the larger thermal expansion coefficients. In these structures and other organic crystalline materials the molecules are held together by van der Waals and hydrogen-bonding interactions which have the ability to expand more with temperature.

3.3 Methyl Stearate *C*2 phase

To confirm the methyl stearate phase from the melt, the following temperature treatment based on the MS-*C*2 phase were run using the Oxford cryostream on the capillary lab diffractometer, with the resulting scan shown in Figure 3.20 pattern B.

- Heat to 333 K and dwell for 5 minutes,

- Cool to 233 K at 100 K/hr and dwell for 5 minutes,

- Record XRD scan.
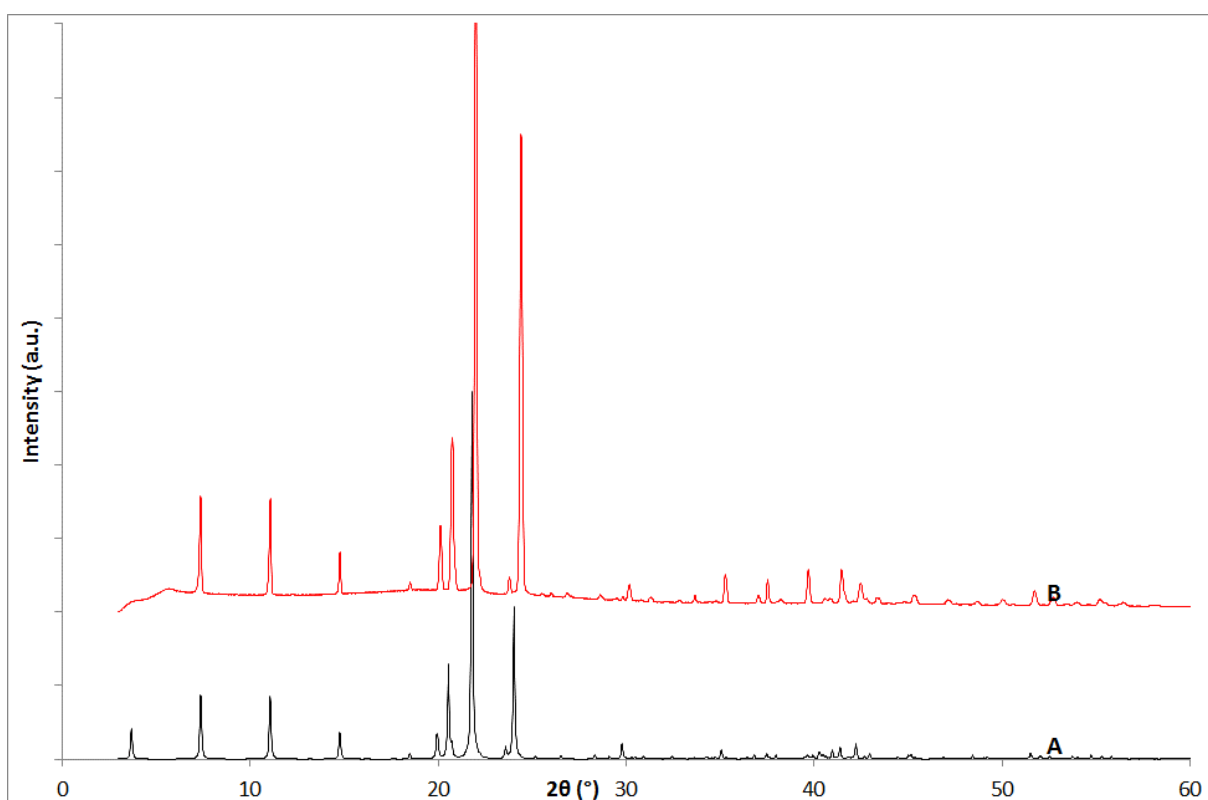
Figure 3.20 (A) Simulated PXRD pattern of MS-*C*2 (233 K)[75], (B) PXRD pattern of the product from variable temperature recrystallisation from the melt of methyl stearate 333 K to 233 K at 100 K/hr. *λ* = 1.54056 Å

As shown in Figure 3.20, the data from the in house melt experiment confirmed formation of the MS-*C*2 phase as solved from synchrotron I11 data[75]. A

71

Rietveld refinement was run as shown in Figure 3.21, with the refined lattice parameters in Table 3.6 and the atomic positions in appendix 3.1.3, confirming the structure from the melt is the same as the MS-*C*2 phase.
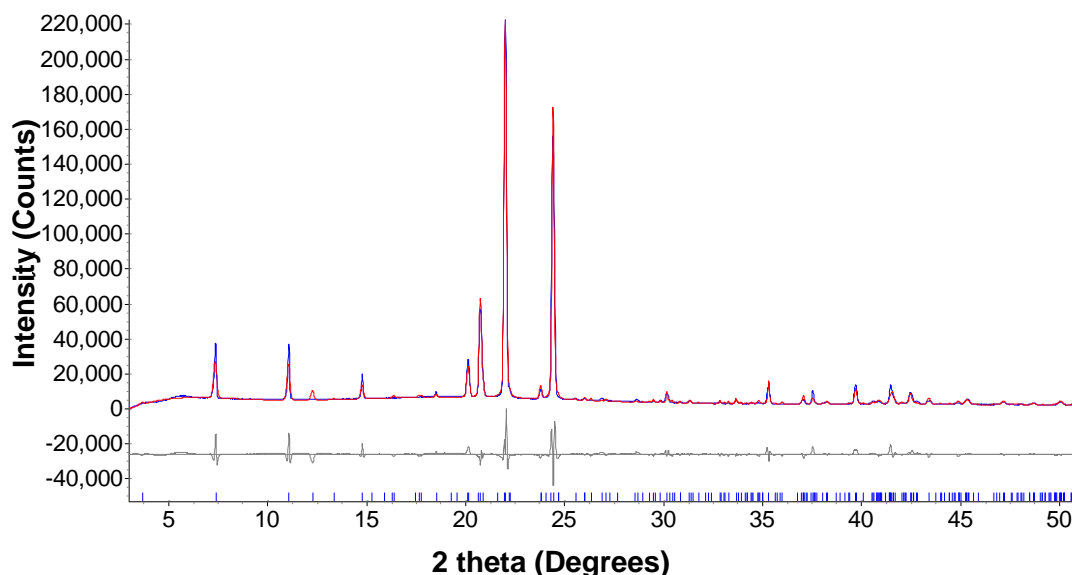
Figure 3.21 Observed (blue line) and calculated (red line) profiles for the Rietveld refinement of methyl stearate variable temperature recrystallisation from the melt with the MS-*C*2 phase[75]. (R_{wp} = 11.50, R_p = 7.73, χ = 7.76). The tick marks represent calculated peak positions. λ = 1.54056 Å

Table 3.6 Refined lattice parameters from lab data for methyl stearate variable temperature recrystallisation from the melt with the MS-*C*2 phase.

Parameter	Value
Phase / Space group	MS-*C*2 / *C*2
***a* (Å)**	47.898(4)
***b* (Å)**	7.2822(5)
***c* (Å)**	5.5705(4)
***β* (°)**	90.856(5)
Volume (Å³)	1942.8(2)

3.3.1 Thermal expansion coefficients

Further data for melted and slow cooled methyl stearate data were collected at Diamond I11 with the following long and short scans recorded.

- Long scan recorded at 295 K after melt (Figure 3.22 pattern D),
- Short scans recorded every 25 K from 295 K to 100 K (Figure 3.24),
- Long scan recorded at 100 K (Figure 3.22 pattern C),
- Long scan on return to 295 K after cooling (Figure 3.22 pattern B).
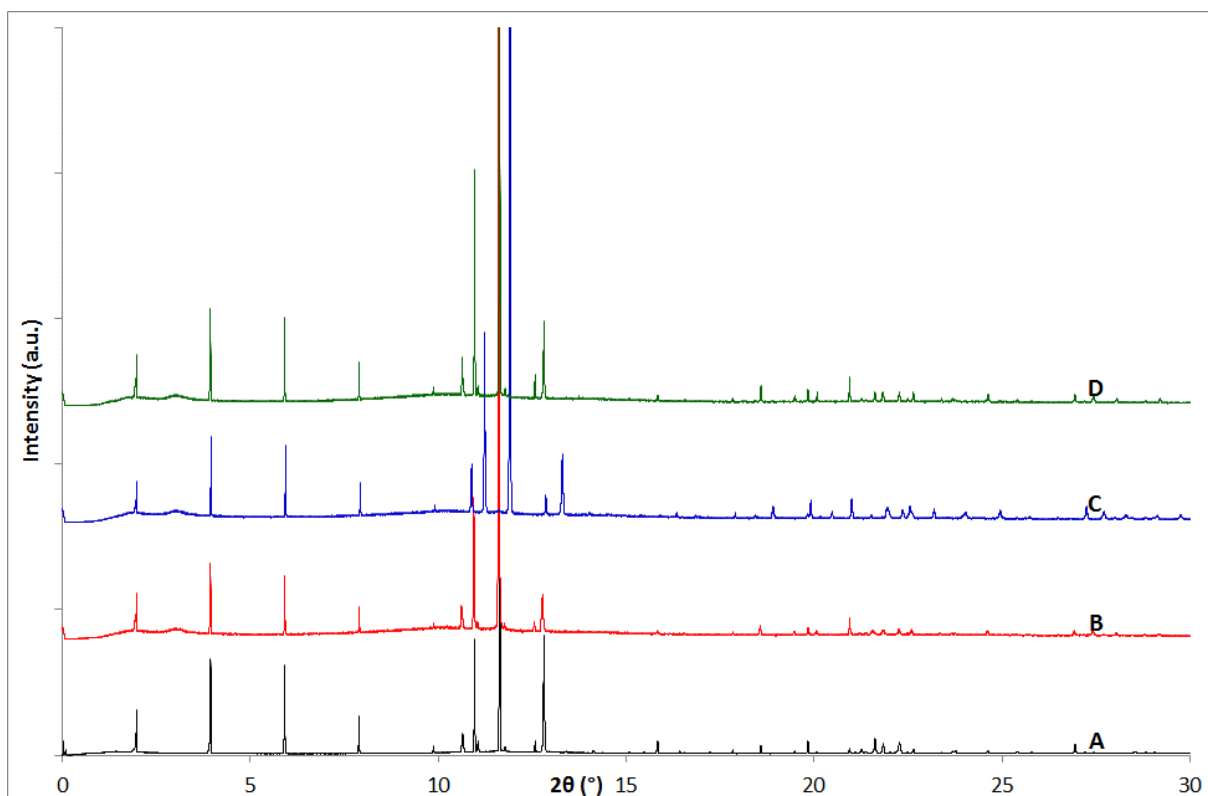
Figure 3.22 Methyl stearate synchrotron data sets recorded at (A) 295 K, (B) return to 295 K after cooling, (C) slow cooled melt 100 K scan, (D) return to 295 K after melt phase taken to 100 K. λ = 0.826056 Å

All three long melt scans shown in Figure 3.22, patterns B, C and D, are the same as the data set of MS-*C*2 phase (pattern A). Whilst the scans all confirm the same phase is present with no change on cooling to 100 K, the 100 K scan does show small subtle differences which can be seen in the zoomed in PXRD stack plot in Figure 3.23.
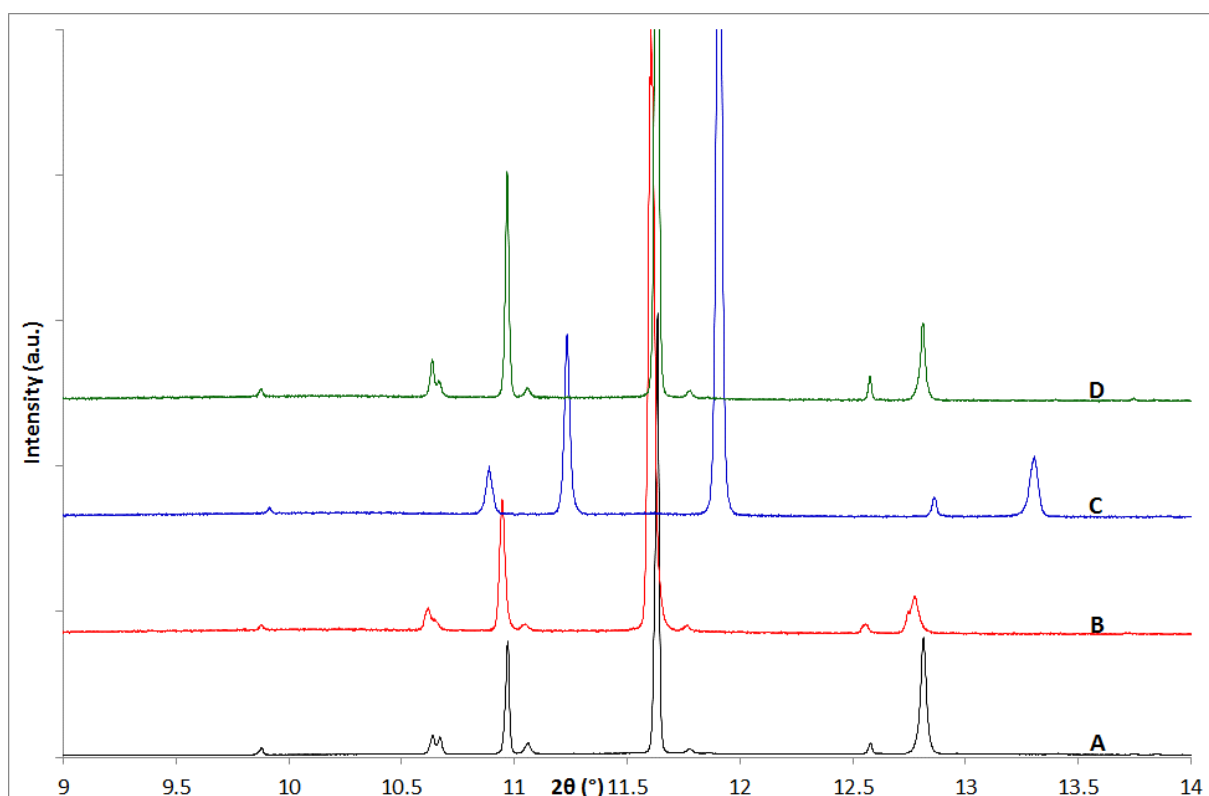
Figure 3.23 Zoomed in synchrotron data sets for methyl stearate slow cooled from the melt recorded at (A) 295 K, (B) return to 295 K after cooling, (C) slow cooled melt 100 K scan, (D) return to 295 K after melt phase taken to 100 K. λ = 0.826056 Å

All three room temperature scans in Figure 3.23 show a split peak at 10.63° however in the 100 K scan the same peak at 10.89° is a single peak. The room

temperature scans also contain two small peaks at 11.06° and 11.77° 2θ which disappear at 100 K.

To determine the thermal expansion coefficients for the MS-$C2$ phase, short scans were run on cooling from 295 K to 100 K, with the two small peaks disappearing below 200 K. Whilst there are subtle differences between the room temperature and 100 K scans, the small peaks reappear on returning to room temperature after cooling, and all scans on cooling still refine to the $C2$ phase as shown in appendix 3.3. This is due to the peaks overlapping at 100 K as the lattice parameters expand at different rates.

Full Rietveld refinements of the short scans shown in appendix 3.2 were run to determine lattice parameters.
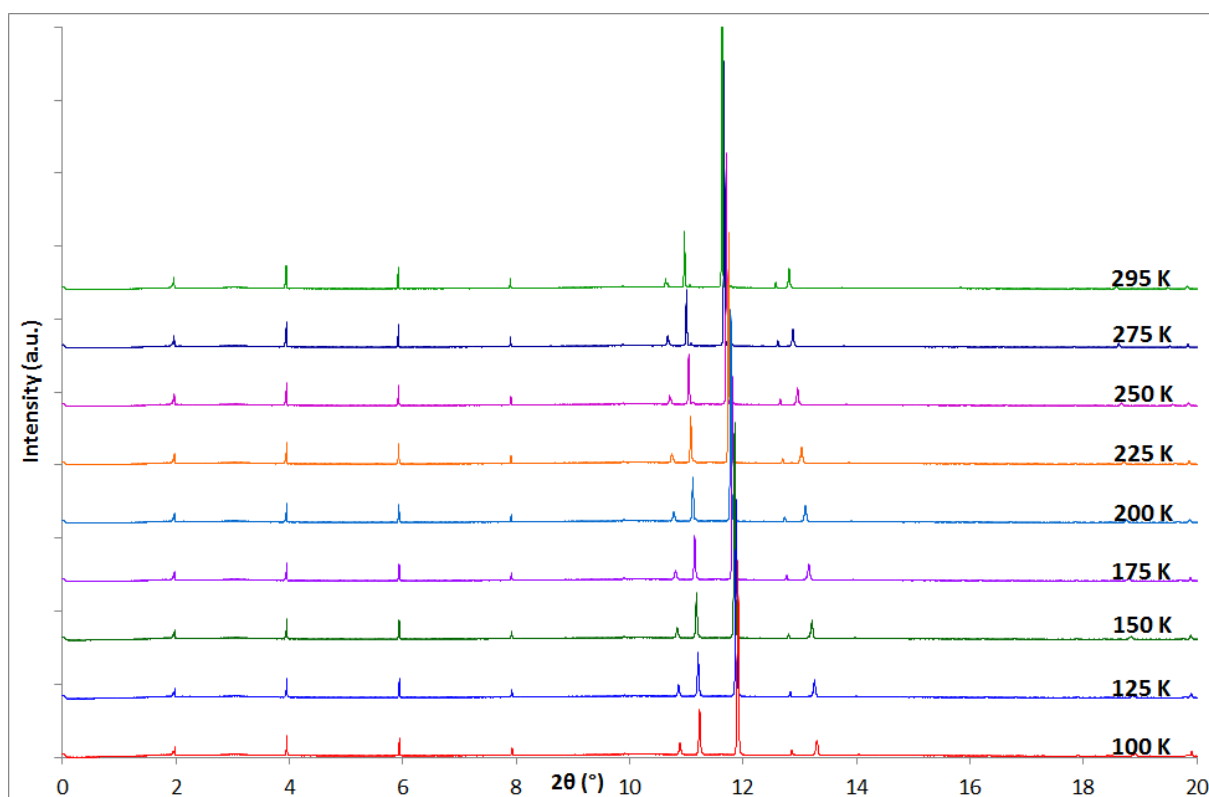
Figure 3.24 MS-$C2$ scans cooling from 295 K to 100 K at 25 K intervals. λ = 0.826056 Å

Figures 3.25 – 3.29 and Table 3.7 contain the refined lattice parameters for the cooling scans and the scan on returning to room temperature, which show a uniform contraction of the unit cell in all axes.

Table 3.7 Refined lattice parameters and errors for MS-*C*2 phase cooling scans and return to 295 K.

Temperature (K)	*a* lattice parameter (Å)	*b* lattice parameter (Å)	*c* lattice parameter (Å)	*β* lattice parameter (°)	Volume lattice parameter (Å^3)
295	47.95256(5)	7.39957(3)	5.601510(8)	91.1303(4)	1987.17(3)
275	47.9260(6)	7.3605(1)	5.59244(8)	91.054(1)	1972.46(5)
250	47.8996(9)	7.3138(1)	5.58322(8)	90.930(1)	1955.69(6)
225	47.8599(7)	7.2742(1)	5.5726(1)	90.824(3)	1939.87(6)
200	47.839(5)	7.2371(5)	5.5619(4)	90.717(5)	1925.4(3)
175	47.817(2)	7.2049(3)	5.5540(2)	90.608(3)	1913.3(2)
150	47.795(3)	7.1754(2)	5.5448(2)	90.497(3)	1901.5(2)
125	47.7780(6)	7.1504(2)	5.5366(1)	90.402(4)	1891.42(6)
100	47.759(1)	7.12705(8)	5.5287(3)	90.305(4)	1881.8(1)
295	47.9365(8)	7.419(1)	5.6083(6)	91.248(5)	1994.2(4)
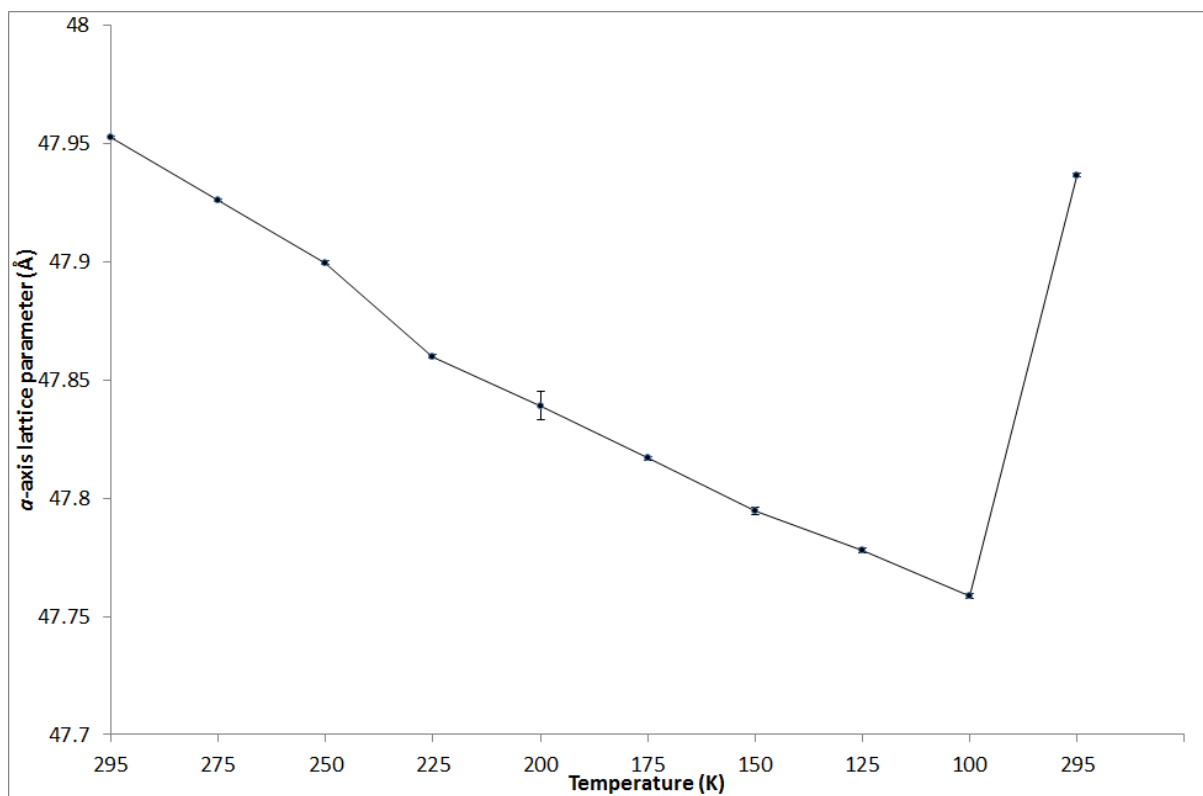
Figure 3.25 Refined *a*-axis lattice parameters for MS-*C*2 phase cooling scans and return to 295 K.
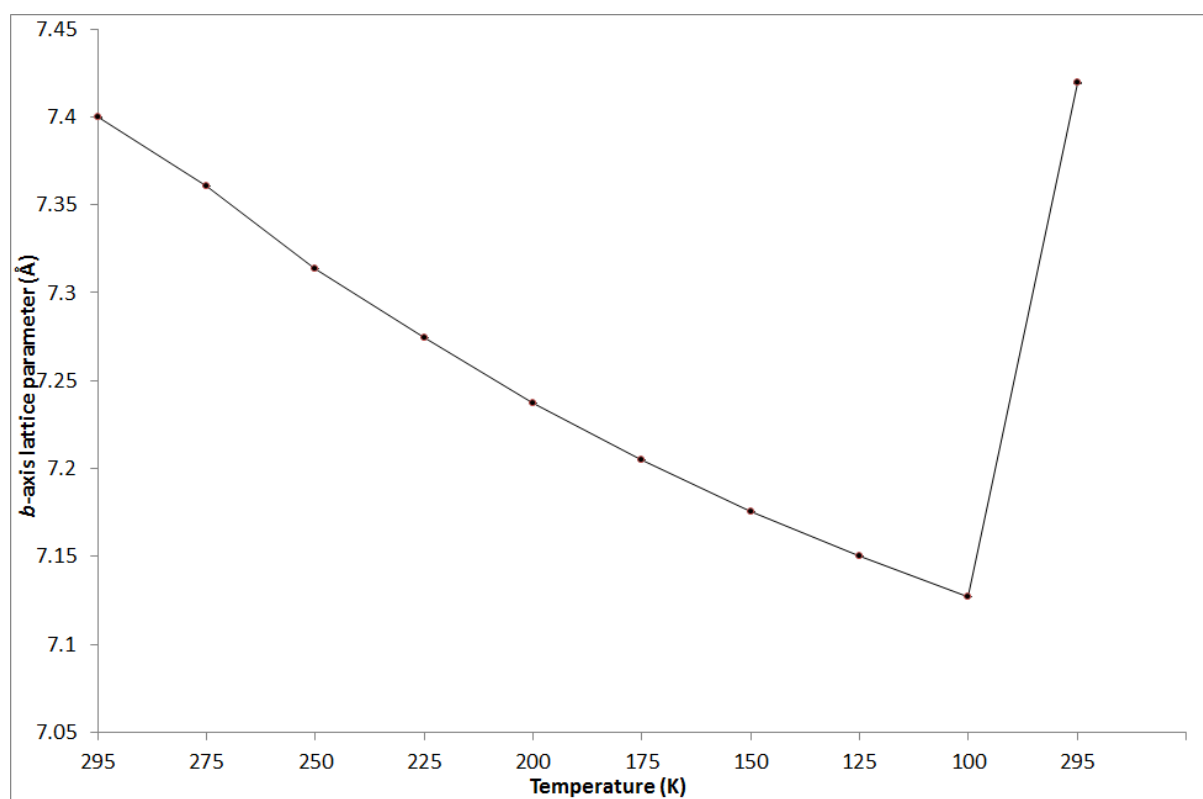
Figure 3.26 Refined *b*-axis lattice parameters for MS-*C*2 phase cooling scans and return to 295 K.
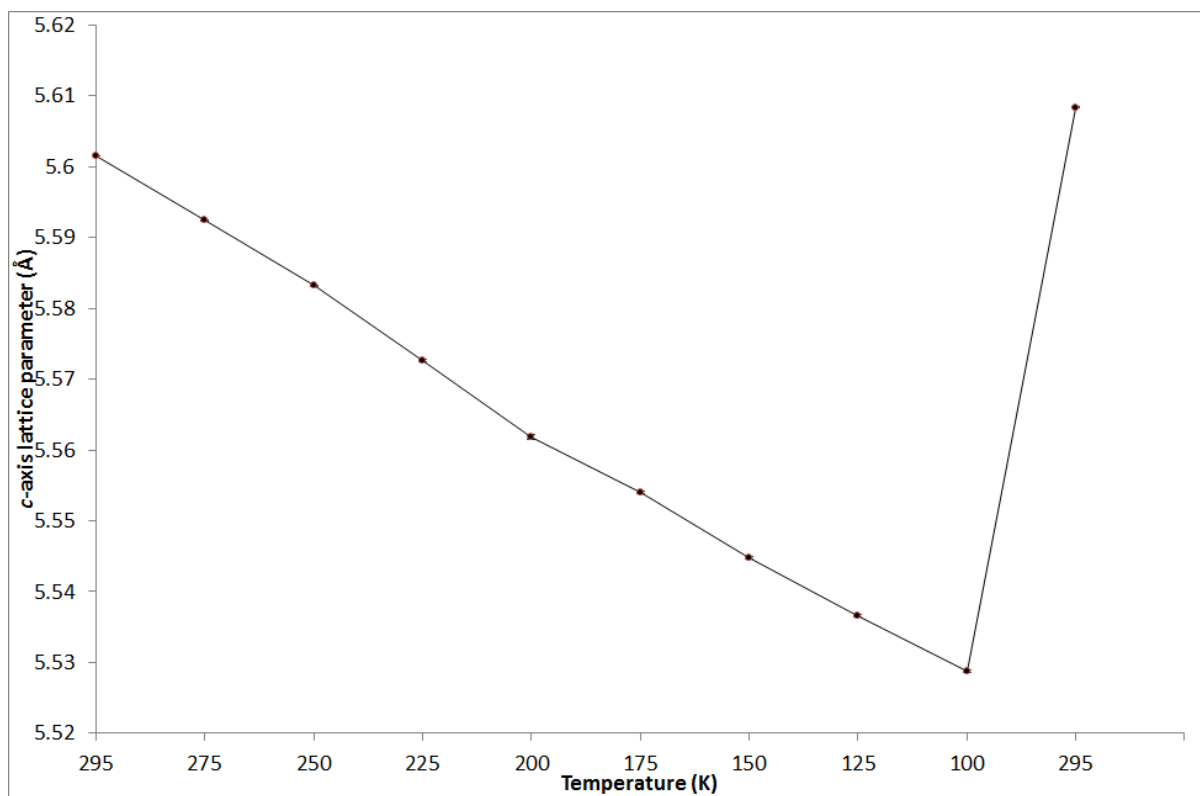
Figure 3.27 Refined *c*-axis lattice parameters for MS-*C*2 phase cooling scans and return to 295 K.
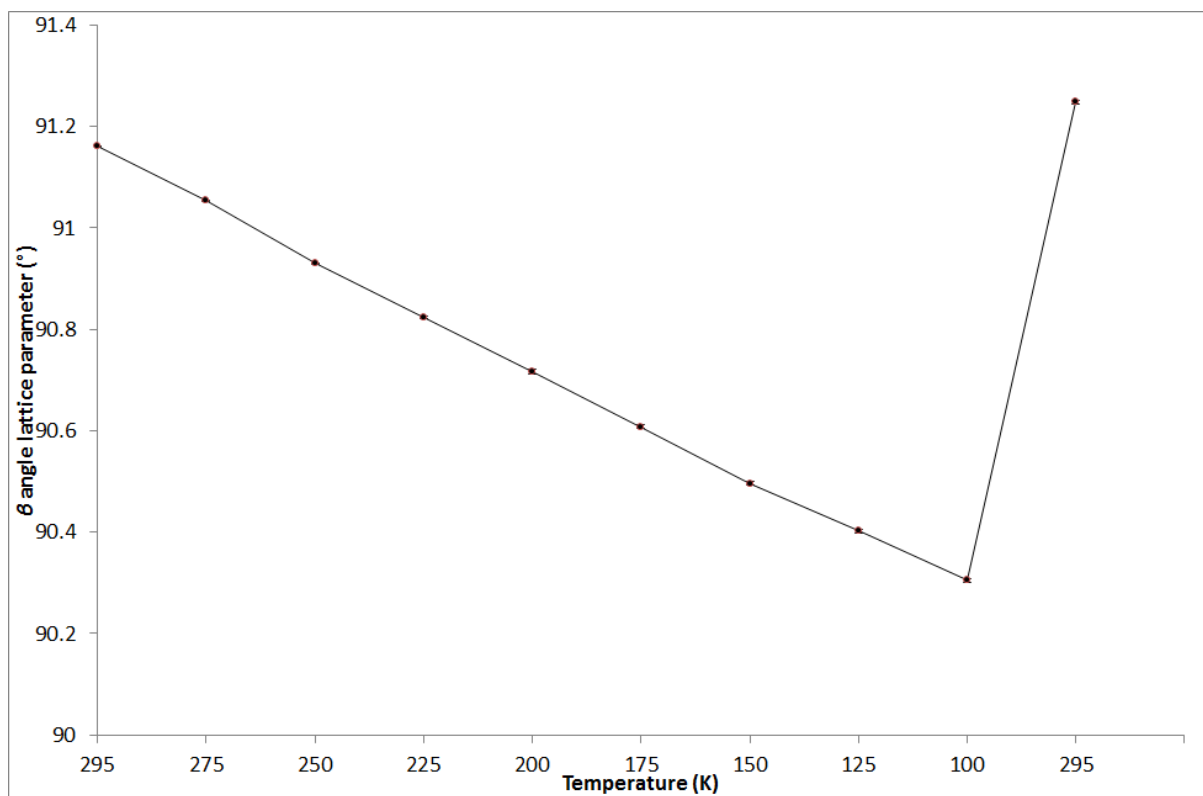
Figure 3.28 Refined *β* angle lattice parameters for MS-*C*2 phase cooling scans and return to 295 K.
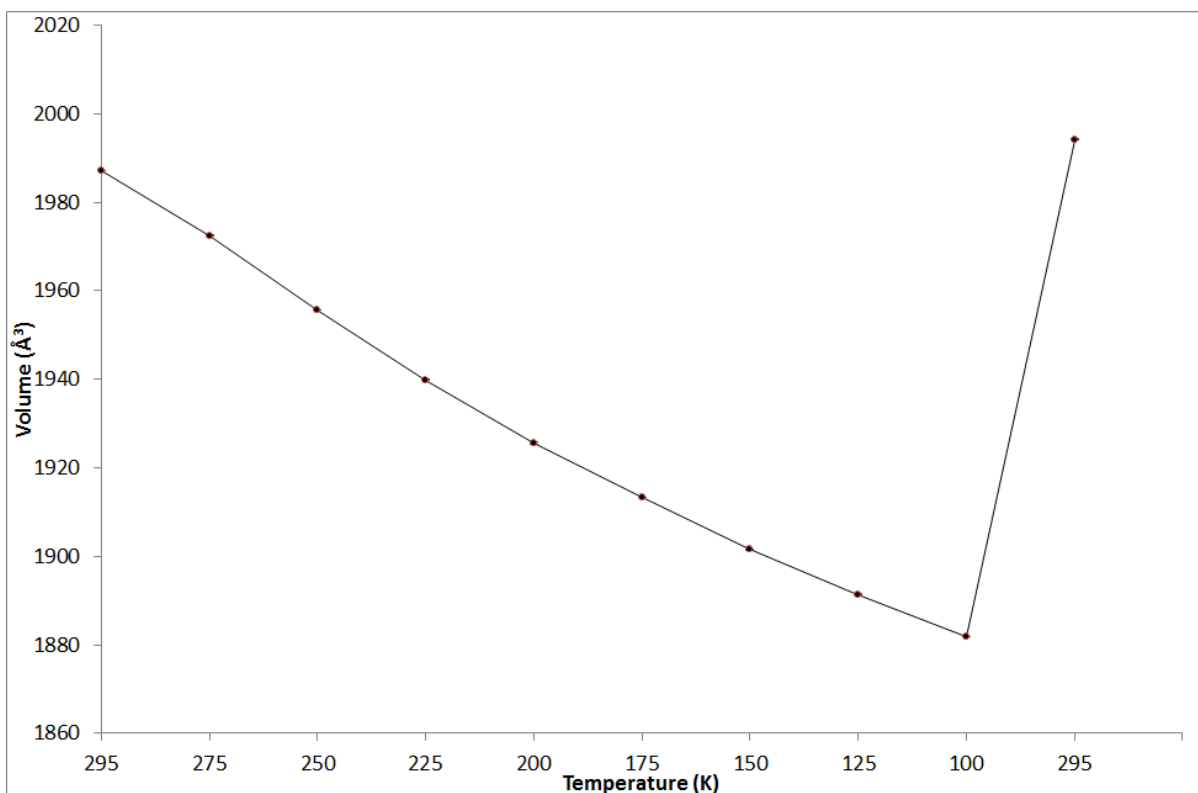
Figure 3.29 Refined unit cell volumes for MS-*C*2 phase cooling scans and return to 295 K.

From the lattice parameters determined from the Rietveld refinements, linear thermal expansion coefficients shown in Table 3.8 were determined using Equation 3.1.

Table 3.8 Calculated thermal expansion coefficients for the MS-*C*2 phase.

Lattice Parameter	Thermal Expansion Coefficient (K^{-1})
a (Å)	2.08216×10^{-5}
b (Å)	1.96086×10^{-4}
c (Å)	6.75094×10^{-5}
β (°)	4.85813×10^{-5}
Volume (Å^3)	2.87044×10^{-4}

As with the MS-*Pnab* thermal expansion coefficients, those calculated for the MS-*C*2 phase are also larger than those reported in literature, and closer to those calculated for the MS-*Pnab*. As stated previously the methyl stearate phases are all less rigid with more space in the unit cells, therefore potentially allowing for greater thermal expansion.

3.4 Methyl Stearate recrystallisations

As shown in section 3.1, methyl stearate has been reported to exist in five different polymorphs. To determine which of those are likely to exist in the conditions of a fuel tank, various solvent and temperature recrystallisations using conditions as outlined in Table 3.9 were used to recrystallise methyl stearate and PXRD patterns collected to identify the polymorph.

Table 3.9 Methyl stearate recrystallisation conditions.

Figure / Pattern	Solvent	Experiment Type	Temp 1	Temp 2	Cooling Rate
3.30 / C	Toluene	Solvent recrystallisation	-	298 K	-
3.30 / D	Toluene	Solvent recrystallisation	298 K	255 K	-
3.30 / E	Kerosene	Solvent recrystallisation	298 K	255 K	-
3.30 / F	Toluene	Variable temperature	333 K	233 K	100 K/hr
3.30 / G	Kerosene	Variable temperature	333 K	233 K	100 K/hr
3.31 / C	-	From melt	353 K	298 K	-
3.31 / D	-	From melt	353 K	255 K	-
3.31 / E	Toluene	From melt then solvent recrystallisation	353 K	255 K	-
3.31 / F	Kerosene	From melt then solvent recrystallisation	353 K	255 K	-
3.32 / C	-	Cyclic variable temperature	Cycle 3 – 233 K	290 K	100 K/hr
3.32 / D	-	Cyclic variable temperature	Cycle 2 – 333 K	233 K	100 K/hr
3.32 / E	-	Cyclic variable temperature	Cycle 2 – 290 K	333 K	100 K/hr
3.32 / F	-	Cyclic variable temperature	Cycle 2 – 233 K	290 K	100 K/hr
3.32 / G	-	Cyclic variable temperature	Cycle 1 – 333 K	233 K	100 K/hr
3.32 / H	-	Cyclic variable temperature	Cycle 1 – 290 K	333 K	100 K/hr
3.32 / I	-	Cyclic variable temperature	Cycle 1 – 290 K	290 K	100 K/hr
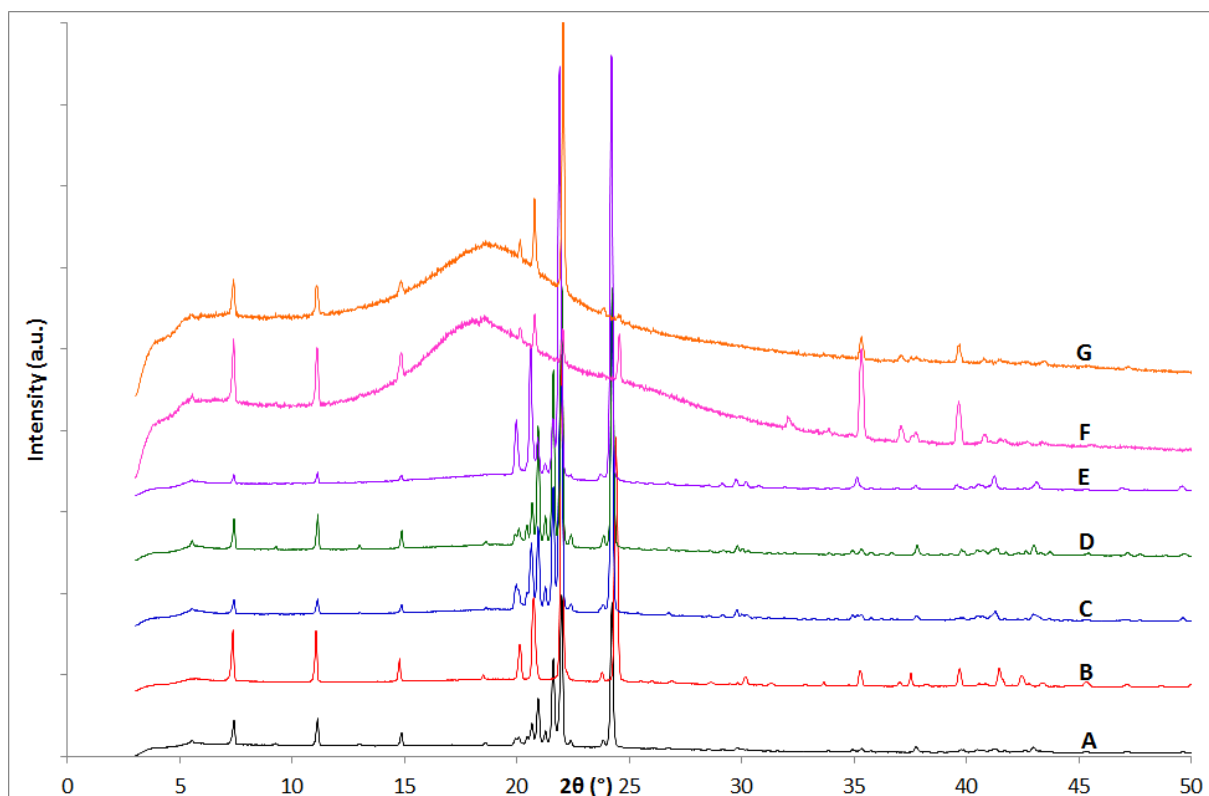
Figure 3.30 PXRD patterns of (A) MS-*Pnab* (room temperature), (B) MS-*C*2 (233K), (C) the product from solvent recrystallisation experiment methyl stearate in toluene at 298 K, (D) the product from solvent recrystallisation experiment methyl stearate in toluene at 255 K, (E) the product from solvent recrystallisation experiment methyl stearate in kerosene at 255 K, (F) the product from variable temperature experiment methyl stearate in toluene 333 K to 233 K at 100 K/hr, (G) the product from variable temperature experiment methyl stearate in kerosene 333 K to 233 K at 100 K/hr. *λ* = 1.54056 Å

From visual comparison of the data in Figure 3.30, from the three recrystallisation conditions that didn't involve heating the solution, patterns C, D, and E, the phase which crystallised out was the MS-*Pnab* phase. However, the in situ recrystallisations F and G in which the solutions were taken above the melting point of methyl stearate, recrystallised into the MS-*C*2 phase. For patterns F and G there is a high background and amorphous bump in the PXRD pattern due to the

crystallisation process being carried out in a solution of either toluene or kerosene which are still liquid at the measurement temperature. This will be seen throughout this work due to the nature of the crystallisation experiments.
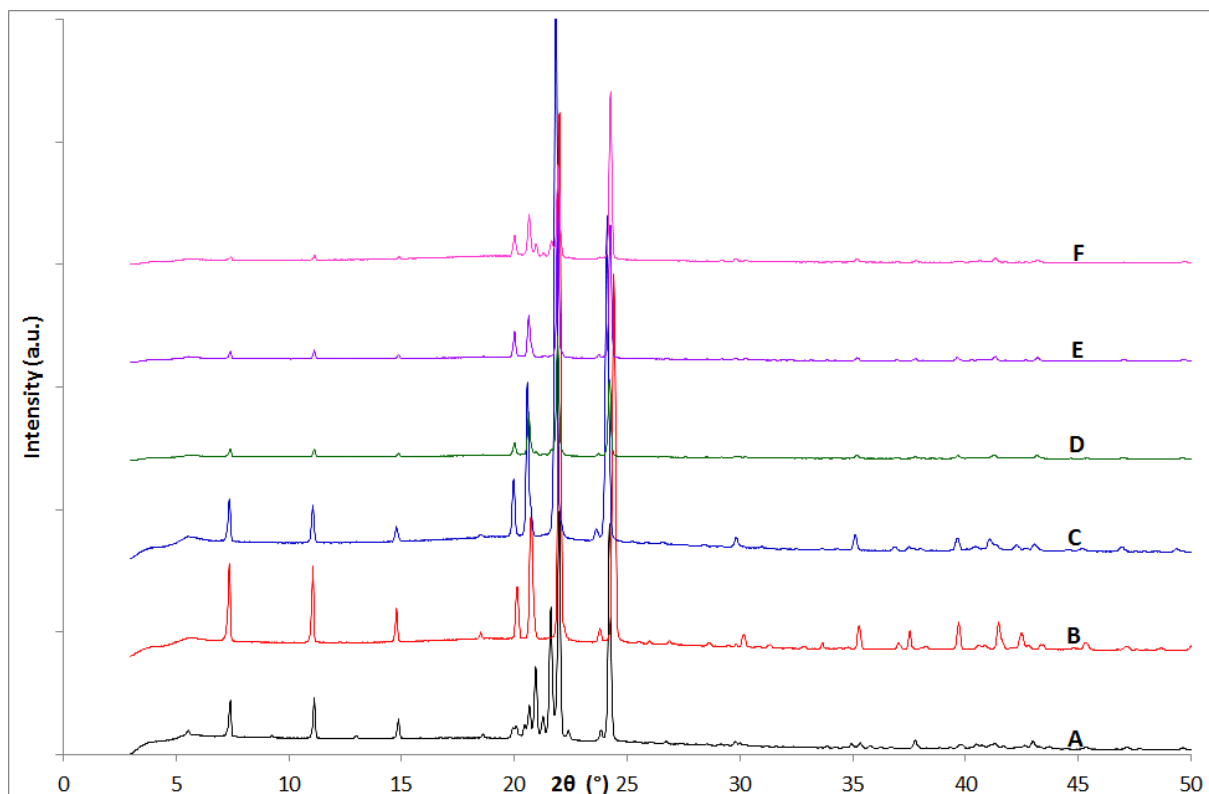
Figure 3.31 PXRD patterns of (A) MS-*Pnab* (room temperature), (B) MS-*C*2 (233K), (C) the product from the melt experiment in a Teflon pot and cooled at room temperature methyl stearate, (D) the product from the melt experiment in a Teflon pot and cooled in the freezer methyl stearate recorded at room temperature, (E) the product from the melt experiment in a Teflon pot and cooled at room temperature methyl stearate then recrystallised in toluene, (F) the product from the melt experiment in a Teflon pot and cooled at room temperature methyl stearate then recrystallised in kerosene. *λ* = 1.54056 Å

Figure 3.31 shows the PXRD data from the recrystallisation of methyl stearate from the melt in a Teflon pot with two different cooling rates (patterns C and D), and

then this material is recrystallised in toluene and kerosene (patterns E and F). All recrystallisations produced the MS-*C*2 phase, showing that toluene and kerosene solvents don't appear to affect the phase crystallised and confirming that once melted, the MS-*C*2 phase appears the most likely phase to crystallise out even after being dissolved.
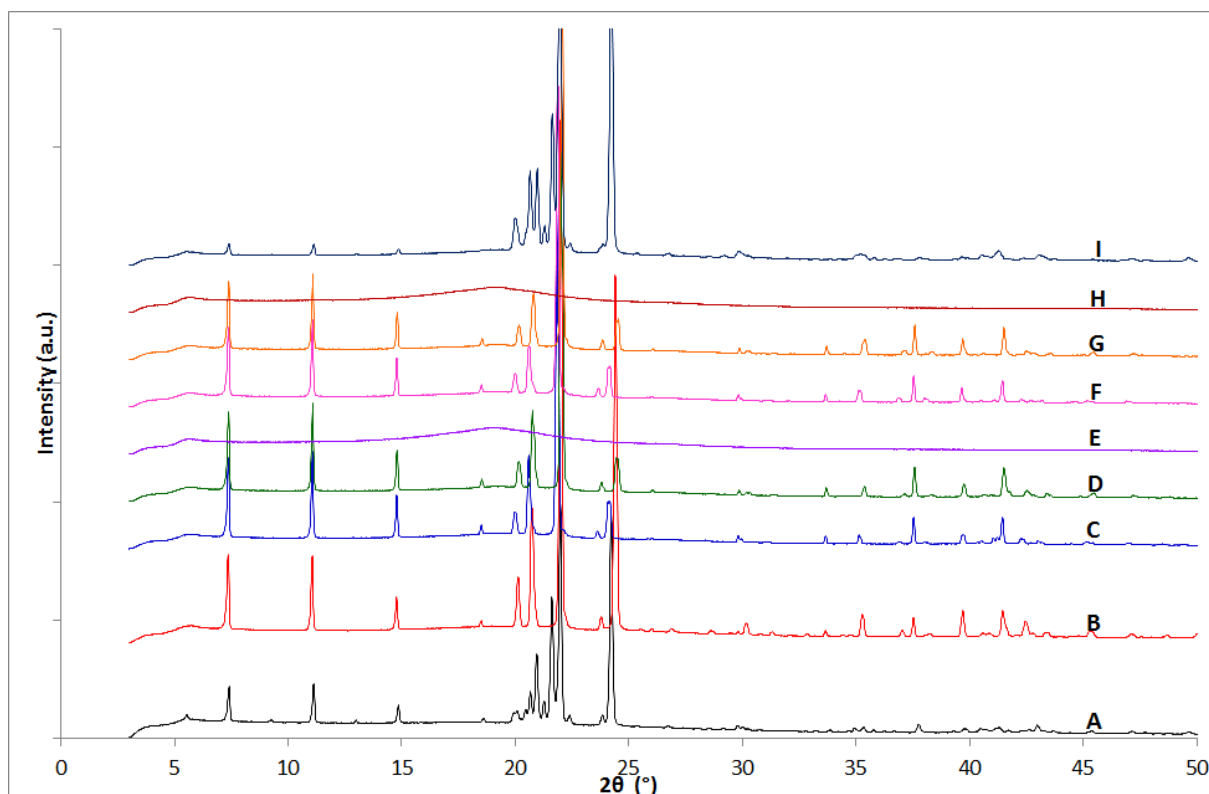
Figure 3.32 PXRD patterns of (A) MS-*Pnab* (room temperature), (B) MS-*C*2 (233K), (C) methyl stearate cyclic variable temperature cycle 3 recorded at 290 K, (D) methyl stearate cyclic variable temperature cycle 2 recorded at 233 K, (E) methyl stearate cyclic variable temperature cycle 2 recorded at 333 K, (F) methyl stearate cyclic variable temperature cycle 2 recorded at 290 K, (G) methyl stearate cyclic variable temperature cycle 1 recorded at 233 K, (H) methyl stearate cyclic variable temperature cycle 1 recorded at 333 K, (I) methyl stearate cyclic variable temperature cycle 1 recorded at 290 K. λ = 1.54056 Å

Figure 3.32 shows the PXRD patterns from cyclic recrystallisation of methyl stearate whereby the capillary containing the sample was taken above the melting point before being cooled to 233 K twice, with scans at the high temperature of 333 K to confirm melting of methyl stearate between each cycle.

The first room temperature scan, pattern I, shows the initial MS-*Pnab* phase but all scans after that, both room temperature and 233 K scans, were of the MS-*C*2 phase with confirmation of melting of the sample between each cycle in patterns E and H.

As shown in Figures 3.30 – 3.32 once methyl stearate has been melted the phase which crystallises out is the MS-*C*2 phase, and the material will not return to the MS-*Pnab* phase. However, providing the sample hasn't been above the melting point of methyl stearate, the MS-*Pnab* phase is the phase which is likely to be present.

Rietveld refinements of the recrystallisations shown in section 3.4 can be found in appendix 3.4.

3.5 Methyl Stearate *Cc* phase

Figure 3.2 shows the simulated powder patterns of the five methyl stearate structures which includes two phases from the melt. Figure 3.33 shows direct comparison of the two simulated powder patterns of the melt phases, which are visually very similar. This is to be expected as the structures are fairly similar as shown in section 3.1.1.
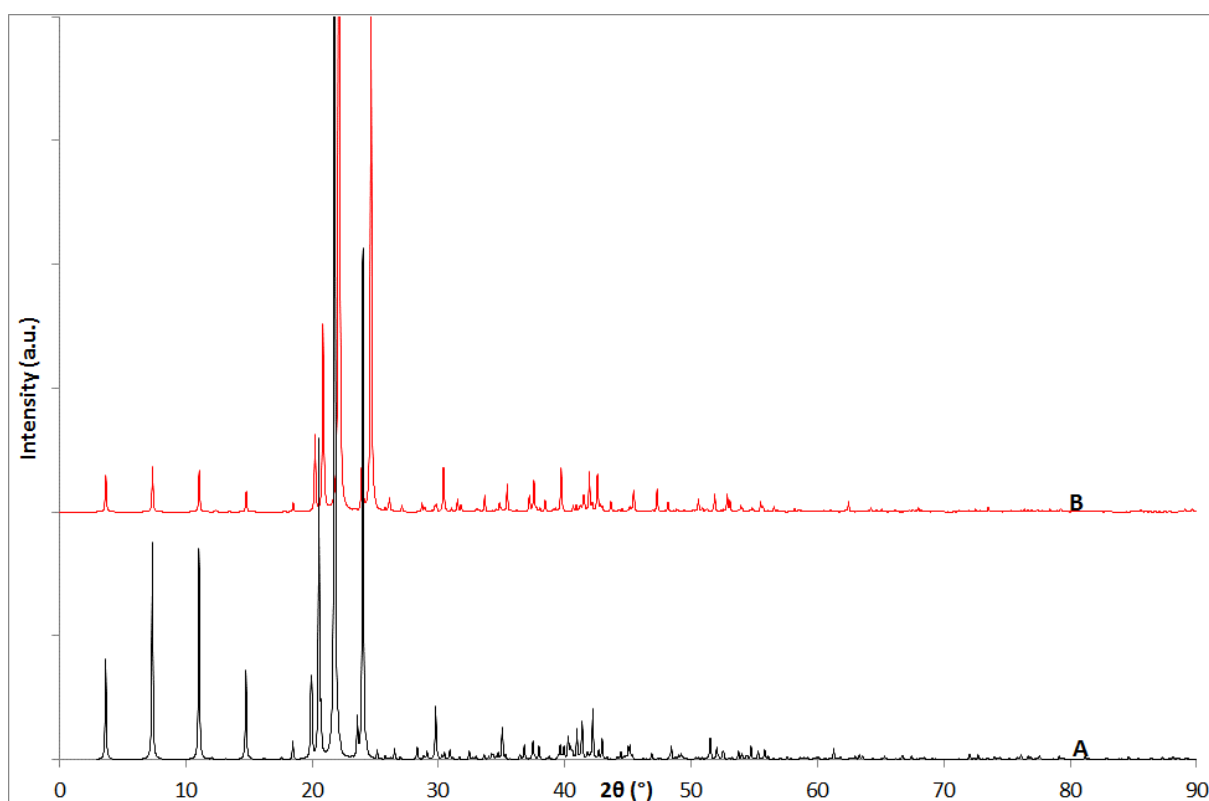
Figure 3.33 Simulated PXRD patterns of methyl stearate based on (A) MS-*C*2 (233 K)[75], (B) the MS-*Cc* (193 K)[76]. λ = 1.54056 Å

The main difference between the structures is the head to tail alignment within the layers and also between the layers; however with XRD, the diffraction of the x-rays is from their interaction with electrons in the sample, varying linearly with

increasing number of electrons. Oxygen and carbon are likely to diffract x-rays similarly due to similar numbers of electrons; therefore swapping the head to tail alignment within or between the layers, averaged over the whole sample is unlikely to make much difference between the XRD patterns produced.

In neutron diffraction, however, the neutron beam is scattered by the atomic nuclei of the atoms, and neighbouring atoms in the periodic table and even isotopes of the same element can have significantly different scattering cross sections; therefore neutron diffraction is likely to be better than XRD to differentiate between the two melt phases. For example the total bound scattering cross section for carbon is 5.551(3) barn but is 4.232(6) barn for oxygen[77].

Deuterated methyl stearate was made from deuterated steric acid and deuterated methanol, which were transesterfied together. Deuterated materials were used to reduce incoherent background in the scans. The methyl stearate quench cooled phase was produced from melting the deuterated methyl stearate and quench cooling the sample using liquid nitrogen, before being ground and loaded into a vanadium sample can.

The sample can was loaded onto the HRPD beamline at ISIS and the temperature was lowered to 4.2 K where a long 300 µA hour scan was recorded. Short 10 µA hour scans were then recorded on heating the sample every 20 K from 20 K up to 300 K with long scans at 193 K and 300 K. Short scans were also recorded every 20 K on cooling from 290 K to 10 K. Detector banks are 30° (bank 3), 90° (bank 2) and 168° (bank 1).

Figures 3.34, 3.35 and 3.36 show banks 3, 2 and 1, respectively for the three long scans.
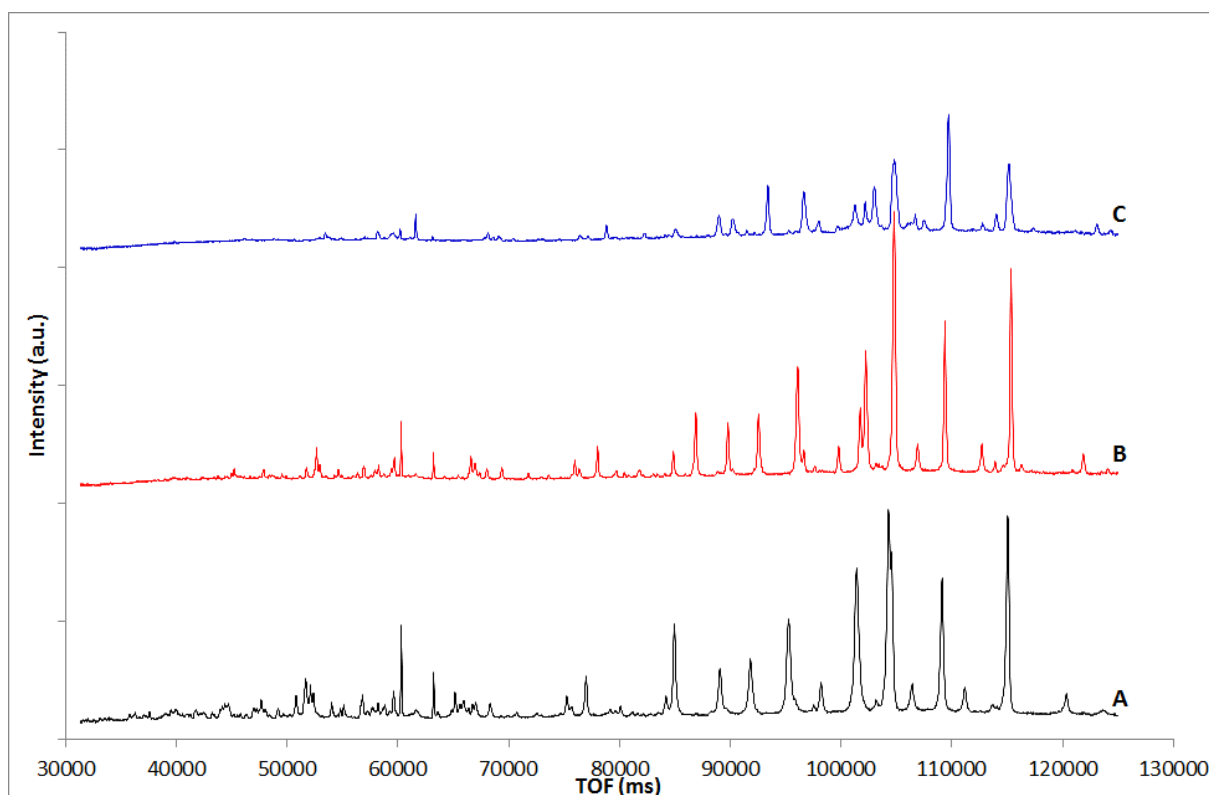
Figure 3.34 HRPD TOF methyl stearate quench cooled from the melt, bank 3 recorded at (A) 4.2 K, (B) 193 K, (C) 300 K.

Figure 3.34 shows the three bank 3 long scans at 4.2 K, 193 K and 300 K with increasingly better quality data on decreasing the temperature. There are however a few differences in splitting of peaks between 95000 and 105000 ms, in addition to peaks shifting to different degrees on change of temperature.
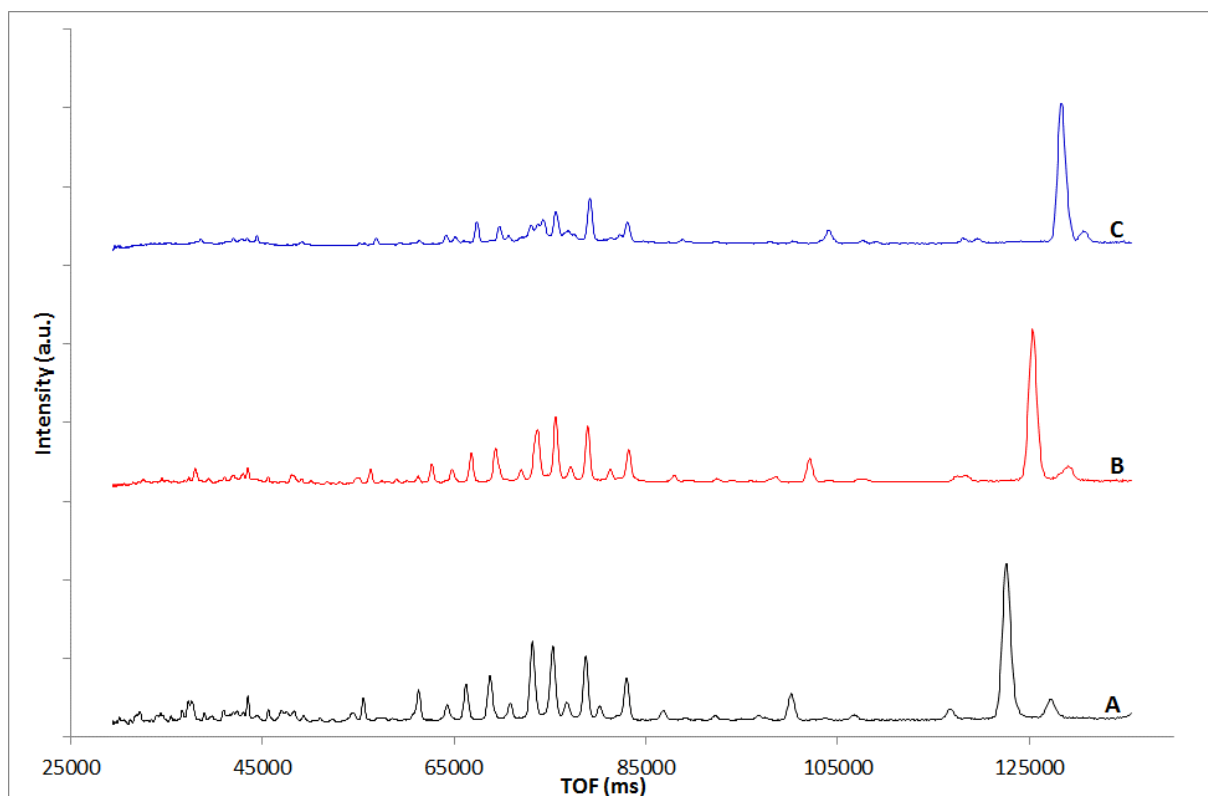
Figure 3.35 HRPD TOF methyl stearate quench cooled from the melt, bank 2 recorded at (A) 4.2 K, (B) 193 K, (C) 300 K.

Unlike bank 3, the bank 2 data shown in Figure 3.35 show no change in splitting, but just sharper and more resolved peaks on decreasing the temperature.
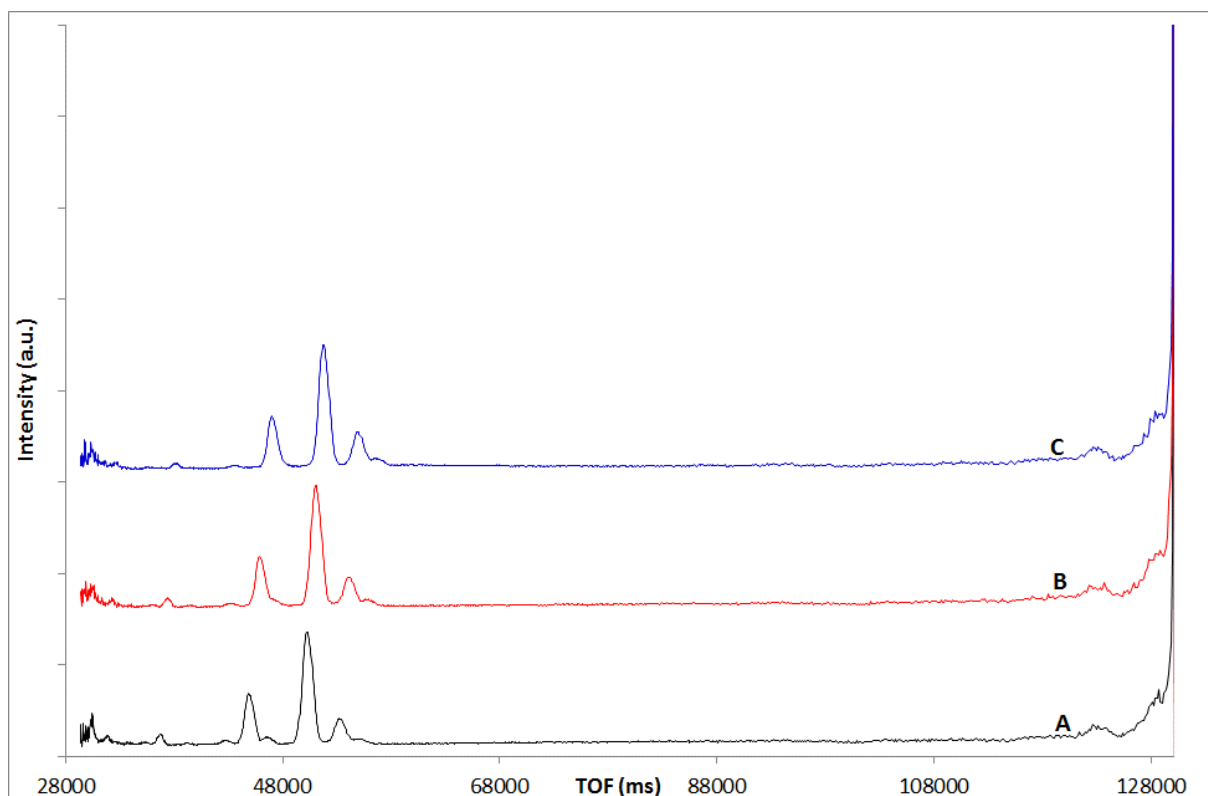
Figure 3.36 HRPD TOF methyl stearate quench cooled from the melt, bank 1 recorded at (A) 4.2 K, (B) 193 K, (C) 300 K.

Figure 3.36 shows the bank 1 low angle data for the three long scans however there is no difference between the different temperature scans.

Figures 3.37 and 3.38 are Rietveld refinements for the 4.2 K and 193 K bank 3 scans, respectively, with the refined lattice parameters shown in Table 3.10 and the atomic positions in appendices 3.1.4 and 3.1.5. Both refinements show that the data fits well to the MS-*Cc* [76] even with a slight difference in peak splitting, which was the targeted phase during crystallisation. A refinement was not however run with the 300 K bank 3 scan due to the data being of too poor quality, which is probably due to the phase being near its melting point.
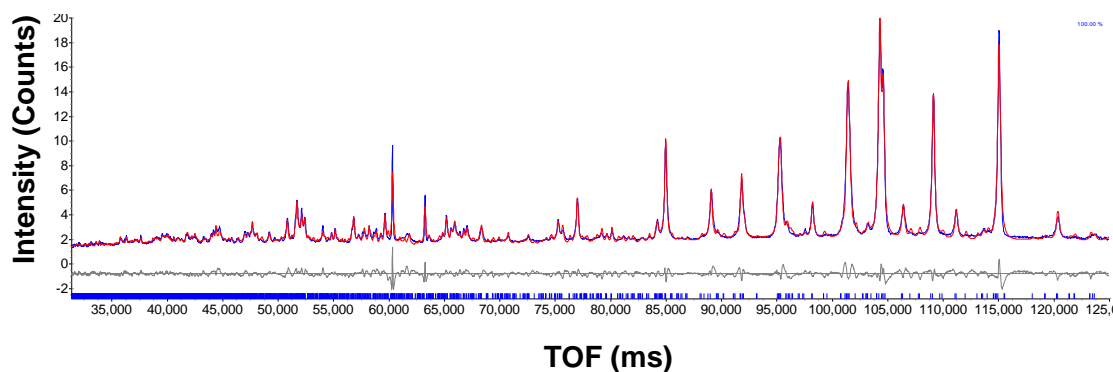
Figure 3.37 Observed (blue line) and calculated (red line) profiles from the Rietveld refinement using HRPD bank 3 data for methyl stearate quench cooled from the melt recorded at 4.2 K with the MS-*Cc* phase[76]. (R_{wp} = 6.55, R_p = 5.18, χ = 0.19). The tick marks represent calculated peak positions.
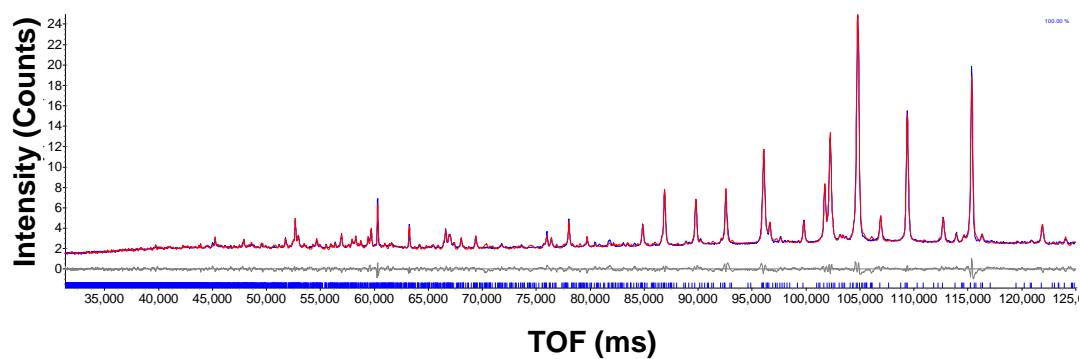
Figure 3.38 Observed (blue line) and calculated (red line) profiles from the Rietveld refinement using HRPD bank 3 data for methyl stearate quench cooled from the melt recorded at 193 K with the MS-*Cc* phase[76]. (R_{wp} = 4.37, R_p = 3.52, χ = 0.13). The tick marks represent calculated peak positions.

Table 3.10 Refined lattice parameters for methyl stearate quench cooled from the melt, recorded at 4.2 K and 193 K.

Parameter	4.2 K	193 K
Phase / Space group	MS-*Cc* / *Cc*	MS-*Cc* / *Cc*
a (Å)	48.9543(4)	48.9865(2)
b (Å)	7.0437(1)	7.2034(1)
c (Å)	5.4957(1)	5.5513(1)
β (°)	76.9569(14)	77.4588(8)
Volume (Å^3)	1846.153(50)	1912.151(35)

3.5.1 Thermal expansion coefficients

As mentioned previously, short scans were run on heating and cooling the MS-*Cc* phase to determine whether there were any structural changes and determine thermal expansion coefficients. Figures 3.39, 3.40 and 3.41 show the short scans on heating from 20 K to 300 K for banks 3, 2 and 1, respectively. As shown in the long scans banks 2 and 1 don't seem change on temperature apart from shifting of the patterns due to thermal expansion of the unit cell.
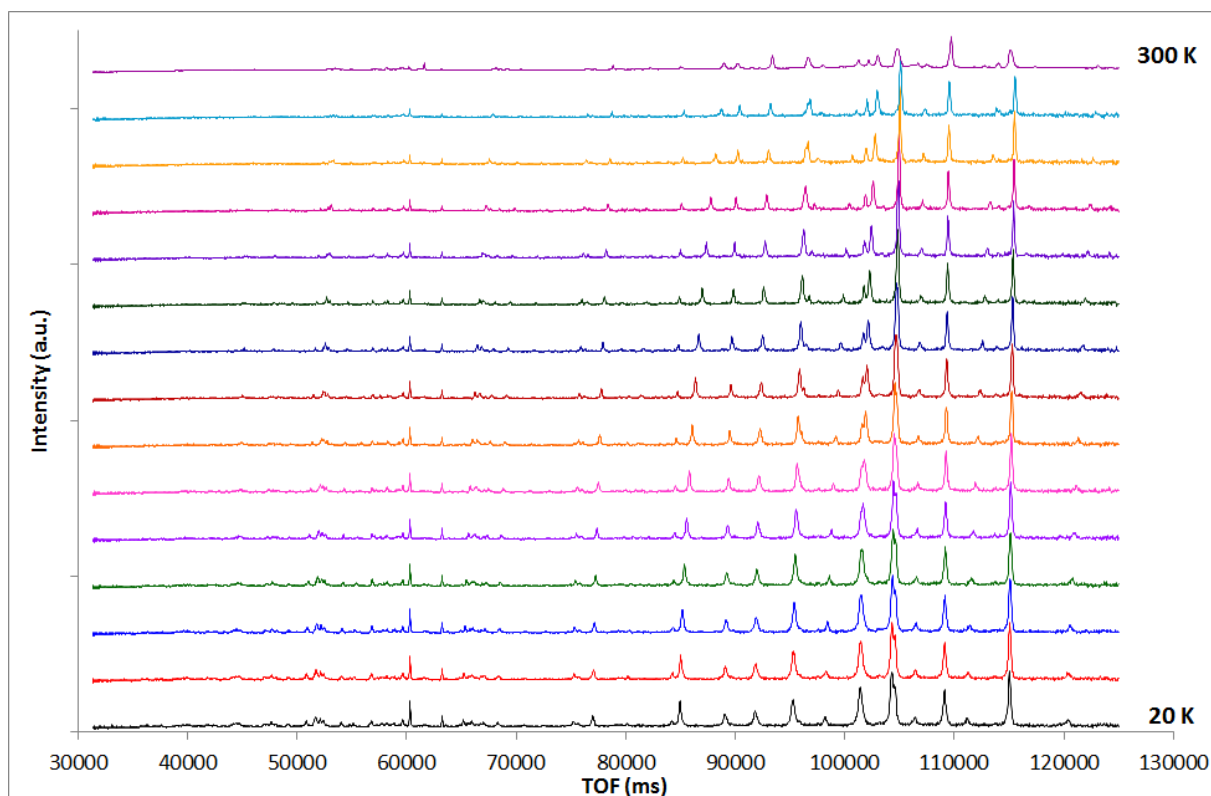
Figure 3.39 MS-*Cc* HRPD TOF bank 3 scans heating from 20 K to 300 K at 20 K intervals.

Bank 3 scans shown in Figure 3.34, however, show several changes in splitting on changing the temperature. This is due to bank 3 (backscattering) being the high resolution detector bank. Table 3.11 summarises the changes in peak splitting shown in Figure 3.39 comparing the 20 K and 300 K scans, however thermal expansion will account for some peak shifting in the scan.

Table 3.11 Summary of peak splitting differences in the *MS-Cc* phase.

20 K	300 K
1 peak at 95287 ms	2 peaks at 96466 s and 98277 ms
1 peak at 101360 ms	2 peaks at 102246 s and 103139 ms
1 split peak at 104823 ms	1 peak at 104698 ms

Two of the peaks are seen as single peaks at 20 K, however by 300 K they appear as two separate peaks, whereas one peak is a split peak at 20 K but appears as a single peak at 300 K. Whilst these changes can be seen gradually changing on change in temperature, around 140 K is where they switch from being one peak to two peaks and vice versa. This is due to relative thermal expansion of the lattice parameters at different rates.
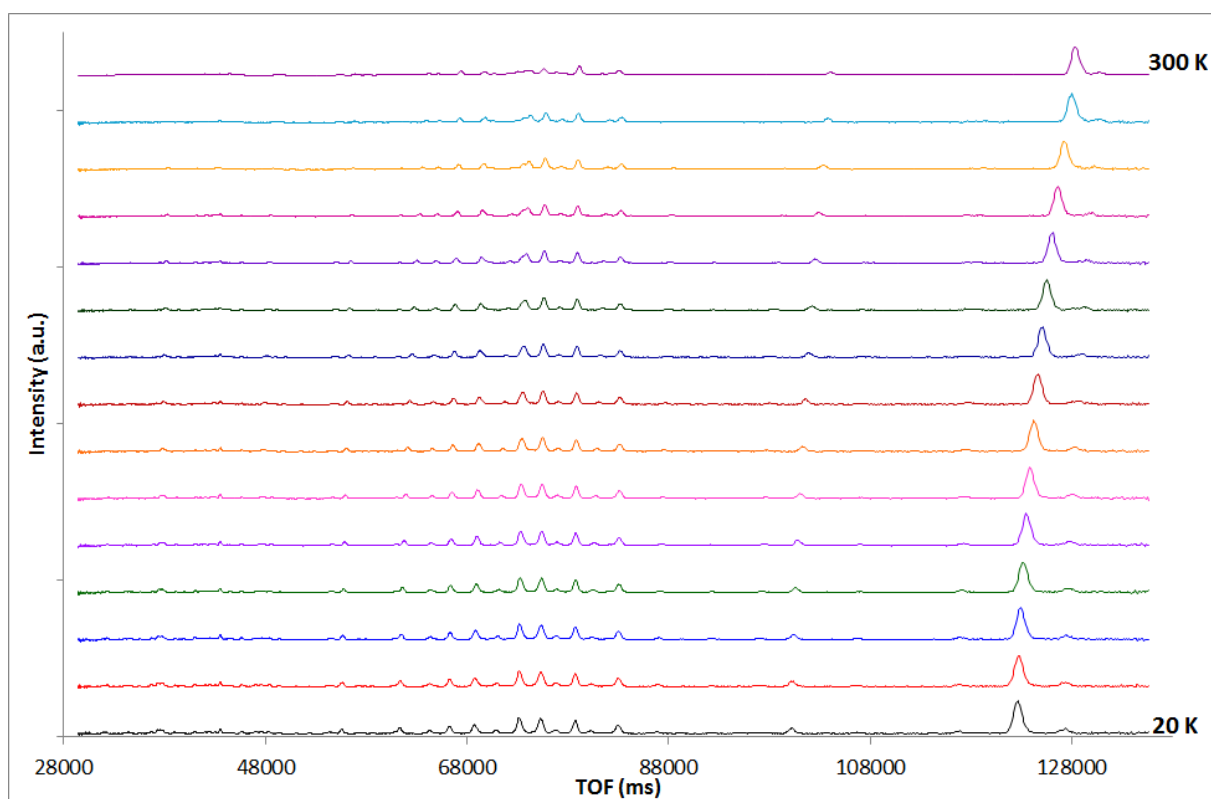
Figure 3.40 MS-*Cc* HRPD TOF bank 2 scans heating from 20 K to 300 K at 20 K intervals.
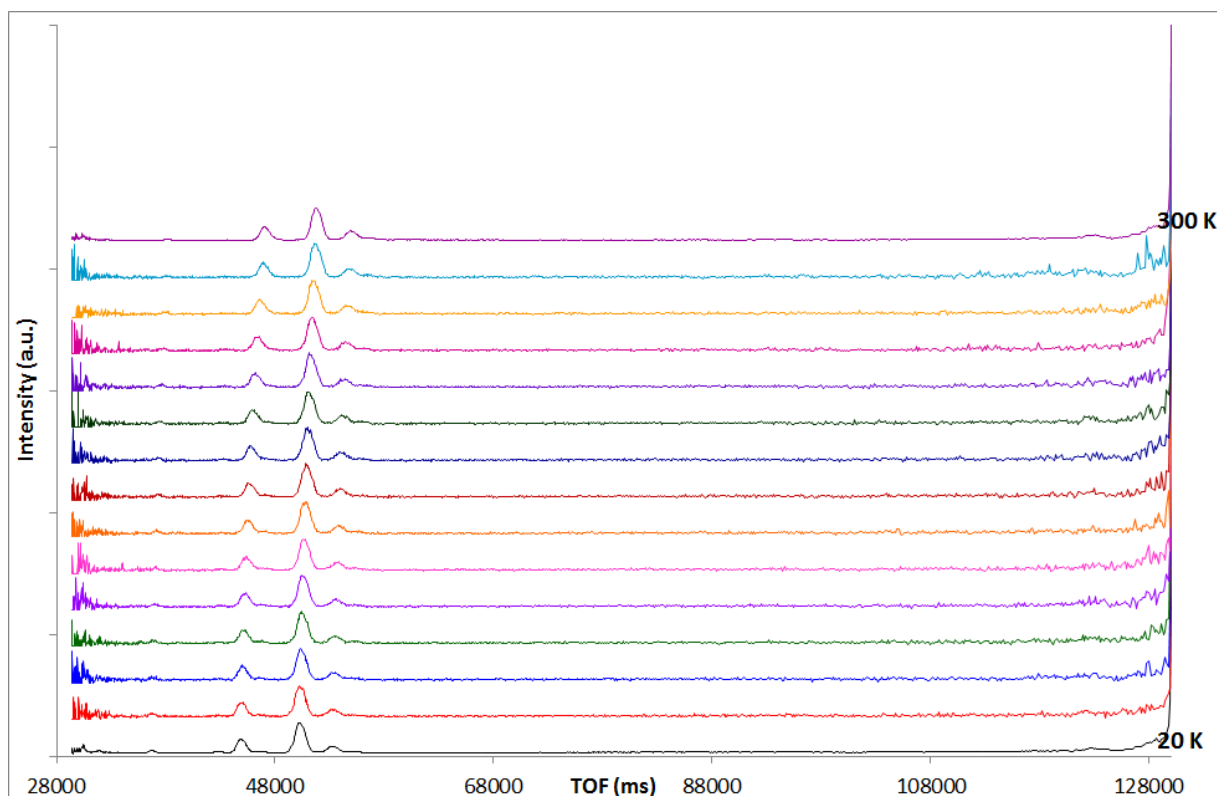
Figure 3.41 MS-*Cc* HRPD TOF bank 1 scans heating from 20 K to 300 K at 20 K intervals.

Figures 3.42, 3.43 and 3.44 show the short scans on cooling from 290 K to 10 K for banks 3, 2 and 1, respectively. As with the heating scans the cooling scans for banks 2 and 1 don't change with temperature, but the bank 3 scans also don't change on cooling. The data appears of less quality with less sharp and defined peaks, and all peaks which appeared as two peaks or split peaks at either 20 K or 300 K on heating, just appear as one peak in the cooling scans. During the heating scans the sample was heated to near its melting point and then cooled. The sample would have been exposed to enough heat for the molecules to partially rearrange compared to the initial quench cooling of the sample.

97
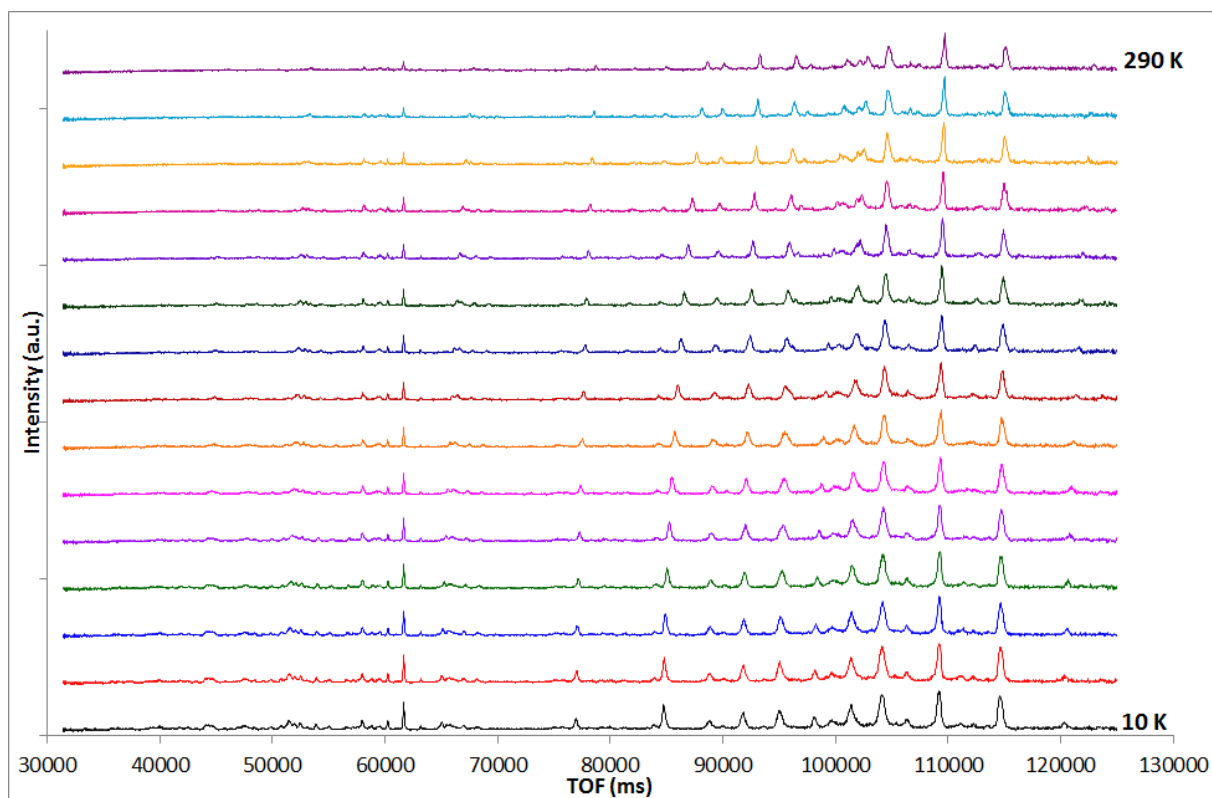
Figure 3.42 MS-*Cc* HRPD TOF bank 3 scans cooling from 290 K to 10 K at 20 K intervals.
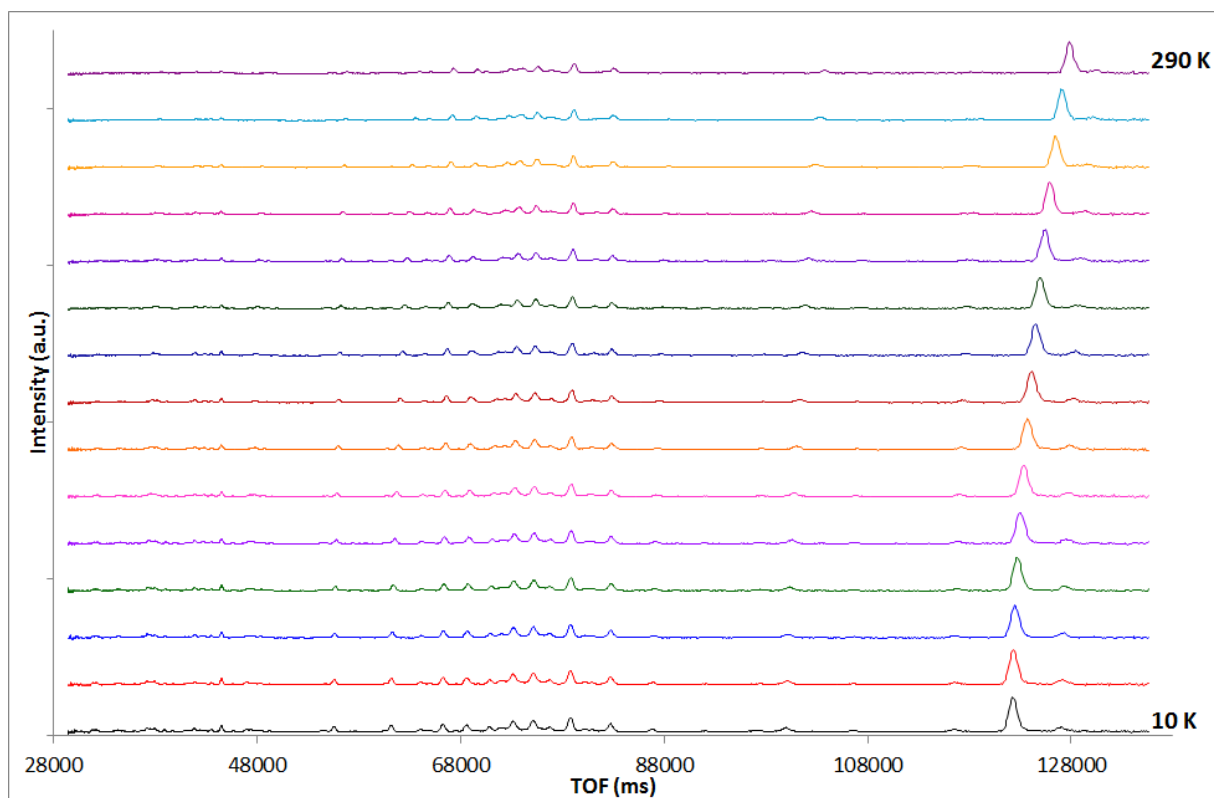
Figure 3.43 MS-*Cc* HRPD TOF bank 2 scans cooling from 290 K to 10 K at 20 K intervals.
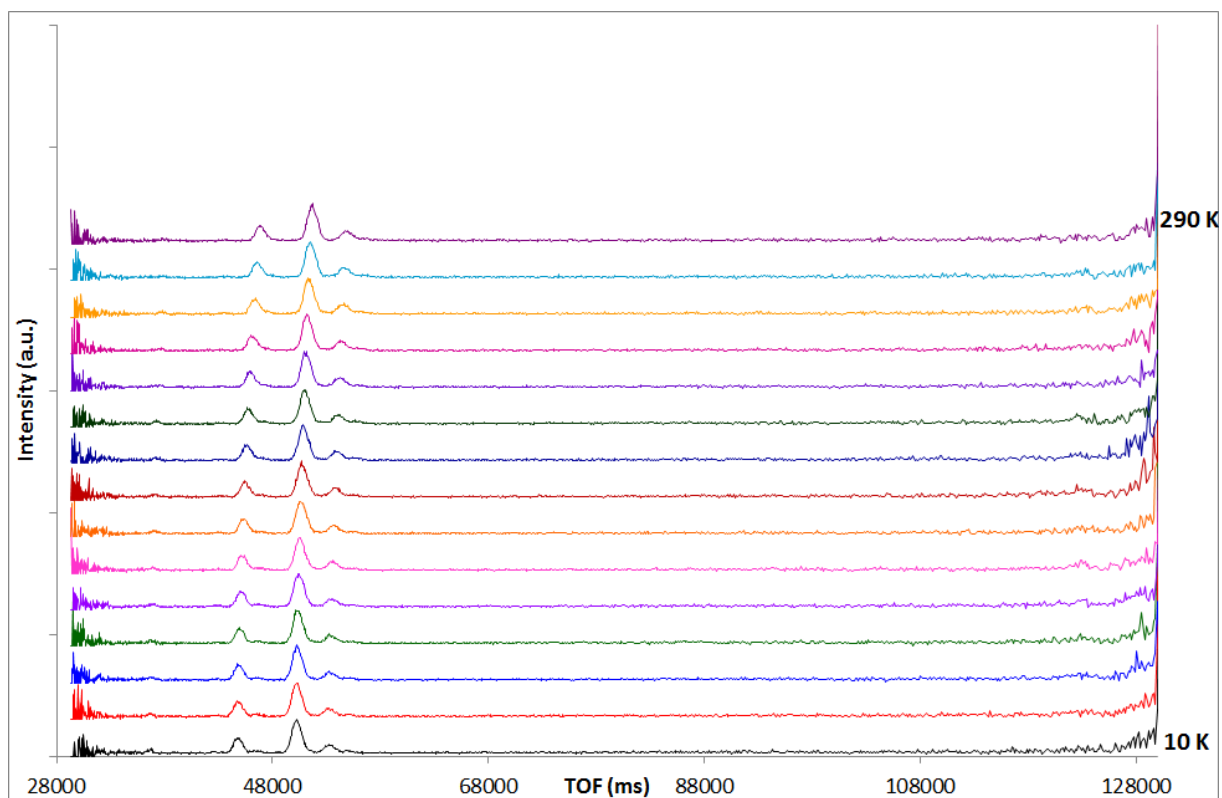
Figure 3.44 MS-*Cc* HRPD TOF bank 1 scans cooling from 290 K to 10 K at 20 K intervals.

Rietveld refinements were run for the bank 3 short scans from 20 K to 260 K to obtain lattice parameters and calculate thermal expansion coefficients, however they were not able to be obtained for the 280 K and 300 K scans due to the poorer quality of the data as the sample neared its melting point.

Figures 3.45 to 3.49 and Table 3.12 contain the refined lattice parameters for the quench cooled melt phase with good linear contraction of the unit cell, and the refinements can be found in appendix 3.5.

Table 3.12 Refined lattice parameters and errors for MS-*Cc* phase heating scans.

Temperature (K)	*a* lattice parameter (Å)	*b* lattice parameter (Å)	*c* lattice parameter (Å)	*β* lattice parameter (°)	Volume lattice parameter (Å^3)
260	49.0093(4)	7.3148(2)	5.5786(1)	77.704(1)	1953.99(7)
240	49.0018(3)	7.2765(2)	5.5698(1)	77.627(1)	1939.86(6)
220	48.9961(3)	7.2437(2)	5.5615(1)	77.550(1)	1927.42(5)
200	48.9891(4)	7.2132(1)	5.5539(1)	77.483(2)	1915.90(5)
180	48.9824(4)	7.1860(1)	5.5470(1)	77.418(2)	1905.57(5)
160	48.9768(4)	7.1609(1)	5.5387(1)	77.345(2)	1895.33(6)
140	48.9741(4)	7.1370(1)	5.5307(1)	77.277(1)	1885.68(6)
120	48.9687(4)	7.1147(1)	5.5245(1)	77.217(2)	1877.00(6)
100	48.9624(4)	7.0945(1)	5.5180(1)	77.164(2)	1868.85(6)
80	48.9604(5)	7.0768(1)	5.5108(1)	77.095(2)	1861.18(7)
60	48.9588(5)	7.0612(1)	5.5044(1)	77.046(2)	1854.46(6)
40	48.9556(5)	7.0498(2)	5.4991(1)	76.991(2)	1849.18(7)
20	48.9555(5)	7.0447(2)	5.4964(1)	76.962(2)	1846.71(6)
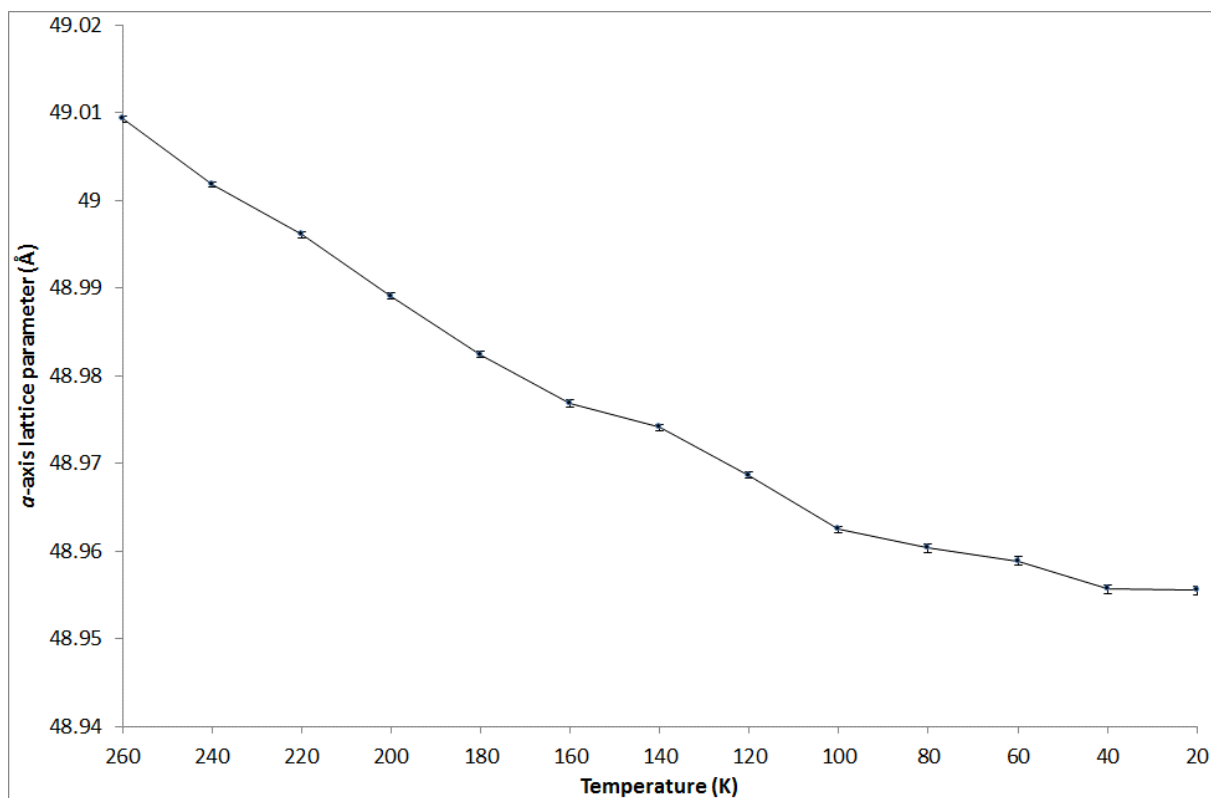
Figure 3.45 Refined *a*-axis lattice parameters from MS-*Cc* phase heating scans.
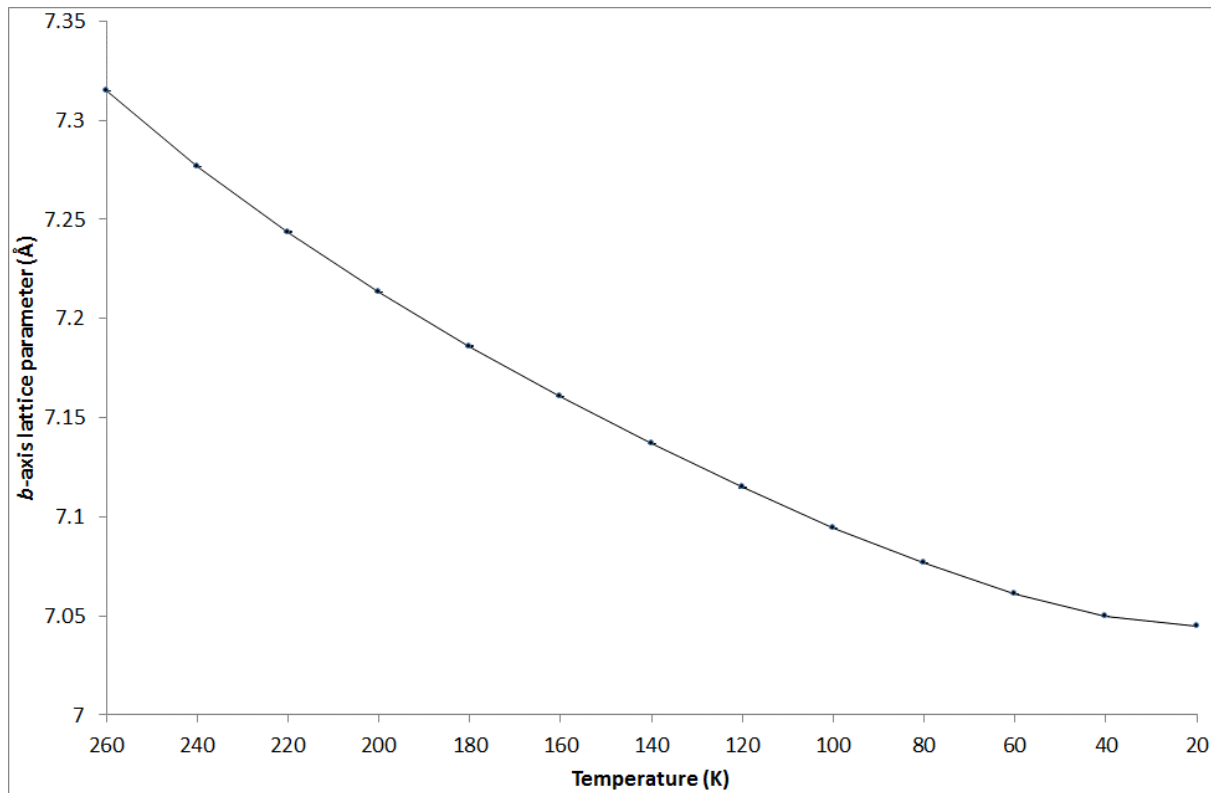
Figure 3.46 Refined *b*-axis lattice parameters from MS-*Cc* phase heating scans.
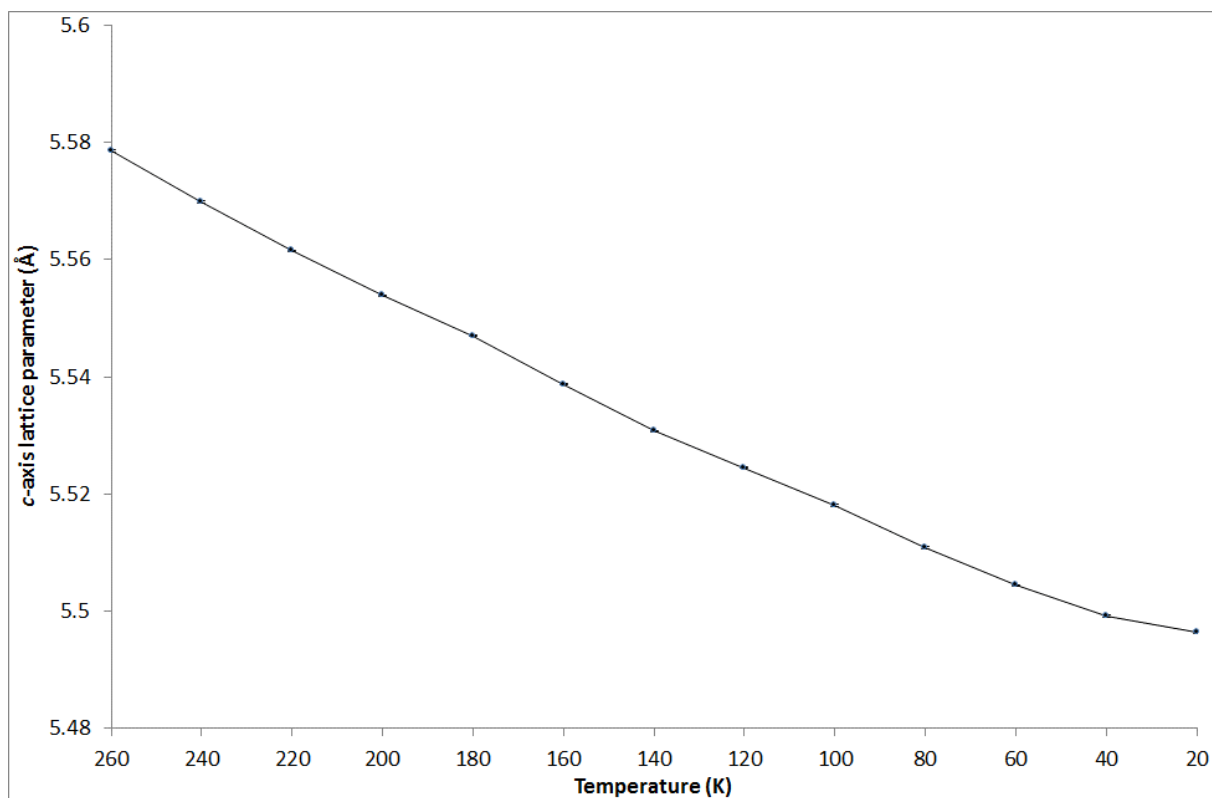
Figure 3.47 Refined *c*-axis lattice parameters from MS-*Cc* phase heating scans.
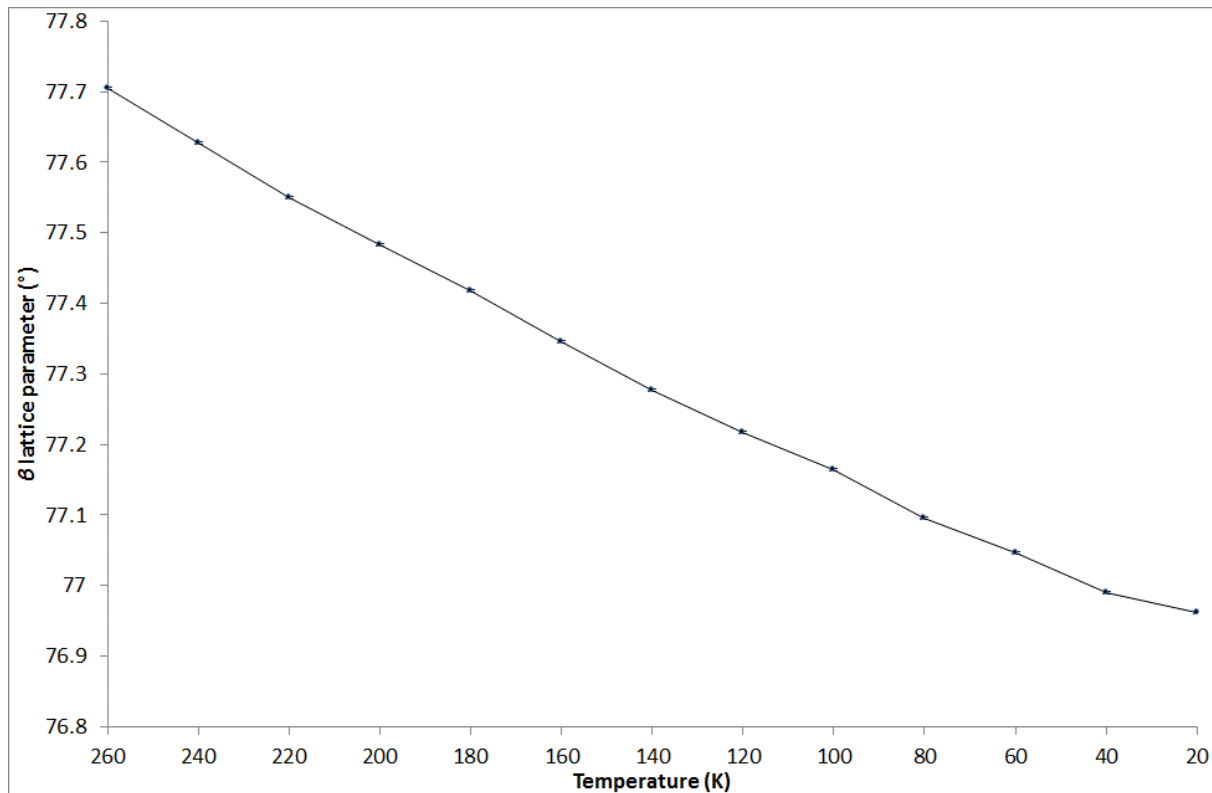
Figure 3.48 Refined *β* angle from MS-*Cc* phase heating scans.

103
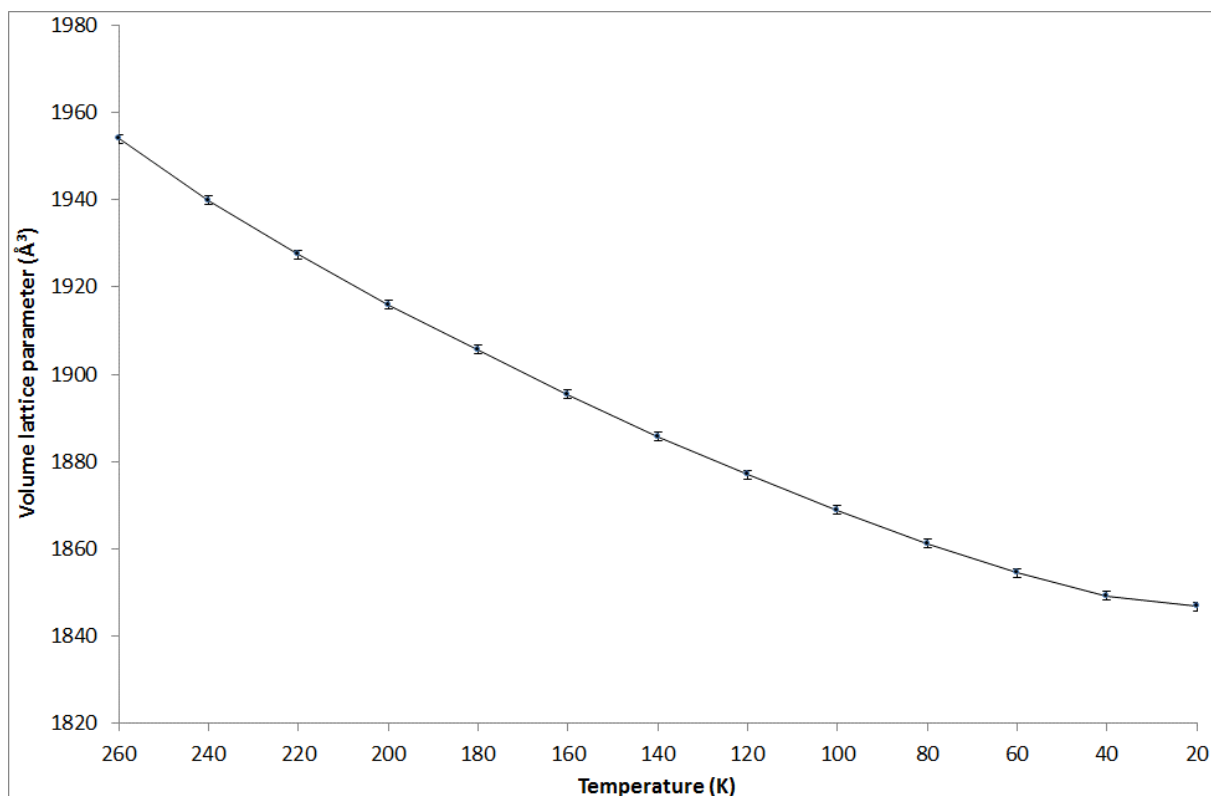
Figure 3.49 Refined volumes from MS-*Cc* phase heating scans.

Table 3.13 Calculated linear thermal expansion coefficients for the MS-*Cc* phase.

Lattice Parameter	Thermal Expansion Coefficient (K^{-1})
a (Å)	4.57993×10^{-6}
b (Å)	1.59732×10^{-4}
c (Å)	6.22895×10^{-5}
β (°)	4.01898×10^{-5}
Volume ($Å^3$)	2.42057×10^{-4}

Table 3.13 contains the calculated linear thermal expansion coefficients using Equation 3.1 for the MS-*Cc* phase, which, like the slow cooled melt phase, are larger than those typically reported in the literature.

Comparing the two sets of thermal expansion coefficients calculated for the two melt phases they are all very similar with the same magnitude, apart from the coefficient for the *a*-axis, which is 5 times larger for the MS-*C*2 phase, than the MS-*Cc* phase. The difference in thermal expansion coefficients for the two melt phases confirms that, whilst the structures may have very similar PXRD patterns, they behave slightly differently when exposed to differences in temperature, as the structures don't expand and contract at the same rate in all axes.

3.6 Converting the unit cell of the Methyl Stearate *C*2/*c* Phase to Room Temperature

One problem throughout the project was that the data used to solve the structure of the MS-*C*2/*c*[74] polymorph was recorded at 100 K and no room temperature values were recorded for comparison to the other phases. To estimate what they might be, the three sets of methyl stearate thermal expansion coefficients were used to modify the 100 K lattice parameters and estimate the changes up to 295 K.

Table 3.14 Comparison of original MS-*C*2/*c* (100 K)[74] lattice parameters, and 295 K lattice parameters for the MS-*C*2/*c* phase calculated from the *Pnab*, *C*2 and *C*c methyl stearate thermal expansion coefficients.

	a (Å)	*b* (Å)	*c* (Å)	*β* (°)	Volume (Å^3)
Original MS-*C*2/*c* (100 K)[74]	95.24	7.09	5.54	93.22	3735
295 K with *Pnab* coefficients	96.5427	7.4073	5.6175	-	3969.557
295 K with *C*2 coefficients	95.6267	7.3610	5.6129	94.1031	3944.029
295 K with *C*c coefficients	95.3251	7.3108	5.6073	93.9506	3911.296

Table 3.14 contains the original 100 K lattice parameters and the parameters calculated at 295 K with the three sets of coefficients, with Figure 3.50 showing simulated PXRD patterns for the four sets of parameters. All three simulated patterns at 295 K have nearly identical PXRD patterns; however the small peak at 24.18° 2θ in the 100 K PXRD pattern, is a shoulder on the large peak at 24.2° 2θ with the three room temperature simulated patterns.
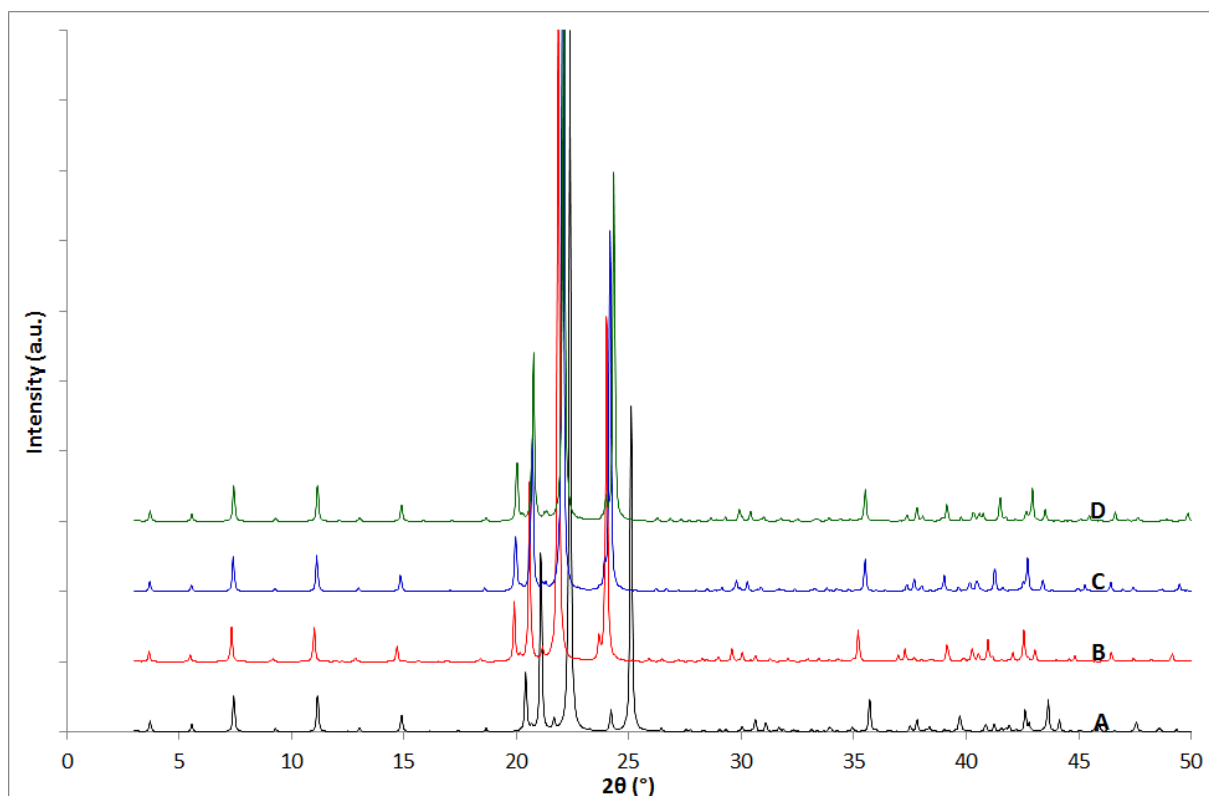
Figure 3.50 Simulated PXRD patterns of methyl stearate structures based on (A) the MS-*C*2/*c* structure (100 K)[74], (B) the MS-*C*2/*c* structure with 295 K lattice parameters calculated from *Pnab* thermal expansion coefficients, (C) the MS-*C*2/*c* structure with 295 K lattice parameters calculated from *C*2 thermal expansion coefficients, (D) the MS-*C*2/*c* structure with 295 K lattice parameters calculated from *Cc* thermal expansion coefficients. *λ* = 1.54056 Å
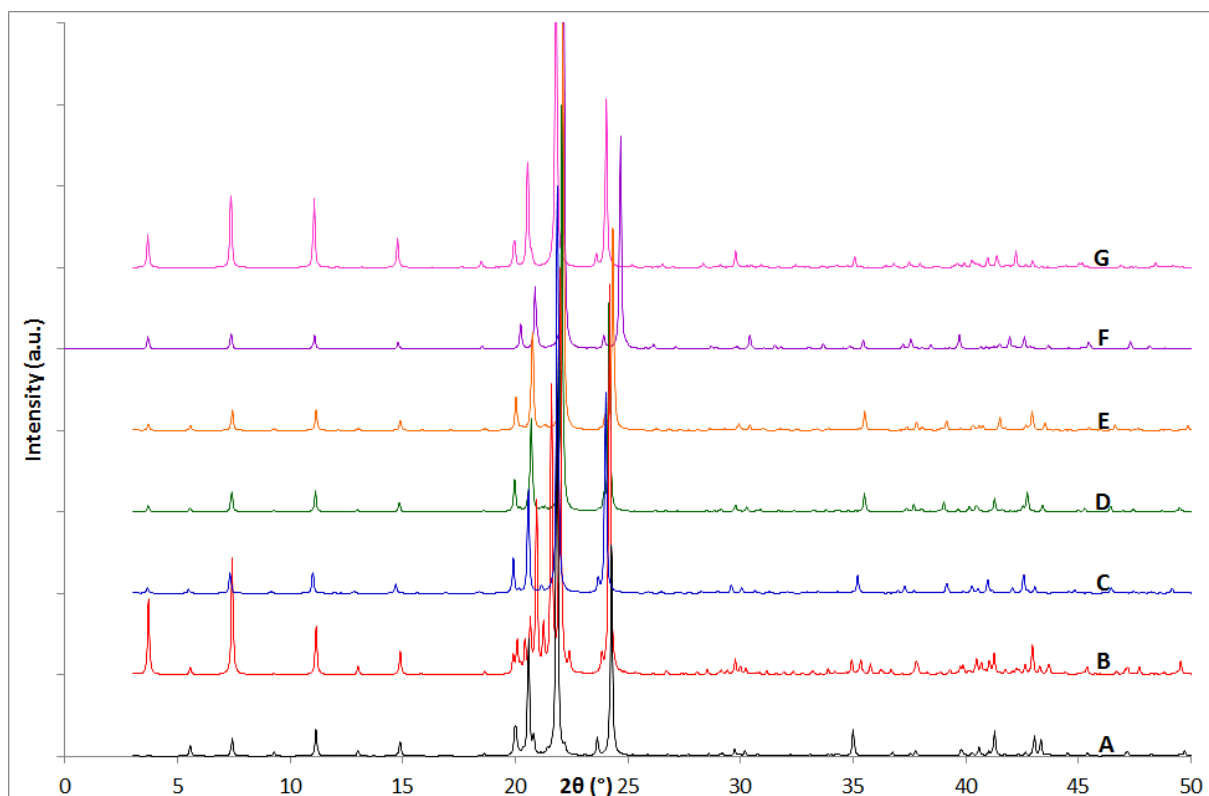
Figure 3.51 Simulated PXRD patterns of methyl stearate based on (A) the MS-*A*2/*a* structure (room temperature)[45], (B) the MS-*Pnab* structure (room temperature)[46], (C) the MS-*C*2/*c* structure with 295 K lattice parameters calculated from *Pnab* thermal expansion coefficients, (D) the MS-*C*2/*c* structure with 295 K lattice parameters from *C*2 thermal expansion coefficients, (E) the MS-*C*2/*c* structure with 295 K lattice parameters calculated from *Cc* thermal expansion coefficients, (F) the MS-*C*2 (233 K)[75] phase, (G) the MS-*Cc* (193 K)[76] phase. *λ* = 1.54056 Å

Figure 3.51 compares the three MS-*C*2/*c* methyl stearate simulated PXRD patterns with the other four polymorphs. Whilst now the peaks of the MS-*C*2/*c* phase line up with the other methyl stearate polymorphs, due to less temperature difference between the simulated patterns, the pattern for the MS-*C*2/*c* phase is still different enough to the other monoclinic phases that it could be identified.

3.7 Gaussian Dipole Calculations

Due to the different arrangements of the molecules in the crystal structures of the methyl stearate polymorphs, and the polarity of the methyl stearate molecule, dipole calculations using the Gaussian[72] computer program were run to determine the overall dipole of the crystal structures. Dipole calculations were used to assess whether the two melt phase crystal structures are correct, assuming that for a stable solid crystal structure, the net dipole should be zero.

Five different theories and basis sets were used to compute the dipoles, to determine whether they all produced similar results and therefore produce reliable comparable results.

Figures 3.52 to 3.57 show the molecular layouts of the molecules that were run, building up from one molecule to the full unit cell to determine how the dipole is affected by more molecules in the crystal system and to determine whether a net zero dipole is achieved.
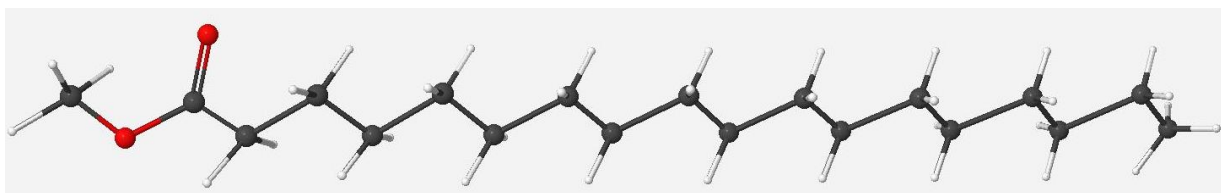
Figure 3.52 Gaussian molecular layout of 1 molecule.
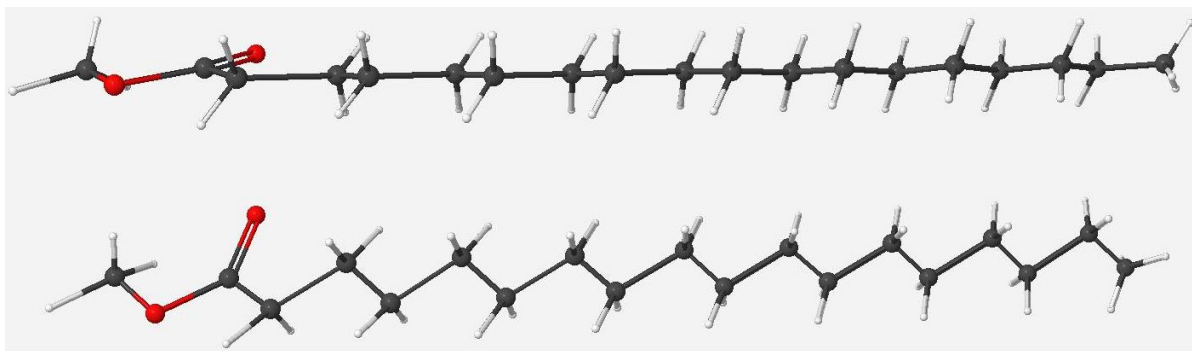
Figure 3.53 Gaussian molecular layout of 2 molecules stacking.
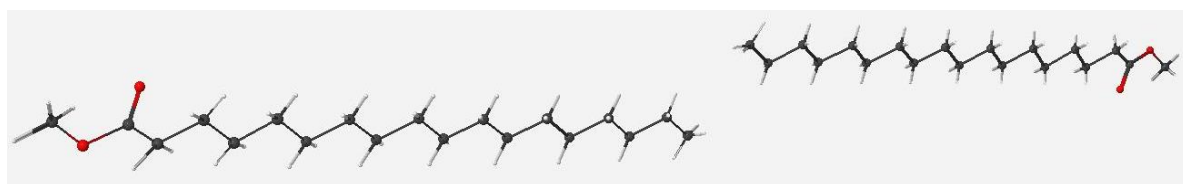
Figure 3.54 Gaussian molecular layout of 2 molecules in a layer.
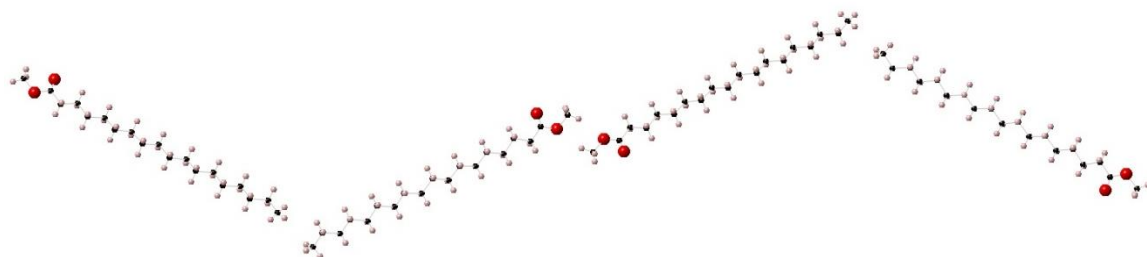
Figure 3.55 Gaussian molecular layout of 4 molecules in a layer.
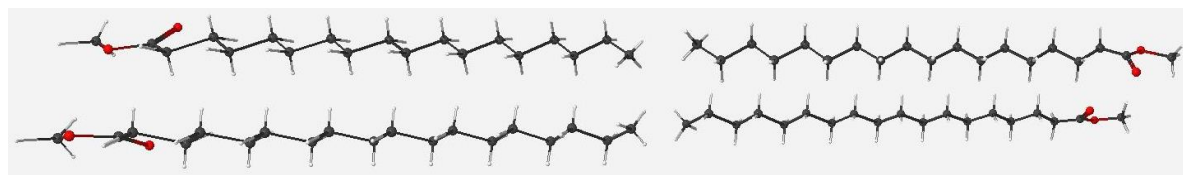
Figure 3.56 Gaussian molecular layout of 4 molecules in a half cell.
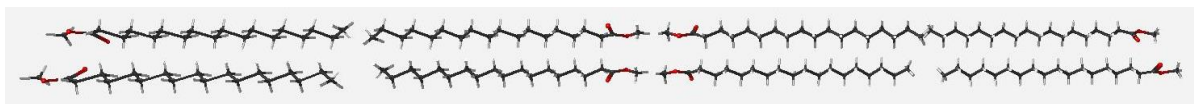
Figure 3.57 Gaussian molecular layout of 8 molecules in a full unit cell.

3.7.1 Gaussian dipole calculations

Gaussian dipole calculations were run for the five methyl stearate polymorphs. For the Hartree-Fock routine and B3LYP routine calculations with eight molecules in the unit cell, results could not be obtained due to insufficient memory in the program to complete the job run.

MS-*A2/a*[45] structure

Table 3.15 Gaussian molecular dipole results for MS-*A2/a* [45] structure.

	Hartree-Fock basic (Debye)	Hartree-Fock routine (Debye)	B3LYP routine (Debye)	AM1 (Debye)	PM3 (Debye)
1 molecule	2.2246	2.9002	2.6485	2.9262	2.8802
2 molecules stacking	4.2205	5.4788	5.0837	5.2103	5.0221
2 molecules in a layer	0	0	0	0	0
4 molecules in a layer	0.0032	0.0094	0.0042	0.0014	0.0017
4 molecules in a half cell	0.7349	0.8399	0.9024	0.4654	0.5421
4 molecules in a central half cell	0	0	0	0	0
8 molecules full cell	0	-	-	0	0

Results for the MS-*A*2/*a* dipole calculations are fairly consistent between the different basis sets used. As the molecules build up a zero dipole is calculated for 2 molecules in a layer, a central 4 molecule half-cell and the full unit cell. There is also a fairly small dipole within the 4 molecules in a layer.

MS-*Pnab*[46] structure

Table 3.16 Gaussian molecular dipole results for MS-*Pnab* [46] structure.

	Hartree-Fock basic (Debye)	Hartree-Fock routine (Debye)	B3LYP routine (Debye)	AM1 (Debye)	PM3 (Debye)
1 molecule	1.4238	1.6095	1.4434	1.4290	1.5840
2 molecules stacking	2.5483	2.8705	2.7135	2.3516	2.6611
2 molecules in a layer	1.5645	1.6739	1.4762	1.5107	1.6490
4 molecules in a layer	0.0502	0.0612	0.0771	0.0133	0.0098
4 molecules in a half cell	3.9608	4.5445	3.9794	4.5053	4.9529
4 molecules in a central half cell	0	0	0	0.0001	0.0001
8 molecules full cell	0	-	-	0	0

As with the MS-*A*2/*a* phase the MS-*Pnab* phase also has a net zero dipole for the 4 molecules central half-cell and the full unit cell. The dipole of a single molecule is also at least 0.8 Debye less with the MS-*Pnab* molecule than the MS-*A*2/*a* due to the molecular structure.

MS-*C*2/*c*[74] structure

Table 3.17 Gaussian molecular dipole results for MS-*C*2/*c*[74] structure.

	Hartree-Fock basic (Debye)	Hartree-Fock routine (Debye)	B3LYP routine (Debye)	AM1 (Debye)	PM3 (Debye)
1 molecule	1.2965	1.5052	1.3414	1.3407	1.4685
2 molecules stacking	2.1197	2.5295	2.1596	2.3429	2.5550
2 molecules in a layer	0	0	0	0	0
4 molecules in a layer	0.0008	0.0013	0.0020	0.0020	0.0035
4 molecules in a half cell	0.5338	0.5208	0.6102	0.1754	0.2067
4 molecules in a central half cell	0	0	0	0.0001	0.0001
8 molecules full cell	0	-	-	0.0001	0.0001

The dipole of the MS-*C*2/*c* single molecule is lower than both the MS-*A*2/*a* and MS-*Pnab*; and like the MS-*A*2/*a* structure there is a net zero dipole for 2 molecules in a layer, 4 molecules in a central half-cell and the full unit cell.

MS-*C2* structure[75]

Table 3.18 Gaussian molecular dipole results for MS-*C2* structure[75].

	Hartree-Fock basic (Debye)	Hartree-Fock routine (Debye)	B3LYP routine (Debye)	AM1 (Debye)	PM3 (Debye)
1 molecule	0.9953	0.9880	2.9658	0.7368	0.7240
2 molecules stacking	0.2772	0.3031	0.4107	0.7584	0.8495
2 molecules in a layer	0.5147	0.5513	0.3687	0.7710	0.9316
4 molecules full cell	0.2765	0.5017	0.3883	1.4669	1.6324
8 molecules 2 unit cells *a* + 1	0.4778	-	-	2.8568	3.1918
8 molecules 2 unit cells *b* + 1	0.5185	-	-	2.7636	2.9945
8 molecules 2 unit cells *c* + 1	1.4931	-	-	3.0996	3.4328
4 molecules in a layer	1.0279	1.1024	0.7354	1.5382	1.8589
4 molecules in a central half cell	0.2271	0.4421	0.0412	1.4330	1.6032

The MS-*C2* phase has a lower dipole for 1 molecule than all three single crystal structures; however there is no zero net dipole for any molecular arrangement. The two unit cells with *a* + 1 are directly comparable to the full unit cell of the three single crystal structures by extending the cell along the long axis. There also seems to a greater difference between the basis set results for the 4 and 8 molecule calculations. Whilst there is a difference in the results between the basis

sets the results confirm that there is a small overall dipole in the *C2* polymorph, but a smaller dipole along the *a* and *b* cell directions than the *c* cell direction.

MS-*Cc* structure[76]

Table 3.19 Gaussian molecular dipole results for MS-*Cc* structure[76].

	Hartree-Fock basic (Debye)	Hartree-Fock routine (Debye)	B3LYP routine (Debye)	AM1 (Debye)	PM3 (Debye)
1 molecule	0.7670	0.9382	0.8949	1.2185	1.3487
2 molecules stacking	1.2812	1.6394	1.5547	2.1845	2.4772
2 molecules in a layer	1.5283	1.8678	1.7737	2.3494	2.5898
4 molecules full cell	2.8565	3.5206	3.2909	4.5096	5.0154
8 molecules 2 unit cells *a* + 1	5.8085	-	-	9.0491	10.0309
8 molecules 2 unit cells *b* + 1	5.3820	-	-	8.6110	9.5563
8 molecules 2 unit cells *c* + 1	7.9236	-	-	10.0989	11.4885
4 molecules in a layer	2.9561	3.6387	3.4567	4.6434	5.1542
4 molecules in a central half cell	2.8441	3.5049	3.2969	4.5007	4.9974

The dipole of the MS-*Cc* molecule is very similar to that of the MS-*C2* phase, but due to slight differences between the results from the basis sets it is not possible to say which has the lower dipole. The dipole however for the full unit cell and larger

calculations increases with increasing number of molecules as they all align in the same direction with the dipole building up.

Overall the dipole calculations have determined that there is some variation between the basis sets and therefore it is impossible to say with certainty the exact dipoles for the different polymorphs, the dipole for the individual molecules is *Cc* < *C*2 < *C*2/*c* < *Pnab* < *A*2/*a*, but for the overall unit cell the three single crystals have a net zero dipole and the *Cc* melt phase has much greater dipole than the *C*2 melt phase.

3.7.2 Gaussian dipole calculations with 1 disordered molecule

Due to there being a net dipole in both melt phases, and the possibility that the phases may be disordered due to the similarity in the phases and the PXRD patterns; disordered structures were run, where one molecule has been flipped around as shown in Figure 3.58. A dipole calculation run for one flipped round molecule in each of the 8 positions in unit cell, with all five methyl stearate polymorphs. This was done to see whether introducing a small amount of disorderd in each of the five polymorphs would increase or decrease the dipole of the unit cell.
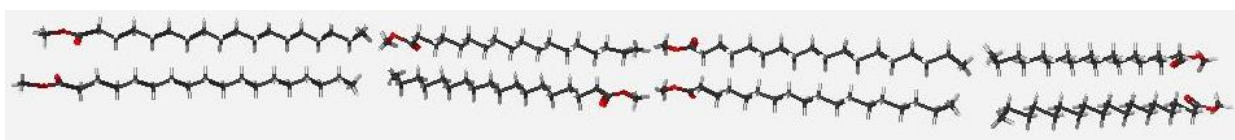
Figure 3.58 Gaussian molecular of disordered molecular structure with figure showing MS-*Pnab* disordered structure 1.

Disordered structures – MS-A2/a [45]

Table 3.20 Gaussian molecular dipole results for MS-*A2/a* [45] disordered structures.

	Hartree-Fock basic (Debye)	Hartree-Fock routine (Debye)	B3LYP routine (Debye)	AM1 (Debye)	PM3 (Debye)
Disordered structure 1	4.4053	-	-	5.6861	5.3001
Disordered structure 2	4.0307	-	-	5.7073	5.1428
Disordered structure 3	4.1551	-	-	5.7829	5.2363
Disordered structure 4	4.6072	-	-	5.7703	5.4339
Disordered structure 5	3.6373	-	-	5.2004	4.0221
Disordered structure 6	4.0307	-	-	5.7073	5.1428
Disordered structure 7	4.1551	-	-	5.7829	5.2363
Disordered structure 8	4.6072	-	-	5.7703	5.4339

Disordered structures – MS-Pnab[46]

Table 3.21 Gaussian molecular dipole results for MS-*Pnab* [46] disordered structures.

	Hartree-Fock basic (Debye)	Hartree-Fock routine (Debye)	B3LYP routine (Debye)	AM1 (Debye)	PM3 (Debye)
Disordered structure 1	2.9281	-	-	2.7941	2.8664
Disordered structure 2	2.6042	-	-	2.7717	2.7885
Disordered structure 3	2.6207	-	-	2.7236	2.7395
Disordered structure 4	2.7724	-	-	2.7816	2.8299
Disordered structure 5	2.9281	-	-	2.7941	2.8663
Disordered structure 6	2.6042	-	-	2.7717	2.7885
Disordered structure 7	2.6207	-	-	2.7235	2.7394
Disordered structure 8	1.3115	-	-	1.8168	0.8960

Disordered structures – MS-C2/c[74]

Table 3.22 Gaussian molecular dipole results for MS-C2/c [74] disordered structures.

	Hartree-Fock basic (Debye)	Hartree-Fock routine (Debye)	B3LYP routine (Debye)	AM1 (Debye)	PM3 (Debye)
Disordered structure 1	3.8458	-	-	4.5531	4.6777
Disordered structure 2	4.1384	-	-	4.7525	4.8922
Disordered structure 3	3.2980	-	-	3.8860	4.0516
Disordered structure 4	4.1274	-	-	4.7431	4.8884
Disordered structure 5	3.8117	-	-	4.5532	4.6815
Disordered structure 6	4.1274	-	-	4.7431	4.8883
Disordered structure 7	3.8458	-	-	4.5530	4.6777
Disordered structure 8	4.1384	-	-	4.7524	4.8921

Disordered structures – MS-C2[75]

Table 3.23 Gaussian molecular dipole results for MS-*C*2 [75] disordered structures.

	Hartree-Fock basic (Debye)	Hartree-Fock routine (Debye)	B3LYP routine (Debye)	AM1 (Debye)	PM3 (Debye)
Disordered structure 1	2.7011	2.9274	3.0908	3.3747	3.5735
Disordered structure 2	3.2383	3.4300	3.3307	3.5899	3.9025
Disordered structure 3	3.2383	3.4300	3.3307	3.5900	3.9025
Disordered structure 4	2.7011	2.9274	3.0908	3.3746	3.5735

Disordered structures – MS-*C2*[75] *a* + 1

Table 3.24 Gaussian molecular dipole results for MS-*C2*[75] *a* + 1 disordered structures.

	Hartree-Fock basic (Debye)	Hartree-Fock routine (Debye)	B3LYP routine (Debye)	AM1 (Debye)	PM3 (Debye)
Disordered structure 1	2.8758	-	-	4.7367	5.0827
Disordered structure 2	3.4454	-	-	4.9706	5.4137
Disordered structure 3	3.4252	-	-	4.9486	5.3948
Disordered structure 4	2.8969	-	-	4.7522	5.0977
Disordered structure 5	3.5691	-	-	4.7942	5.3305
Disordered structure 6	2.8969	-	-	4.7520	5.0975
Disordered structure 7	3.4252	-	-	4.9485	5.3947
Disordered structure 8	3.4454	-	-	4.9705	5.4136

Disordered structures – MS-C2^{75} b + 1

Table 3.25 Gaussian molecular dipole results for MS-C2 ^{75} b + 1 disordered structures.

	Hartree-Fock basic (Debye)	Hartree-Fock routine (Debye)	B3LYP routine (Debye)	AM1 (Debye)	PM3 (Debye)
Disordered structure 1	2.0025	-	-	4.7316	4.9650
Disordered structure 2	2.0025	-	-	4.7317	4.9650
Disordered structure 3	2.5483	-	-	4.9071	5.2128
Disordered structure 4	2.5483	-	-	4.9071	5.2128
Disordered structure 5	2.5962	-	-	4.9181	5.2185
Disordered structure 6	2.5962	-	-	4.9180	5.2183
Disordered structure 7	2.5879	-	-	4.9021	5.2420
Disordered structure 8	2.5879	-	-	4.9020	5.2419

Disordered structures – MS-C2^{75} c + 1

Table 3.26 Gaussian molecular dipole results for MS-C2 ^{75} c + 1 disordered structures.

	Hartree-Fock basic (Debye)	Hartree-Fock routine (Debye)	B3LYP routine (Debye)	AM1 (Debye)	PM3 (Debye)
Disordered structure 1	3.7077	-	-	4.8701	5.2254
Disordered structure 2	3.7342	-	-	4.8656	5.2475
Disordered structure 3	4.2321	-	-	5.0902	5.5583
Disordered structure 4	4.3328	-	-	5.1014	5.4971
Disordered structure 5	3.7342	-	-	4.8656	5.2475
Disordered structure 6	3.7078	-	-	4.8701	5.2255
Disordered structure 7	4.3328	-	-	5.1013	5.4970
Disordered structure 8	4.2321	-	-	5.0900	5.5581

Disordered structures – **MS-*Cc*[76]**

Table 3.27 Gaussian molecular dipole results for MS-*Cc*[76] disordered structures.

	Hartree-Fock basic (Debye)	Hartree-Fock routine (Debye)	B3LYP routine (Debye)	AM1 (Debye)	PM3 (Debye)
Disordered structure 1	2.1718	2.4407	1.7393	2.5791	3.0731
Disordered structure 2	2.1402	2.3693	1.6404	2.6787	3.1142
Disordered structure 3	1.9832	2.3368	1.7737	2.5982	3.0461
Disordered structure 4	1.9642	2.2403	1.3733	2.6390	3.0896

Disordered structures – MS-Cc[76] a + 1

Table 3.28 Gaussian molecular dipole results for MS-Cc[76] a + 1 disordered structures.

	Hartree-Fock basic (Debye)	Hartree-Fock routine (Debye)	B3LYP routine (Debye)	AM1 (Debye)	PM3 (Debye)
Disordered structure 1	5.0716	-	-	6.9978	-
Disordered structure 2	5.0521	-	-	7.0583	-
Disordered structure 3	4.8671	-	-	7.0012	7.9292
Disordered structure 4	4.8235	-	-	7.0365	7.9929
Disordered structure 5	5.0202	-	-	6.9961	8.0168
Disordered structure 6	5.0638	-	-	7.0750	8.0088
Disordered structure 7	4.8754	-	-	6.9983	7.9294
Disordered structure 8	4.9120	-	-	7.0712	8.0083

Disordered structures – MS-Cc[76] b + 1

Table 3.29 Gaussian molecular dipole results for MS-Cc[76] b + 1 disordered structures.

	Hartree-Fock basic (Debye)	Hartree-Fock routine (Debye)	B3LYP routine (Debye)	AM1 (Debye)	PM3 (Debye)
Disordered structure 1	4.6464	-	-	6.6830	7.5784
Disordered structure 2	4.7154	-	-	6.7341	7.6281
Disordered structure 3	4.4685	-	-	6.6175	7.5316
Disordered structure 4	4.6734	-	-	6.8212	7.7057
Disordered structure 5	4.6314	-	-	6.6000	7.5572
Disordered structure 6	4.5673	-	-	6.7607	7.6577
Disordered structure 7	4.5674	-	-	6.6613	7.6051
Disordered structure 8	4.5558	-	-	6.7459	7.6434

Disordered structures – MS-Cc[76] c + 1

Table 3.30 Gaussian molecular dipole results for MS-Cc[76] c + 1 disordered structures.

	Hartree-Fock basic (Debye)	Hartree-Fock routine (Debye)	B3LYP routine (Debye)	AM1 (Debye)	PM3 (Debye)
Disordered structure 1	6.6488	-	-	7.8474	9.1320
Disordered structure 2	6.5926	-	-	7.8149	8.9907
Disordered structure 3	6.4451	-	-	7.9033	9.1592
Disordered structure 4	6.4574	-	-	7.8068	9.0652
Disordered structure 5	7.0888	-	-	7.9461	9.2617
Disordered structure 6	7.1175	-	-	8.0625	9.3664
Disordered structure 7	6.8217	-	-	7.9371	9.1779
Disordered structure 8	6.8290	-	-	8.0826	8.3646

The dipoles for the 1 molecule disordered unit cells all increase apart from the MS-*Cc* when compared to the full unit cell of the original crystal structures. The MS-*Cc* which has the greatest dipole with the original structure has a decrease in dipole of around 1 Debye with the rotation of one molecule in the unit cell structure. The MS-*C*2 phase, however, has a substantial net dipole increase, with the disorder of one molecule when compared to the original crystal structure, which contained a small net dipole for the unit cell.

3.7.3 Gaussian dipole calculations with 2 disordered molecules

As shown in section 3.7.2 the net dipole for 1 disordered molecule in the unit cell increases for the MS-*C*2 structure but decreases the dipole for the MS-*Cc* structure. To see what effect increasing the disorder in the unit cell would have on the two melt structures, dipole calculations with two disordered molecules were run with three combinations of layouts as shown in Figure 3.59 below. The arrows represent which two molecules would be flipped, and the numbers correspond to the results in Tables 3.31 and 3.32.
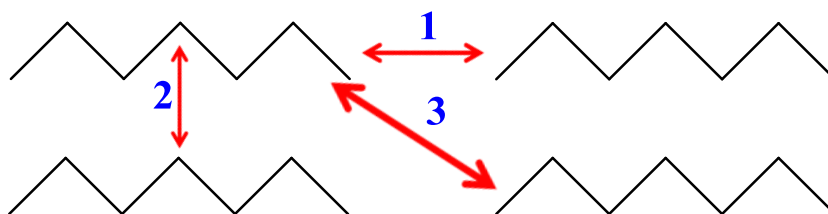
Figure 3.59 Schematic of two disordered molecules layout.

2-molecule disordered structures **MS-*C*2**[75]

Table 3.31 Gaussian molecular dipole results for MS-*C*2 [75] 2-molecule disordered structures.

	Hartree-Fock basic (Debye)	Hartree-Fock routine (Debye)	B3LYP routine (Debye)	AM1 (Debye)	PM3 (Debye)
Disordered structure 1	4.9762	5.1911	2.8589	5.2065	5.2866
Disordered structure 2	5.3506	5.5980	4.1559	5.3534	5.4855
Disordered structure 3	5.6568	5.8708	6.0248	5.5245	5.9267

On increasing the disorder from one to two molecules in the unit cell the MS-*C*2 net dipole increases by at least 1 Debye, and is around 4 Debye higher than the non-disordered crystal structure. The highest dipole is for disordered structure 3 which has the same molecular layout of the molecules as the non-disordered MS-*Cc* phase.

MS-*C*2 Non-disordered Structure
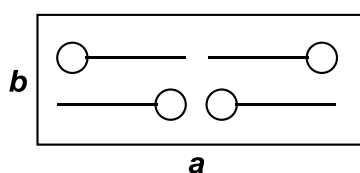
MS-*Cc* Non-disordered Structure
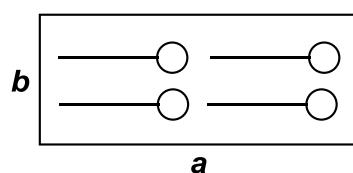
MS-*C*2 Disordered Structure 1
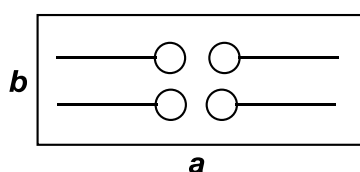
MS-*Cc* Disordered Structure 1
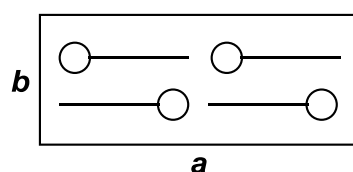
MS-*C*2 Disordered Structure 2
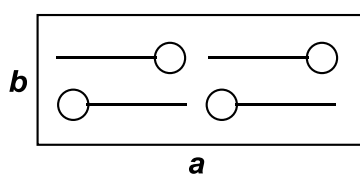
MS-*Cc* Disordered Structure 2
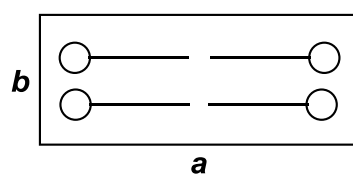
MS-*C*2 Disordered Structure 3
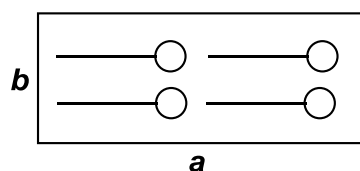
MS-*Cc* Disordered Structure 3
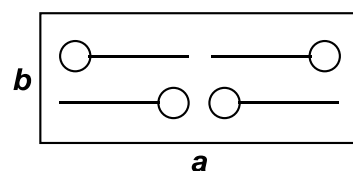
Figure 3.60 Layouts for the two molecule disordered structures of the MS-*C*2 and MS-*Cc* phases compared to their non-disordered structures viewed down the *c*-axis. The circle represents the ester headgroup and the straight line the hydrocarbon tailgroup.

2-molecule disordered structures **MS-*Cc*[76]**

Table 3.32 Gaussian molecular dipole results for MS-*Cc*[76] 2-molecule disordered structures.

	Hartree-Fock basic (Debye)	Hartree-Fock routine (Debye)	B3LYP routine (Debye)	AM1 (Debye)	PM3 (Debye)
Disordered structure 1	1.9348	2.3335	1.5186	1.7771	1.9522
Disordered structure 2	1.4650	1.9003	1.0426	1.3938	1.7556
Disordered structure 3	3.2917	3.6518	2.8577	3.7429	3.6289

Figure 3.60 shows the molecular layouts of the two molecule disordered structures for both of the two melt phases, comparing them to the their non-disordered structures. Whilst there is an increase in dipole on increasing the disorder for the MS-*C*2 phase, there is a decrease in dipole for two of the 2 molecule disordered structures for MS-*Cc*. There is a decrease for layouts 1 and 2 however there is an increase for layout 3. The dipole calculated for layout 3 is larger than for the 1 molecule disordered structures, and is slightly higher or around the same as the non-disordered structure. Layout 1 has head to tail alignment of the molecules along the long axis (*a*) of the unit cell and on stacking along *b*, but head to head alignment along *c*. Layout 2 has head to tail alignment along *a* but head to head alignment along both the *b* and *c* axis. Disordered layout 3, however, has head to head alignment along the *a* and *c*-axis but head to tail alignment along *b*. This is the same molecular layout of the molecules as the non-disordered MS-*C*2 phase, however, is not reflected in the dipole value which is much higher for this disordered structure.

The difference is probably due to orientation of the individual molecules and the dipoles not cancelling out rather than the overal layout of the molecules. Whilst all three molecular layouts have two head to head alignments in the axes it appears that head to tail alignment along the *b*-axis in layout 3 approximately doubles the dipole of the unit cell.

Overall the Gaussian dipole calculations produce a net zero dipole for the three methyl stearate single crystal structures, the two melt phases produce a small unit cell net dipole and the dipole generally increases on introducing disorder into the methyl stearate phases. Whilst on the surface it may not seem that the two melt structures have the most stable structures with the orientation of some of the molecues, these results along with those for the three single crystal structures, show that their molecular layouts have lower dipoles generally for the non-disordered structures, and therefore these structures are less likely to contain disorder.

3.8 Ethyl Stearate

As methyl esters are often the cause of cold flow problems in biodiesel, there is the alternative to use longer chain alcohols such as ethanol, propanol and butanol in the transesterification with the fatty acid esters, as they can lower the melting points of the resulting fatty acid alkyl esters. Ethanol is often a common affordable alternative to methanol with the common compounds likely to cause cold flow problems being ethyl stearate (Figure 3.61) and ethyl palmitate.
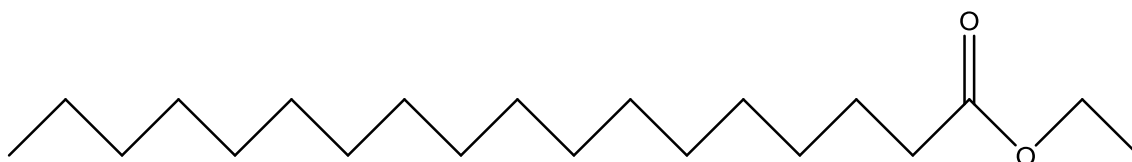
Figure 3.61 Chemical structure of Ethyl Stearate.

3.8.1 Previously known structures

There is one complete published structure from 1968 by Aleby[44] (which will be referred to as ES-*Aa*), which is very similar to the MS-*Cc* phase and longer chain alkyl esters reported in the literature. The crystal used to determine the ethyl stearate structure was crystallised from glacial acetic acid and the structure determined in a monoclinic *Aa* space group, with four molecules in the unit cell. The molecules are aligned along the long *z* axis of the unit cell, with head to tail alignment within the layers, and head to head alignment between the layers as shown in Figure 3.62, with the lattice parameters detailed in Table 3.33.

Table 3.33 Lattice parameters of the ES-*Aa* phase by Aleby[44].

Unit cell & space group	a (Å)	b (Å)	c (Å)	β (°)	Volume (Å³)	Z
Monoclinic *Aa*	5.59	7.40	55.00	113.50	2086.43	4
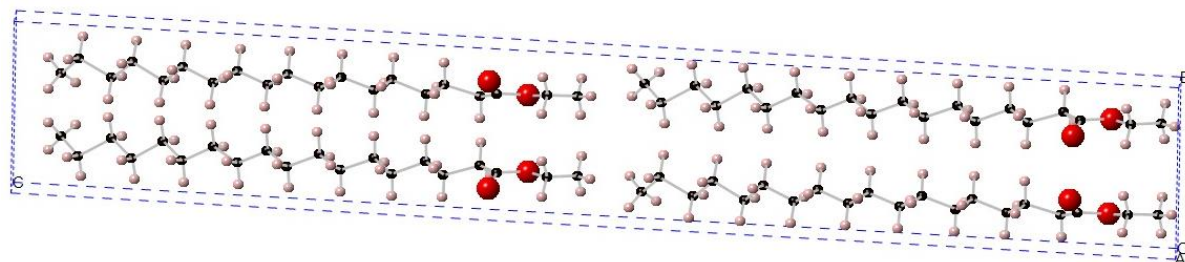
Figure 3.62 Ethyl Stearate structure viewed down the *a*-axis[44].

3.8.2 Ethyl Stearate as-bought lab data

To determine whether the as-bought phase of ethyl stearate is the same as the published ES-*Aa* structure by Aleby[44], a PXRD pattern was run and compared to the simulated PXRD pattern of the known structure, shown in Figure 3.63.
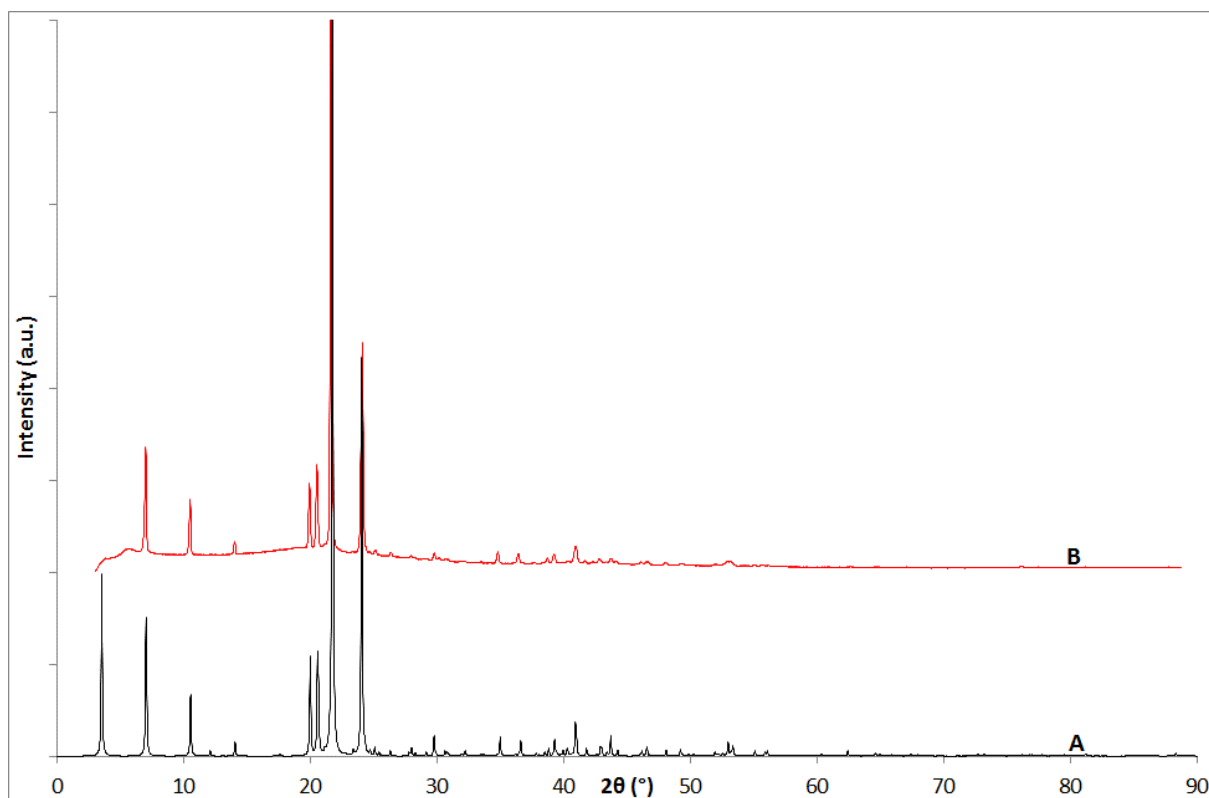
Figure 3.63 (A) Simulated PXRD pattern of ES-*Aa* structure (room temperature)[44], (B) PXRD pattern of ethyl stearate as bought (room temperature). λ = 1.54056 Å

From visual comparison the PXRD pattern run matched the known structure of ethyl stearate, so a Rietveld refinement was run as shown in Figure 3.64 with the refined lattice parameters shown in Table 3.34 and the atomic positions in appendix 3.1.6. A good fit was produced, confirming the as-bought phase is the ES-*Aa*[44] structure.
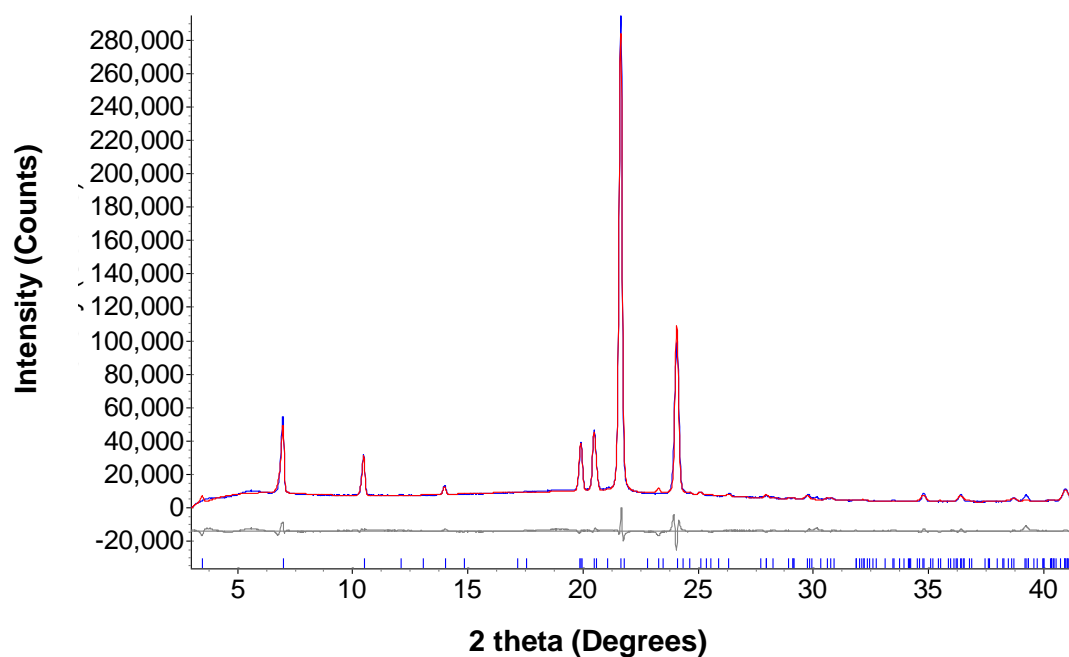
Figure 3.64 Observed (blue line) and calculated (red line) profiles for the Rietveld refinement of ethyl stearate as bought with the ES-*Aa* structure by Aleby[44]. (R_{wp} = 7.25, R_p = 4.96, χ = 5.49). The tick marks represent calculated peak positions. λ = 1.54056 Å

Table 3.34 Refined lattice parameters of the Rietveld refinement of ethyl stearate as bought with the ES-*Aa* structure.

Parameter	Value
Phase / Space group	Ethyl Stearate / *Aa*
***a* (Å)**	5.6163(6)
***b* (Å)**	7.3849(5)
***c* (Å)**	55.0644(88)
***β* (°)**	113.404(12)
Volume (Å³)	2095.94(46)

3.8.3 Ethyl Stearate as-bought synchrotron data

Data for ethyl stearate as-bought was also collected at Diamond beamline I11 with a long PXRD pattern recorded at 293 K. A Rietveld refinement of that data set was run as shown in Figure 3.65 with the refined lattice parameters shown in Table 3.35 and atomic positions in appendix 3.1.7.
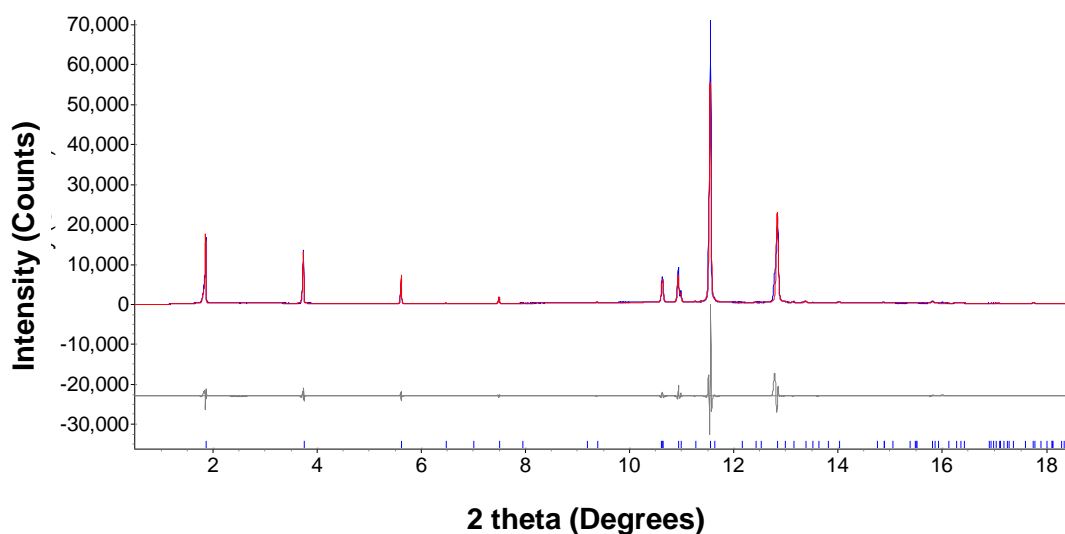
Figure 3.65 Observed (blue line) and calculated (red line) profiles for the Rietveld refinement of ethyl stearate as-bought synchrotron data set with the ES-*Aa* structure by Aleby[44]. (R_{wp} = 16.10, R_p = 11.11, χ = 5.11). The tick marks represent calculated peak positions. λ = 0.826056 Å

Table 3.35 Refined lattice parameters of the Rietveld refinement of ethyl stearate as-bought synchrotron data set with the ES-*Aa* structure.

Parameter	Value
Phase / Space group	Ethyl Stearate / *Aa*
a (Å)	5.6208(2)
b (Å)	7.3855(1)
c (Å)	55.0354(27)
β (°)	113.4746(44)
Volume (Å³)	2095.56(15)

A good fit was produced between the synchrotron data set and the known phase, however even with preferred orientation corrections the large mid angle peak is not fitted to its full intensity. From both the lab data and synchrotron PXRD data the ethyl stearate as-bought phase at room temperature is the same as the ES-*Aa* phase by Aleby[44].

Further I11 data were collected, with shorter scans on cooling from 300 K to 100 K at 25 K intervals. This data which is shown in Figure 3.66 on visual comparison, shows thermal contraction of the unit cell with the patterns shifting to higher 2θ. However there is a small shoulder / peak at 10.96° 2θ in the 300 K scan that by the 225 K scan has merged with the main peak. On trying to obtain lattice parameters of the unit cell as the temperature decreases through both Pawley phase fit and Rietveld refinement, linear thermal contraction was not for all parameters obtained. Whilst thermal contraction of the *a* and *b*-axis was linear, the *c*-axis and *β* angle don't decrease and fluctuate around the room temperature value, or increase in value. This could be due to a subtle phase change as temperature decreases from

room temperature, and the reason why linear thermal contraction lattice parameters could not be obtained.
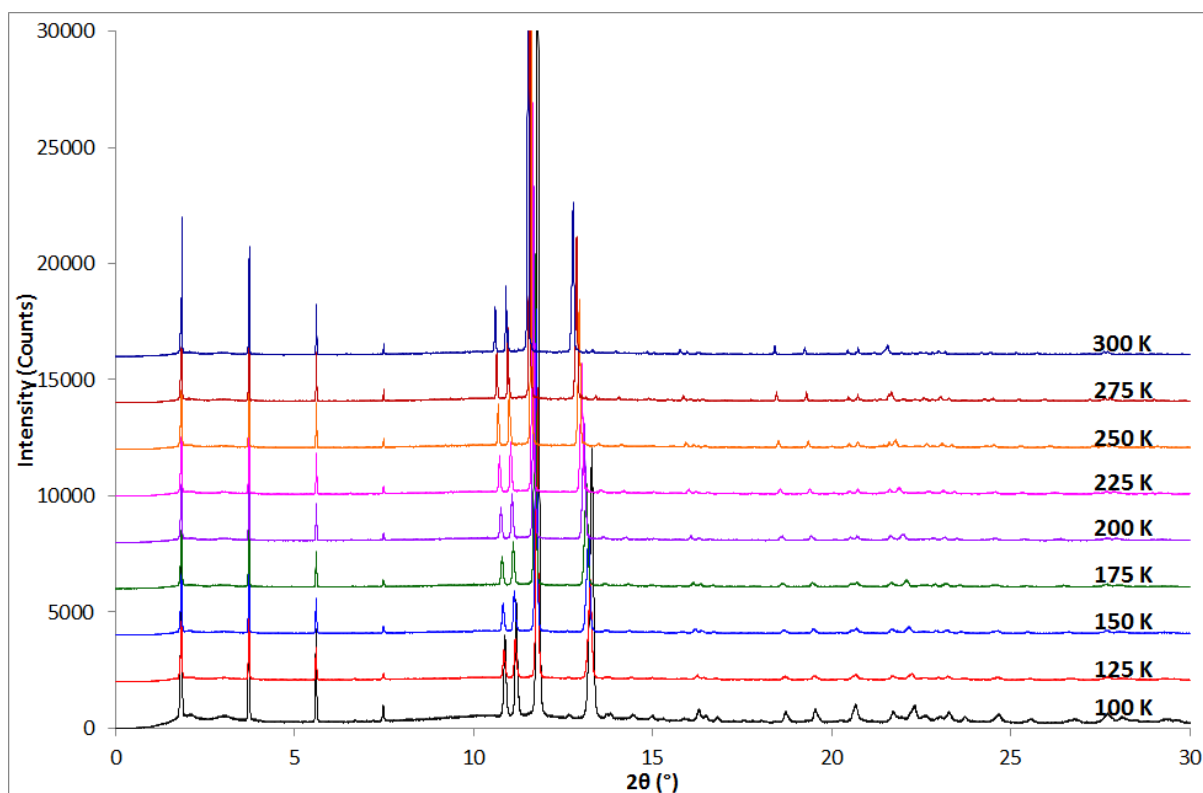
Figure 3.66 Ethyl stearate as bought cooling scans from 300 K to 100 K at 25 K intervals.

3.8.3 Ethyl Stearate recrystallisations

Due to the many different polymorphs of methyl stearate that have been reported in this chapter, similar molecules with similar crystal structures may also have several different polymorphs; therefore ethyl stearate recrystallisations were carried out, to determine whether there is more than one crystal structure of ethyl stearate.

Table 3.36 Ethyl stearate recrystallisation conditions.

Figure / Pattern	Solvent	Experiment Type	Temp 1	Temp 2	Cooling Rate
3.66 / B	-	VT melt	333 K	233 K	100 K/hr
3.66 / C	-	From melt	353 K	298 K	-
3.66 / D	-	From melt	353 K	255 K	-
3.67 / B	Toluene	Solvent recrystallisation	298 K	255 K	-
3.67 / C	Toluene	Variable temperature	333 K	233 K	100 K/hr
3.67 / D	Toluene	Variable temperature	333 K	190 K	100 K/hr
3.67 / E	Kerosene	Variable temperature	333 K	233 K	100 K/hr
3.68 / B	-	Cyclic variable temperature	Cycle 3 – 233 K	290 K	100 K/hr
3.68 / C	-	Cyclic variable temperature	Cycle 2 – 333 K	233 K	100 K/hr
3.68 / D	-	Cyclic variable temperature	Cycle 2 – 290 K	333 K	100 K/hr
3.68 / E	-	Cyclic variable temperature	Cycle 2 – 233 K	290 K	100 K/hr
3.68 / F	-	Cyclic variable temperature	Cycle 1 – 333 K	233 K	100 K/hr
3.68 / G	-	Cyclic variable temperature	Cycle 1 – 290 K	333 K	100 K/hr
3.68 / H	-	Cyclic variable temperature	Cycle 1 – room temperature	290 K	100 K/hr
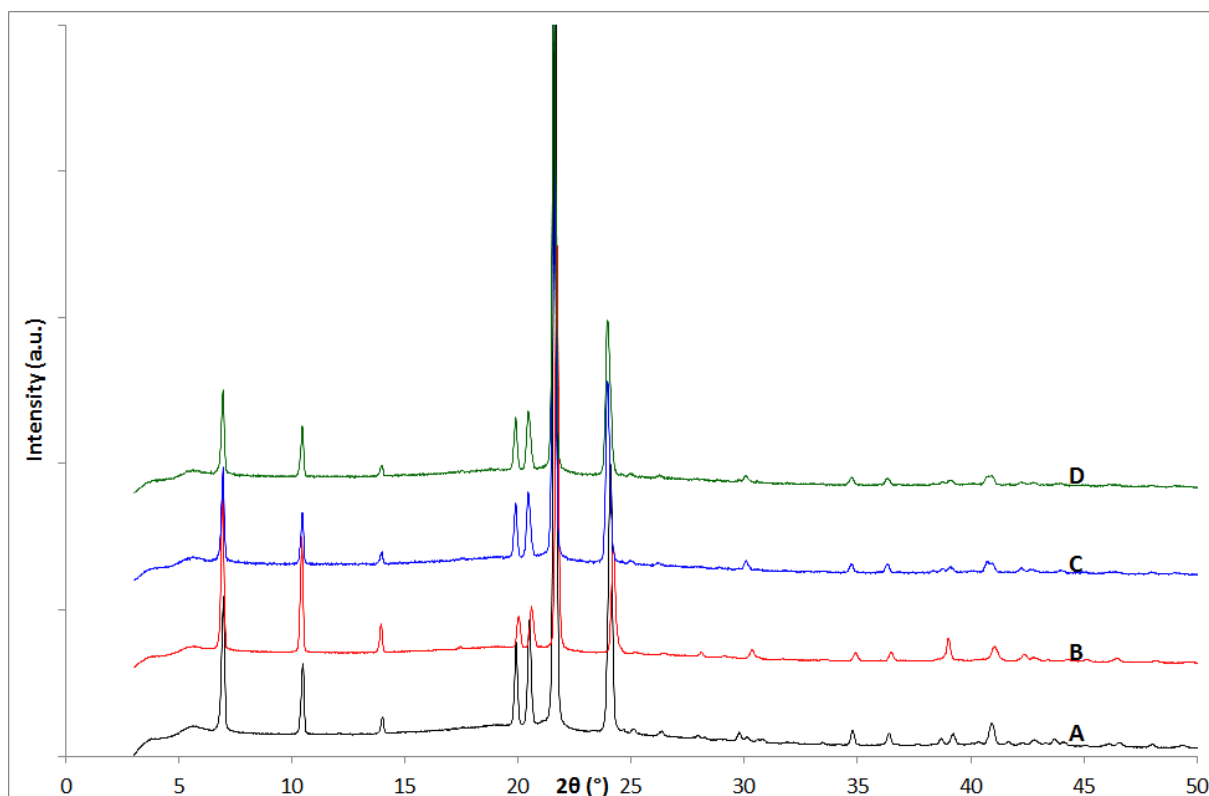
Figure 3.67 PXRD patterns of ethyl stearate (A) as-bought (room temperature), (B) the product from variable temperature recrystallisation from the melt 333 K to 233 K at 100 K/hr, (C) the product from the melt experiment in a Teflon pot and cooled at room temperature, (D) the product from the melt experiment in a Teflon pot and cooled in the freezer recorded at room temperature. λ = 1.54056 Å

Figure 3.67 shows the comparison of variable temperature PXRD patterns from the melt recrystallisations with different cooling rates and the ethyl stearate as-bought phase. All three recrystallisations show that after melting ethyl stearate crystallises back into the as bought phase, compared to methyl stearate which under the same conditions recrystallises into the MS-*C*2 phase.
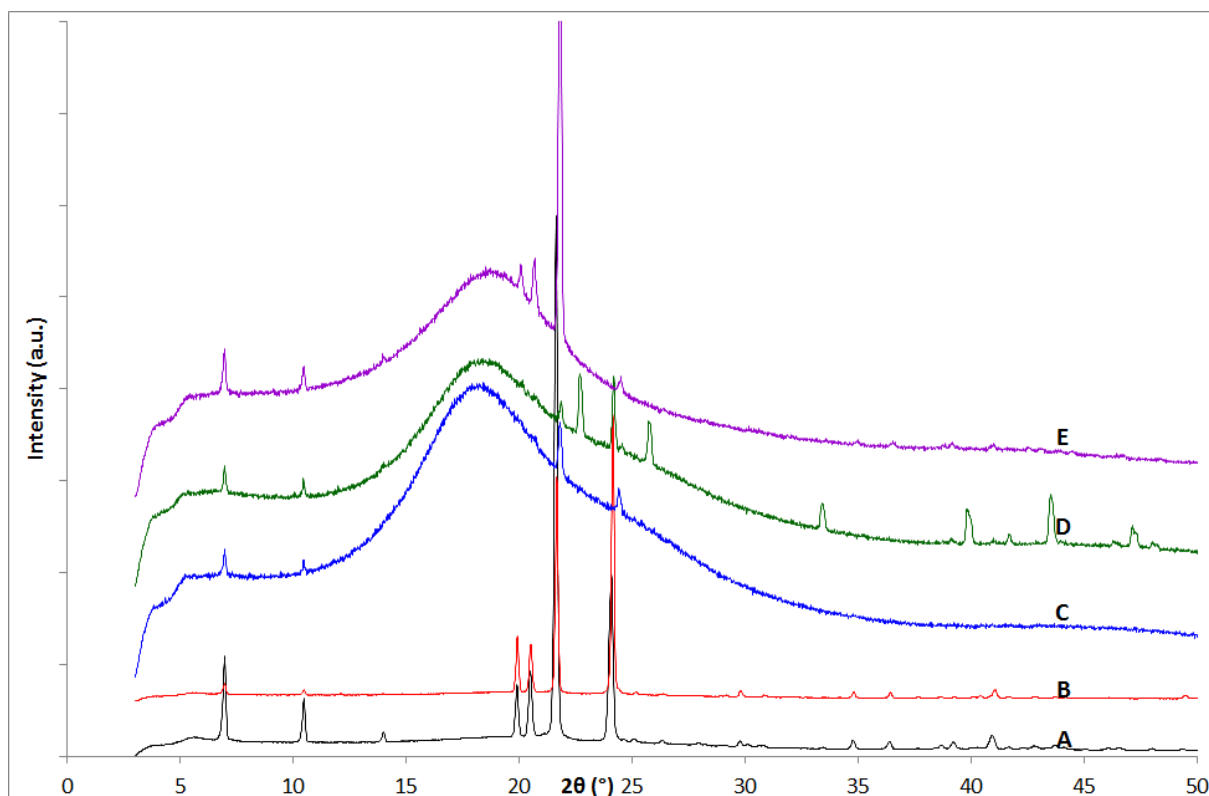
Figure 3.68 PXRD patterns of ethyl stearate (A) as bought (room temperature), (B) the product from solvent recrystallisation experiment of ethyl stearate in toluene at 255 K, (C) the product from variable temperature experiment ethyl stearate in toluene 333 K to 233 K at 100 K/hr, (D) the product from variable temperature experiment ethyl stearate in toluene 333 K to 190 K at 100 K/hr, (E) the product from variable temperature experiment ethyl stearate in kerosene 333 K to 233 K at 100 K/hr. λ = 1.54056 Å

Figure 3.68 shows the comparison of ethyl stearate solvent recrystallisations with the as-bought phase. All recrystallisations regardless of solvent and temperature used recrystallise back into the ethyl stearate as bought starting phase. Not all peaks are present in patterns C and E which were both recorded at 233 K, whereas pattern D recorded at the lower temperature of 190 K has all peaks present for ethyl stearate, due to the material not being fully crystalline at 233 K. The crystallisation at

190 K also has a few more relatively intense peaks between 30 and 50° 2θ than the other scans, however this is probably due to preferred orientation.
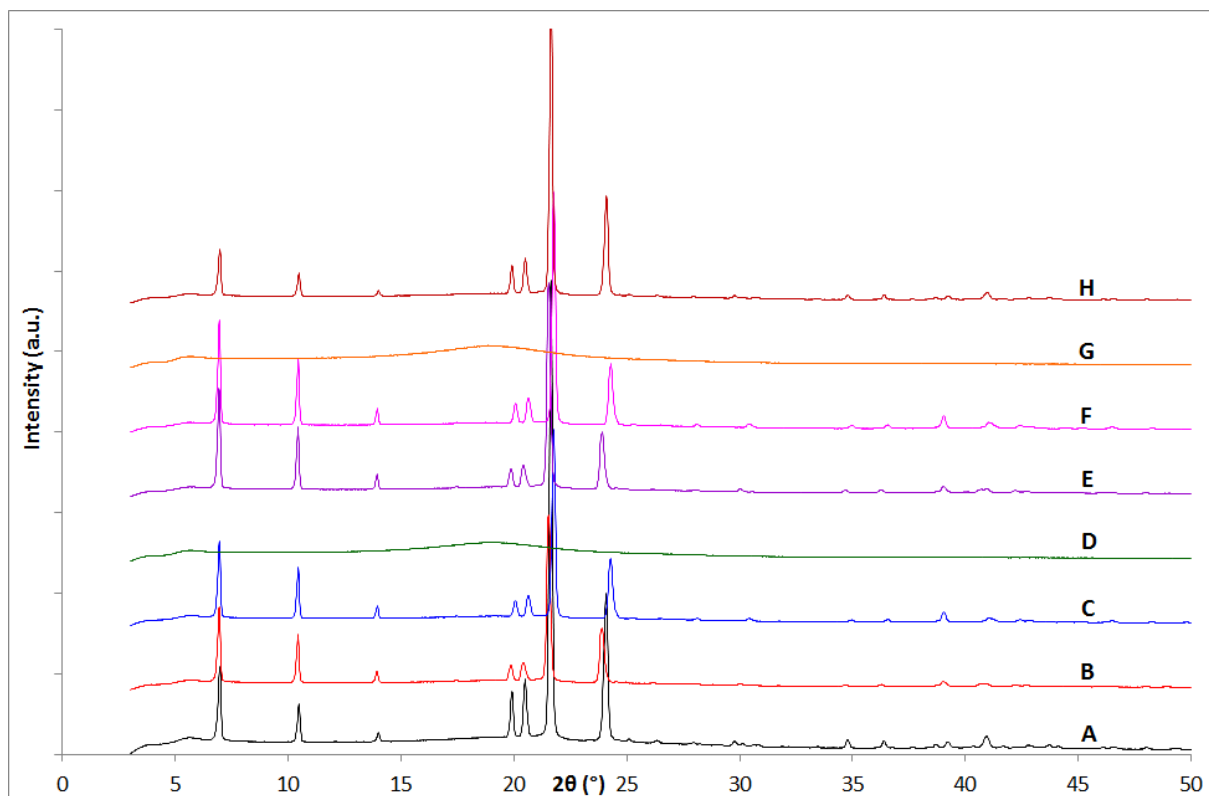
Figure 3.69 PXRD patterns of ethyl stearate (A) as bought (room temperature), (B) cyclic variable temperature cycle 3 recorded at 290 K, (C) cyclic variable temperature cycle 2 recorded at 233 K, (D) cyclic variable temperature cycle 2 recorded at 333 K, (E) cyclic variable temperature cycle 2 recorded at 290 K, (F) cyclic variable temperature cycle 1 recorded at 233 K, (G) cyclic variable temperature cycle 1 recorded at 333 K, (H) cyclic variable temperature cycle 1 recorded at 290 K. λ = 1.54056 Å

Figure 3.69 shows the cyclic recrystallisation of ethyl stearate using the same conditions as used for methyl stearate. Apart from patterns D and G which confirm melting of ethyl stearate between each cycle, all temperature scans in all three cycles show the same ethyl stearate as-bought phase.

142

All crystallisations of ethyl stearate recrystallised back into the ES-*Aa* phase, showing that only one phase of ethyl stearate exists under the solvent, temperature and pressure conditions used. Rietveld refinements of ethyl stearate can be found in appendix 3.6.

The subtle phase change which was potentially found in the I11 data with the small shoulder is not present in any of the lab data due to the poorer quality of the data.

3.8.4 Gaussian calculations

As with the five methyl stearate polymorphs dipole calculations were run for the ES-*Aa* as-bought phase.

Table 3.37 Gaussian molecular dipole results for ES-*Aa*.

	Hartree-Fock basic (Debye)	Hartree-Fock routine (Debye)	B3LYP routine (Debye)	AM1 (Debye)	PM3 (Debye)
1 molecule	1.8619	2.4200	2.4776	2.8260	2.4122
2 molecules stacking	3.2810	4.3709	4.5917	5.0666	4.1512
2 molecules in a layer	3.4223	4.6224	4.8617	5.4485	4.4206
4 molecules full cell	6.5903	8.9464	9.3260	10.4630	8.5321
8 molecules 2 unit cells *a* + 1	12.9336	-	-	20.2184	16.5708
8 molecules 2 unit cells *b* + 1	13.1928	-	-	21.1343	17.1906
8 molecules 2 unit cells *c* + 1	12.7350	-	-	19.7225	16.4021
4 molecules in a layer (*a* + 1)	6.7760	9.2175	9.6695	10.9354	8.8593
4 molecules in a layer (*b* +1)	6.6063	8.9266	9.3040	10.4282	8.6094
4 molecules in a layer (*c* + 1)	7.4118	9.6491	9.8547	11.2422	9.6156
4 molecules in a central half cell	6.5844	8.9381	9.3136	10.4816	8.5542

The dipole calculations for the single ethyl stearate molecule produce a dipole of similar size to the MS-*A*2/*a* phase, which was the methyl stearate phase with the

highest dipole for the individual molecule. As the head to tail molecular alignment is the same for the ES-*Aa* phase, and the MS-*Cc* phase; the dipole calculation results reflect the same result, as the number of molecules in the calculation increases the dipole also increases with no net zero dipole. The 8 molecules with $c + 1$ is the arrangement closest to the three 8 molecule methyl stearate single crystal structures.

These results confirm that crystal structures which are solid can contain permanent dipoles. The two methyl stearate melt phases were both solved from PXRD data, so there is always some uncertainly whether the structure is completely correct with the molecular arrangement. However as the ethyl stearate structure has a larger dipole and the crystal structure has been confirmed, the dipoles calculated with methyl stearate melt phases are likely to be reasonable.

3.9 Propyl stearate

There is only one other published alkyl stearate structure, which is propyl stearate with the chemical structure, shown in Figure 3.70.
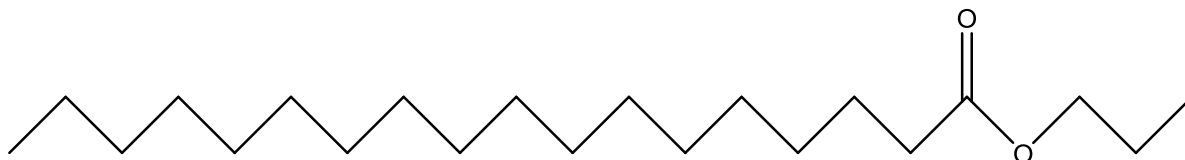
Figure 3.70 Chemical structure of Propyl Stearate.

3.9.1 Previously known structures

There is one previously known structure of propyl stearate from 1968 by Aleby (which will be referred to as PS-*Pa)* [48]. The single crystal was grown from ethanol at room temperature and crystallised in a *Pa* monoclinic unit cell with the lattice parameters shown in Table 3.38[48].

Table 3.38 Lattice parameters for the PS-*Pa* structure by Aleby[48].

Unit cell & space group	*a* (Å)	*b* (Å)	*c* (Å)	*β* (°)	Volume (Å^3)	Z
Monoclinic *Pa*	5.59	7.39	30.0	119.20	1081.81	2

As with the ES-*Aa* structure published by the same author, there is head-to-tail alignment of the molecules within the layers, but head to head alignment between the layers as they stack up as showing in Figure 3.71. Unlike ES-*Aa* the unit cell has been halved to two molecules stacked on top of one another in the cell.
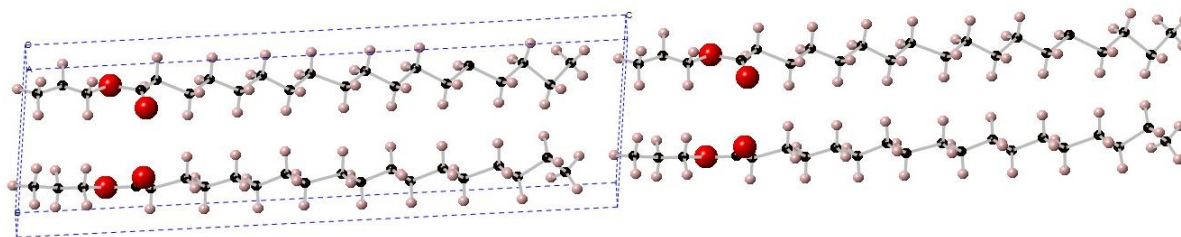
Figure 3.71 PS-*Pa* structure viewed down the *a* axis of 2 unit cells[48].

3.9.2 Gaussian calculations

Due to the molecular layout, Gaussian dipole calculations were also run for the published propyl stearate phase.

Table 3.39 Gaussian molecular dipole results for PS-*Pa*.

	Hartree-Fock basic (Debye)	Hartree-Fock routine (Debye)	B3LYP routine (Debye)	AM1 (Debye)	PM3 (Debye)
1 molecule	3.3833	4.1829	4.1716	4.5708	3.7539
2 molecules full cell	6.3937	7.9202	7.8812	8.4850	6.8728
4 molecules 2 unit cells *a* + 1	12.1273	14.9448	14.8028	15.6134	12.8838
4 molecules 2 unit cells *b* + 1	12.4443	15.3661	15.1777	16.2051	13.2426
4 molecules 2 unit cells *c* + 1	13.2399	16.4207	16.4604	17.4117	14.0154
8 molecules 4 unit cell *c* + 1 +2 +3	26.9908	-	-	35.3497	28.3511

The dipole calculations for PS-*Pa* are larger for all molecular arrangements when comparing them to the all methyl stearate and ethyl stearate calculations. The

147

dipole doubles on doubling the number of molecules due to the adoption of the same molecular arrangement as ethyl stearate.

3.10 Conclusions

In this chapter methyl stearate and ethyl stearate structures have been investigated. As introduced in the beginning methyl stearate has been reported to crystallise in five different polymorphs. However, throughout this chapter it has been shown that they only exist in certain conditions.

The as-bought phase of methyl stearate has been proven, through both lab and synchrotron data, to be the MS-*Pnab* phase, with thermal expansion coefficients successfully calculated. Whilst these coefficients are slightly larger than those typically reported in literature (rigid inorganic materials), methyl stearate is an organic ester with much more flexibility and space in the unit cell, for contraction and expansion.

Both lab and further synchrotron data has confirmed the MS-*C*2 phase, with thermal expansion coefficients also calculated for this phase. The coefficients calculated are fairly similar to those calculated for the MS-*Pnab* phase, confirming that compounds of this type are likely to expand and contract more with temperature.

Various methyl stearate recrystallisations using heat and solvent were carried out, to determine which phases may crystallise out in a fuel tank. Only the MS-*Pnab* phase and the MS-*C*2 phase were found to form; with the MS-*C*2 phase forming if the compound was taken above its melting point, but if the material stayed below the melting point, the as-bought MS-*Pnab* phase will form.

The third and final phase that was shown to crystallise was the MS-*Cc* phase, which was confirmed from neutron HRPD data. Thermal expansion data and coefficients were also produced for this phase, with similar results to the previous two

sets calculated; however the coefficient for the *a*-axis with the quench cooled *Cc* phase is five times smaller than the slow cooled *C*2 *a*-axis.

Whilst the MS-*C*2/*c* phase could not be replicated in this project, the structure was originally solved from 100 K data; therefore the three sets of thermal expansion coefficients were used to convert the MS-*C*2/*c* phase to room temperature lattice parameters. All three sets of coefficients produced similar simulated PXRD patterns for the MS-*C*2/*c* phase at 295 K, which are different from the other four methyl stearate phases but now several main peaks line up as they do with all the other phases.

Extensive dipole calculations were carried out using Gaussian, for all five polymorphs of methyl stearate. Overall there is some variation between the basis sets of the dipole calculations, so results are approximations. A net zero dipole was calculated for the three single crystal unit cells, but both melt phases contain a net dipole with the MS-*Cc* dipole much bigger than the MS-*C*2 phase.

One molecule disordered calculations showed an increase in dipole for each methyl stearate phase apart from the *Cc* phase with a decrease in dipole of around 1 Debye for the rotation of one molecule. Two molecule disordered calculations also showed a decrease in dipole for the MS-*Cc* phase in two out of three molecular arrangements but an increase in dipole for the MS-*C*2 phase and one of the MS-*Cc* structures.

Ethyl stearate as-bought room temperature lab and synchrotron data confirmed the ES-*Aa* phase, which was the phase that crystallised out in all the solvent and temperature recrystallisations. However, low temperature higher quality data indicates that there may be a subtle phase change on decreasing the

temperature, due to the low temperature data not refining to the ES-*Aa* phase, and no linear thermal contraction of the unit cell with the synchrotron data collected.

Gaussian calculations, however, show large dipoles for both ES-*Aa* and PS-*Pa* published structures, due to their molecules aligning in one direction and in a similar arrangement to the MS-*Cc* phase. This confirms that it's not necessary for the methyl stearate melt phases to have a net zero dipole for their full unit cells.

Whilst three of the five polymorphs have been investigated throughout this project, the MS-*A*2/*a* and MS-*C*2/*c* methyl stearate phases have not been made so whether these phases exist, or whether they are likely to be found in biodiesel fuel tanks, is unknown.

4.   Chapter 4 – Methyl Palmitate

4.1 Introduction

Methyl palmitate ($CH_3(CH_2)_{14}C(O)CH_3$, shown in Figure 4.1) is the second major component of biodiesel, which is likely to cause poor cold flow properties when biodiesel is cooled in a fuel tank.
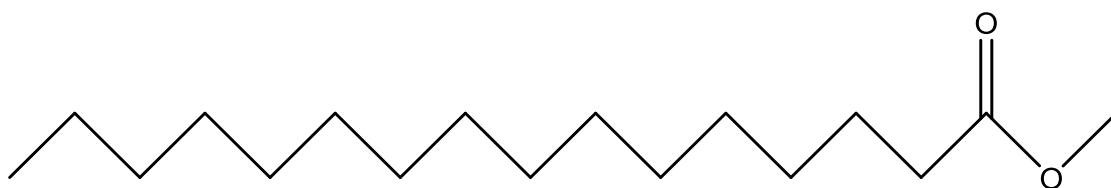
Figure 4.1 Chemical structure of Methyl Palmitate.

There were no known published structures of methyl palmitate prior to the start of this project.

4.2 Methyl Palmitate as-bought

As there were no known structures of methyl palmitate, both synchrotron and lab PXRD data were collected for the as-bought phase, to determine whether a structure could be solved.

4.2.1 Synchrotron Diamond beamline I11 data

Two long PXRD scans of methyl palmitate as-bought were recorded at Diamond beamline I11, at 293 K and 100 K, which can be seen in Figure 4.2. The 100 K data set was of higher quality, and was used to see whether a structure could be solved.
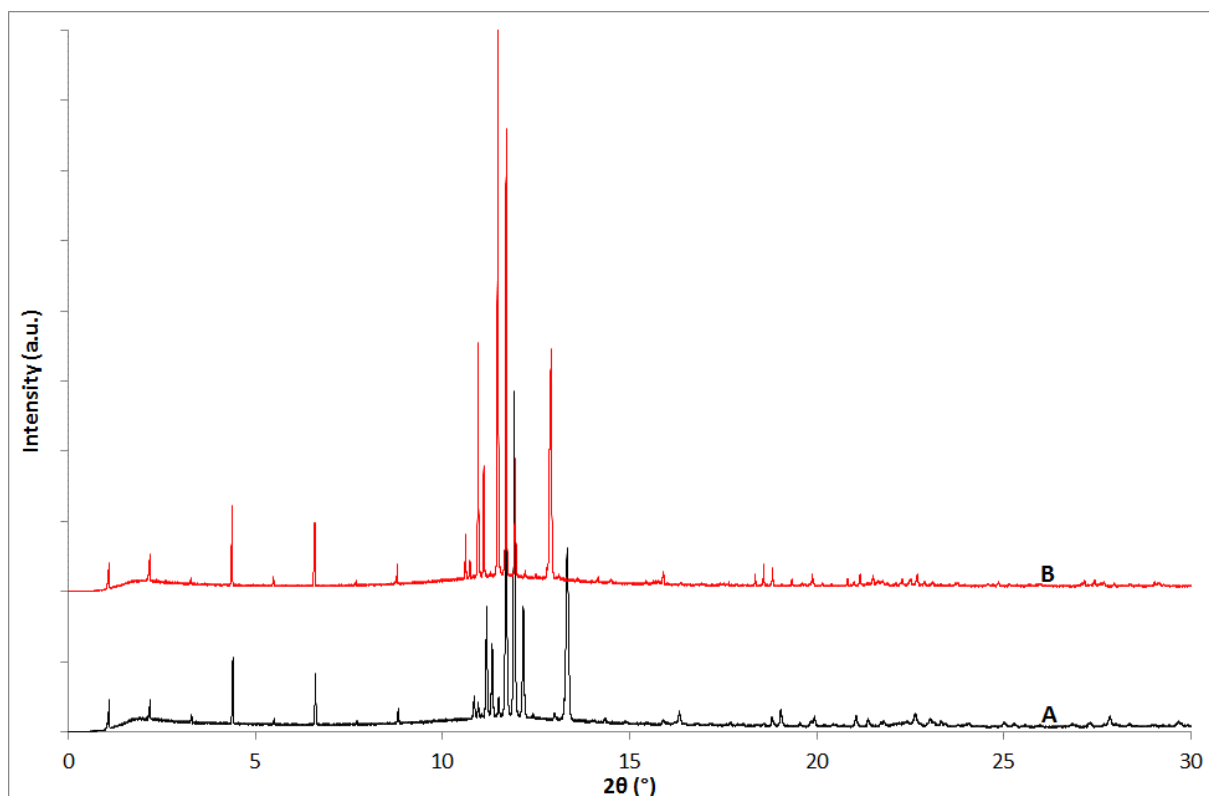
Figure 4.2 Methyl Palmitate as bought synchrotron data set recorded at (A) 100 K, (B) 293 K. λ = 0.826056 Å

4.2.2 Structure solution with I11 100 K data

As the PXRD patterns of the as-bought phases of methyl stearate and methyl palmitate are visually very similar, their structures may also be fairly similar. The 100 K I11 scan was indexed using TOPAS, and suitable lattice parameters were produced. A Pawley fit shown in Figure 4.3 was run with these parameters, and the refined parameters are shown in Table 4.1.
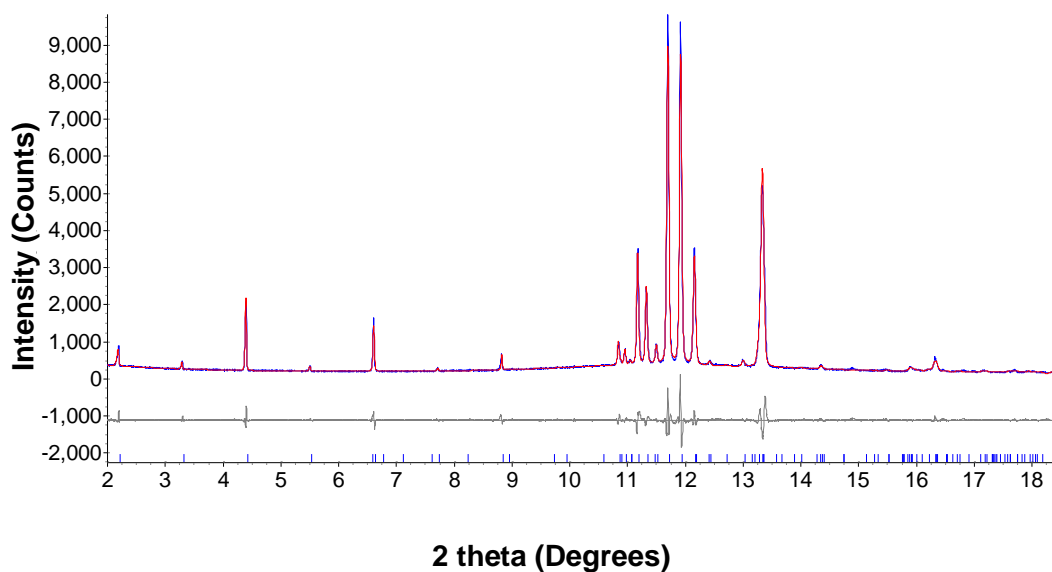
Figure 4.3 Observed (blue line) and calculated (red line) profile for the Pawley fit of methyl palmitate as-bought phase with the indexing results show in Table 4.1. The bottom curve is the difference plot on the same intensity scale. (Rwp = 7.13, Rp = 5.13, χ = 1.76). The tick marks represent calculated peak positions. λ = 0.826056 Å

Table 4.1 Refined lattice parameters for methyl palmitate as-bought phase from the Pawley fit.

Parameter	Value
Space group	*Pnab*
a (Å)	5.490(1)
b (Å)	7.210(2)
c (Å)	85.661(5)

The low difference curve in Figure 4.3 shows a good fit, and the space group is the same as the MS-*Pnab* phase. Due to the potential similarity between the phases, a model structure was created from the MS-*Pnab* phase by removing two carbons from the long hydrocarbon chain. The refined Pawley lattice parameters along with the model structure were simulated together to produce the model, which can be seen in Figure 4.4. The model is very similar to that of the MS-*Pnab* phase

154

with the head to head alignment of the molecules across the *ac* plane of the unit cell, and head to head stacking between the layers along the *b*-axis. This carbon – oxygen backbone was used as a starting point for structure solution.
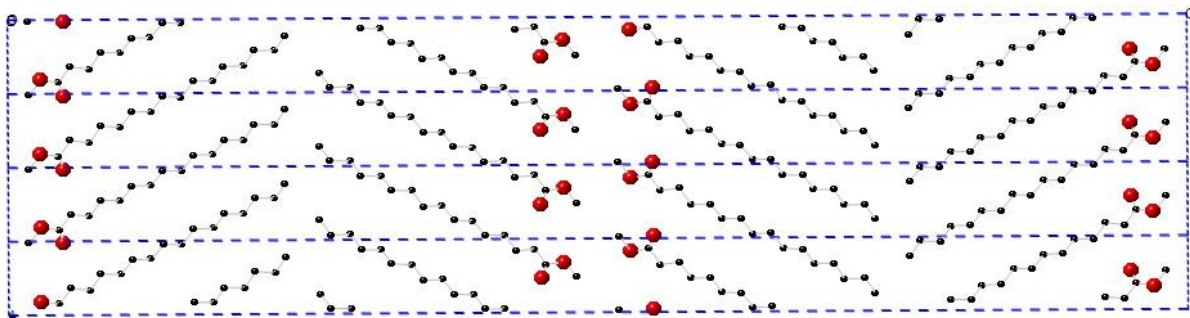
Figure 4.4 Methyl palmitate as-bought model created from the methyl stearate 1970 phase, viewed down the b-axis at ac plane.

The lattice parameters and atomic positions were refined with spherical harmonics to correct for preferred orientation, as these structures are prone to forming large flat platelet crystals. Once the final carbon – oxygen backbone structure was produced, hydrogens were added using Olex2[78] in idealised positions. A final refinement shown in Figure 4.5 was run using H-riding to prevent the hydrogens refining to unrealistic positions.
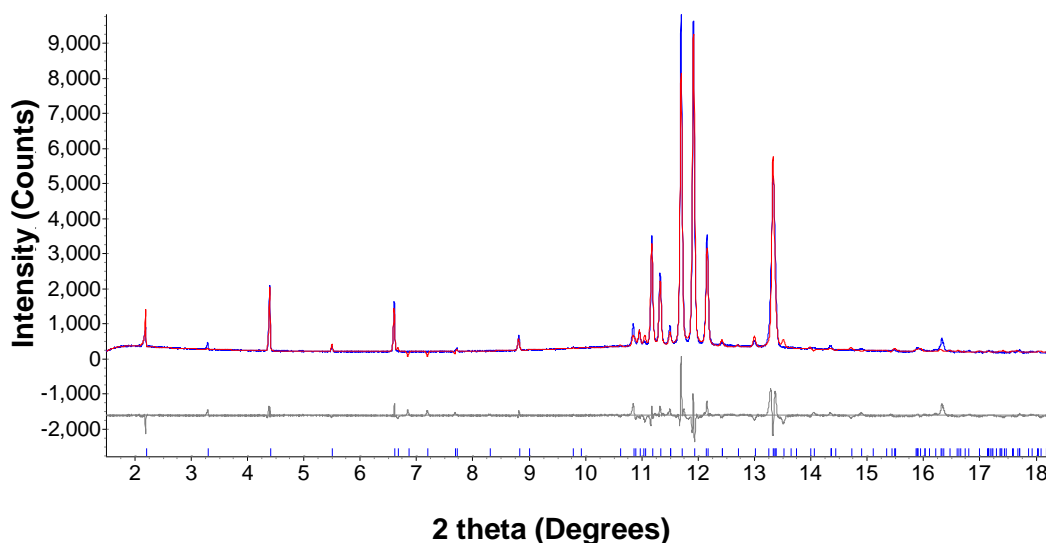
Figure 4.5 Observed (blue line) and calculated (red line) profiles for the final Rietveld refinement of methyl palmitate as-bought proposed structure. The bottom curve is the difference plot on the same intensity scale. (Rwp = 13.79, Rp = 9.04, χ = 3.32). The tick marks represent calculated peak positions. λ = 0.826056 Å

The final crystal structure is shown in Figure 4.6 and a labelled molecule in Figure 4.7. The head to head alignment within and between the layers is the same as all three of the methyl stearate single crystal structures, and the diagonal molecular layout is the same as the MS-*Pnab*. Whilst the hydrocarbon chain is fairly planar from C14 to C5, both ends of the molecular chain are twisted slightly in opposite directions which can be seen in Figure 4.7. As all the single crystal methyl stearate phases mentioned in chapter 3 have a planar carbon – oxygen chain, this may seem to suggest that the proposed methyl palmitate structure is incorrect; however both methyl stearate melt phases which were solved from PXRD data, have very slightly twisted ends to the chain.

156
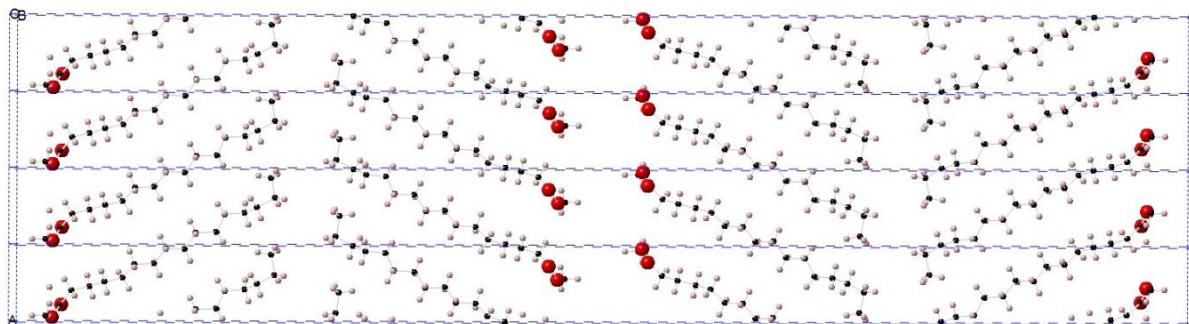
Figure 4.6 Final methyl palmitate as-bought structure viewed down the *b*-axis at the *ac*-plane.

Table 4.2 Selected crystallographic data of the methyl palmitate as-bought phase.

Parameter	Data
Chemical Formula	$C_{17}H_{34}O_2$
Formula weight (g mol^{-1})	270.45
Crystal system	Orthorhombic
Space group	*Pnab*
a (Å)	5.5426(2)
b (Å)	7.1109(2)
c (Å)	85.867(6)
V (Å^3)	3384.3(3)
T (K)	100
Z	8
λ (Å)	0.826056
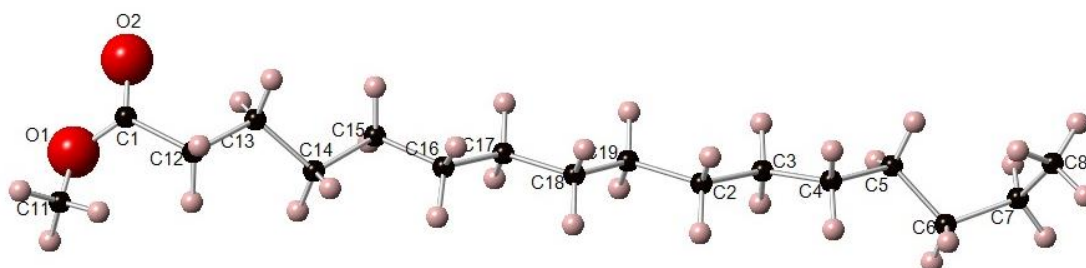
Figure 4.7 Labelled methyl palmitate as-bought molecule.

This may be due to the nature of structural solution from PXRD data where substantial data is lost in data collection, compared to structure solution from single crystal data and therefore the end results may not be exactly the same.

Table 4.3 Atomic coordinates for the methyl palmitate as-bought structure.

Atom number	*x*	*y*	*z*
C1	0.781(8)	0.296(5)	0.0418(6)
C2	0.846(8)	0.213(6)	0.1576(6)
C3	0.835(7)	0.290(5)	0.1743(5)
C4	0.603(7)	0.231(5)	0.1820(5)
C5	0.583(8)	0.314(5)	0.1981(5)
C6	0.513(9)	0.162(5)	0.2099(6)
C7	0.393(6)	0.248(6)	0.2241(5)
C8	0.127(6)	0.281(5)	0.2208(5)
C11	0.931(10)	0.059(4)	0.0311(5)
C12	0.605(8)	0.187(6)	0.0524(5)
C13	0.544(8)	0.305(5)	0.0666(6)
C14	0.490(8)	0.181(6)	0.0807(5)
C15	0.430(8)	0.306(5)	0.0947(6)
C16	0.259(7)	0.212(6)	0.1056(6)
C17	0.247(7)	0.289(5)	0.1216(6)
C18	0.050(8)	0.212(4)	0.1318(6)
C19	0.059(8)	0.294(5)	0.1474(6)
O1	0.953(6)	0.215(4)	0.0359(4)
O2	0.777(6)	0.460(4)	0.0421(2)

Table 4.4 Methyl palmitate as-bought carbon – carbon / carbon – oxygen bond lengths.

Bond	Distance (Å)
C8 – C7	1.52(5)
C7 – C6	1.52(7)
C6 – C5	1.53(6)
C5 – C4	1.51(6)
C4 – C3	1.51(6)
C3 – C2	1.54(6)
C2 – C19	1.58(6)
C19 – C18	1.46(6)
C18 – C17	1.51(6)
C17 – C16	1.48(7)
C16 – C15	1.49(6)
C15 – C14	1.53(6)
C14 – C13	1.52(6)
C13 – C12	1.52(6)
C12 – C1	1.54(6)
C1 – O2	1.17(4)
C1 – O1	1.22(5)
O1 – C11	1.19(4)

Selected crystallographic data is recorded in Table 4.2 and atomic coordinates, carbon and oxygen bond lengths and bond angles are shown in Tables 4.3, 4.4 and 4.5 respectively.

Table 4.5 Methyl palmitate as-bought carbon / oxygen backbone bond angles.

Bond	Angle (°)
C8 – C7 – C6	110(4)
C7 – C6 – C5	111(3)
C6 – C5 – C4	110(3)
C5 – C4 – C3	111(3)
C4 – C3 – C2	110(3)
C3 – C2 – C19	114(3)
C2 – C19 – C18	110(4)
C19 – C18 – C17	111(3)
C18 – C17 – C16	116(3)
C17 – C16 – C15	116(4)
C16 – C15 – C14	112(3)
C15 – C14 – C13	109(3)
C14 – C13 – C12	111(3)
C13 – C12 – C1	110(3)
C12 – C1 – O2	118(4)
C12 – C1 – O1	120(3)
C11 – O1 – C1	120(4)

The methyl palmitate as-bought structure was thus solved from I11 PXRD data, with a fairly similar structure to the MS-*Pnab* phase (and will be referred to in this project as MP-*Pnab*).

4.2.3 Thermal expansion coefficients

Between the two methyl palmitate long scans at I11, shorter scans were recorded (shown in Figure 4.8) on cooling at 25 K intervals from 293 K to 100 K. This was to see whether there were any phase transitions on cooling this new phase. As the PXRD patterns showed no phase transitions this data was used to extract thermal expansion coefficients.
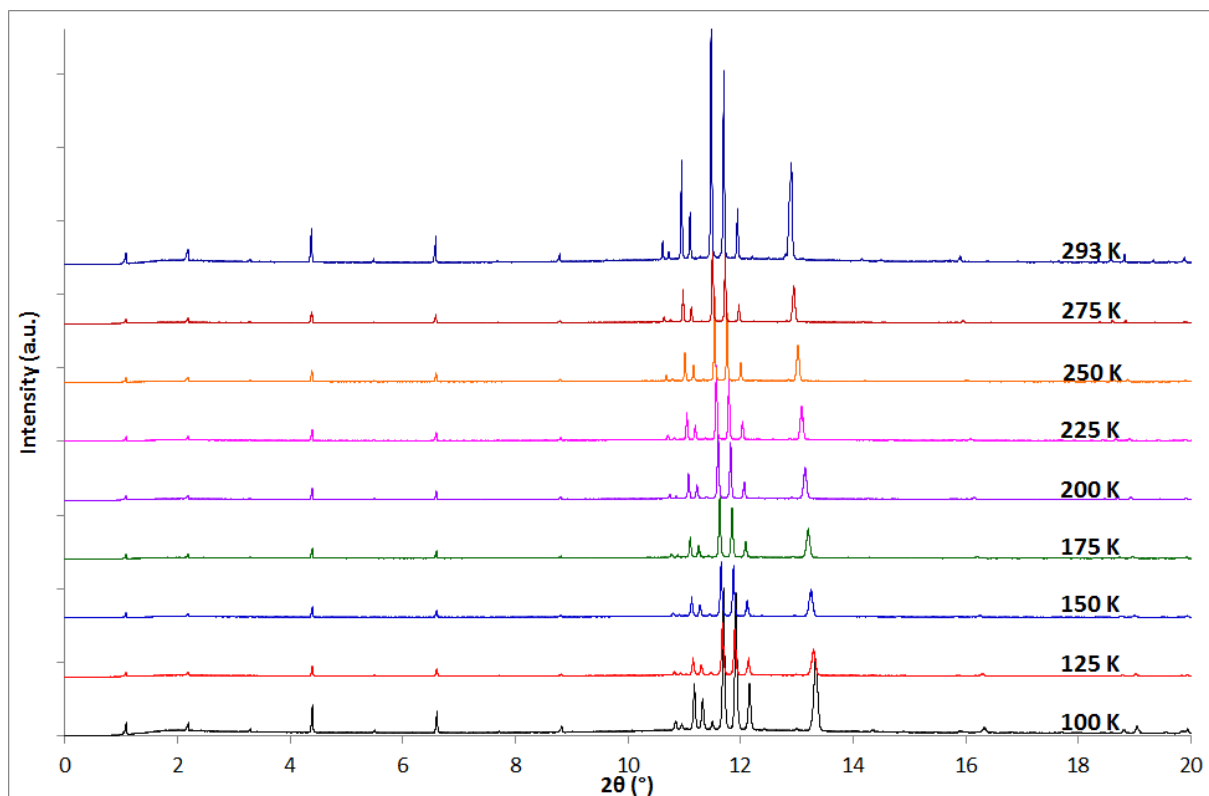
Figure 4.8 MP-*Pnab* short scans on cooling from 293 K to 100 K. *λ* = 0.826056 Å

Rietveld refinement of the scans with the MP-*Pnab* structure produced lattice parameters for the structure on cooling, which can be seen in Figures 4.9 – 4.12 and Table 4.6. The Rietveld refinements can be found in appendix 4.2.

Table 4.6 Refined lattice parameters for MP-*Pnab* cooling scans to 100 K.

Temperature (K)	*a* lattice parameter (Å)	*b* lattice parameter (Å)	*c* lattice parameter (Å)	Volume lattice parameter (Å^3)
293	5.6213(2)	7.3496(2)	86.193(5)	3561.0(3)
275	5.6135(2)	7.3207(2)	86.103(5)	3538.4(3)
250	5.6014(2)	7.2792(2)	86.045(5)	3508.4(3)
225	5.5900(2)	7.2430(2)	85.998(5)	3481.9(3)
200	5.5787(2)	7.2093(2)	85.943(5)	3456.5(3)
175	5.5688(2)	7.1816(2)	85.939(6)	3437.0(3)
150	5.5573(2)	7.1617(2)	85.925(5)	3419.8(2)
125	5.5504(2)	7.1312(2)	85.885(5)	3399.4(3)
100	5.5426(2)	7.1109(2)	85.867(6)	3384.3(3)
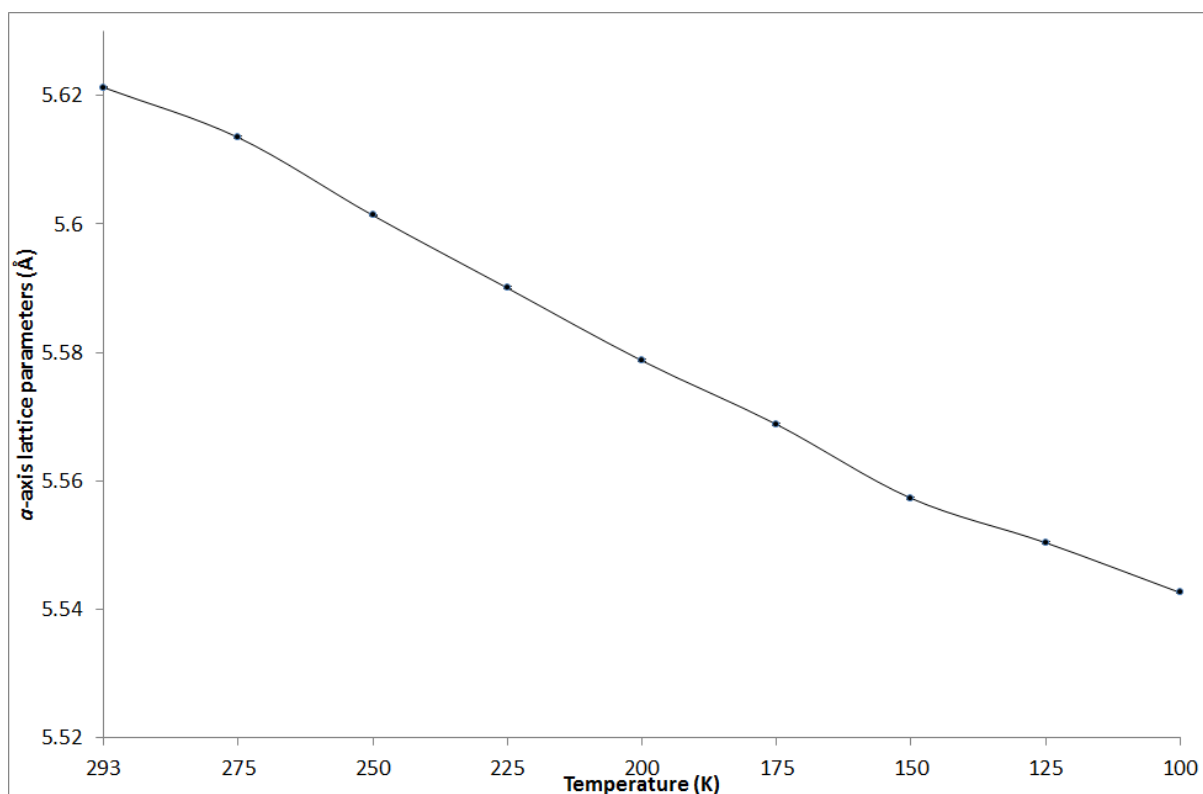
Figure 4.9 Refined *a*-axis lattice parameters for MP-Pnab cooling scans to 100 K.
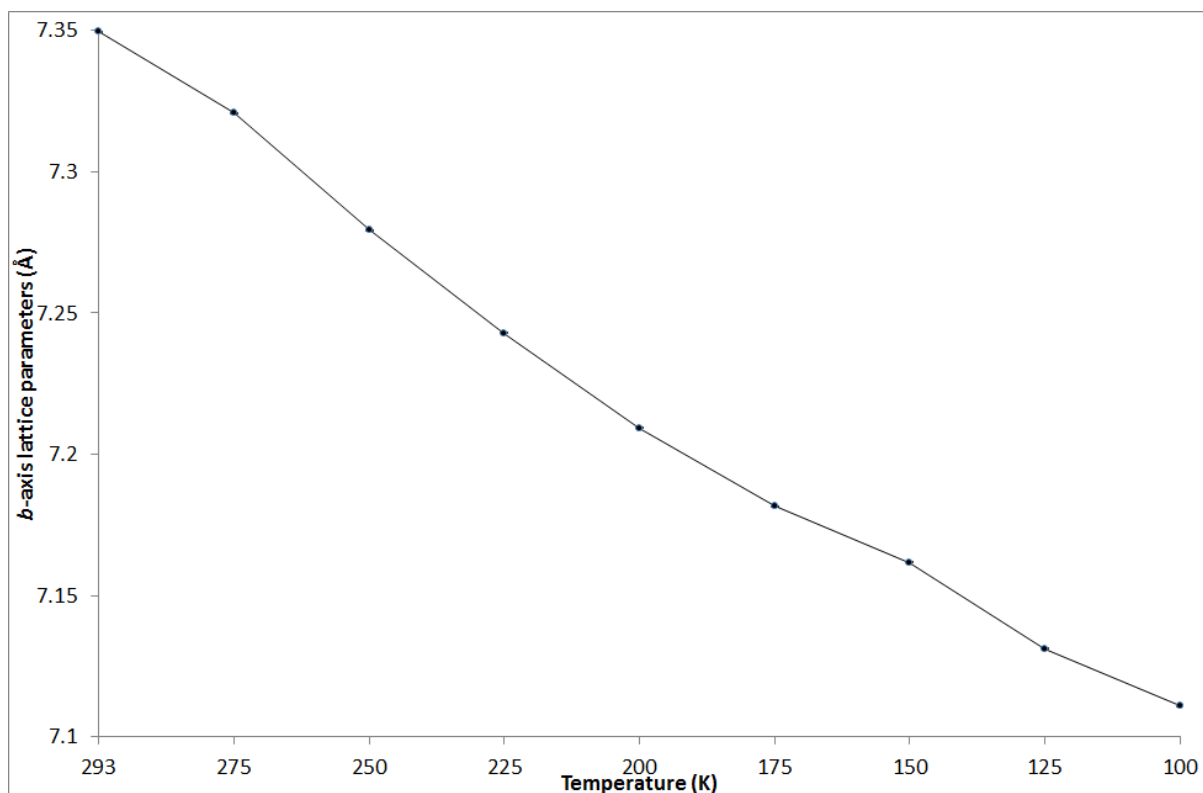
Figure 4.10 Refined *b*-axis lattice parameters for MP-Pnab cooling scans to 100 K.
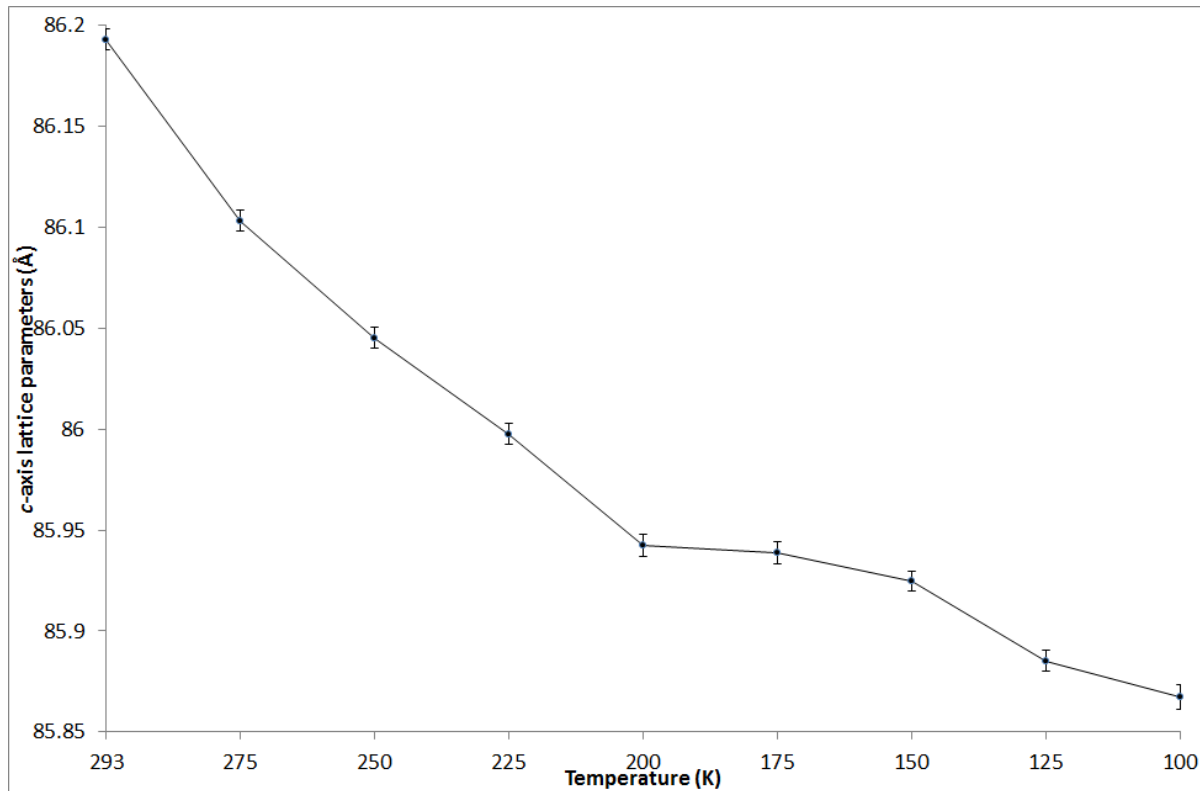
Figure 4.11 Refined *c*-axis lattice parameters for MP-Pnab cooling scans to 100 K.
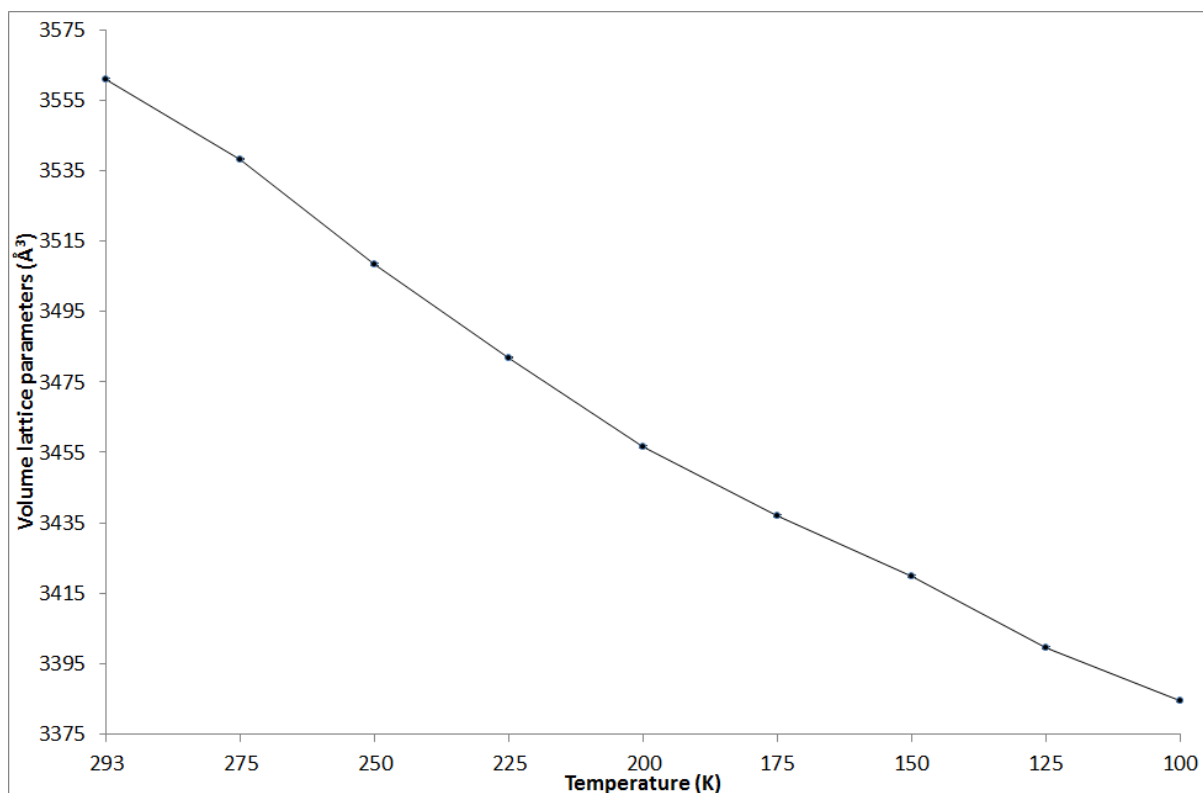
Figure 4.12 Refined volume lattice parameters for MP-Pnab cooling scans to 100 K.

The lattice parameters are fairly uniform in contraction in all directions, apart from the *c*-axis between 200 K and 125 K. The errors are also much larger than those calculated for the other lattice parameters, in which both the 200 K and 175 K parameters are within the error of one another. Whilst the results for *c*-axis are not uniform, the overall volume of the unit cell contracts linearly. From the lattice parameters obtained on cooling, thermal expansion coefficients were calculated using Equation 3.1, and are shown in Table 4.7.

Table 4.7 Calculated thermal expansion coefficients for MP-*Pnab* phase.

Lattice Parameter	Thermal Expansion Coefficient (K^{-1})
a (Å)	7.3504 x 10^{-5}
b (Å)	1.7393 x 10^{-4}
c (Å)	1.9652 x 10^{-5}
Volume (Å^3)	2.7050 x 10^{-4}

As with the three sets of thermal expansion coefficients calculated for methyl stearate structures in chapter 3, the MP-*Pnab* coefficients are also slightly larger than those traditionally reported in literature. They are however consistent in magnitude with those reported in this work, and so are therefore plausible due to these similar structures all expanding and contracting to a greater extent, than more rigid inorganic structures.

4.2.4 MP-*Pnab* lab PXRD data

A MP-*Pnab* lab PXRD data scan Figure 4.13, was recorded to confirm the structure, for comparison throughout this project.
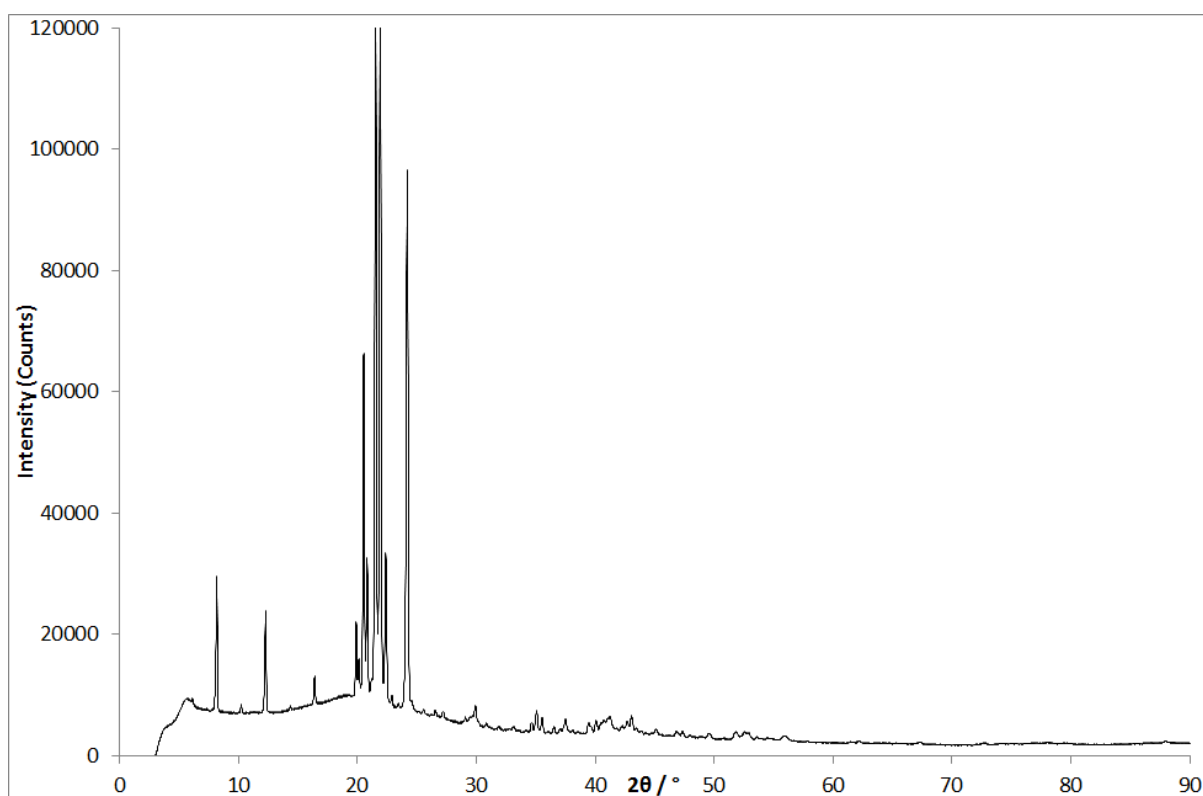
Figure 4.13 Laboratory PXRD pattern of methyl palmitate as-bought (room temperature). *λ* = 1.54056 Å

2 theta (Degrees)
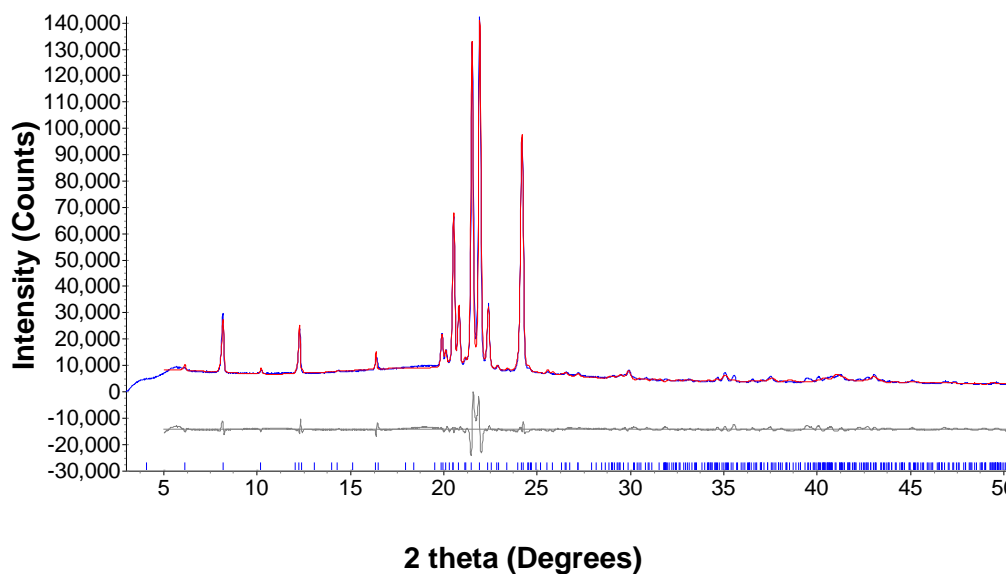
Figure 4.14 Observed (blue line) and calculated (red line) profile for the Rietveld refinement of methyl palmitate as-bought lab data with the MP-Pnab phase. The bottom curve is the difference plot on the same intensity scale. (Rwp = 7.19, Rp = 5.34, χ = 5.29). The tick marks represent calculated peak positions. λ = 1.54056 Å

Table 4.8 Refined lattice parameters for methyl palmitate as-bought lab data Rietveld refinement with MP-*Pnab* phase.

Parameter	Value
Space group	*Pnab*
a (Å)	5.6255(5)
b (Å)	7.3621(6)
c (Å)	86.68(1)
Volume (Å^3)	3589.7(7)

A Rietveld refinement was run with the MP-*Pnab* structure solved from synchrotron data, the fit is shown in Figure 4.14 and the refined lattice parameters in Table 4.8 and atomic positions in appendix 4.1.1. A good fit was produced with the phase solved from synchrotron data and will be used as a comparison for the rest of the project.

167

4.3 Methyl Palmitate from the melt

To determine whether methyl palmitate behaves the same as methyl stearate after melting, the same conditions used to produce the MS-*C*2 phase at Diamond beamline I11 were used to recrystallise methyl palmitate. The scan recorded on this material by Infineum at I11 was then indexed using TOPAS[65], with a suitable result similar to that of the MS-*C*2 phase, and the lattice parameters shown in Table 4.9.

Table 4.9 Lattice parameters from indexing results of the methyl palmitate melt phase.

Parameter	Value
Space group	*C*2
a (Å)	43.5086
b (Å)	7.3419
c (Å)	5.5986
α (°)	90
β (°)	94.2
γ (°)	90

A Pawley fit was run starting from the indexing result and is shown in Figure 4.15, with the refined lattice parameters shown in Table 4.10.
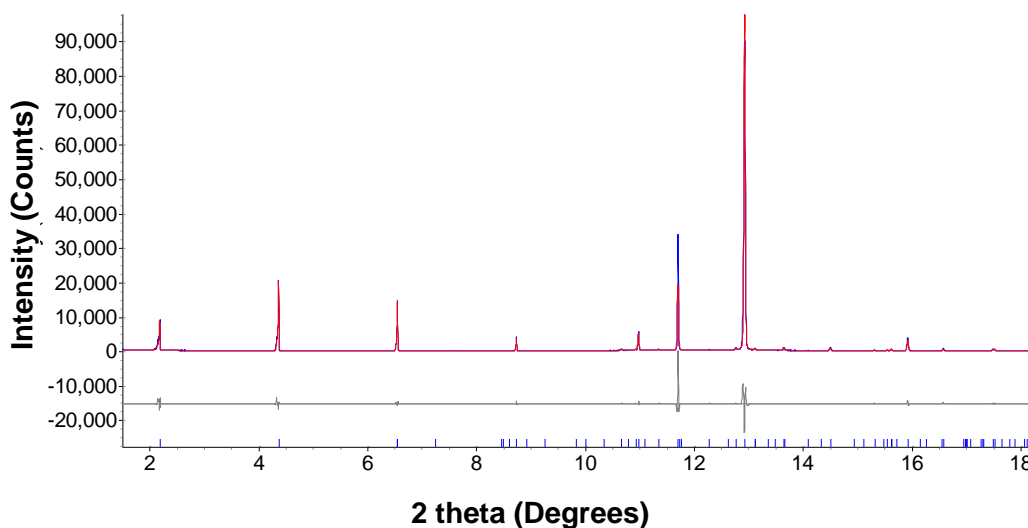
Figure 4.15 Observed (blue line) and calculated (red line) profile for the Pawley fit of methyl palmitate melt phase with the indexing results shown in Table 4.9. The bottom curve is the difference plot on the same intensity scale. (Rwp = 13.48, Rp = 7.94, χ = 4.14). The tick marks represent calculated peak positions. λ = 0.825992 Å

Table 4.10 Refined lattice parameters for methyl palmitate melt phase Pawley fit indexed parameters.

Parameter	Value
Space group	$C2$
a (Å)	43.5112(11)
b (Å)	7.3386(1)
c (Å)	5.5983(3)
β (°)	94.1685(51)

The Pawley fit appears good; however the full intensity of the peak at 11.7° 2θ was not fully fitted.

4.3.1 Structure solution with I11 data

A model building approach was used to solve this structure, with a model produced from the MS-*C*2 phase with two carbons removed, and the refined Pawley lattice parameters applied to produce the model structure shown in Figures 4.16 and 4.17.
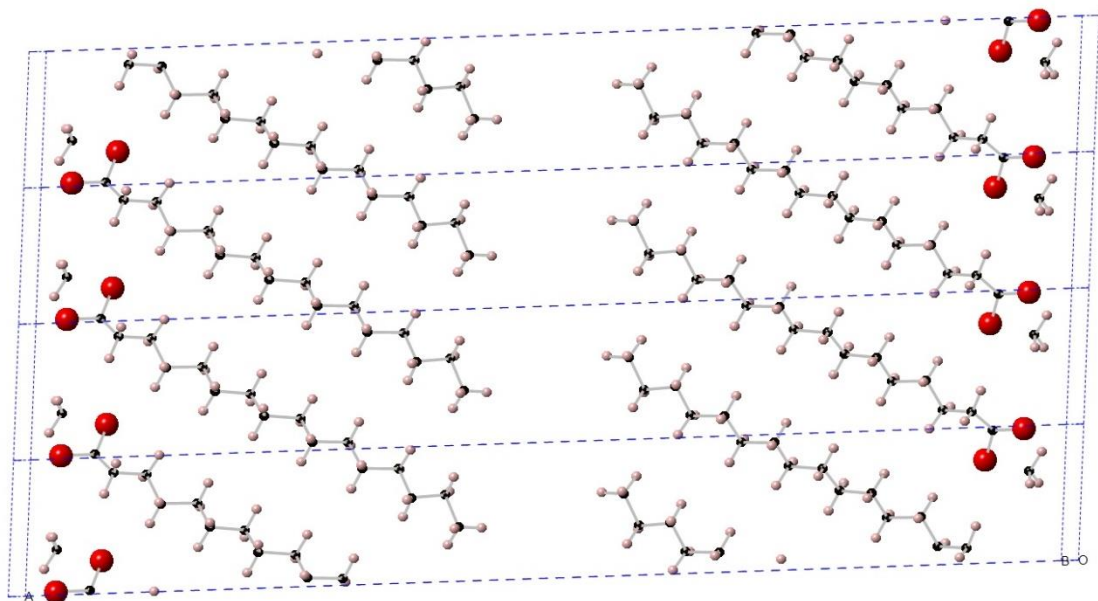
Figure 4.16 Methyl Palmitate melt starting model with Pawley fit lattice parameters viewed down the *b*-axis at the *ac* plane.
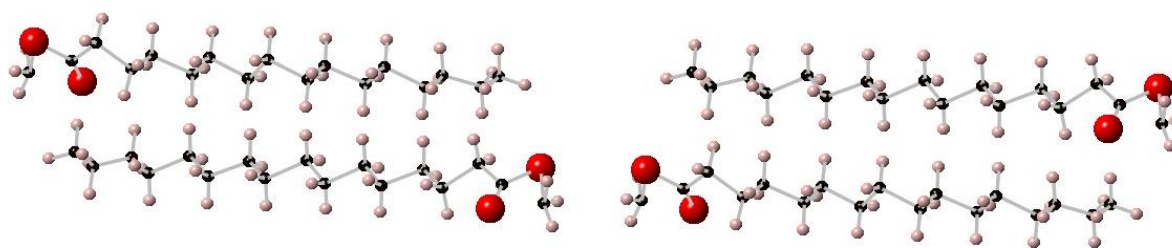
Figure 4.17 Methyl Palmitate melt starting model with Pawley fit lattice parameters viewed down the *c*-axis at the *ab* plane.

The model carbon – oxygen backbone structure was then refined in TOPAS[65] using soft bond distance and bond angle restraints, to prevent the atoms moving to

unrealistic positions, and spherical harmonics to correct for preferred orientation. Once the backbone had been refined, hydrogens were added in idealised positions using Olex2[78], and a final refinement was run using H-riding to keep the hydrogens in position along the carbon backbone as shown in Figure 4.18.

2 theta (Degrees)
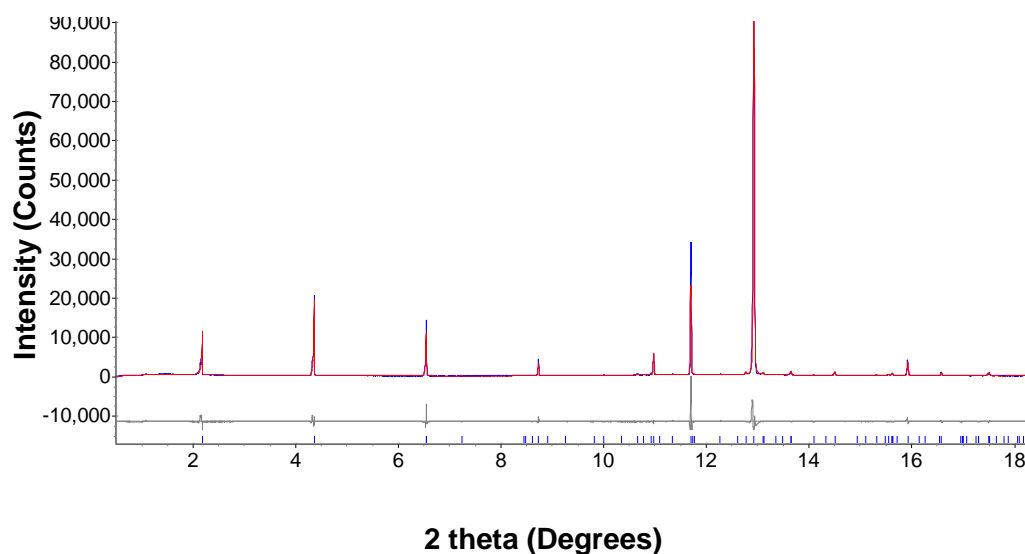
Figure 4.18 Observed (blue line) and calculated (red line) profiles for the final Rietveld refinement of methyl palmitate melt proposed structure. The bottom curve is the difference plot on the same intensity scale. (Rwp = 14.52, Rp = 9.15, χ = 4.40). The tick marks represent calculated peak positions. λ = 0.825992 Å
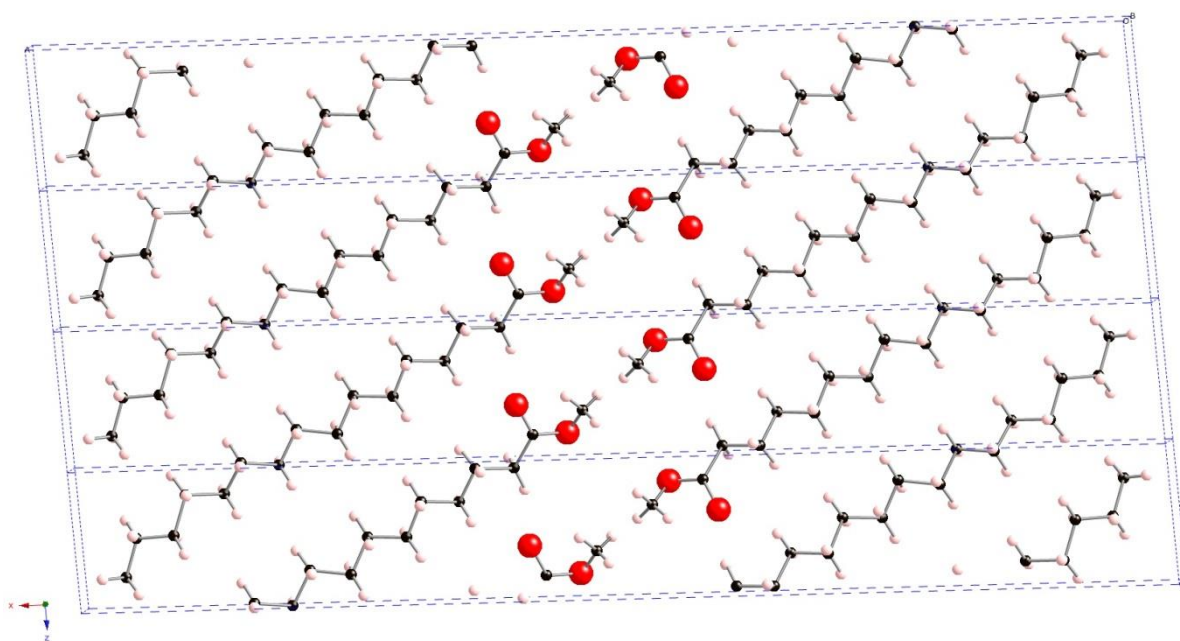
Figure 4.19 Methyl Palmitate melt final crystal structure viewed down the *b*-axis at the *ac* plane.
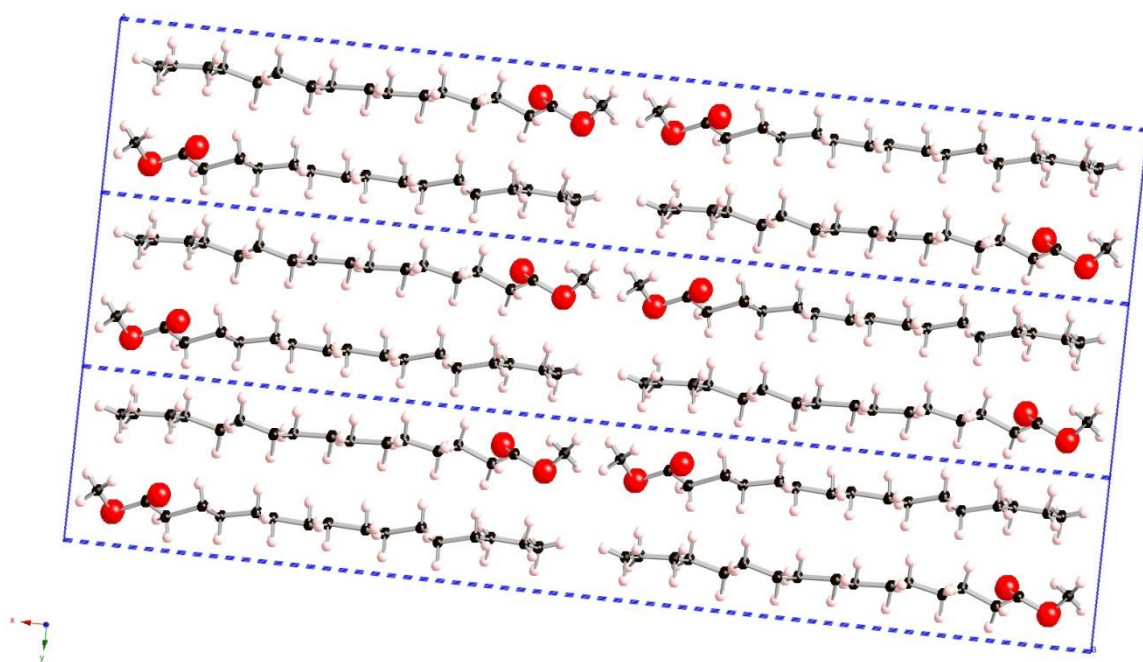
Figure 4.20 Methyl Palmitate melt final crystal structure viewed down the *c*-axis at the *ab* plane.

Figures 4.19 and 4.20 show the final methyl palmitate melt crystal structure which is analogous to the MS-*C*2 structure. Head to head alignment is found in the layers (along the *a*-axis), and head to tail alignment remains between the layers (along the *b*-axis), with the molecules orientated diagonally across the unit cell. Table 4.11 contains selected crystallographic data with Tables 4.12, 4.13 and 4.14 containing atomic coordinates, carbon and oxygen bond distance and angles respectively, with a labelled molecule in Figure 4.21.

Table 4.11 Selected crystallographic data of the methyl palmitate melt phase.

Parameter	Data
Chemical Formula	$C_{17}H_{34}O_2$
Formula weight (g mol^{-1})	270.45
Crystal system	Monoclinic
Space group	*C*2
a (Å)	43.526(11)
b (Å)	7.3391(7)
c (Å)	5.6009(8)
β (°)	94.131(22)
V (Å^3)	1784.50(53)
T (K)	233 K
Z	4
λ (Å)	0.825992
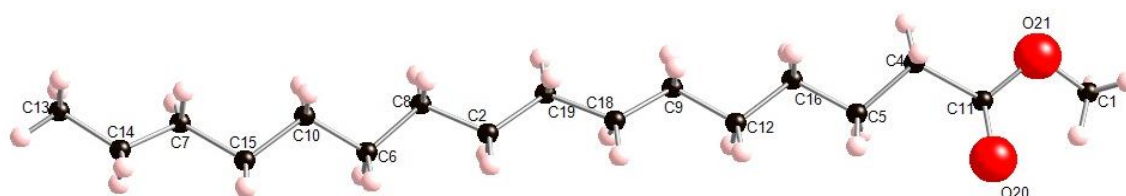
Figure 4.21 Labelled methyl palmitate melt molecule.

173

Table 4.12 Atomic coordinates for MP-*C*2 structure.

Atom Number	*x*	*y*	*z*
C1	0.4755(12)	0.2104(9)	2.313(15)
C2	0.2063(9)	0.2383(7)	1.248(14)
C4	0.3905(7)	0.3206(8)	1.857(14)
C5	0.3595(10)	0.2034(9)	1.819(15)
C6	0.1558(7)	0.2167(8)	1.039(17)
C7	0.0891(13)	0.2455(8)	0.506(15)
C8	0.1925(13)	0.2626(7)	1.023(16)
C9	0.2981(10)	0.2494(8)	1.448(13)
C10	0.1406(14)	0.2742(6)	0.799(16)
C11	0.4174(13)	0.2084(6)	2.131(16)
C12	0.3116(12)	0.2042(7)	1.676(18)
C13	0.0300(9)	0.2601(6)	0.287(16)
C14	0.0590(10)	0.2003(9)	0.525(13)
C15	0.1016(12)	0.2382(9)	0.781(16)
C16	0.3351(7)	0.3134(9)	1.723(14)
C18	0.2641(8)	0.2034(8)	1.453(14)
C19	0.2409(10)	0.2679(7)	1.209(16)
O20	0.4054(5)	0.1854(8)	2.337(10)
O21	0.4468(8)	0.3059(6)	2.1719(9)

Table 4.13 Methyl palmitate melt carbon – carbon / carbon – oxygen bond lengths.

Bond	Distance (Å)
C13 – C14	1.59(5)
C14 – C7	1.49(4)
C7 – C15	1.66(6)
C15 – C10	1.59(4)
C10 – C6	1.50(6)
C6 – C8	1.56(4)
C8 – C2	1.56(4)
C2 – C19	1.65(6)
C19 – C18	1.62(3)
C18 – C9	1.56(7)
C9 – C12	1.54(4)
C12 – C16	1.53(5)
C16 – C5	1.52(5)
C5 – C4	1.62(3)
C4 – C11	1.62(4)
C11 – O20	1.39(4)
C11 – O21	1.47(5)
O21 – C1	1.40(6)

Table 4.14 Methyl palmitate melt carbon / oxygen backbone bond angles.

Bond	Angle (°)
C13 – C14 – C7	110(3)
C14 – C7 – C15	111(3)
C7 – C15 – C10	107(4)
C15 – C10 – C6	112(3)
C10 – C6 – C8	107(4)
C6 – C8 – C2	103(4)
C8 – C2 – C19	110(3)
C2 – C19 – C18	107(4)
C19 – C18 – C9	112(4)
C18 – C9 – C12	111(4)
C9 – C12 – C16	108(3)
C12 – C16 – C5	112(4)
C16 – C5 – C4	109(3)
C5 – C4 – C11	109(3)
C4 – C11 – O20	123(4)
C4 – C11 – O21	110(4)
C11 – O21 – C1	103(3)

The methyl palmitate melt structure (which will be referred to as MP-$C2$), was thus successfully solved from I11 PXRD data with a similar structure to the MS-$C2$ phase.

4.3.2 MP-*C2* phase lab data

To confirm whether the MP-*C2* phase can be replicated in a lab environment, the same conditions were run on a lab capillary diffractometer fitted with an Oxford cryostream, with the resulting PXRD pattern shown in Figure 4.22.
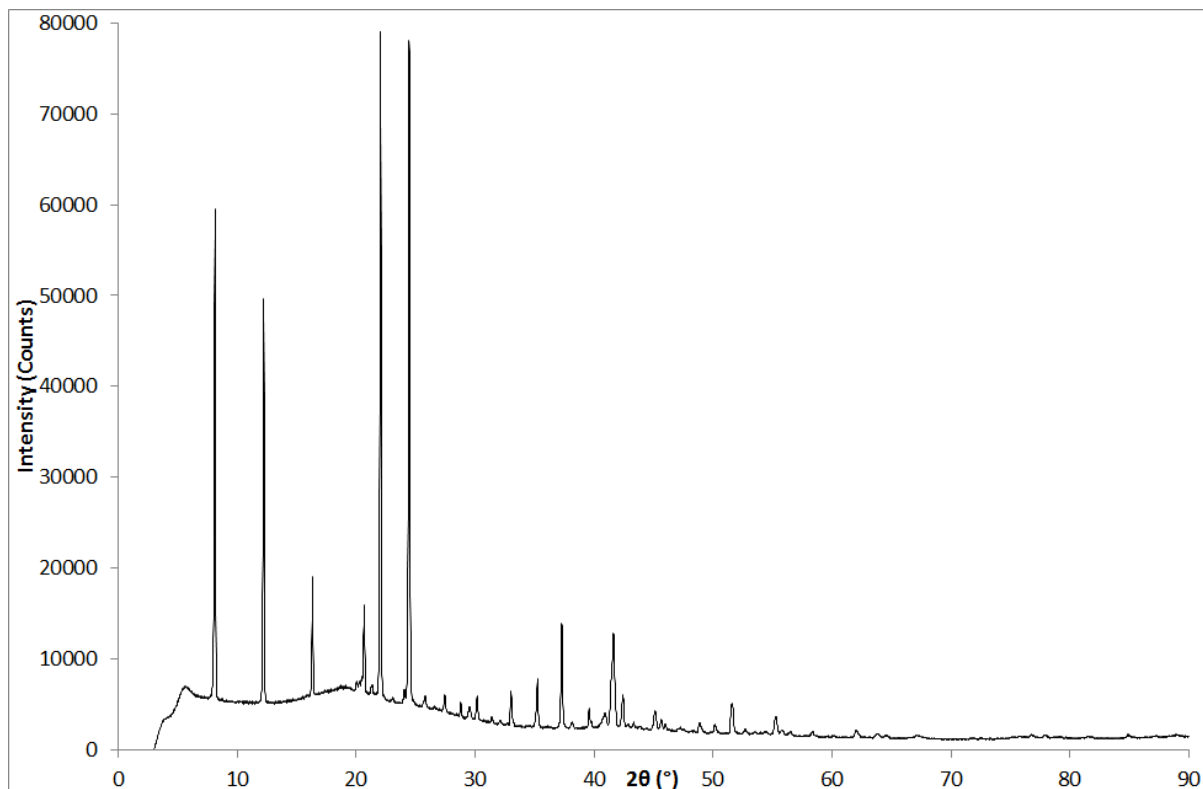
Figure 4.22 PXRD pattern of the product from variable temperature recrystallisation from the melt of methyl palmitate 333 K to 233 K at 100 K/hr. *λ* = 1.54056 Å
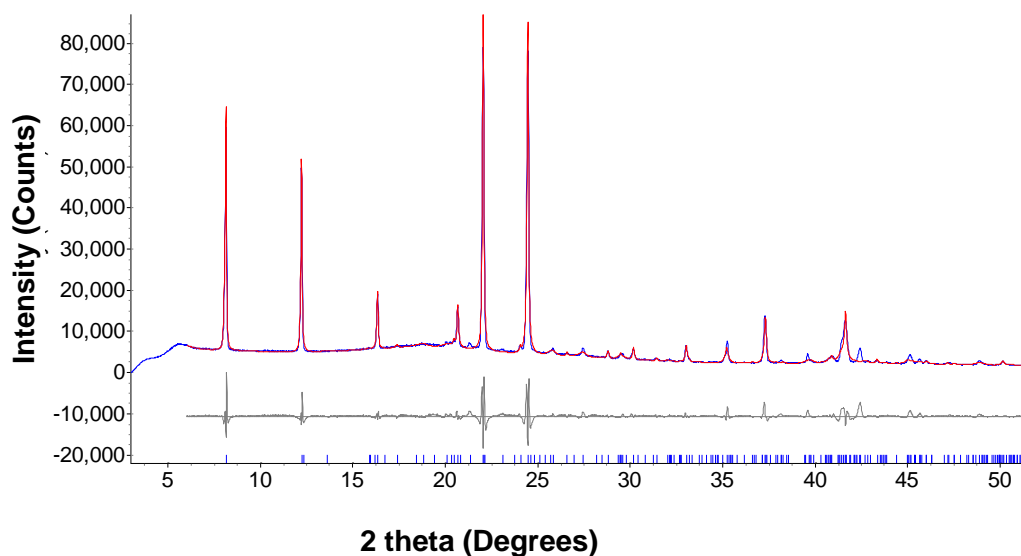
Figure 4.23 Observed (blue line) and calculated (red line) profile for the Rietveld refinement of methyl palmitate variable temperature recrystallisation from the melt with the MP-C2 phase. (Rwp = 9.14. Rp = 5.86, χ = 5.41). The tick marks represent calculated peak positions. λ = 1.54056 Å

A Rietveld refinement of the lab data with the MP-*C*2 phase was run as shown in Figure 4.23 with refined lattice parameters shown in Table 4.15 and atomic positions in appendix 4.1.2, confirming that the phase can be replicated in a lab environment.

Table 4.15 Refined lattice parameters for methyl palmitate variable temperature recrystallisation from the melt lab data with the MP-*C*2 phase.

Parameter	Value
Phase / Space group	MP-*C*2 / *C*2
a (Å)	43.4495(13)
b (Å)	7.2691(1)
c (Å)	5.5677(8)
β (°)	94.087(15)
Volume (Å^3)	1754.04(28)

4.4 Methyl Palmitate recrystallisations

To determine whether methyl palmitate has more than two polymorphs and under which conditions the phases crystallise out, various recrystallisation experiments were run, outlined in Table 4.16.

Table 4.16 Methyl palmitate recrystallisation conditions.

Figure / Pattern	Solvent	Experiment Type	Temp 1	Temp 2	Cooling Rate
4.24 / C	Toluene	Solvent recrystallisation	298 K	255 K	-
4.24 / D	Kerosene	Solvent recrystallisation	298 K	255 K	-
4.24 / E	Toluene	Variable temperature	333 K	233 K	100 K/hr
4.24 / F	Kerosene	Variable temperature	333 K	233 K	100 K/hr
4.25 / C	-	From melt	353 K	298 K	-
4.25 / D	-	From melt	353 K	255 K	-
4.25 / E	Toluene	From melt then solvent recrystallisation	353 K	255 K	-
4.25 / F	Kerosene	From melt then solvent recrystallisation	353 K	255 K	-
4.26 / C	-	Cyclic variable temperature	Cycle 3 – 233 K	290 K	100 K/hr
4.26 / D	-	Cyclic variable temperature	Cycle 2 – 333 K	233 K	100 K/hr
4.26 / E	-	Cyclic variable temperature	Cycle 2 – 290 K	333 K	100 K/hr
4.26 / F	-	Cyclic variable temperature	Cycle 2 – 233 K	290 K	100 K/hr
4.26 / G	-	Cyclic variable temperature	Cycle 1 – 333 K	233 K	100 K/hr
4.26 / H	-	Cyclic variable temperature	Cycle 1 – 290 K	333 K	100 K/hr
4.26 / I	-	Cyclic variable temperature	Cycle 1 – room temperature	290 K	100 K/hr
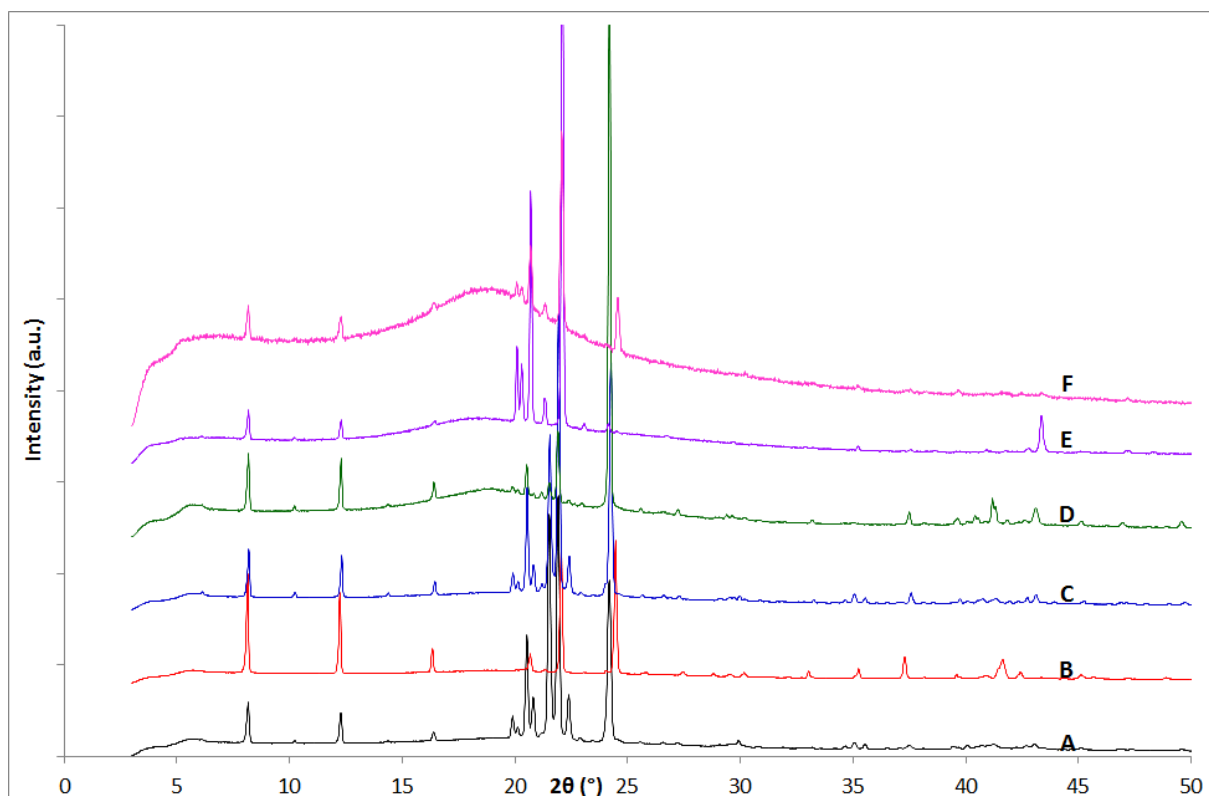
Figure 4.24 PXRD patterns of (A) MP-Pnab (room temperature), (B) MP-C2 (233 K), (C) the product from solvent recrystallisation experiment methyl palmitate in toluene at 255 K, (D) the product from solvent recrystallisation experiment methyl palmitate in kerosene at 255 K, (E) the product from variable temperature experiment methyl palmitate in toluene 333 K to 233 K at 100 K/hr, (F) the product from variable temperature experiment methyl palmitate in kerosene 333 K to 233 K at 100 K/hr. λ = 1.54056 Å

Figure 4.24 shows two solvent recrystallisations, patterns C and D, carried out not using any heat, which crystallise back into the MP-*Pnab* phase; but the two solvent recrystallisations, patterns E and F, which bring the solutions above the melting point of methyl palmitate in a capillary, crystallise in the MP-*C*2 polymorph. Whilst solvent doesn't appear to have influence on the crystal structure, it appears, like methyl stearate, that once heated the MP-*C*2 phase crystallises out.
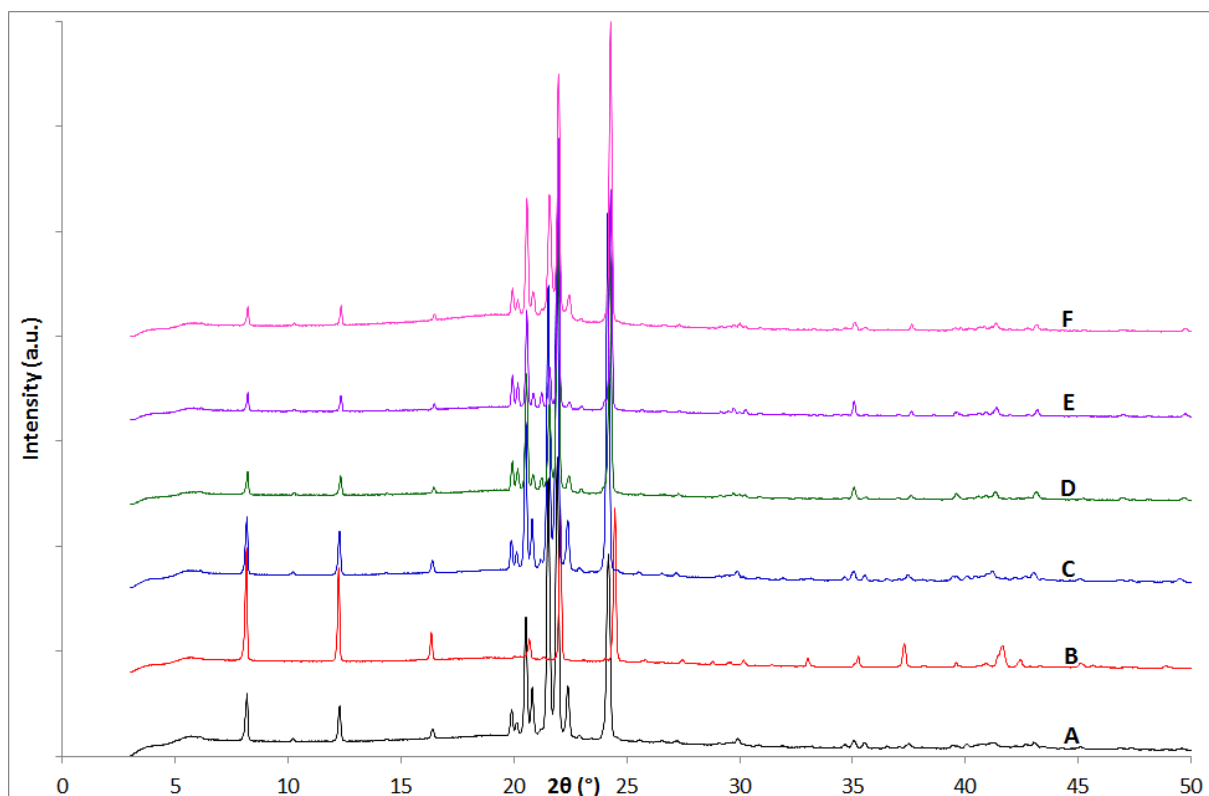
Figure 4.25 PXRD patterns of (A) MP-Pnab (room temperature), (B) MP-C2 (233 K), (C) the product from the melt experiment in a Teflon pot and cooled at room temperature methyl palmitate, (D) the product from the melt experiment in a Teflon pot and cooled in the freezer methyl palmitate recorded at room temperature, (E) the product from the melt experiment in a Teflon pot and cooled at room temperature methyl palmitate then recrystallised in toluene, (F) the product from the melt experiment in a Teflon pot and cooled at room temperature methyl palmitate then recrystallised in kerosene. λ = 1.54056 Å

Figure 4.25 shows PXRD patterns from methyl palmitate recrystallised in a Teflon pot from the melt with different cooling rates (patterns C and D); and then recrystallised in toluene and kerosene (patterns E and F), which all produced the MP-*Pnab* phase. Unlike the melt phase produced in Figure 4.24 patterns E and F, which were recrystallised in a capillary and as the phase was originally produced, all the phases recorded in Figure 4.25 were not recrystallised in a capillary. This therefore

shows in some inconsistency in producing the melt phase. This is most likely due to the surfaces on which the crystals grow, therefore showing that methyl palmitate is likely to recrystallise into the melt phase in small quantities with a relative large surface area like in a capillary; but in the bulk material it is more likely to crystallise into the MP-*Pnab*.
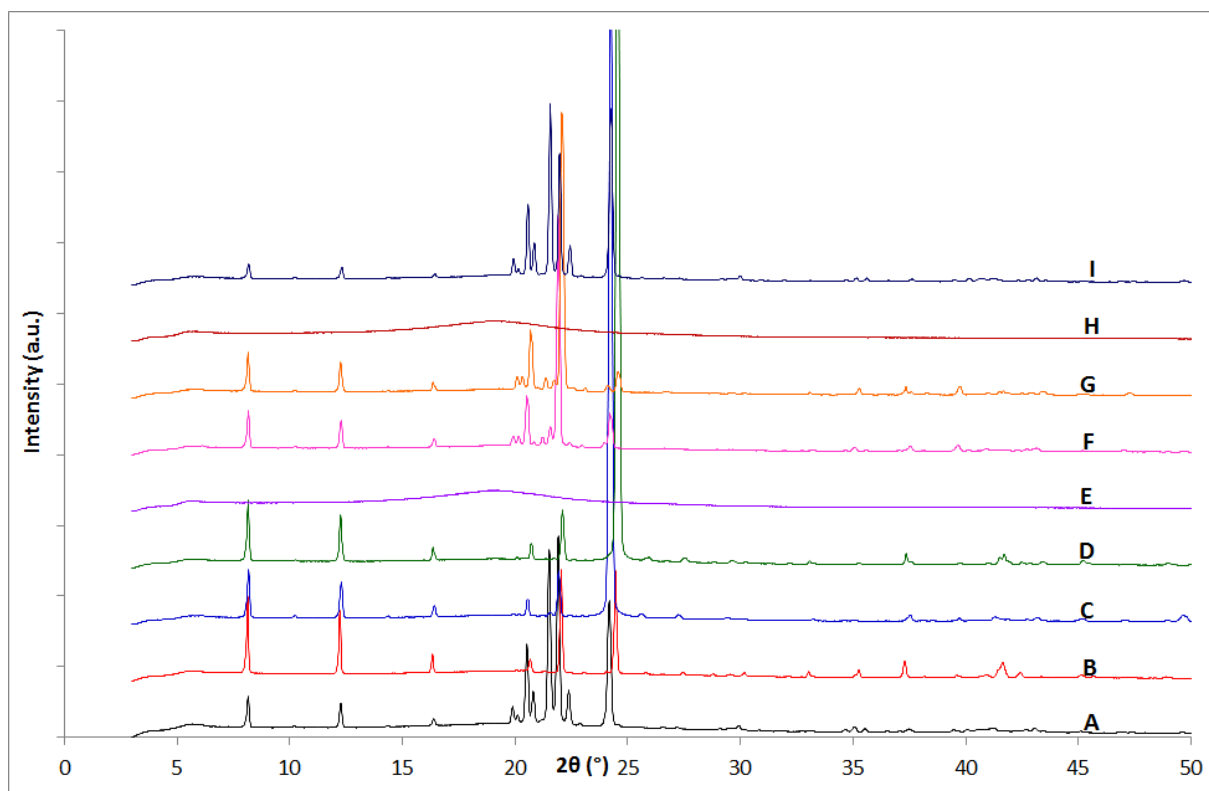
Figure 4.26 PXRD patterns of (A) MP-Pnab (room temperature), (B) MP-C2 (233 K), (C) methyl palmitate cyclic variable temperature cycle 3 recorded at 290 K, (D) methyl palmitate cyclic variable temperature cycle 2 recorded at 233 K, (E) methyl palmitate cyclic variable temperature cycle 2 recorded at 333 K, (F) methyl palmitate cyclic variable temperature cycle 2 recorded at 290 K, (G) methyl palmitate cyclic variable temperature cycle 1 recorded at 233 K, (H) methyl palmitate cyclic variable temperature cycle 1 recorded at 333 K, (I) methyl palmitate cyclic variable temperature cycle 1 recorded at 290 K. λ = 1.54056 Å

Figure 4.26 shows the cyclic recrystallisation of methyl palmitate under the same conditions used with the cyclic methyl stearate and ethyl stearate recrystallisations. Patterns E and H confirm melting of the sample between each cycle at 333 K. Pattern I is the starting scan confirming the sample starts in the MP-*Pnab* phase but all other scans are the MP-*C*2 phase.

All the recrystallisations of methyl palmitate show that once heated in a capillary the MP-*C*2 phase crystallises out, however if the sample is heated not in a capillary or recrystallised without using heat then the MP-*Pnab* phase crystallises back out.

Rietveld refinements of the methyl palmitate recrystallisations can be found in appendix 4.3.

4.5 Gaussian dipole calculations

As with the methyl stearate polymorphs, dipole calculations were carried out for the methyl palmitate as-bought and melt phases.

4.5.1 MP-*Pnab* phase

Table 4.17 Gaussian molecular dipole results for MP-*Pnab* structure.

	Hartree-Fock basic (Debye)	Hartree-Fock routine (Debye)	B3LYP routine (Debye)	AM1 (Debye)	PM3 (Debye)
1 molecule	4.3098	4.0651	3.5931	3.4034	3.3589
2 molecules stacking	2.5791	1.8271	1.3663	1.7947	1.4720
2 molecules in a layer	2.4065	1.6914	1.2091	1.7999	1.4658
4 molecules in a layer	0.0772	0.0785	0.0736	0.0601	0.0566
4 molecules in a half cell	5.0420	3.6166	2.7098	3.6096	2.9662
4 molecules in a central half cell	0	0	0	0	0
8 molecules full cell	0	-	-	0	0

The MP-*Pnab* individual molecule dipole is larger than those calculated for all the methyl stearate phases. There is however both a zero dipole for the full unit cell and a central half-cell, along with a small dipole within each layer, which is consistent with the three single crystal methyl stearate structures.

4.5.2 MP-*C*2 phase

Table 4.18 Gaussian molecular dipole results for MP-*C*2 structure.

	Hartree-Fock basic (Debye)	Hartree-Fock routine (Debye)	B3LYP routine (Debye)	AM1 (Debye)	PM3 (Debye)
1 molecule	2.4744	2.7056	2.1291	2.4050	2.2919
2 molecules stacking	0.3281	0.1777	0.4943	0.1784	0.1708
2 molecules in a layer	0.8801	0.5954	0.3253	0.2161	0.2053
4 molecules full cell	0.5788	0.0003	0.9658	0.3289	0.2710
8 molecules 2 unit cells *a* + 1	1.1490	-	-	0.6537	0.5433
8 molecules 2 unit cells *b* + 1	0.3391	-	-	0.5564	0.4257
8 molecules 2 unit cells *c* + 1	1.6828	-	-	0.5339	0.4306
4 molecules in a layer	1.7627	1.1943	0.6545	0.4326	0.4109
4 molecules in a central half cell	0.6012	0.0287	0.9389	0.3407	0.2876

The MP-*C*2 single molecule has a similar dipole to the MS-*A*2/*a* molecule and a smaller dipole than the MP-*Pnab* molecule. This means that the MP-*C*2 phase has a much larger dipole than its counterpart MS-*C*2 phase, which has one of the smallest single molecule dipoles of the five methyl stearate polymorphs. There is no zero dipole for any molecular arrangement, with a similar sized dipole to the MS-*C*2 phase both in the full unit cell and *a* + 1 calculations. The ES-*Aa* and PS-*Pa* dipole calculations presented earlier show that a dipole can be present in solid crystal

structures; therefore confirming that both MS-*C*2 phases and the MP-*C*2 structure, with non-zero dipoles are plausible structures.

4.5.3 MP-*Pnab* 1-molecule disordered structures

As for the five methyl stearate structures 1-molecule disordered structures for the MP-*Pnab* phase were created, using the same method of rotating one molecule at a time, whilst keeping the other seven molecules in their original orientation.

Table 4.19 Gaussian molecular dipole results for MP-*Pnab* 1-molecule disordered structures.

	Hartree-Fock basic (Debye)	Hartree-Fock routine (Debye)	B3LYP routine (Debye)	AM1 (Debye)	PM3 (Debye)
Disordered structure 1	7.4873	-	-	5.7846	5.5220
Disordered structure 2	7.3693	-	-	5.6159	5.3284
Disordered structure 3	7.2114	-	-	5.5986	5.3051
Disordered structure 4	7.5598	-	-	5.8018	5.5253
Disordered structure 5	7.4873	-	-	5.7848	5.5222
Disordered structure 6	7.3693	-	-	5.6159	5.3284
Disordered structure 7	7.2114	-	-	5.5987	5.3050
Disordered structure 8	7.5598	-	-	5.8019	5.5255

The dipoles for the disordered structures of the MP-*Pnab* phase are all significantly larger than the standard structure, this is consistent with the findings for the methyl stearate phases in chapter 3. On rotating one molecule in the unit cell, the dipole increases to values larger than any of the disordered methyl stearate structures; but are smaller than the ethyl and propyl stearate non disordered structures, with eight molecules in the calculation.

4.5.4 MP-*C*2 1-molecule disordered structures

As with all five methyl stearate polymorphs and the MP-*Pnab* phase, disordered structures were created with dipole calculations calculated for the MP-*C*2 phase and $a + 1$, $b + 1$ and $c + 1$ molecular arrangements.

Table 4.20 Gaussian molecular dipole results for MP-*C*2 1-molecule disordered structures.

	Hartree-Fock basic (Debye)	Hartree-Fock routine (Debye)	B3LYP routine (Debye)	AM1 (Debye)	PM3 (Debye)
Disordered structure 1	4.2213	4.5407	3.6268	4.2474	4.0418
Disordered structure 2	4.2213	4.5407	3.6268	4.2475	4.0418
Disordered structure 3	4.3492	4.6175	3.6215	4.3409	4.1621
Disordered structure 4	4.3492	4.6175	3.6215	4.3409	4.1621

The dipole calculations for the disordered structures of MP-*C*2 are all significantly larger than all the dipoles calculated for the standard structure.

Disordered structure calculations were also run of 2 unit cells of MP-*C*2, with *a* + 1, *b* + 1 and *c* + 1 as run with the standard solved structure.

Table 4.21 Gaussian molecular dipole results for MP-*C*2 *a* + 1 1-molecule disordered structures.

	Hartree-Fock basic (Debye)	Hartree-Fock routine (Debye)	B3LYP routine (Debye)	AM1 (Debye)	PM3 (Debye)
Disordered structure 1	4.3767	-	-	4.3210	4.1068
Disordered structure 2	4.3573	-	-	4.3034	4.0931
Disordered structure 3	4.5235	-	-	4.4203	4.2320
Disordered structure 4	4.5019	-	-	4.4011	4.2218
Disordered structure 5	4.3573	-	-	4.3034	4.0931
Disordered structure 6	4.3767	-	-	4.3210	4.1068
Disordered structure 7	4.5019	-	-	4.4010	4.2217
Disordered structure 8	4.5235	-	-	4.4202	4.2319

Table 4.22 Gaussian molecular dipole results for MP-*C*2 *b* + 1 1-molecule disordered structures.

	Hartree-Fock basic (Debye)	Hartree-Fock routine (Debye)	B3LYP routine (Debye)	AM1 (Debye)	PM3 (Debye)
Disordered structure 1	3.9742	-	-	4.1844	3.9789
Disordered structure 2	3.9742	-	-	4.1844	3.9788
Disordered structure 3	3.8990	-	-	4.0965	3.9136
Disordered structure 4	3.8990	-	-	4.0965	3.9136
Disordered structure 5	3.8880	-	-	4.1014	3.9194
Disordered structure 6	3.8880	-	-	4.1014	3.9194
Disordered structure 7	4.1023	-	-	4.3144	4.1276
Disordered structure 8	4.1023	-	-	4.3143	4.1275

Table 4.23 Gaussian molecular dipole results for MP-$C2$ $c + 1$ 1-molecule disordered structures.

	Hartree-Fock basic (Debye)	Hartree-Fock routine (Debye)	B3LYP routine (Debye)	AM1 (Debye)	PM3 (Debye)
Disordered structure 1	5.0913	-	-	4.5152	4.3603
Disordered structure 2	5.5082	-	-	4.7126	4.5906
Disordered structure 3	5.4856	-	-	4.6865	4.5468
Disordered structure 4	5.3594	-	-	4.7201	4.5997
Disordered structure 5	5.5082	-	-	4.7125	4.5906
Disordered structure 6	5.0913	-	-	4.5152	4.3603
Disordered structure 7	5.3594	-	-	4.7201	4.5997
Disordered structure 8	5.4856	-	-	4.6864	4.5467

All the dipole calculations are larger than the two unit cell results for the non-disordered phases. The dipole results are greater for the $c + 1$ unit cell and smallest for the $b + 1$, however they are quite similar to the single unit cell disordered structures.

4.5.5 MP-*C*2 2 molecule disordered structures

Two molecule disordered structures were run with the MP-*C*2 phase with the same molecular layouts as produced with the two methyl stearate melt phases in section 3.7.3.

Table 4.24 Gaussian molecular dipole results for MP-*C*2 2 molecule disordered structures.

	Hartree-Fock basic (Debye)	Hartree-Fock routine (Debye)	B3LYP routine (Debye)	AM1 (Debye)	PM3 (Debye)
Disordered structure 1	1.2463	0.7804	0.1738	1.3719	1.4822
Disordered structure 2	1.2569	0.9578	0.0972	1.4398	1.5466
Disordered structure 3	8.4522	9.1537	7.1870	8.5250	8.1465

On increasing the disorder from one molecule to two molecules there is a decrease in dipole for disordered structure layouts 1 and 2 but a significant increase in dipole for layout 3. The dipole for disordered layouts 1 and 2 is, however, on average slightly larger than the non-disordered unit cell.

The structures described have the same molecular arrangement as the 2-molecule disordered structures for the MS-*C*2 phase, shown in Figure 3.60. Structure 1 has head to head, tail to tail alignment of the molecules in all axis directions. Structure 2, however, which has a similar dipole to structure 1, has head to tail alignment along the *a* and *b* axis, but head to head alignment along the *c* axis. Structure 3 which has around double the dipole compared to the 1 molecule

disordered structures has head to tail alignment along the *a* long axis but head to head alignment along *b* and *c*.

4.6 Conclusions

Two methyl palmitate structures were solved in this chapter from synchrotron PXRD data, the MP-*Pnab* phase and one from the melt (MP-*C*2) phase. The MP-*Pnab* phase is very similar to the MS-*Pnab* phase. Whilst the MS-*Pnab* phase was solved from single crystal data, and has a planar carbon – oxygen backbone structure, the MP-*Pnab* phase was solved from PXRD data, and both ends of the carbon – oxygen chain are slightly twisted. This may be due to the nature of structural solution from PXRD data whereby some information is lost compared to structural solution from single crystal data and therefore the end structure may not be completely perfect.

Thermal expansion coefficients were also calculated for the MS-*Pnab* from PXRD scans on cooling, with similar values to those calculated for the three methyl stearate structures in chapter 3. Whilst these values are all larger than those typically reported in the literature, these values are all consistent with the three other phases and have very similar structures; therefore it is likely that organic structures with greater flexibility in their structures, will have larger thermal expansion coefficients.

A second methyl palmitate structure was solved from I11 PXRD data but this phase was from the melt. The crystallisation conditions were the same as the MS-*C*2 phase on which the initial model was based. The structure was successfully solved and is very similar to the MS-*C*2 phase.

Both new methyl palmitate phases were confirmed with lab data for comparison with the rest of the data collected in this work.

Various methyl palmitate recrystallisations were carried out using heat and solvent to mimic conditions that may be experienced in a fuel tank. The MP-*Pnab* phase crystallises out when no heat is applied to the sample, or the sample has been melted and cooled not in a capillary. The MP-*C*2 phase forms only when the sample has been melted and cooled in a capillary. This is in contrast to methyl stearate, which, once melted, will always crystallise in a melt phase. Whilst there is an inconsistency between the melt phases, this may be due to the material surface or surface area on which the crystallisation takes place, affecting the phase which crystallises out with methyl palmitate.

The Gaussian dipole results for the MP-*Pnab* phase produced the highest dipole for the single molecule, out of all the structures studied in this project. But like its methyl stearate counterpart (MS-*Pnab*), has a net zero dipole for the unit cell and central half-cell. Similarly, the MP-*C*2 phase has a net unit cell dipole, of a similar size as the MS-*C*2 phase. The individual molecule, however, has a larger dipole than the MS-*C*2 phase, and is similar in value to the individual MS-*A*2/*a* phase.

The 1-molecule disordered structure dipole results as with those discussed in chapter 3 are larger than the standard structures, but there is a greater dipole in the disordered *c* + 1 melt phase, and a smaller dipole for the *b* + 1 molecular arrangement.

The 2-molecule disordered structures for the MP-*C*2 phase also all show an increase in dipole when compared to the non-disordered structures however there is

a decrease in dipole for two layouts when compared to the 1 molecule disordered structures.

Overall, disorder in the unit cells increases the dipole of both methyl palmitate phases.

5.   Chapter 5 – Structures of n-alkanes and crystallisations of Methyl Stearate or Methyl Palmitate with hydrocarbons

5.1 Introduction

The `middle distillates` which make up petroleum diesel contain a large proportion of straight chain hydrocarbons, with the range of 8 to 24 carbons in the chain. As *n*-alkanes in this range can be similar in length to the methyl esters found in biodiesel, with long straight chains of carbons there is potential for them to cocrystallise or form coordinated crystals when the alkanes and methyl esters are melted, or are mixed together under conditions experienced in manufacture, or in the process of using the diesel / biodiesel blends in an engine. It is therefore important to take into account the crystal structures of the *n*-alkane hydrocarbons in the diesel fuel as when blended together with biodiesel, new crystals structures may form, and therefore any additives designed for petroleum diesel or biodiesel may not be selective for the new crystal structures that may form.

5.2 *n* – alkane structures

There are both full published structures and predicted lattice parameters for many even numbered *n*-alkanes in the carbon range C8 to C24. Lattice parameters for the known and predicted cells are shown in Table 5.1.

Table 5.1 Lattice parameters of *n*-alkane hydrocarbons of both known structures (KS) and known lattice parameters (KLP).

Name & Year Published	Unit cell & Space Group	*a* (Å)	*b* (Å)	*c* (Å)	*α* (°)	*β* (°)	*γ* (°)	Z
Octane 1967[79] (KS)	Triclinic *P*-1	4.220	4.790	11.020	94.70	84.30	105.80	1
Octane 1999[80] (KLP)	Triclinic *P*-1	4.123	4.686	10.974	85.063	83.72	75.10	1
Decane 1972[51] (KLP)	Triclinic *P*-1	4.200	4.750	13.570	93.40	81.80	105.60	1
Decane 2002[81] (KS)	Triclinic *P*-1	4.174	4.724	13.507	85.97	81.46	74.64	1
Dodecane 1972[51] (KLP)	Triclinic *P*-1	4.28	4.81	16.12	93.3	79.9	106.6	1
Tetradecane 1972[51] (KLP)	Triclinic *P*-1	4.29	4.82	18.58	93.1	78.8	107.0	1
Tetradecane 1994[34] (KLP)	Triclinic *P*-1	4.256	4.822	20.733	80.733	61.439	72.711	1
Hexadecane 1972[51] (KLP)	Triclinic *P*-1	4.29	4.81	20.87	91.9	80.5	106.9	1
Hexadecane 1994[34] (KLP)	Triclinic *P*-1	4.286	4.820	22.357	84.570	67.309	72.728	1
Octadecane 1972[53] (KS)	Triclinic *P*-1	4.285	4.82	24.898	85.15	67.8	72.7	1
Eicosane 1992[52] (KS)	Triclinic *P*-1	4.293	4.84	27.35	85.3	68.2	72.6	1
Docosane 1994[34] (KLP)	Triclinic *P*-1	4.288	4.828	29.552	86.424	70.755	72.199	1
Tetracosane 1992[82] (KLP)	Triclinic *P*-1	4.289	4.820	32.540	86.19	68.55	72.20	1
Tetracosane 1994[34] (KLP)	Triclinic *P*-1	4.265	4.810	33.725	88.618	76.250	72.675	1

In the range of petroleum diesel all the even *n*-alkanes have triclinic unit cells with the long axis being the *c*-axis and one molecule in the unit cell, at standard temperature and pressure.

Five *n*-alkanes will be studied in this chapter, and their interactions with the two methyl esters previously studied in chapters 3 and 4. Octadecane, eicosane and docosane, are hydrocarbons which are similar in length to methyl palmitate and methyl stearate; but dodecane and tetradecane are similar in length to the hydrocarbon chain in the methyl esters, and could possibly slot into the crystal structure. All five *n*-alkanes have the potential to interact with the esters through hydrogen-bonding and van der Waals interactions, either along the whole length of the molecule, or just with the hydrocarbon tail group. Only octadecane and eicosane have published structures, therefore structure solution was needed with the other three alkanes, to assist with phase determination in this work.

5.2.1 Dodecane

Norman[51] produced a set of lattice parameters (as shown in Table 5.1) from PXRD Debye-Scherrer diagrams, and indexed by hand using previously known structures to help predict the lattice parameters, due to the many possible reflections of a triclinic system. As there are no known structures only lattice parameters for dodecane, these lattice parameters were carried forward to see whether a structure could be solved.

5.2.1.1 Characterisation

A powder X-ray diffraction pattern of dodecane, Figure 5.1, was collected. As the melting point of dodecane is 263.4 K the liquid was syringed into a 1.0 mm special glass capillary and cooled to 233 K at 100 K to crystallise, using the Oxford cryostream attached to the lab diffractometer before the scan was started.
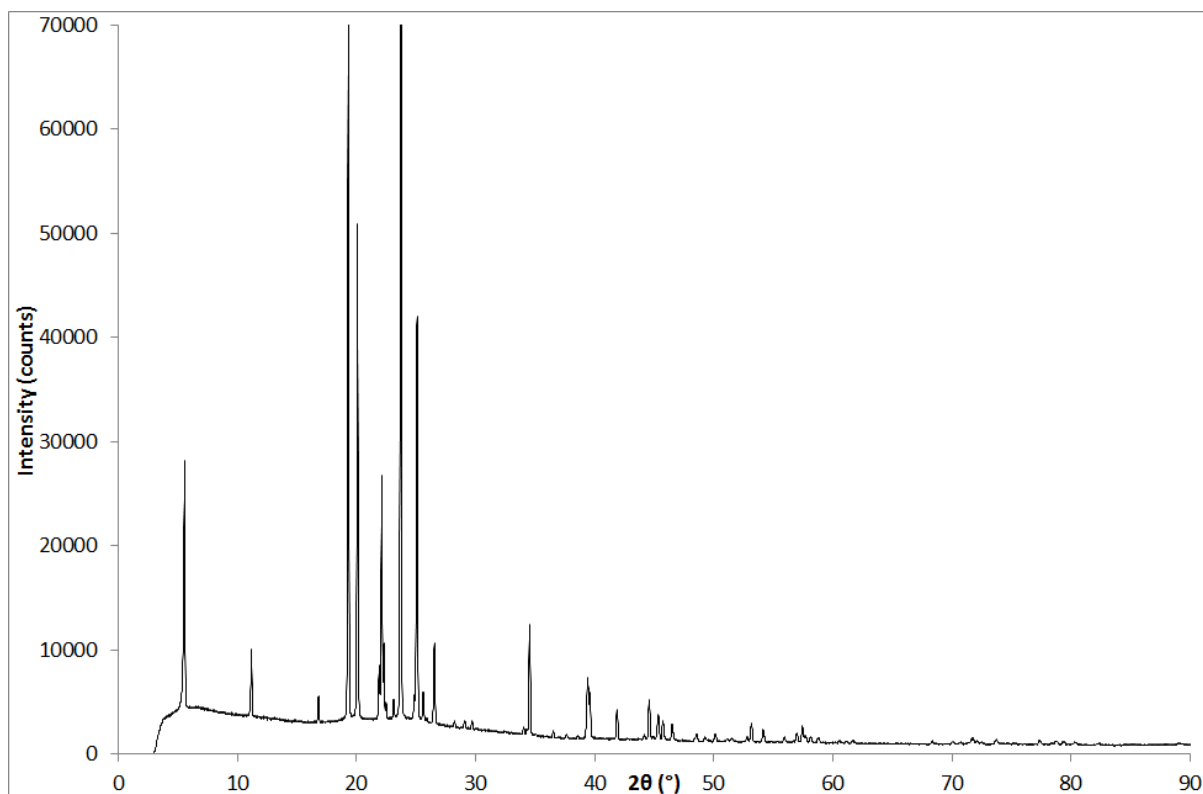
Figure 5.1 PXRD pattern of dodecane as bought crystallised at 233 K. λ = 1.54056 Å

5.2.1.2 Unit cell and space group determination

A Pawley fit shown in Figure 5.2 was run with the lattice parameters and P-1 space group reported by Norman[51] to see whether they fitted the PXRD pattern recorded.
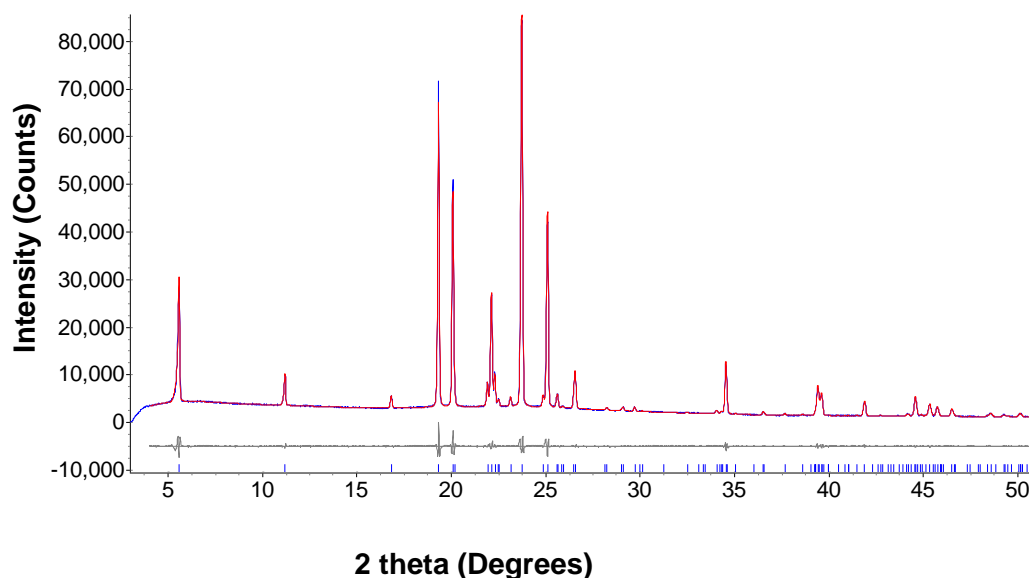
Figure 5.2 Observed (blue line) and calculated (red line) profiles for the Pawley fit of Dodecane as bought crystallised at 233 K, with the lattice parameters reported by Norman[51]. The bottom curve is the difference plot on the same intensity scale. (R_{wp} = 3.64, R_p = 2.61, χ = 1.88). The tick marks represent calculated peak positions. λ = 1.54056 Å

The Pawley fit produced a good fit to the predicted parameters which were refined to the values listed in Table 5.2, and were deemed suitable to be carried forward for structure solution.

Table 5.2 Refined lattice parameters for Dodecane as bought from Pawley fit.

Parameter	Value
Space group	*P*-1
a (Å)	4.23930(5)
b (Å)	4.78060(4)
c (Å)	16.0226(4)
α (°)	93.2601(22)
β (°)	80.0392(23)
γ (°)	106.3726(82)
Volume (Å^3)	306.848(9)

5.2.1.3 Model Building

As the structure of dodecane was likely to be similar to that of previously solved *n*-alkane structures, a dodecane model was created using the octane crystal structure solved by Mathisen[79]. The model structure was created by converting the atomic position of the octane structure into Cartesian coordinates, and calculating the position of the extra carbons required for a dodecane molecule. The Cartesian coordinates were then converted back into fractional coordinates, using the lattice parameters produced from the Pawley fit, with the model structure shown in Figure 5.3.
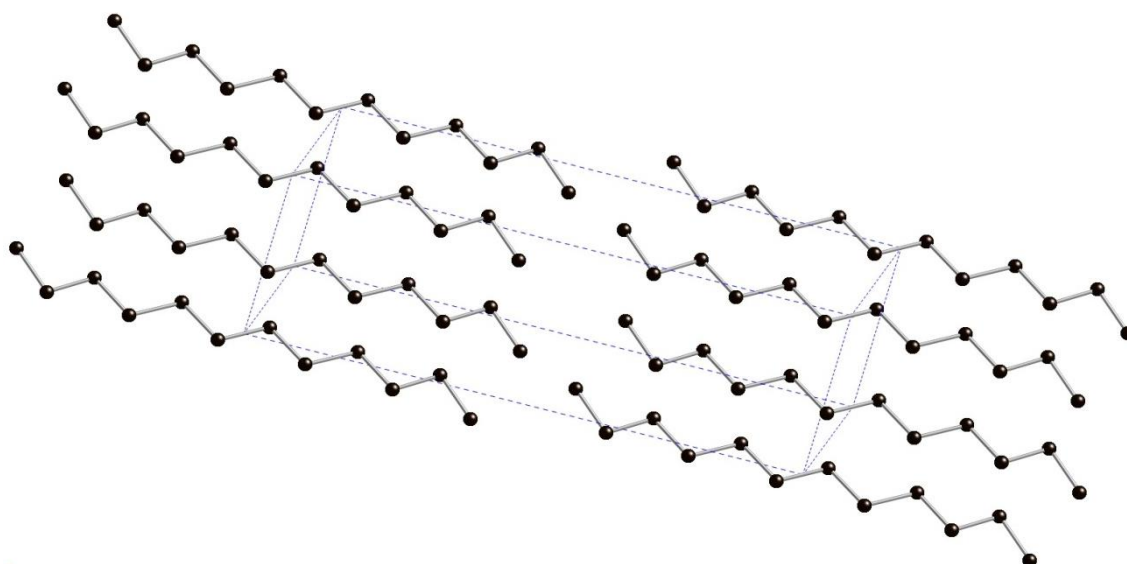
Figure 5.3 Dodecane structure starting model created from octane structure by Mathisen[79].

5.2.1.4 Structure solution and Rietveld Refinement

The dodecane carbon backbone model was refined using TOPAS[65], with bond distance and bond angle restrains applied to prevent the carbon backbone refining the carbons to unrealistic positions. Hydrogens were added in idealised positions to

the refined carbon backbone structure using Olex2[78], with a final refinement run using H-riding to keep the hydrogens in position. The final refinement and final crystal structure are shown in Figures 5.4 and 5.5 respectively.
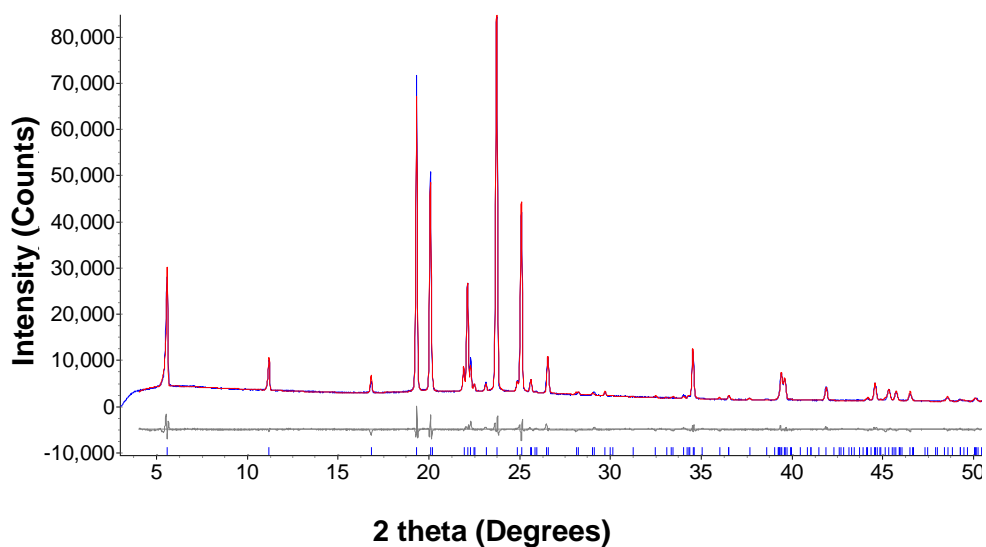
Figure 5.4 Observed (blue line) and calculated (red line) profiles for the final Rietveld refinement of the dodecane crystal structure solved from PXRD data. The bottom curve is the difference plot on the same intensity scale. (R_{wp} = 5.33, R_p = 3.77, χ = 2.63). The tick marks represent calculated peak positions. λ = 1.54056 Å
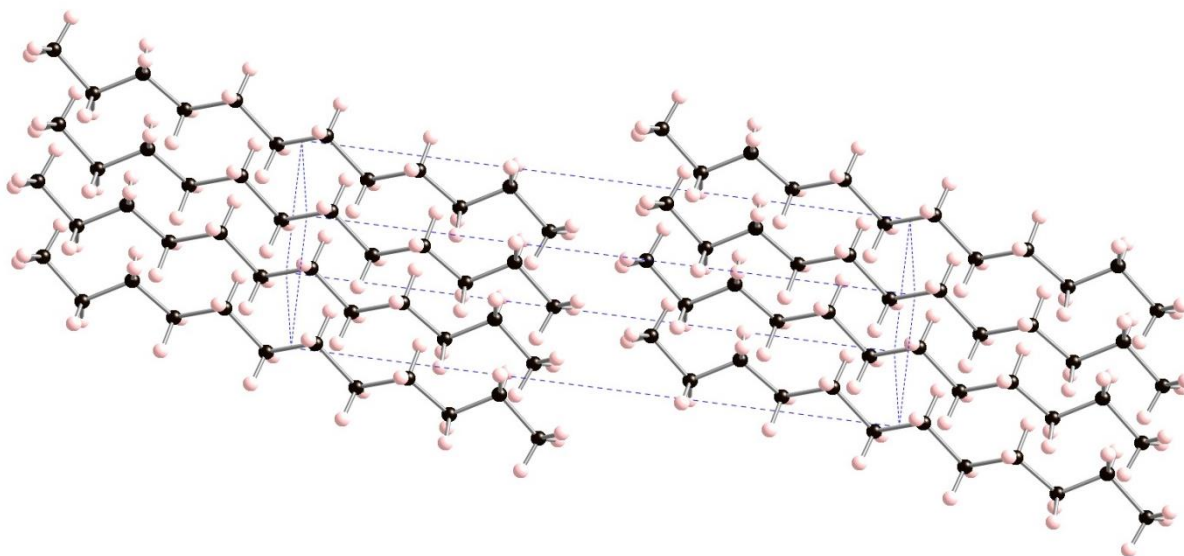
Figure 5.5 Refined crystal structure of dodecane.

201

Table 5.3 shows selected crystallographic data of the final refined dodecane structure with the atomic coordinates, carbon bond lengths and bond angles recorded in Tables 5.4, 5.5 and 5.6 respectively.

Table 5.3 Selected crystallographic data of dodecane structure.

Parameters	Data
Chemical Formula	$C_{12}H_{26}$
Formula Weight (g mol^{-1})	170.33
Crystal System	Triclinic
Space Group	*P*-1
a (Å)	4.23970(8)
b (Å)	4.78170(8)
c (Å)	16.0268(3)
α (°)	93.2618(19)
β (°)	80.0514(24)
γ (°)	106.3777(9)
Volume (Å^3)	307.032(10)
Temperature (K)	233 K
Z	1
λ (Å)	1.54056
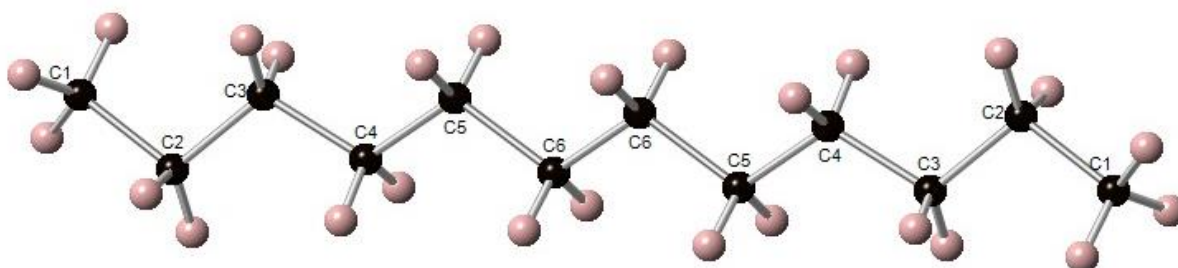
Figure 5.6 Labelled dodecane molecule.

Table 5.4 Atomic coordinates of the dodecane structure.

Atom number	x	y	z
C1	0.301(3)	0.259(3)	0.4116(6)
C2	0.137(2)	0.062(3)	0.3455(5)
C3	0.255(3)	0.218(3)	0.2645(5)
C4	0.171(3)	0.018(3)	0.1913(5)
C5	0.137(3)	0.155(2)	0.1113(5)
C6	0.018(3)	0.933(2)	0.0390(5)

Table 5.5 List of the dodecane structure carbon - carbon bond distances.

Bond	Distance (Å)
C1 – C2	1.544(14)
C2 – C3	1.469(13)
C3 – C4	1.483(13)
C4 – C5	1.518(14)
C5 – C6	1.576(13)
C6 – C6	1.486(20)

Table 5.6 List of the dodecane structure carbon bond angles.

Bond	Angle (°)
C1 – C2 – C3	107.3(9)
C2 – C3 – C4	110.9(10)
C3 – C4 – C5	116.1(11)
C4 – C5 – C6	115.2(9)
C5 – C6 – C6	115.2(11)

The dodecane crystal structure was successfully solved from PXRD lab data, with the final crystal structure shown in Figures 5.5 and 5.6 and the important crystallographic data shown in Tables 5.3, 5.4, 5.5 and 5.6. The structure is very

similar to that of previously known crystal structures such as octane, from which the dodecane initial model was created. As with octane one half of the atomic positions are generated by symmetry due to the triclinic *P*-1 Wyckoff positions.

5.2.2 Tetradecane

There are no known structures of tetradecane, however there are two sets of predicted lattice parameters by Roberts[34] and Norman[51] both produced from PXRD data. Both sets of parameters were brought forward to see which was most suitable for the PXRD data collected.

5.2.2.1 Characterisation

A powder X-ray diffraction pattern of tetradecane, Figure 5.7 was collected. As the melting point of dodecane is 278.5 K the liquid was syringed into a 1.0 mm special glass capillary, and cooled to 233 K at 100 K/hour to crystallise using the Oxford cryostream attached to the lab diffractometer before the scan was started.
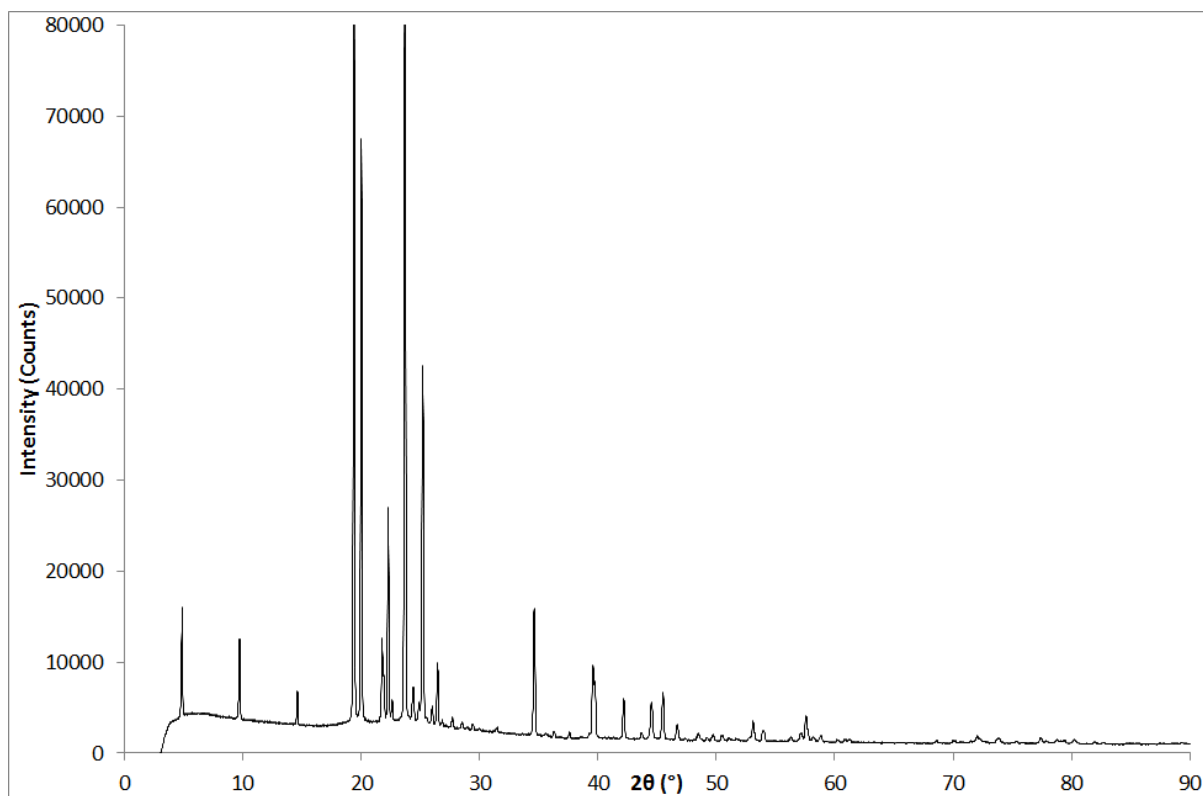
Figure 5.7 PXRD pattern of tetradecane as bought crystallised at 233 K. λ = 1.54056 Å

5.2.2.2 Unit cell and space group determination

Pawley fits were run with both sets of lattice parameters to see which set fit best with the recorded PXRD data.

2 theta (Degrees)
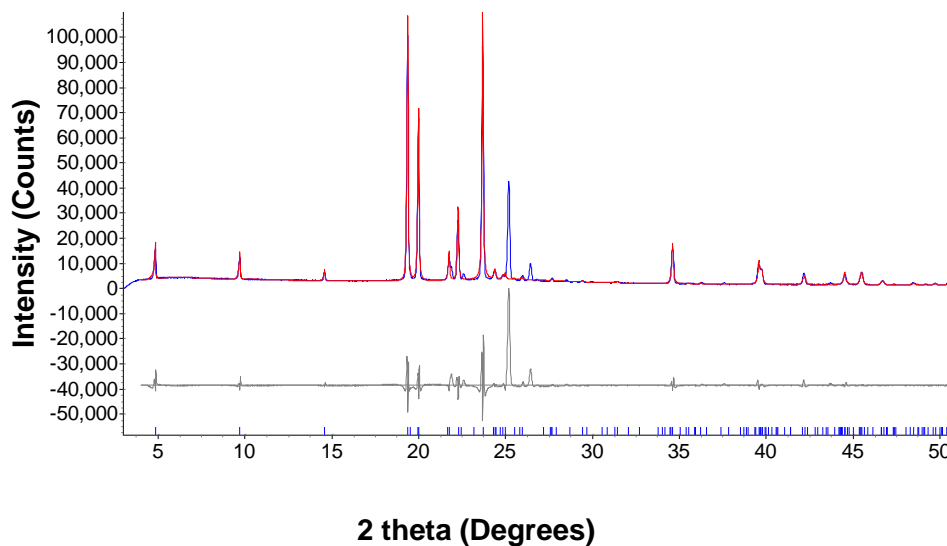
Figure 5.8 Observed (blue line) and calculated (red line) profiles for the Pawley fit of tetradecane as bought crystallised at 233 K, with the lattice parameters reported by Roberts[34]. The bottom curve is the difference plot on the same intensity scale. (R_{wp} = 18.94, R_p = 9.93, χ = 10.50). The tick marks represent calculated peak positions. λ = 1.54056 Å

2 theta (Degrees)
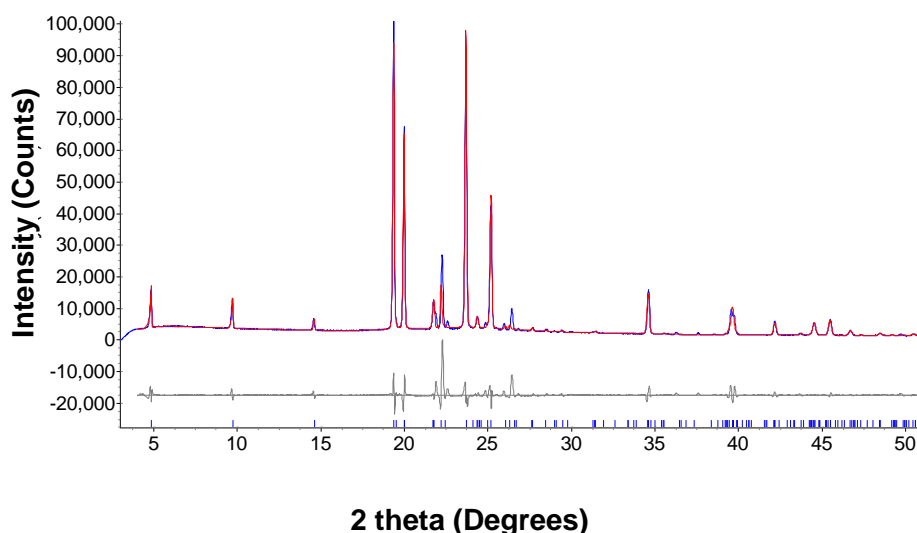
Figure 5.9 Observed (blue line) and calculated (red line) profiles for the Pawley fit of tetradecane as bought crystallised at 233 K, with the lattice parameters reported by Norman[51]. The bottom curve is the difference plot on the same intensity scale. (R_{wp} = 11.92, R_p = 6.42, χ = 6.62). The tick marks represent calculated peak positions. λ = 1.54056 Å

The Pawley fit using the lattice parameters reported by Roberts[34] in Figure 5.8, did not fit the recorded PXRD patterns as well as the Pawley fit using the lattice parameters reported by Norman[51], in Figure 5.9. Whilst neither set of lattice parameters fit all the PXRD peaks fully, (such as the peak at 25° 2θ in Figure 5.8, or the peak at 27° 2θ in Figure 5.9), the Pawley fit in Figure 5.9 has better refinement R values and fitted more of the peaks. The lattice parameters from the second Pawley fit changed slightly, when refined as shown in Table 5.7, and were deemed suitable for structure solution.

Table 5.7 Refined lattice parameters for tetradecane as bought from Pawley fit.

Parameter	Value
Space group	*P*-1
a (Å)	4.2655(3)
b (Å)	4.7877(2)
c (Å)	18.5622(22)
α (°)	93.379(16)
β (°)	78.0984(89)
γ (°)	107.0232(60)
Volume (Å^3)	354.671(53)

5.2.2.3 Model Building

As with dodecane, tetradecane was likely to have a similar structure as previously solved structures. A model structure was created from the 1967 octane crystal structure by Mathisen[79], with the same procedure used for dodecane. The model crystal structure is shown in Figure 5.10.
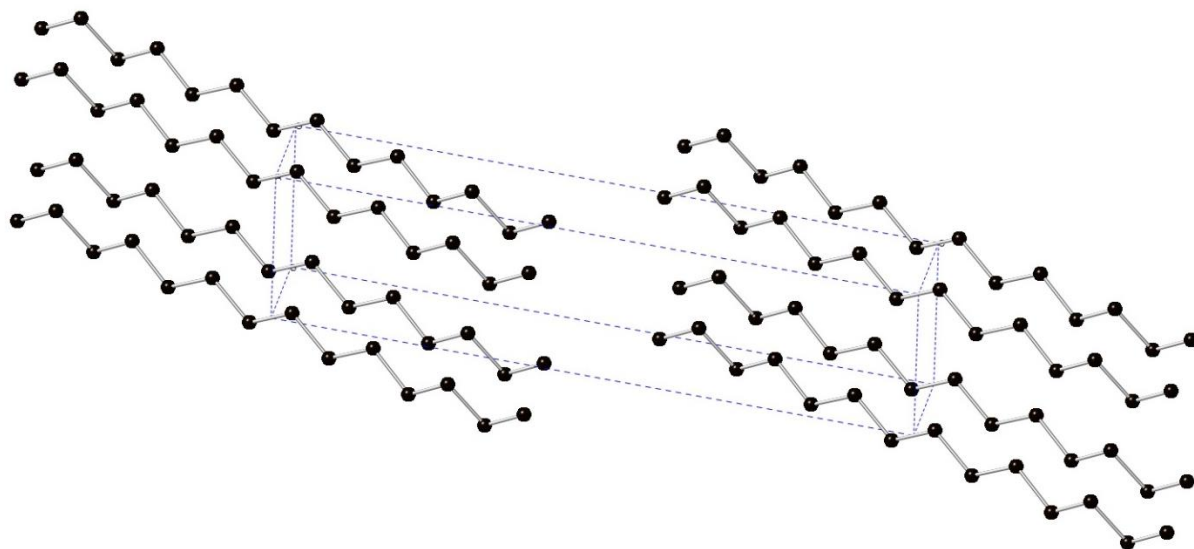
Figure 5.10 Tetradecane structure starting model created from octane structure by Mathisen[79].

5.2.2.4 Structure solution and Rietveld Refinement

As with dodecane, the tetradecane carbon backbone model was refined using TOPAS[65] with added bond distance and bond angle restraints applied to prevent the carbon atoms moving to unrealistic positions. Hydrogens were added in idealised positions to the refined carbon structure using Olex2[78], with a final Rietveld refinement run with H-riding. The final refinement and final crystal structure are shown in Figures 5.11 and 5.12 respectively.
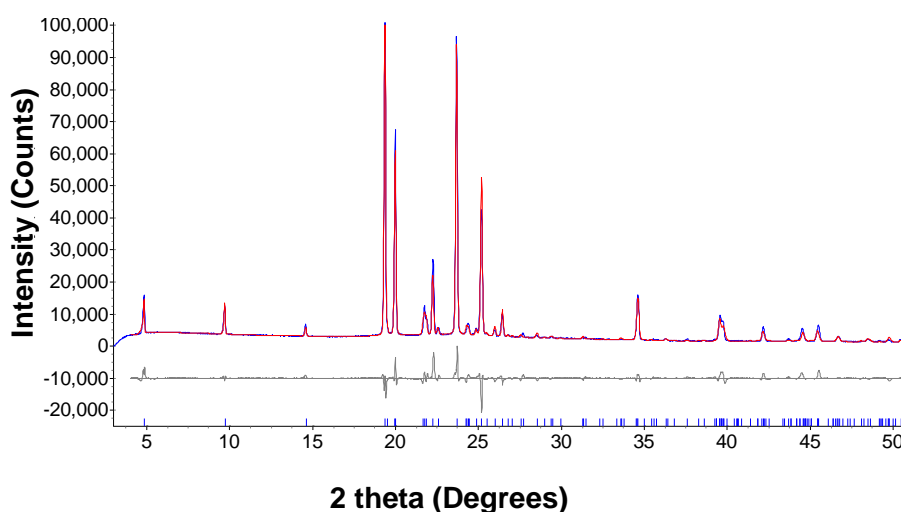
Figure 5.11 Observed (blue line) and calculated (red line) profiles for the final Rietveld refinement of the tetradecane crystal structure solved from PXRD data. The bottom curve is the difference plot on the same scale. (R_{wp} = 9.59, R_p = 6.09, χ = 5.03). The tick marks represent calculated peak positions. λ = 1.54056 Å
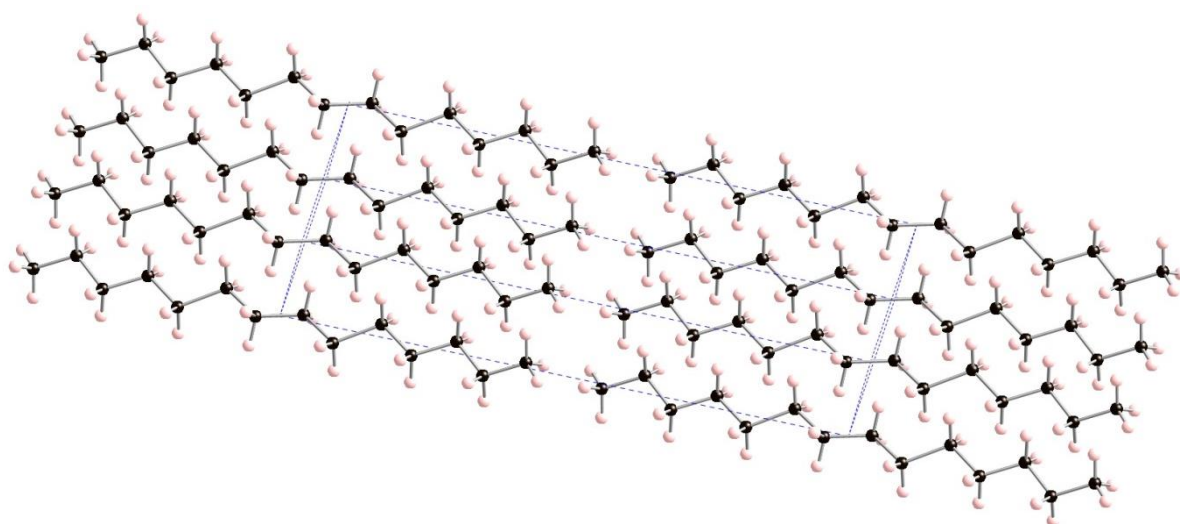
Figure 5.12 Refined crystal structure of tetradecane.

Table 5.8 shows selected crystallographic data of the final refined tetradecane structure with the atomic coordinates, bond lengths and bond angles recorded in Tables 5.9, 5.10 and 5.11 respectively.

Table 5.8 Selected crystallographic data of tetradecane structure.

Parameters	Data
Chemical Formula	$C_{14}H_{30}$
Formula Weight (g mol^{-1})	198.39
Crystal System	Triclinic
Space Group	P-1
a (Å)	4.2334(2)
b (Å)	4.7708(2)
c (Å)	18.5346(9)
α (°)	92.8760(36)
β (°)	78.7967(52)
γ (°)	106.3453(19)
Volume (Å^3)	352.364(29)
Temperature (K)	233 K
Z	1
λ (Å)	1.54056
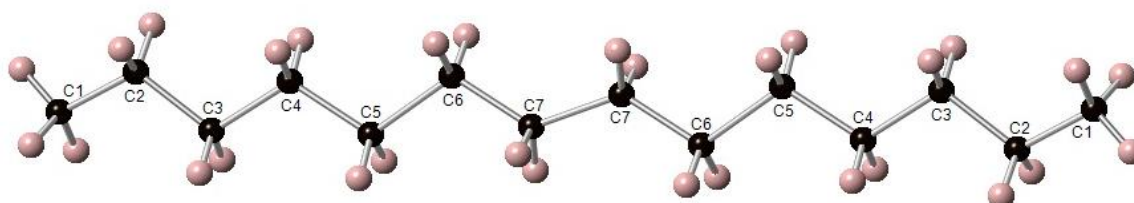
Figure 5.13 Labelled tetradecane molecule.

Table 5.9 Atomic coordinates of the tetradecane structure.

Atom number	x	y	z
C1	0.339(3)	0.149(3)	0.4325(6)
C2	0.258(3)	0.257(3)	0.3680(6)
C3	0.211(3)	0.038(3)	0.3063(6)
C4	0.181(3)	0.180(3)	0.2389(6)
C5	0.131(3)	-0.017(3)	0.1733(6)
C6	0.079(3)	0.152(3)	0.1027(5)
C7	-0.008(4)	-0.044(3)	0.0392(7)

Table 5.10 List of the tetradecane structure carbon - carbon bond distances.

Bond	Distance (Å)
C1 – C2	1.460(19)
C2 – C3	1.511(17)
C3 – C4	1.49(2)
C4 – C5	1.510(17)
C5 – C6	1.650(18)
C6 – C7	1.503(17)
C7 – C7	1.52(3)

Table 5.11 List of the tetradecane structure carbon bond angles.

Bond	Angle (°)
C1 – C2 – C3	114.6(12)
C2 – C3 – C4	110.7(13)
C3 – C4 – C5	115.7(12)
C4 – C5 – C6	112.7(11)
C5 – C6 – C7	114.5(11)
C6 – C7 – C7	128.0(15)

The tetradecane crystal structure was successfully solved from PXRD data with the final structure shown in Figures 5.12 and 5.13, with important crystallographic data in Tables 5.8, 5.9, 5.10 and 5.11. The structure is very similar to the previously solved dodecane structure, and the octane structure from which the original model was made.

5.2.3 Octadecane

There is one known structure of octadecane by Nyburg[53] from 1972 with the lattice parameters reported in Table 5.1. PXRD of octadecane as-bought was carried out to see whether the material that was used in this project had the same structure as this phase.

5.2.3.1 Characterisation of as bought phase

A PXRD pattern of octadecane as-bought shown in Figure 5.14 pattern B was collected at room temperature. Figure 5.14 compares the collected data with a simulated PXRD pattern (pattern A) of the Nyburg[53] octadecane structure.
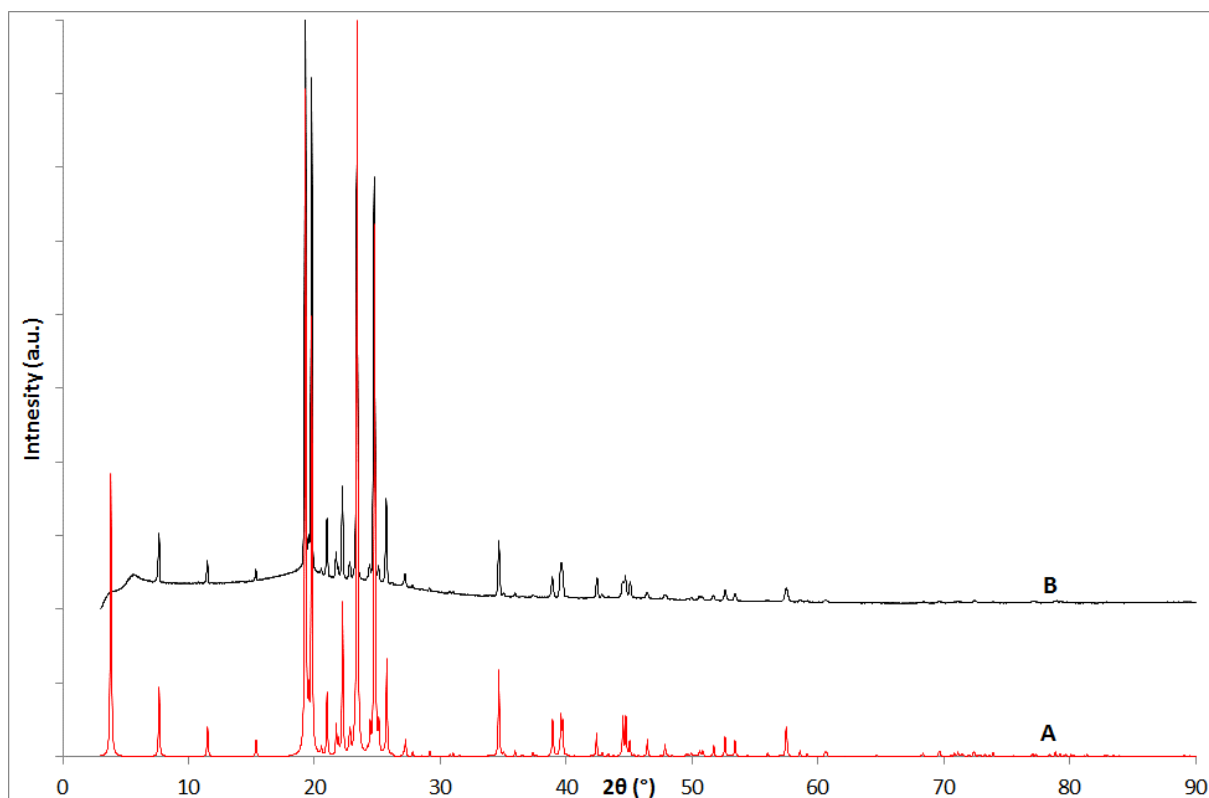
Figure 5.14 (A) Simulated PXRD pattern of octadecane 1972 (room temperature)[53], (B) PXRD pattern of octadecane as bought (room temperature). λ = 1.54056 Å

As the PXRD patterns of the simulated and recorded octadecane phase are the same, a Rietveld refinement was carried out as shown in Figure 5.15, with the refined lattice parameters recorded in Table 5.12 and atomic positions in appendix 5.1.1.

2 theta (Degrees)
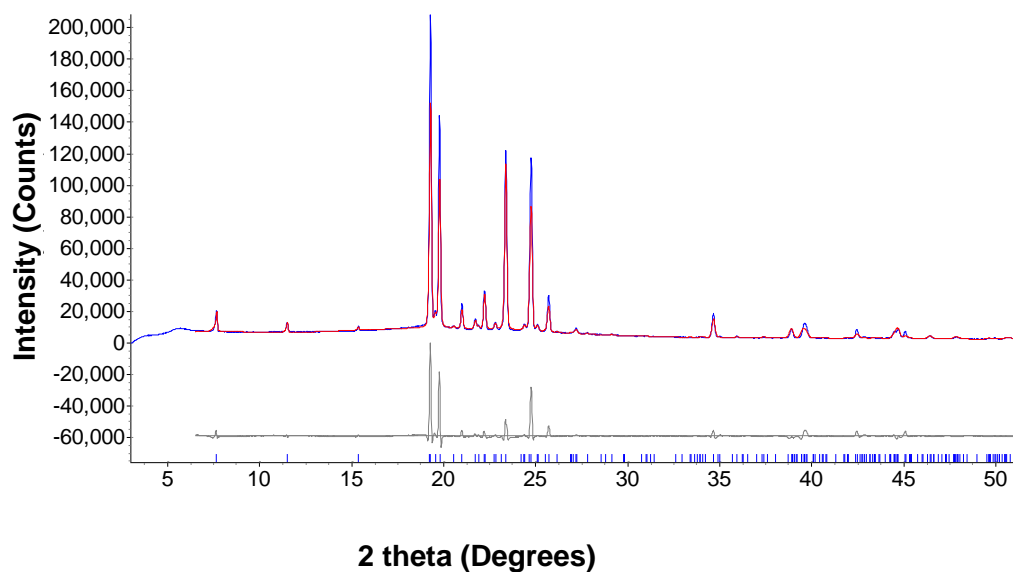
Figure 5.15 Observed (blue line) and calculated (red line) profiles for the Rietveld refinement of octadecane as bought with the 1972 octadecane structure by Nyburg[53]. The bottom curve is the difference plot on the same intensity scale. (R_{wp} = 10.95, R_p = 7.44, χ = 8.07). The tick marks represent calculated peak positions. λ = 1.54056 Å

Table 5.12 Refined lattice parameters of octadecane as bought.

Parameter	Value
Space group	*P*-1
***a* (Å)**	4.2881(4)
***b* (Å)**	4.8227(4)
***c* (Å)**	24.8935(38)
***α* (°)**	85.1139(85)
***β* (°)**	67.894(15)
***γ* (°)**	72.6000(31)
Volume (Å³)	454.92(11)

From both visual comparison and Rietveld refinement, the as-bought phase of octadecane has been confirmed as the same as the 1972 phase by Nyburg[53].

5.2.3.2 Recrystallisations of octadecane

As octadecane is likely to experience various solution and temperature environments as it's used combined in a fuel, various recrystallisations experiments were carried out to determine whether octadecane changes phase in certain conditions. The recrystallisation conditions are shown in Table 5.13 and the PXRD patterns in Figure 5.16.

Table 5.13 Conditions of octadecane recrystallisation experiments.

Pattern	Material	Experiment Conditions	Solvent	Heat	Cool	Rate
B	Octadecane	Variable Temperature	N/A	333 K	233 K	100 K/hr
C	Octadecane	Variable Temperature	N/A	353 K	298 K	N/A
D	Octadecane	Variable Temperature	N/A	353 K	255 K	N/A
E	Octadecane	Solvent Recrystallisation	Toluene	298 K	255 K	N/A
F	Octadecane	Solvent Recrystallisation	Kerosene	298 K	255 K	N/A
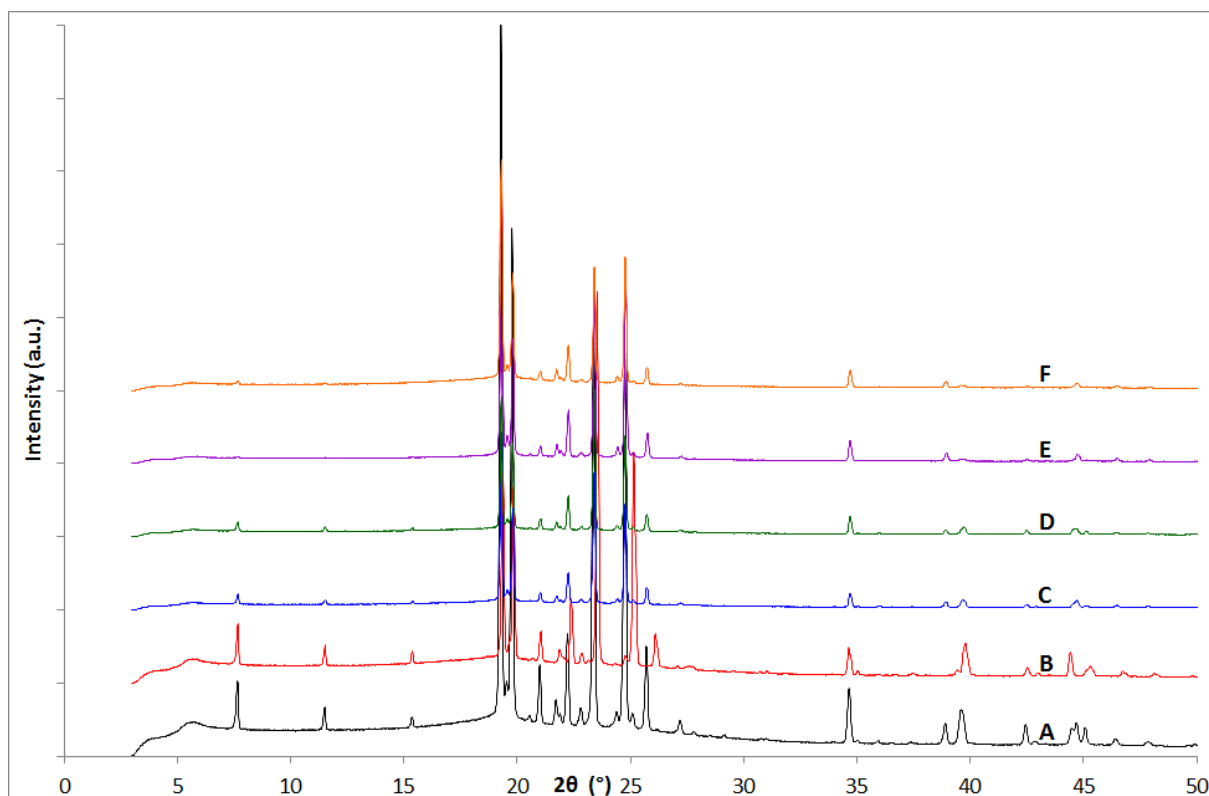
Figure 5.16 PXRD patterns of (A) octadecane as bought (room temperature), (B) the product from variable temperature recrystallisation experiment 333 K to 233 K at 100 K/hr, (C) the product from recrystallisation from the melt experiment in a Teflon pot and cooled at room temperature, (D) the product from recrystallisation from the melt experiment in a Teflon pot and cooled in the freezer (room temperature), (E) the product from recrystallisation in Toluene in the freezer (room temperature), (F) the product from recrystallisation in Kerosene in the freezer (room temperature). λ = 1.54056 Å

All recrystallisations of octadecane produced the same octadecane 1972 phase. The variable temperature recrystallisation in situ on the D5000 (pattern B), is slightly shifted to higher 2θ values as the scan was recorded at 233 K. From the melt recrystallisations not carried out using the cryostream, and the solvent recrystallisations, all have relatively lower intensity low angle peaks in comparison to patterns A and B. There are few changes in the intensity of several small peaks

around 40° 2θ, which may be due to preferred orientation as the hydrocarbon *n*-alkanes form flat platelet crystals, which are prone to orientation in one direction on crystallisation and packing. Overall these experiments show that octadecane doesn't change phase, when exposed to certain conditions used for recrystallisations in this project. Full Rietveld refinements for these recrystallisations can be found in appendix 5.2.

5.2.4 Eicosane

There is one known phase of eicosane that was published by Nyburg[52] in 1992 from single crystal data. A PXRD of eicosane as bought was run to see whether it was the same as the known phase.

5.2.4.1 Characterisation of Eicosane as bought phase

A PXRD pattern of eicosane as-bought was collected at room temperature, shown in Figure 5.17 pattern B. Figure 5.17 compares the data collected with a simulated PXRD pattern (pattern A) of the 1992 eicosane structure by Nyburg[52].
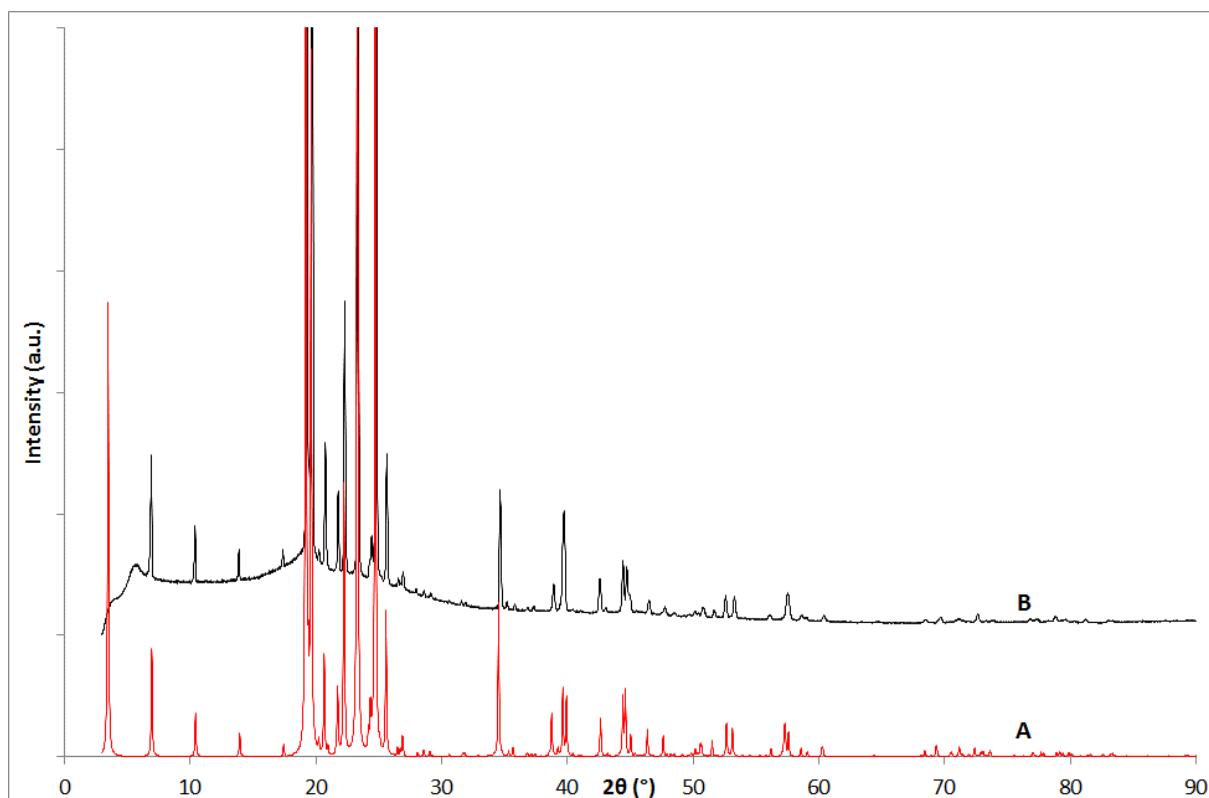
Figure 5.17 (A) Simulated PXRD pattern of eicosane 1992 (room temperature)[52], (B) PXRD pattern of eicosane as bought (room temperature). λ = 1.54056 Å

As the PXRD pattern of eicosane was visually the same as the known phase a Rietveld refinement shown in Figure 5.18 was run with the refined lattice parameters shown in Table 5.14 and atomic positions in appendix 5.1.2.

2 theta (Degrees)
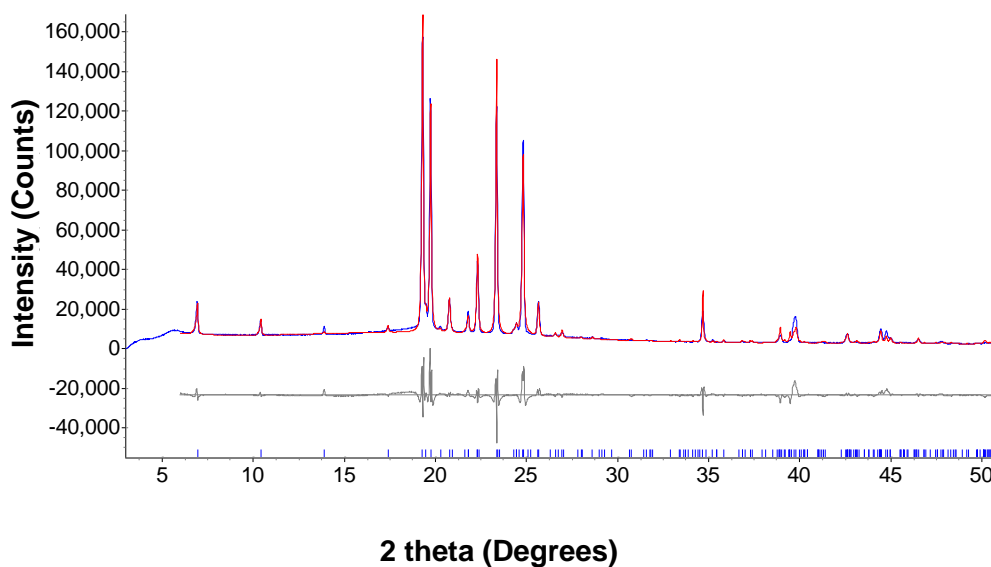
Figure 5.18 Observed (blue line) and calculated (red line) profiles for the Rietveld refinement of eicosane as bought with the 1992 eicosane structure by Nyburg[52]. The bottom curve is the difference plot on the same intensity scale. (R_{wp} = 10.92, R_p = 7.59, χ = 7.81). The tick marks represent calculated peak positions. λ = 1.54056 Å

Table 5.14 Refined lattice parameters of eicosane as bought phase.

Parameter	Value
Space group	*P*-1
a (Å)	4.2812(2)
b (Å)	4.8200(2)
c (Å)	27.4247(14)
α (°)	85.5721(41)
β (°)	68.3305(59)
γ (°)	72.6455(22)
Volume (Å^3)	501.638(47)

From both visual comparison and Rietveld refinement the eicosane as-bought phase has been confirmed as the same as Nyburg's[52] 1992 eicosane structure.

5.2.4.2 Recrystallisations of eicosane

As with octadecane, eicosane is likely to be exposed to various solution and temperature environments, so various experiments were carried out to determine whether eicosane changes phase under certain conditions. The recrystallisation conditions are shown in Table 5.15 and the PXRD patterns in Figure 5.19.

Table 5.15 Conditions of eicosane recrystallisation experiments.

Pattern	Material	Experiment Conditions	Solvent	Heat	Cool	Rate
B	Eicosane	Variable Temperature	N/A	333 K	233 K	100 K/hr
C	Eicosane	Variable Temperature	N/A	353 K	298 K	N/A
D	Eicosane	Variable Temperature	N/A	353 K	255 K	N/A
E	Eicosane	Solvent Recrystallisation	Toluene	298 K	255 K	N/A
F	Eicosane	Solvent Recrystallisation	Kerosene	298 K	255 K	N/A
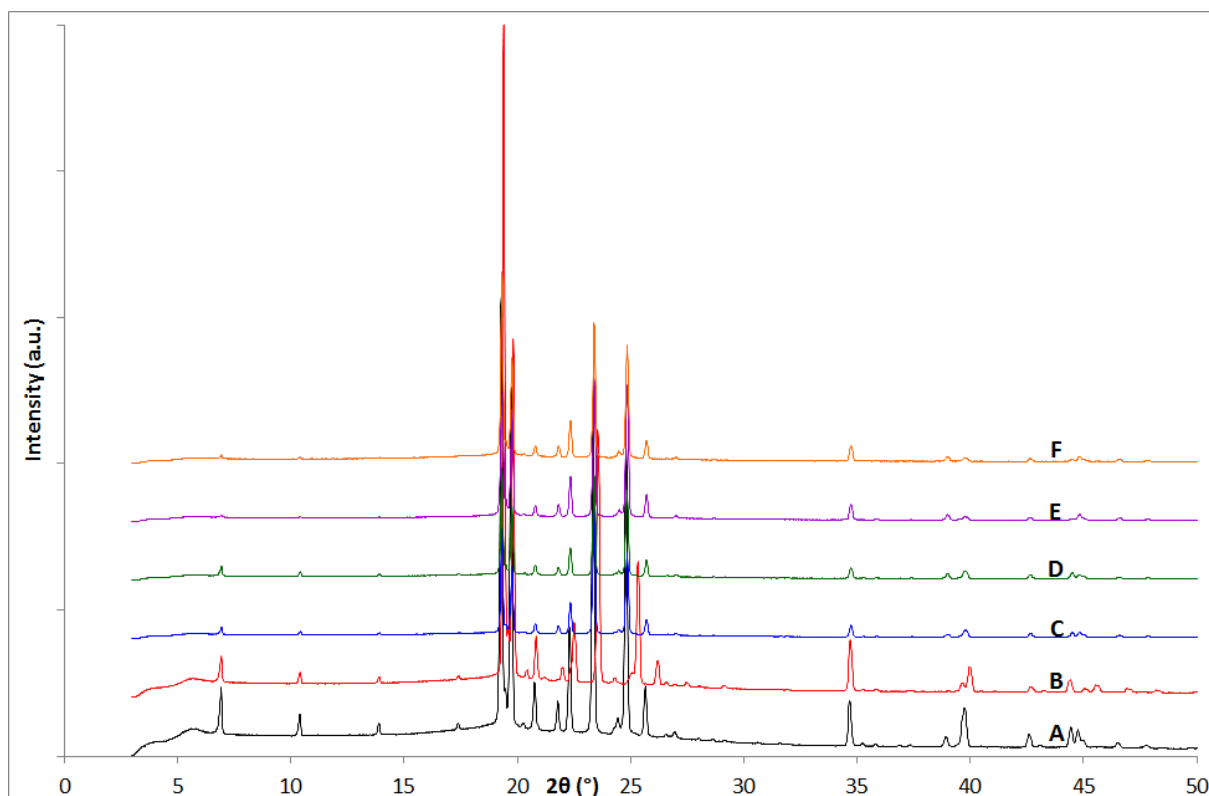
Figure 5.19 PXRD patterns of (A) eicosane as bought (room temperature), (B) the product from variable temperature recrystallisation experiment 333 K to 233 K at 100 K/hr, (C) the product from the melt experiment in a Teflon pot and cool at room temperature, (D) the product from recrystallisation from the melt experiment in a Teflon pot and cooled in the freezer (room temperature), (E) the product from recrystallisation in Toluene in the freezer (room temperature), (F) the product from recrystallisation in Kerosene in the freezer (room temperature). λ = 1.54056 Å

As with octadecane, eicosane recrystallises back into the 1992 eicosane structure on recrystallisation under all conditions tested. Pattern B is slightly shifted to higher 2θ due to the scan being recorded at 233 K rather than room temperature. As with octadecane, the variable temperature recrystallisations not carried out on the cryostream and the solvent recrystallisations, all have much lower intensity of low angle peaks and a change in intensity of a few small peaks around 40 ° 2θ, which may be due to preferred orientation of the crystals. Overall the recrystallisation

experiments carried out show that eicosane does not change phase when exposed to certain conditions. Full Rietveld refinements can be found in appendix 5.3.

5.2.5 Docosane

There are no known structures of docosane however there is a set of determined lattice parameters, from synchrotron PXRD data by Roberts[34] published in 1994. This set of lattice parameters were brought forward to see whether they would fit with the PXRD data collected.

5.2.5.1 Characterisation

A PXRD pattern of docosane as-bought, shown in Figure 5.20, was collected at room temperature.
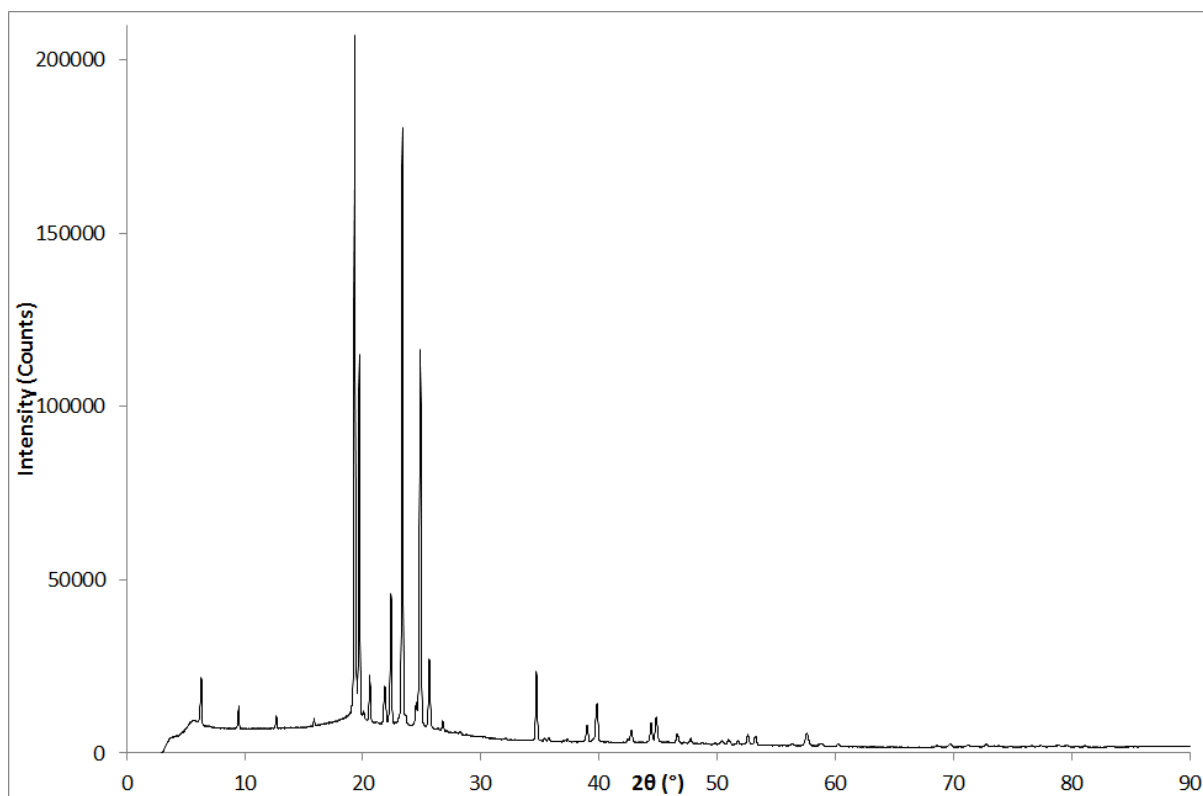
Figure 5.20 PXRD pattern of docosane as bought recorded at room temperature. λ = 1.54056 Å

5.2.5.2 Unit cell and space group determination

A Pawley fit, shown in Figure 5.21, was run with the lattice parameters predicted by Roberts[34] to determine whether they are suitable for structure solution with the refined parameters shown in Table 5.16.

2 theta (Degrees)
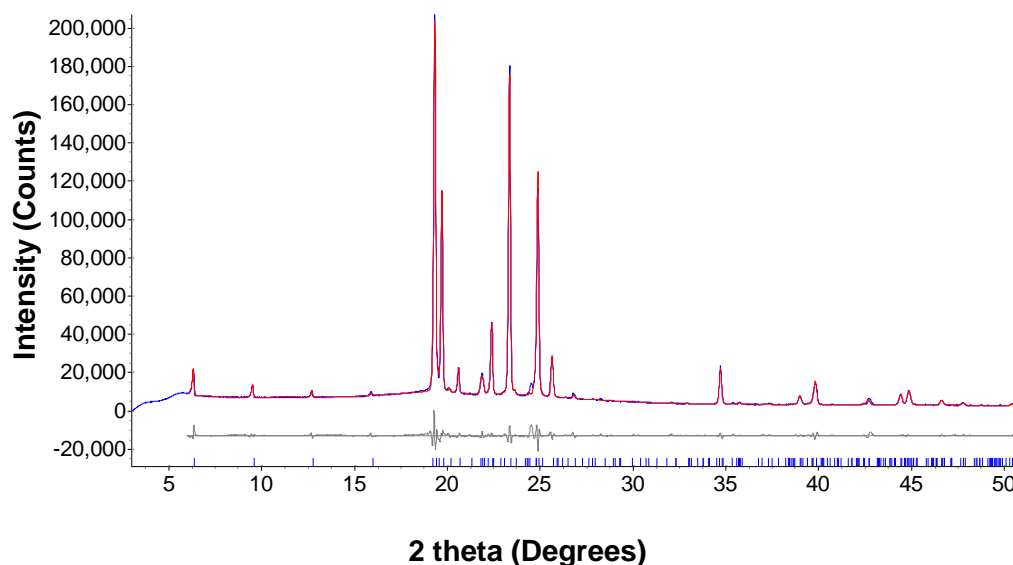
Figure 5.21 Observed (blue line) and calculated (red line) profiles for the Pawley fit of docosane as-bought with the lattice parameters predicted by Roberts[34]. The bottom curve is the difference plot on the same intensity scale. (R_{wp} = 5.63, R_p = 3.65, χ = 5.06). The tick marks represent calculated peak positions. λ = 1.54056 Å

Table 5.16 Refined lattice parameters from Pawley fit of docosane as-bought.

Parameter	Value
Space group	*P*-1
a (Å)	4.2973(5)
b (Å)	4.8245(5)
c (Å)	29.3355(46)
α (°)	85.9449(76)
β (°)	70.714(13)
γ (°)	71.5200(23)
Volume (Å^3)	544.07(13)

As can be seen from the Pawley fit, the predicted lattice parameters fit the docosane as-bought scan, but were refined slightly to the values reported in Table 5.16. These refined parameters were taken forward for structural solution.

5.2.5.3 Model Building

To begin structure solution, a model structure shown in Figure 5.22 was created from the 1992 eicosane structure, by converting the eicosane atomic positions into Cartesian coordinates. Calculation of the position of one extra carbon on both ends of the hydrocarbon chain was done, before converting the coordinates back into fractional coordinates with the refined docosane lattice parameters.
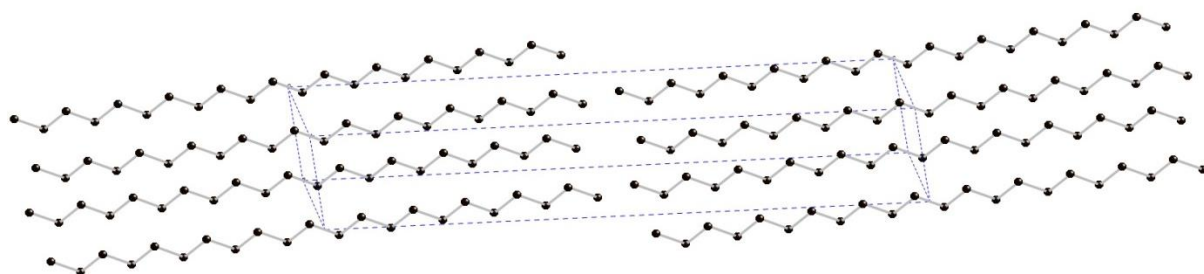
Figure 5.22 Docosane starting structure model created from the eicosane 1992 structure by Nyburg[52].

5.2.5.4 Structure solution and Rietveld Refinement

The docosane carbon backbone starting model was refined using TOPAS[65], using bond distance and bond angles restraints to prevent the atoms refining to unrealistic positions. Hydrogens were added using Olex2[78] and a final Rietveld refinement, shown in Figure 5.23, was run with H-riding to produce the final docosane structure, Figure 5.24.
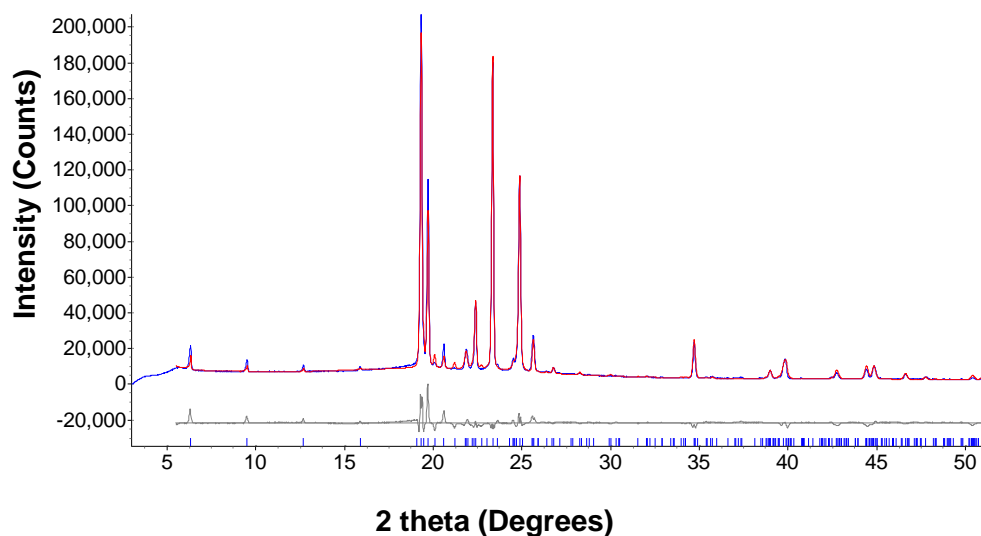
Figure 5.23 Observed (blue line) and calculated (red line) profiles for the final Rietveld refinement of the docosane crystal structure solved from PXRD data. The bottom curve is the difference plot on the same intensity scale. (R_{wp} = 9.36, R_p = 6.38, χ = 6.88). The tick marks represent calculated peak positions. λ = 1.54056 Å
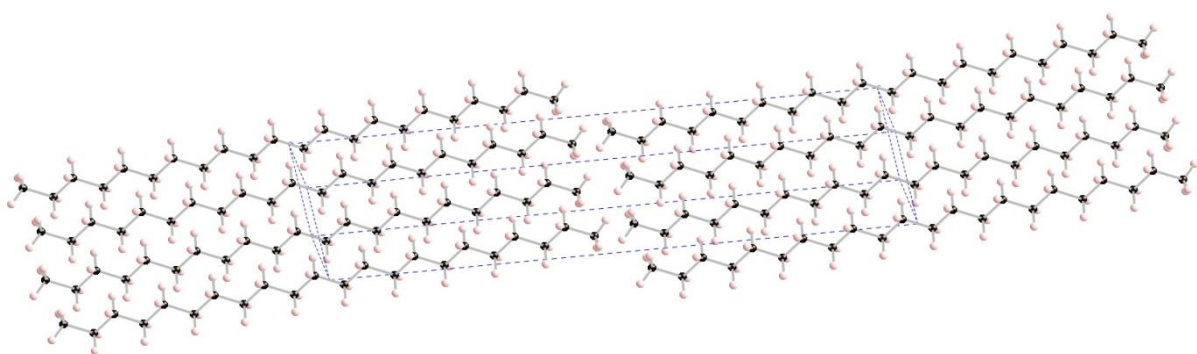
Figure 5.24 Refined crystal structure of docosane.

Table 5.17 shows selected crystallographic data of the final refined docosane structure with the atomic coordinates, bond lengths and bond angles recorded in Tables 5.18, 5.19 and 5.20 respectively.

Table 5.17 Selective crystallographic data of docosane structure.

Parameters	Data
Chemical Formula	$C_{22}H_{46}$
Formula Weight (g mol^{-1})	310.60
Crystal System	Triclinic
Space Group	*P*-1
a (Å)	4.2731(2)
b (Å)	4.8134(3)
c (Å)	29.9497(16)
α (°)	85.9522(51)
β (°)	68.6670(75)
γ (°)	72.7071(21)
Volume (Å^3)	547.371(60)
Temperature (K)	298 K
Z	1
λ (Å)	1.54056
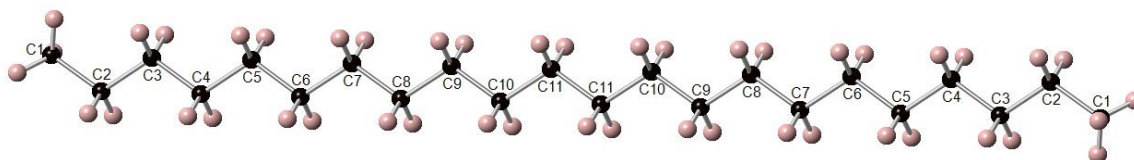
Figure 5.25 Labelled docosane molecule.

Table 5.18 Atomic coordinates of the docosane structure.

Atom number	x	y	z
C1	0.159(5)	0.121(6)	0.5393(8)
C2	0.094(7)	0.278(7)	0.5864(8)
C3	0.135(8)	0.079(8)	0.6268(9)
C4	0.070(8)	0.238(8)	0.6735(9)
C5	0.111(8)	0.037(8)	0.7144(9)
C6	0.046(8)	0.198(8)	0.7610(10)
C7	0.084(8)	0	0.8019(10)
C8	0.018(8)	0.157(8)	0.8486(9)
C9	0.056(9)	0.961(9)	0.8892(10)
C10	0.992(7)	0.118(9)	0.9359(7)
C11	0.031(11)	0.921(10)	0.9767(10)

Table 5.19 List of the docosane structure carbon - carbon bond distances.

Bond	Distance (Å)
C1 – C2	1.54(4)
C2 – C3	1.52(4)
C3 – C4	1.54(5)
C4 – C5	1.54(4)
C5 – C6	1.54(5)
C6 – C7	1.52(4)
C7 – C8	1.53(5)
C8 – C9	1.51(4)
C9 – C10	1.53(5)
C10 – C11	1.52(5)
C11 – C11	1.54(7)

Table 5.20 List of the docosane structure carbon bond angles.

Bond	Angle (°)
C1 – C2 – C3	115(3)
C2 – C3 – C4	114(3)
C3 – C4 – C5	114(3)
C4 – C5 – C6	114(3)
C5 – C6 – C7	114(3)
C6 – C7 – C8	115(3)
C7 – C8 – C9	115(3)
C8 – C9 – C10	115(3)
C9 – C10 – C11	115(3)
C10 – C11 – C11	115(5)

The docosane crystal structure was thus successfully solved using lattice parameters predicted by Roberts[34] and a model crystal structure created from the eicosane 1992 structure by Nyburg[52].

5.2.5.5 Docosane recrystallisation experiments

As with octadecane and eicosane various recrystallisation experiments were carried out with docosane, to see whether it would change phase under certain temperature and solvent conditions. The recrystallisation conditions are shown in Table 5.21 with the PXRD patterns shown in Figure 5.26.

Table 5.21 Conditions of docosane recrystallisation experiments.

Pattern	Material	Experiment Conditions	Solvent	Heat	Cool	Rate
B	Docosane	Variable Temperature	N/A	333 K	233 K	100 K/hr
C	Docosane	Variable Temperature	N/A	353 K	298 K	N/A
D	Docosane	Variable Temperature	N/A	353 K	255 K	N/A
E	Docosane	Solvent Recrystallisation	Toluene	298 K	255 K	N/A
F	Docosane	Solvent Recrystallisation	Kerosene	298 K	255 K	N/A
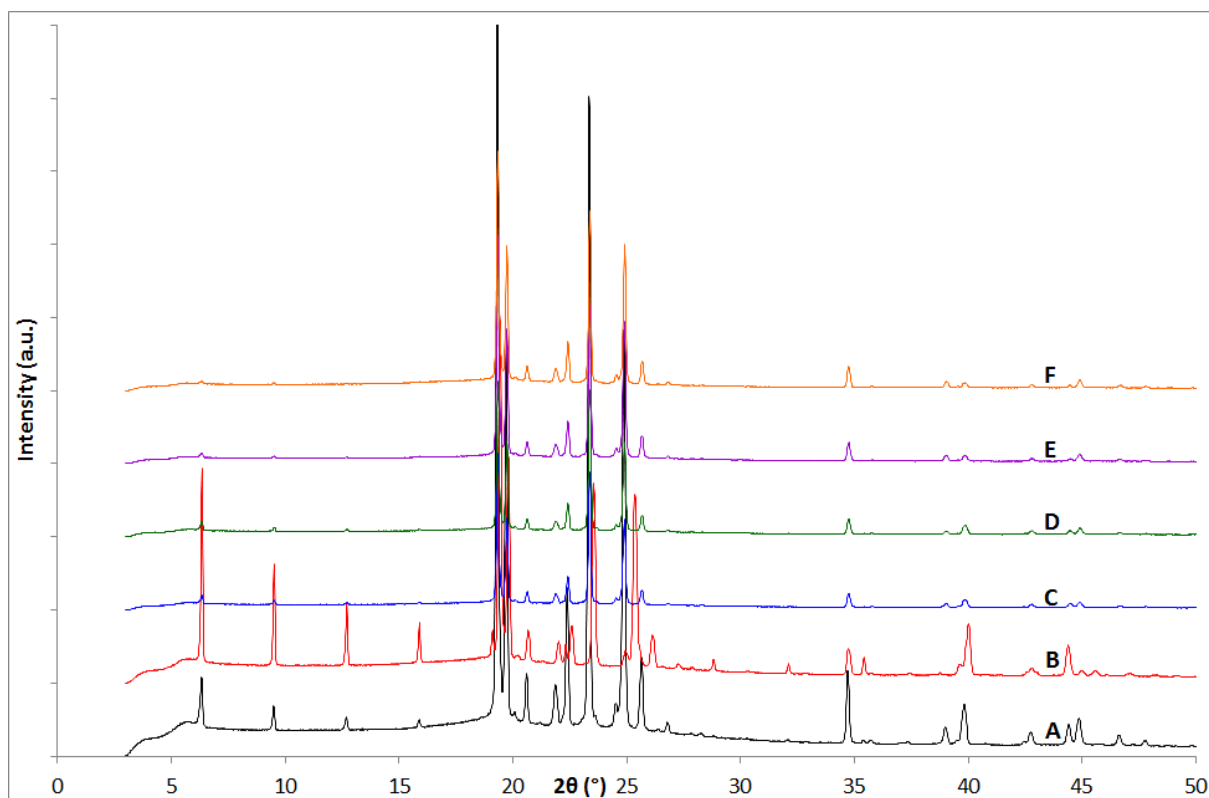
Figure 5.26 PXRD patterns of (A) docosane as-bought (room temperature), (B) the product from variable temperature recrystallisation experiment 333 K to 233 K at 100 K/hr, (C) the product from the melt experiment in a Teflon pot and cool at room temperature, (D) the product from recrystallisation from the melt experiment in a Teflon pot and cooled in the freezer (room temperature), (E) the product from recrystallisation in Toluene in the freezer (room temperature), (F) the product from recrystallisation in Kerosene in the freezer (room temperature). λ = 1.54056 Å

Figure 5.26 shows that docosane does not recrystallise into a different phase on exposure to certain temperature and solvent conditions. All recrystallisations produced the same phase as the as-bought solved docosane structure. Pattern B was shifted slightly to higher 2θ due to the pattern being recorded at 233 K. As with octadecane and eicosane the low angle peaks are reduced in intensity for the recrystallisations not carried on the cryostream, which may be due to preferred orientation. Full Rietveld refinements can be found in appendix 5.4.

5.3 Studies of Methyl Ester / Hydrocarbon mixes

With the increasing amount of biodiesel being blended in with petroleum diesel, there is potential for the *n*-alkane hydrocarbons to interact or react with the methyl esters of the biodiesel. As the mixture of petroleum diesel and biodiesel is likely to undergo a variety of heating and cooling conditions on preparation of the fuel and the use of the fuel, several sets of experimental methods, detailed below, were designed to see whether any new crystal structures would form. Toluene and kerosene solvents were also used to mimic the solution mixes of the other compounds found in diesel (smaller hydrocarbons and aromatic compounds) which are liquid at temperatures likely to be experienced.

Methods 1 and 2

1:1 stoichiometric amounts of methyl ester and hydrocarbon were dissolved in either toluene (method 1) or kerosene (method 2) at room temperature and placed in a fridge overnight at 274 K, and then placed in a freezer at 255 K until crystals formed in the solution. Once crystals had formed the solution was filtered in the freezer and the crystals collected, a PXRD pattern of the products was collected, with the powder packed into a 1.1 mm Kapton capillary, and the scan recorded at room temperature.

Methods 3 and 4

1:1 stoichiometric amounts of methyl ester and hydrocarbon were dissolved in either toluene (method 3) or kerosene (method 4) at room temperature. The solutions were injected into 1.0 mm special glass capillaries, before being mounted on the

diffractometer with an Oxford Cryostream attached. Before data collection the samples were heated to 333 K and held at temperature for 5 minutes to allow for complete melting of the compounds above their melting point. The solutions were then cooled to 233 K at 100 K/hr, held at temperature for 5 minutes and then data collected.

Methods 5 and 6

1:1 stoichiometric amounts of methyl ester and hydrocarbon were placed in a Teflon pot, and placed in an oven at 353 K until the compounds had melted. The melted compounds were mixed together, and then allowed to cool and crystallise at either room temperature (method 5) or in a freezer at 255 K (method 6). PXRD patterns of the products were collected, with the powder packed into a 1.1 mm Kapton capillary, and the scan recorded at room temperature.

Method 7

1:1 stoichiometric amounts of methyl ester and hydrocarbon were ground together and then packed into a 1.1 mm Kapton tube capillary, before being mounted on the diffractometer with an Oxford Cryostream attached. Before data collection the samples were heated to 333 K and held at temperature for 5 minutes to allow for complete melting of the compounds above their melting point. The solutions were then cooled to 233 K at 100 K/hr, dwelled for 5 minutes and then data collection commenced.

Methods 8 and 9

1:1 stoichiometric amounts of methyl ester and hydrocarbon were placed in a Teflon pot, and placed in an oven at 353 K until the compounds had melted. The melted compounds were mixed together, and then allowed to cool and crystallise at room temperature. The recrystallised compounds were then dissolved in either toluene (method 8) or kerosene (method 9) and then placed in a freezer at 255 K until crystals formed in the solution. Once crystals had formed, the solution was filtered in the freezer and the crystals collected. A PXRD pattern of the products was collected, with the powder packed into a 1.1 mm Kapton capillary, and the scan recorded at room temperature.

Methods 10 and 11

1:1 stoichiometric amounts of methyl ester and hydrocarbon were dissolved in toluene at room temperature. The solutions were injected into 1.0 mm special glass capillaries before being mounted on the diffractometer with an Oxford Cryostream attached. Before data collection the samples were heated to 333 K and dwelled for 5 minutes to allow for complete melting of the compounds above their melting point. The solutions were then cooled either to 190 K at 100 K/hr (method 10) or to 190 K at 360 K/hr (method 11), held at temperature for 5 minutes and then data collected.

Method 12

1:1 stoichiometric amounts of methyl ester and hydrocarbon were dissolved in toluene at room temperature. The solutions were injected into 1.0 mm special glass capillaries before being mounted on the diffractometer with an Oxford Cryostream

attached. Before data collection the samples were heated to 333 K and dwelled for 5 minutes to allow for complete melting of the compounds above their melting point. The solutions were then cooled to 250 K at 100 K/hr, held at temperature for 5 minutes and then data was collected. After the first scan had been completed, the solutions were cooled to 225 K at 100 K/hr, held at temperature for 5 minutes and then data collection commenced. Again, after data collection the solutions were cooled to 190 K at 100 K/hr, held at temperature for 5 minutes and then a final data collection scan was run.

5.4 Methyl Stearate : Dodecane

5.4.1 Characterisation

Experiments of mixtures of methyl stearate and dodecane were carried out using the experimental methods noted in Table 5.22 and detailed in section 5.3, with the PXRD patterns of products from these experiments shown in Figures 5.27 and 5.28.

Table 5.22 Conditions of methyl stearate : dodecane cocrystallisation experiments.

Pattern / Figure	Material	Experimental Methods
D / 5.27	Methyl Stearate : Dodecane	3
E / 5.27	Methyl Stearate : Dodecane	4
F / 5.27	Methyl Stearate : Dodecane	10
G / 5.27	Methyl Stearate : Dodecane	11
D / 5.28	Methyl Stearate : Dodecane	12 at 190 K
E / 5.28	Methyl Stearate : Dodecane	12 at 225 K
F / 5.28	Methyl Stearate : Dodecane	12 at 250 K
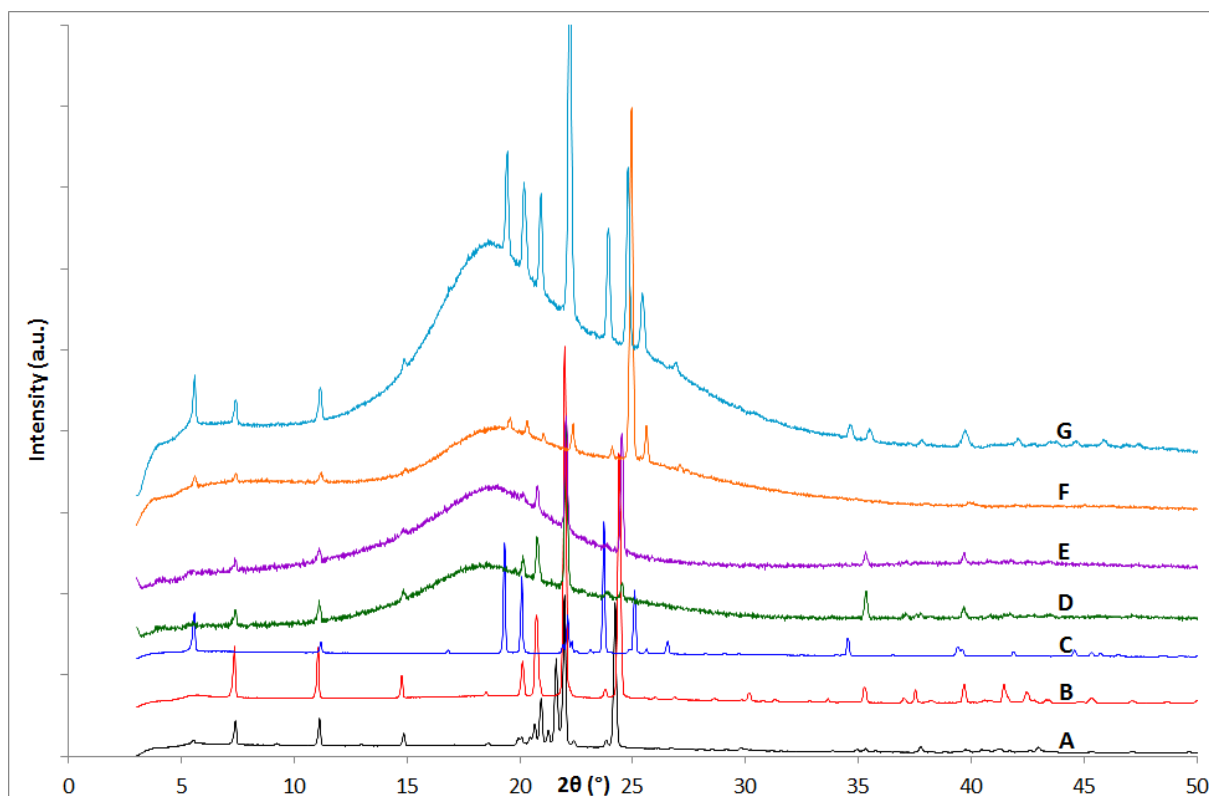
Figure 5.27 PXRD patterns of (A) MS-*Pnab* (ro*om* temperature), (B) MS-*C*2 (233 K), (C) dodecane as bought (233 K), (D) the product from experimental method 3, (E) the product from experimental method 4, (F) the product from experimental method 10, (G) the product from experimental method 11. *λ* = 1.54056 Å

From Figure 5.27 it can be seen that the PXRD pattern patterns D and E are the same as that of the MS-*C*2 phase, and patterns F and G show a mixture of the MS-*C*2 phase and dodecane. The patterns D and E are recorded at 233 K, whereas patterns F and G were recorded at 190 K which suggests that dodecane only crystallises out at temperatures lower than 233 K with the concentrations used in this project, and it remains dissolved in the toluene or kerosene solutions with only the MS-*C*2 phase crystallising out at 233 K. All scans show the MS-*C*2 phase rather than the MS-*Pnab* phase as the solution was taken above the melting point of all compounds present.
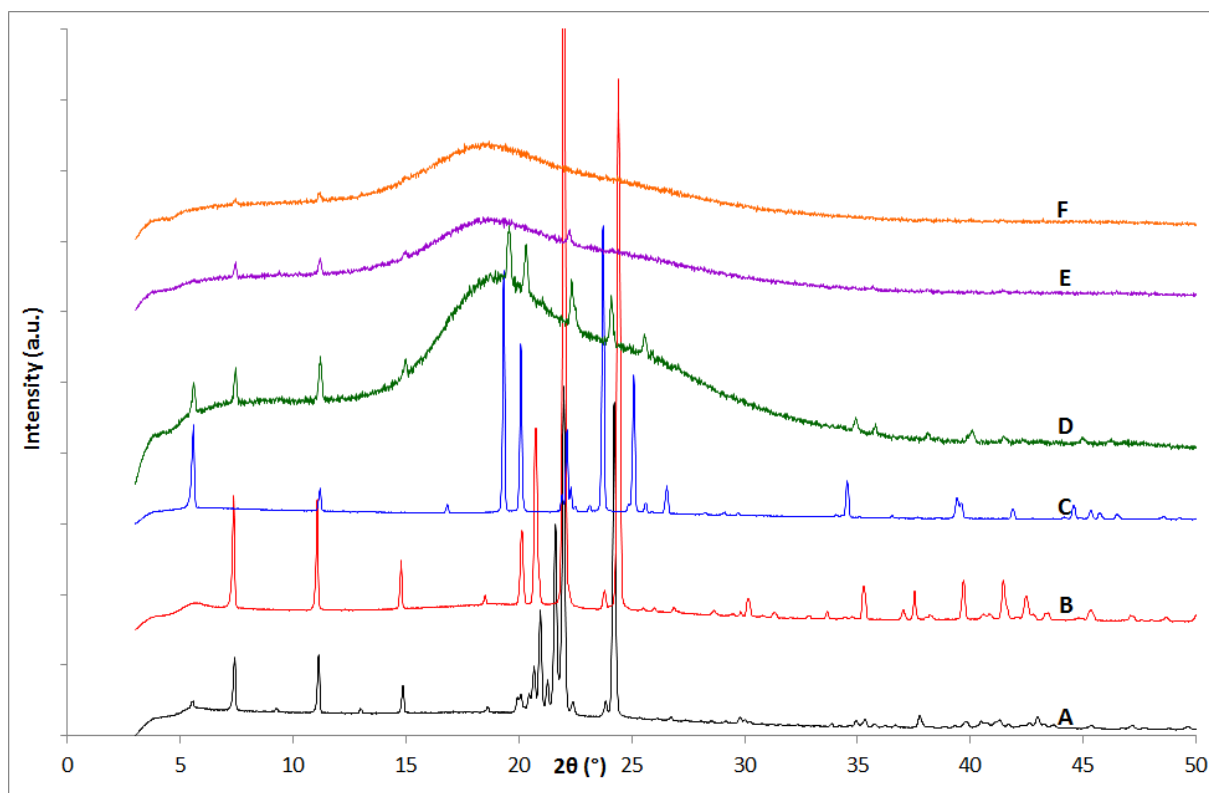
Figure 5.28 PXRD patterns of (A) MS-*Pnab* (ro*om* temperature), (B) MS-*C*2 (233 K), (C) dodecane as bought (233 K), (D) the product from experimental method 12 (190 K), (E) the product from experimental method 12 (225 K), (F) the product from experimental method 12 (250 K). *λ* = 1.54056 Å

As can be seen from Figure 5.28, on stepwise cooling to 190 K (patterns F to E to D) crystallisation increases with the scan at 190 K showing a mixture of MS-*C*2 and dodecane, the same as Figure 5.27 patterns F and G. This shows consistency of a mixed material crystallising out at 190 K in toluene.

All scans for methyl stearate and dodecane and those shown throughout this chapter, often feature a high background and an amorphous bump in the PXRD scans due to the crystallisation process being carried out in solution of either toluene or kerosene which are still liquid at the measurement temperatures. Peaks in

patterns that are recorded at lower temperatures than room temperature, are also slightly shifted to higher 2θ due to thermal contraction of the unit cells.

Rietveld refinements of the products formed between methyl stearate and dodecane can be found in appendix 5.5.

5.5 Methyl Stearate : Tetradecane

5.5.1 Characterisation

Experiments of mixtures of methyl stearate and tetradecane were carried out using the experimental methods noted in Table 5.23 and detailed in section 5.3, with the results of these experiments shown in Figures 5.29 and 5.30.

Table 5.23 Conditions of methyl stearate : tetradecane cocrystallisation experiments.

Pattern / Figure	Material	Experimental Methods
D / 5.29	Methyl Stearate : Tetradecane	3
E / 5.29	Methyl Stearate : Tetradecane	4
F / 5.29	Methyl Stearate : Tetradecane	10
G / 5.29	Methyl Stearate : Tetradecane	11
D / 5.30	Methyl Stearate : Tetradecane	12 at 190 K
E / 5.30	Methyl Stearate : Tetradecane	12 at 225 K
F / 5.30	Methyl Stearate : Tetradecane	12 at 250 K

Figure 5.29 PXRD patterns of (A) MS-*Pnab* (ro*om* temperature), (B) MS-*C*2 (233 K), (C) tetradecane as bought (233 K), (D) the product from experimental method 3, (E) the product from experimental method 4, (F) the product from experimental method 10, (G) the product from experimental method 11. *λ* = 1.54056 Å

As can be shown from this comparison patterns D and E show only the MS-*C*2 phase which is the same as observed in the cocrystallisations with dodecane under the same conditions, and likewise patterns F and G show a mix of the MS-*C*2 phase and tetradecane at the lower crystallisation temperature of 190 K.
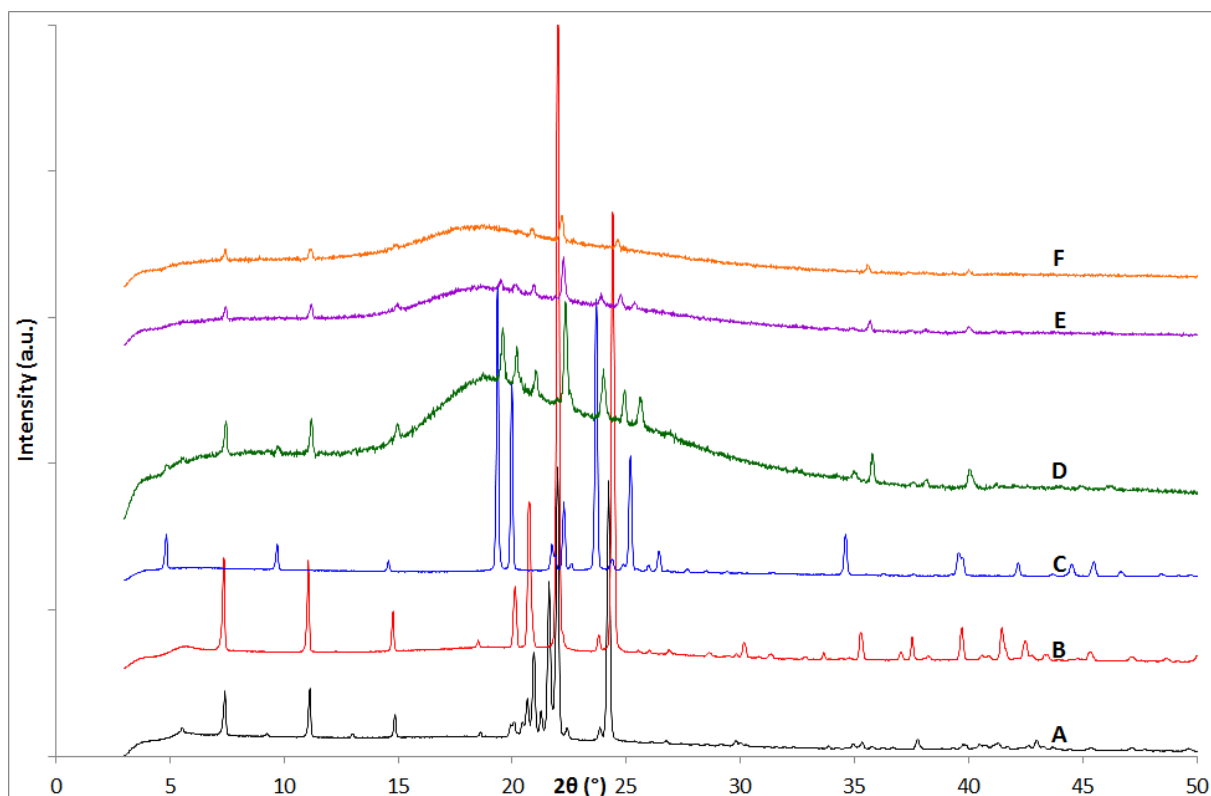
Figure 5.30 PXRD patterns of (A) MS-*Pnab* (ro*om* temperature), (B) MS-*C*2 (233 K), (C) tetradecane as bought (233 K), (D) the product from experimental method 12 (190 K), (E) the product from experimental method 12 (225 K), (F) the product from experimental method 12 (250 K). *λ* = 1.54056 Å

As with the methyl stearate and dodecane stepwise variable temperature experiment, Figure 5.30 shows increasing crystallisation on lowering the temperature to 190 K and a mix of the MS-*C*2 and tetradecane phases. This data shows that no combined phases of methyl stearate and dodecane or tetradecane were formed under these conditions.

Rietveld refinements of the products formed between methyl stearate and tetradecane can be found in appendix 5.6.

5.6 Methyl Stearate : Octadecane

5.6.1 Characterisation

Experiments of mixtures of methyl stearate and octadecane were carried out using the experimental methods noted in Table 5.24 and detailed in section 5.3, with the results of these experiments shown in Figures 5.31, 5.32, 5.33 and 5.34.

Table 5.24 Conditions of methyl stearate : octadecane cocrystallisation experiments.

Pattern / Figure	Material	Experimental Methods
D / 5.31	Methyl Stearate : Octadecane	1
E / 5.31	Methyl Stearate : Octadecane	2
F / 5.31	Methyl Stearate : Octadecane	3
G / 5.31	Methyl Stearate : Octadecane	4
D / 5.32	Methyl Stearate : Octadecane	5
E / 5.32	Methyl Stearate : Octadecane	6
F / 5.32	Methyl Stearate : Octadecane	7
D / 5.33	Methyl Stearate : Octadecane	8
E / 5.33	Methyl Stearate : Octadecane	10
F / 5.33	Methyl Stearate : Octadecane	11
D / 5.34	Methyl Stearate : Octadecane	12 at 190 K
E / 5.34	Methyl Stearate : Octadecane	12 at 225 K
F / 5.34	Methyl Stearate : Octadecane	12 at 250 K

Figure 5.31 PXRD patterns of (A) MS-*Pnab* (ro*om* temperature), (B) MS-*C*2 (233 K), (C) octadecane as bought (room temperature K), (D) the product from experimental method 1, (E) the product from experimental method 2, (F) the product from experimental method 3, (G) the product from experimental method 4. *λ* = 1.54056 Å

Pattern D in Figure 5.31 shows a potentially new phase which has some peaks which do line up with both methyl stearate and octadecane; however there is a large amorphous area in the PXRD pattern where the concentration of peaks are, making it difficult for structural solution to be possible. It does however look similar to that of a rotator phase reported for eicosane by Di Giambattista[83], therefore the scan could show a mixture of methyl stearate and an octadecane rotator phase. Hydrocarbons of a variety of lengths have been known to exist in up to five rotator phases several degrees below their melting points (melting point of octadecane is

299 K, which is close to room temperature), however these phases are often difficult to study by PXRD.

Unlike the solvent cocrystallisation experiment in toluene, pattern E in kerosene shows the MS-*C*2 phase, with no octadecane present and remaining in solution on filtration of the crystallised material. Whilst this experiment was not intentionally known to have melted, the methyl stearate recrystallised into the MS-*C*2 phase rather than the MS-*Pnab* phase. Methyl stearate has a melting point of 310 K and therefore the solution may have been exposed to temperatures high enough to melt it on filtration and handling of the sample on packing into the capillary.

Pattern F also shows that only methyl stearate crystallised out into the MS-*C*2 phase. However, under these conditions the solution was heated to 333 K which is enough to melt the ester. Under the same condition but in kerosene pattern G shows a mix of the MS-*C*2 and octadecane phases crystallised out.

Figure 5.32 PXRD patterns of (A) MS-*Pnab* (ro*om* temperature), (B) MS-*C*2 (233 K), (C) octadecane as bought (room temperature K), (D) the product from experimental method 5, (E) the product from experimental method 6, (F) the product from experimental method 7. *λ* = 1.54056 Å

All three PXRD patterns in Figure 5.32 show similar potential rotator phases to that of the new phase produced in Figure 5.31 pattern D, however the low angle peaks in Figure 5.32 pattern F appear slightly more intense than in the three other potential rotator phases. The difference in peak intensities could suggest a different rotator phase forming that interacts with the X-ray beam more strongly, or preferred orientation in the sample.
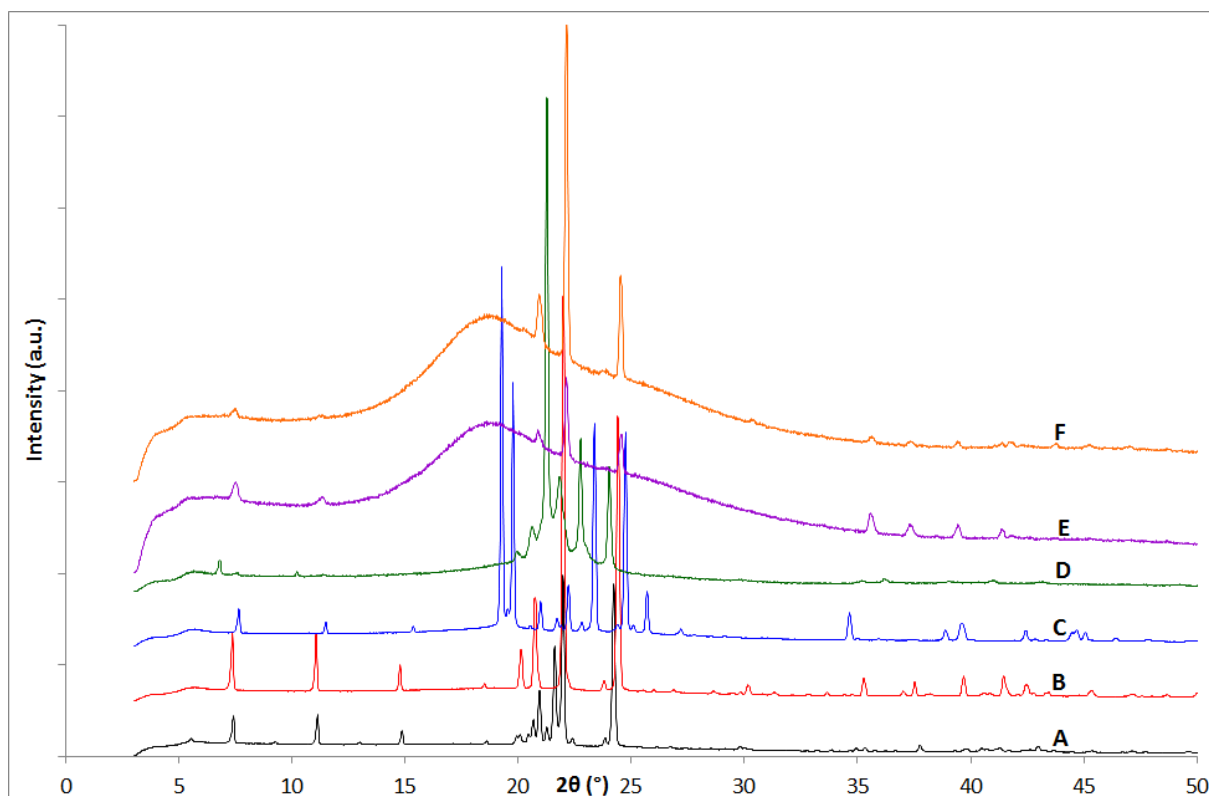
Figure 5.33 PXRD patterns of (A) MS-*Pnab* (ro*om* temperature), (B) MS-*C*2 (233 K), (C) octadecane as bought (room temperature K), (D) the product from experimental method 8, (E) the product from experimental method 10, (F) the product from experimental method 11. *λ* = 1.54056 Å

Pattern D in Figure 5.33 shows the same potential rotator phase as shown previously with methyl stearate and octadecane, and shows that solvent recrystallisation doesn't appear to make any difference to the phase formed as this is the same material used as Figure 5.32 pattern D but after recrystallisation with toluene.

Both cocrystallisation experiments to 190 K, patterns E and F, show that only the MS-*C*2 phase crystallised out and octadecane remained dissolved in the toluene solution.
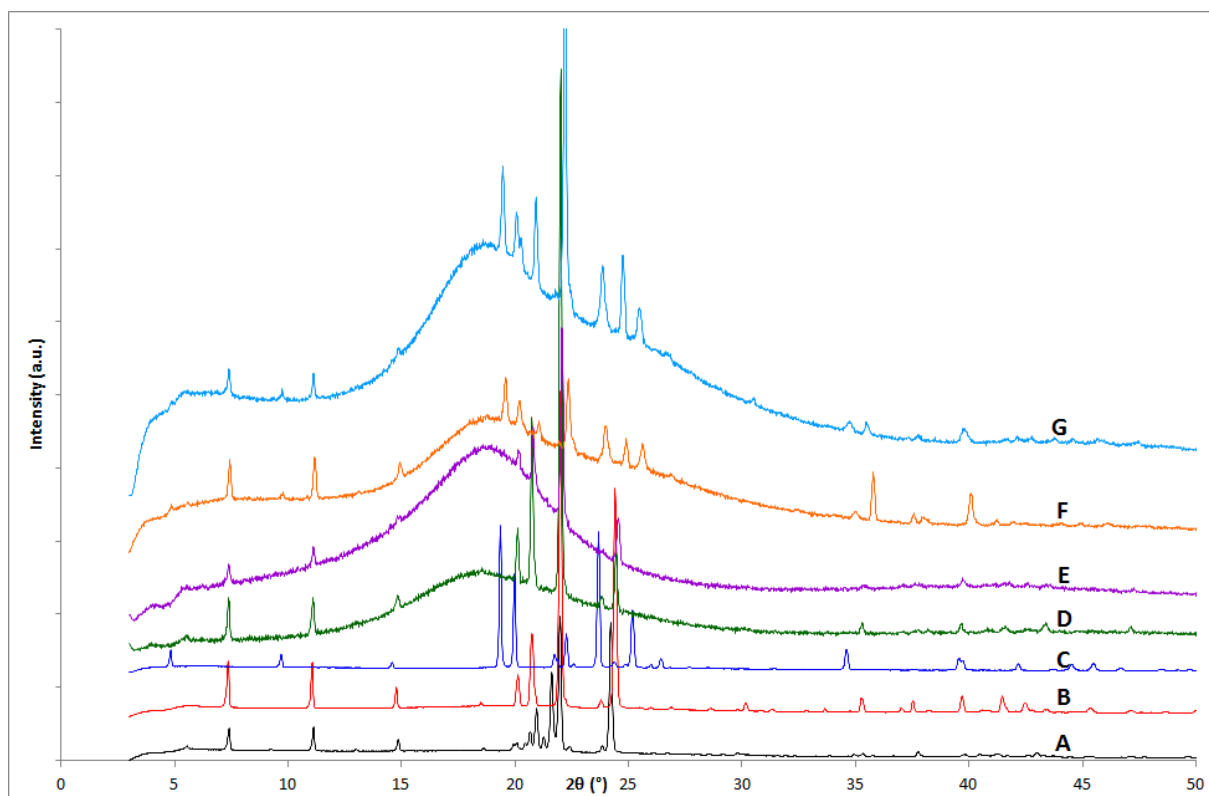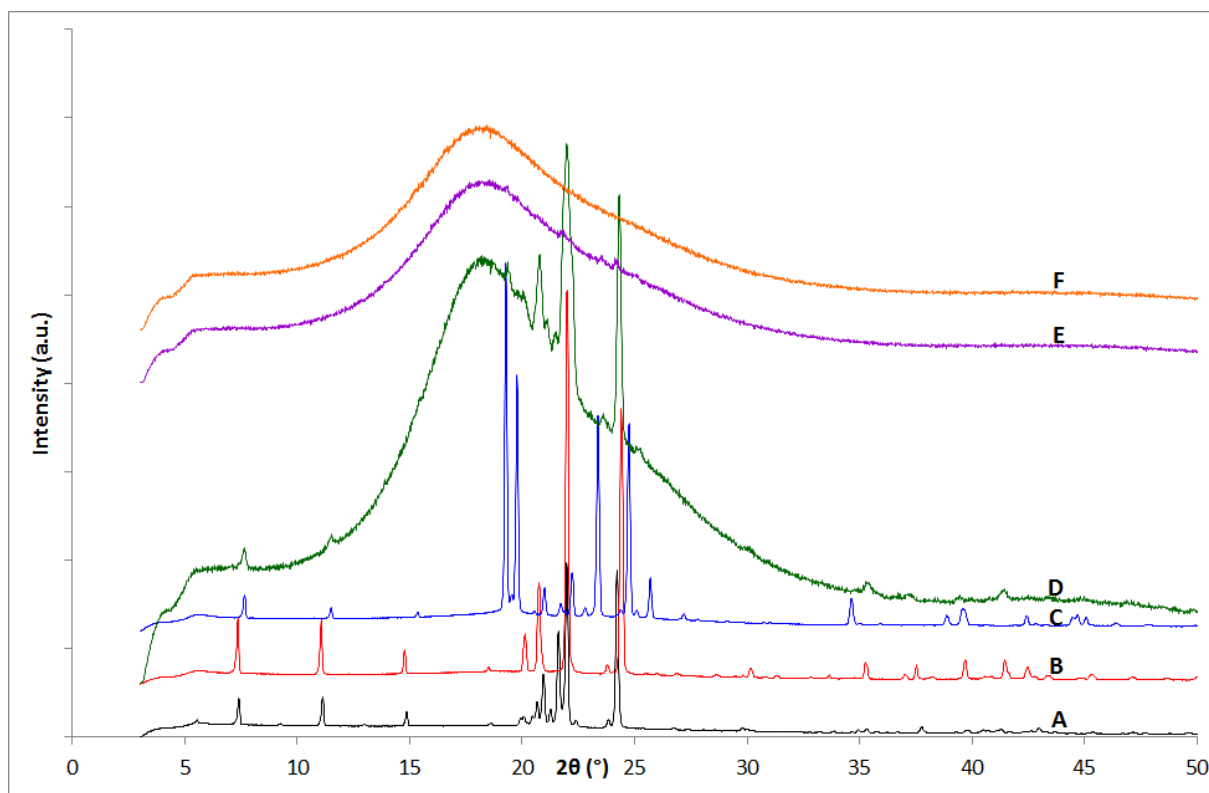
Figure 5.34 PXRD patterns of (A) MS-*Pnab* (ro*om* temperature), (B) MS-*C*2 (233 K), (C) octadecane as bought (233 K), (D) the product from experimental method 12 (190 K), (E) the product from experimental method 12 (225 K), (F) the product from experimental method 12 (250 K). λ = 1.54056 Å

As shown previously on stepwise crystallisation, more product forms but unlike Figure 5.33 which shows only a single phase crystallising out at 190 K with both cooling rates, in Figure 5.34 pattern D a mixed phase of MS-*C*2 and octadecane is present, but the octadecane peaks are very weak.

Rietveld refinements of the products formed between methyl stearate and octadecane can be found in appendix 5.7 apart from those that formed potential rotator phases.

5.7 Methyl Stearate : Eicosane

5.7.1 Characterisation

Experiments of mixtures of methyl stearate and eicosane were carried out using the experimental methods noted in Table 5.25 and detailed in section 5.3, with the results of these experiments shown in Figures 5.35, 5.36, 5.37 and 5.38.

Table 5.25 Conditions of methyl stearate : eicosane cocrystallisation experiments.

| Pattern / Figure	Material	Experimental Methods
D / 5.35	Methyl Stearate : Eicosane	1
E / 5.35	Methyl Stearate : Eicosane	2
F / 5.35	Methyl Stearate : Eicosane	3
G / 5.35	Methyl Stearate : Eicosane	4
D / 5.36	Methyl Stearate : Eicosane	5
E / 5.36	Methyl Stearate : Eicosane	6
F / 5.36	Methyl Stearate : Eicosane	7
D / 5.37	Methyl Stearate : Eicosane	8
E / 5.37	Methyl Stearate : Eicosane	9
F / 5.37	Methyl Stearate : Eicosane	10
G / 5.37	Methyl Stearate : Eicosane	11
D / 5.38	Methyl Stearate : Eicosane	12 at 190 K
E / 5.38	Methyl Stearate : Eicosane	12 at 225 K
F / 5.38	Methyl Stearate : Eicosane	12 at 250 K

Figure 5.35 PXRD patterns of (A) MS-*Pnab* (ro*om* temperature), (B) MS-*C*2 (233 K), (C) eicosane as bought (room temperature K), (D) the product from experimental method 1, (E) the product from experimental method 2, (F) the product from experimental method 3, (G) the product from experimental method 4. *λ* = 1.54056 Å

Under the same conditions solvent cocrystallisation with toluene produced a mix of the MS-*C*2 and eicosane (pattern D) whereas with kerosene (pattern E) only the MS-*C*2 phase crystallised out. Whilst the solutions should not have experienced temperatures nearing the methyl stearate melting point the solution and material may have been accidently melted as previously with octadecane on filtering or packing due to the low melting point.

Both solvent variable temperature experiments, patterns F and G, crystallised as a single MS-*C*2 phase with eicosane remaining dissolved in the solution.
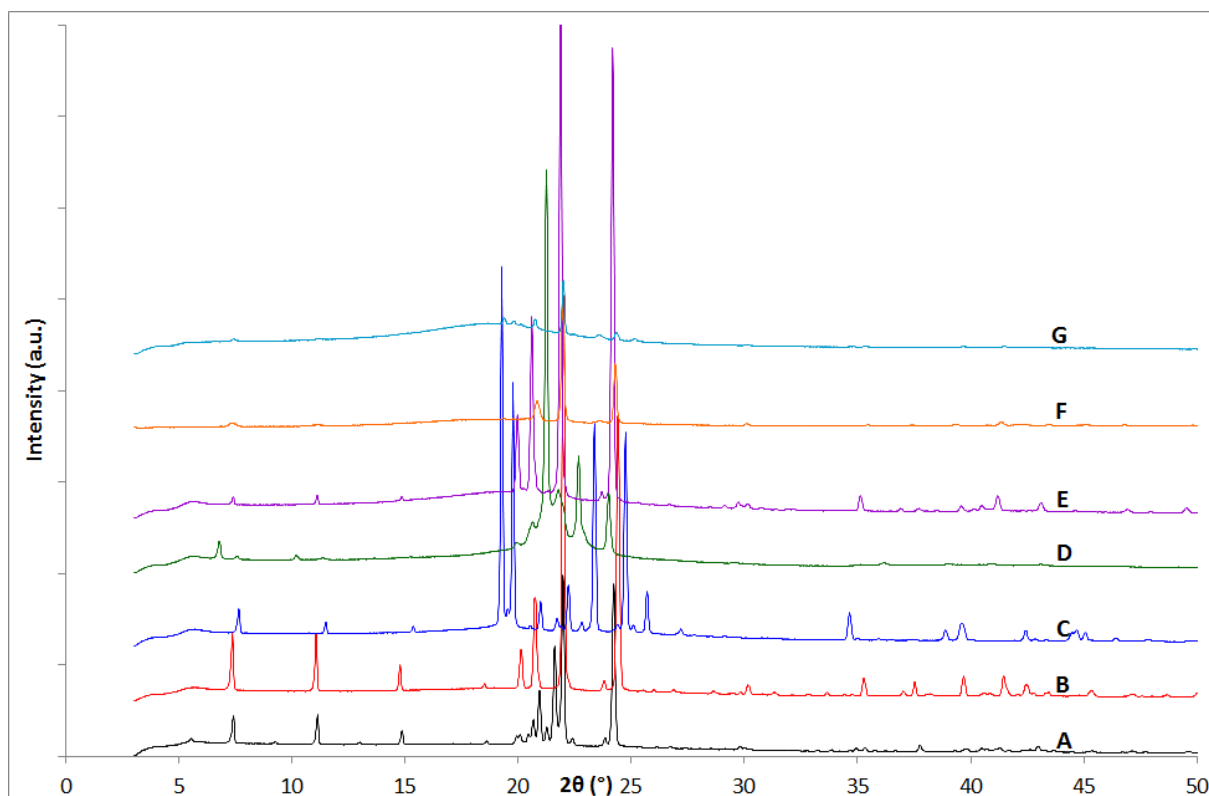
Figure 5.36 PXRD patterns of (A) MS-*Pnab* (ro*om* temperature), (B) MS-*C*2 (233 K), (C) eicosane as bought (room temperature K), (D) the product from experimental method 5, (E) the product from experimental method 6, (F) the product from experimental method 7. λ = 1.54056 Å

From the comparison in Figure 5.36 patterns D and E show the MS-*C*2 phase crystallised with no eicosane present. This is unusual as unless there is evaporation or the eicosane remains amorphous, peaks from crystalline eicosane should be present. The from melt experiment carried out in a capillary, pattern F, is however a mix of the MS-*C*2 phase and eicosane.

Figure 5.37 PXRD patterns of (A) MS-*Pnab* (ro*om* temperature), (B) MS-*C*2 (233 K), (C) eicosane as bought (room temperature K), (D) the product from experimental method 8, (E) the product from experimental method 9, (F) the product from experimental method 10, (G) the product from experimental method 11. *λ* = 1.54056 Å

Figure 5.37 patterns D and E were produced under the same conditions but D was with toluene and E was with kerosene. The recrystallisation of the melted product with toluene produced a mix of the MS-*C*2 phase and eicosane but the kerosene recrystallisation produced a single phase of MS-*C*2 with no eicosane present. Whilst this may seem to indicate that solvent plays a role in phases that crystallise out Figure 5.36 shows that even just a mix of the compounds without solvent can produce different phases.

Pattern F shows a mix of the MS-*C*2 phase and eicosane, however peaks over 23° 2θ have low intensity and this may be due to preferred orientation and the method of crystallisation in solvent in glass capillaries.

Whilst cooling at 100 K/hr to 190 K produced a mix of compounds the quick cooled solution at 360 K/hr, pattern G, produced only a single MS-*C*2 phase with no eicosane present.
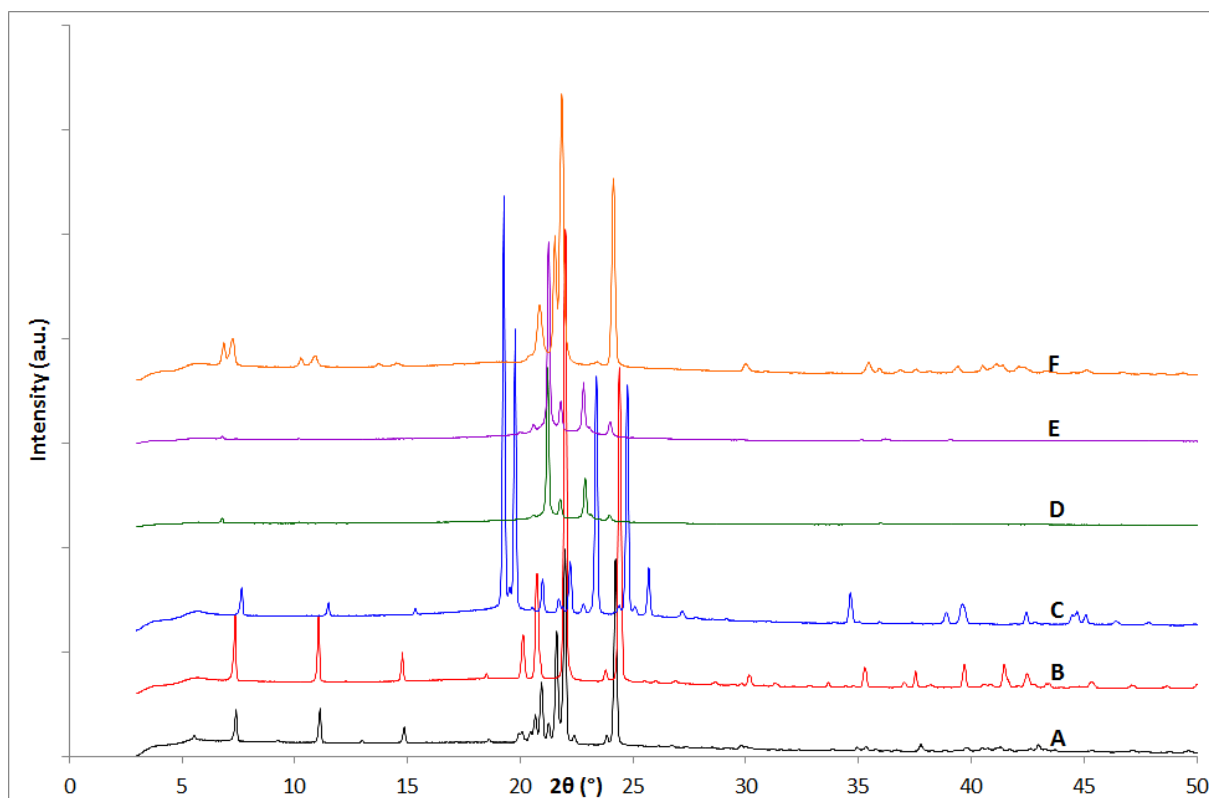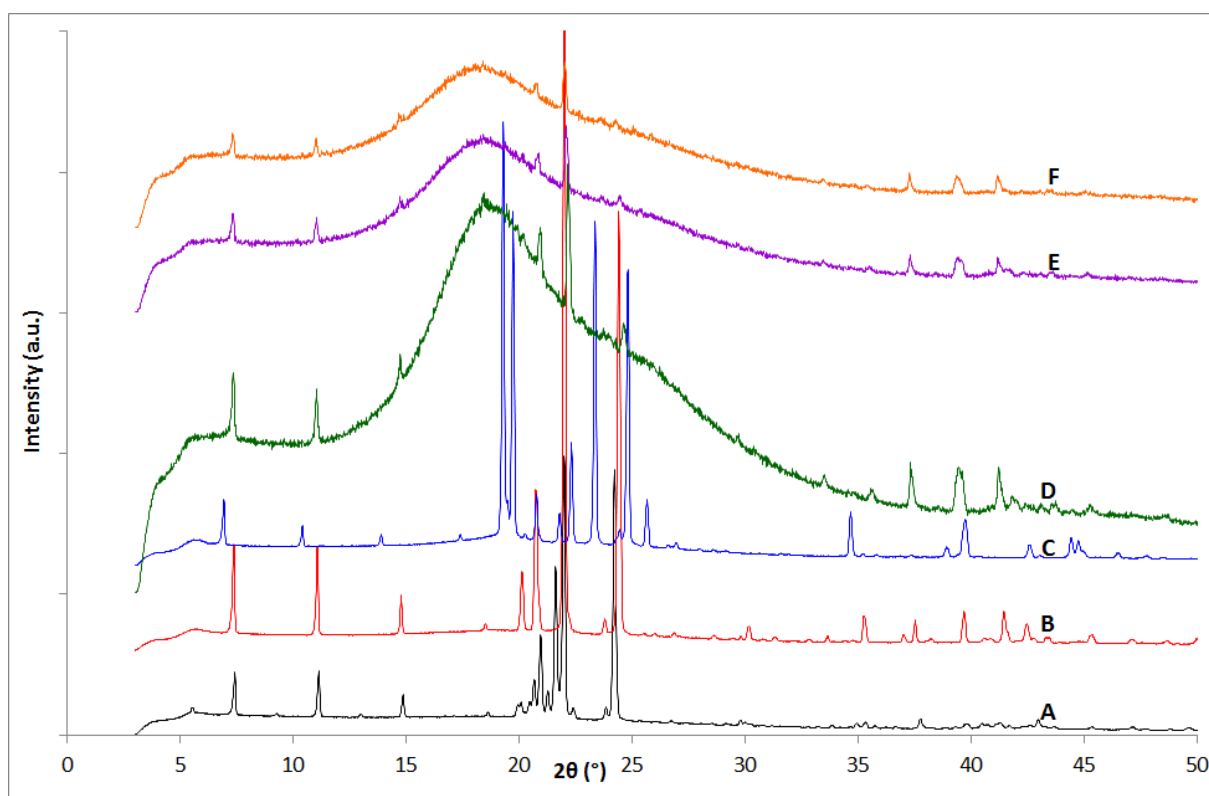

Figure 5.38 PXRD patterns of (A) MS-*Pnab* (ro*om* temperature), (B) MS-*C*2 (233 K), (C) eicosane as bought (233 K), (D) the product from experimental method 12 (190 K), (E) the product from experimental method 12 (225 K), (F) the product from experimental method 12 (250 K). λ = 1.54056 Å

Stepwise crystallisation at 190 K shown in Figure 5.38 pattern D shows a single phase of just MS-*C*2 with no eicosane present.

254

Rietveld refinements of the products formed between methyl stearate and eicosane can be found in appendix 5.8.

5.8 Methyl Stearate : Docosane

5.8.1 Characterisation

Experiments of mixtures of methyl stearate and docosane were carried out using the experimental methods noted in Table 5.26 and detailed in section 5.3, with the results of these experiments shown in Figures 5.39, 5.40, 5.41 and 5.42.

Table 5.26 Conditions of methyl stearate : docosane cocrystallisation experiments.

| Pattern / Figure	Material	Experimental Methods
D / 5.39	Methyl Stearate : Docosane	1
E / 5.39	Methyl Stearate : Docosane	2
F / 5.39	Methyl Stearate : Docosane	3
G / 5.39	Methyl Stearate : Docosane	4
D / 5.40	Methyl Stearate : Docosane	5
E / 5.40	Methyl Stearate : Docosane	6
F / 5.40	Methyl Stearate : Docosane	7
D / 5.41	Methyl Stearate : Docosane	8
E / 5.41	Methyl Stearate : Docosane	9
F / 5.41	Methyl Stearate : Docosane	10
G / 5.41	Methyl Stearate : Docosane	11
D / 5.42	Methyl Stearate : Docosane	12 at 190 K
E / 5.42	Methyl Stearate : Docosane	12 at 225 K
F / 5.42	Methyl Stearate : Docosane	12 at 250 K
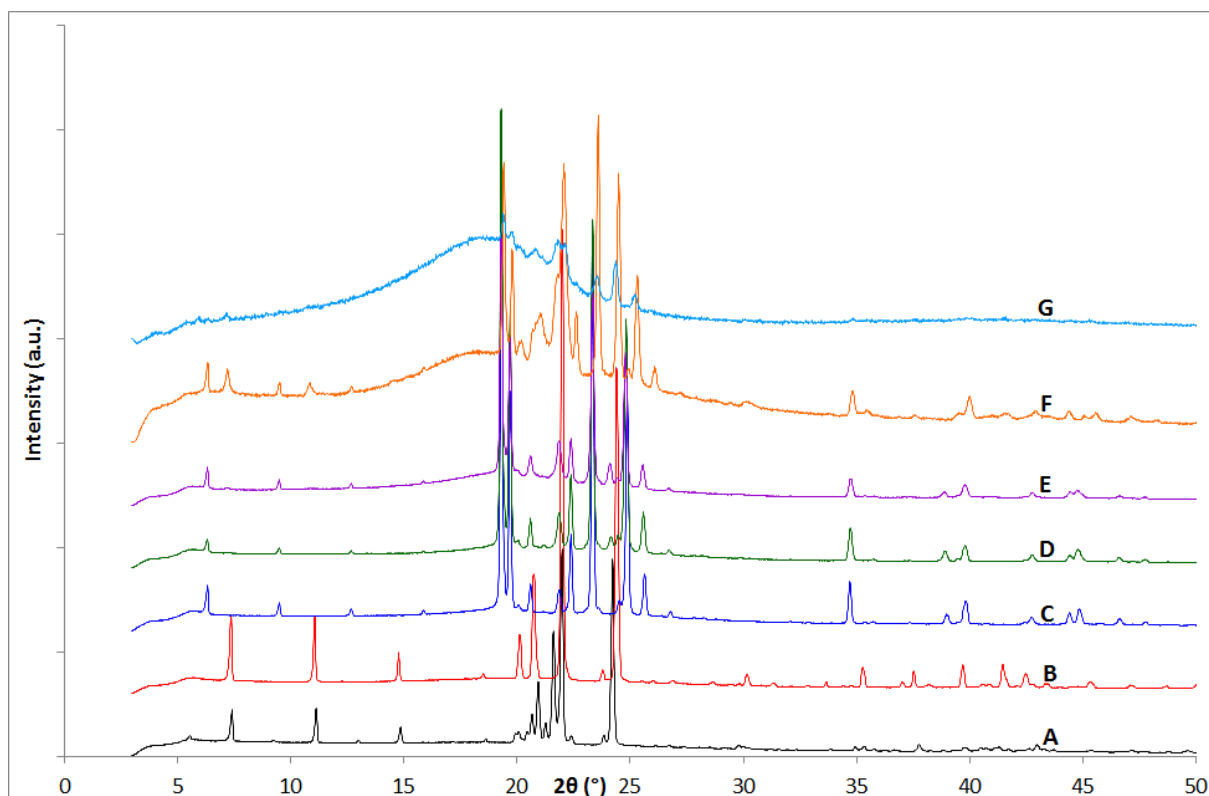
Figure 5.39 PXRD patterns of (A) MS-*Pnab* (ro*om* temperature), (B) MS-*C*2 (233 K), (C) docosane as bought (room temperature K), (D) the product from experimental method 1, (E) the product from experimental method 2, (F) the product from experimental method 3, (G) the product from experimental method 4. λ = 1.54056 Å

From comparison in Figure 5.39 of patterns D and E, in both solvents only docosane crystallised out and methyl stearate remained dissolved in solution. The variable temperature crystallisations at 233 K, patterns F and G, show a mixture of MS-*C*2 and docosane crystallised out, however the data quality is poor due to overlapping mid angle peaks.
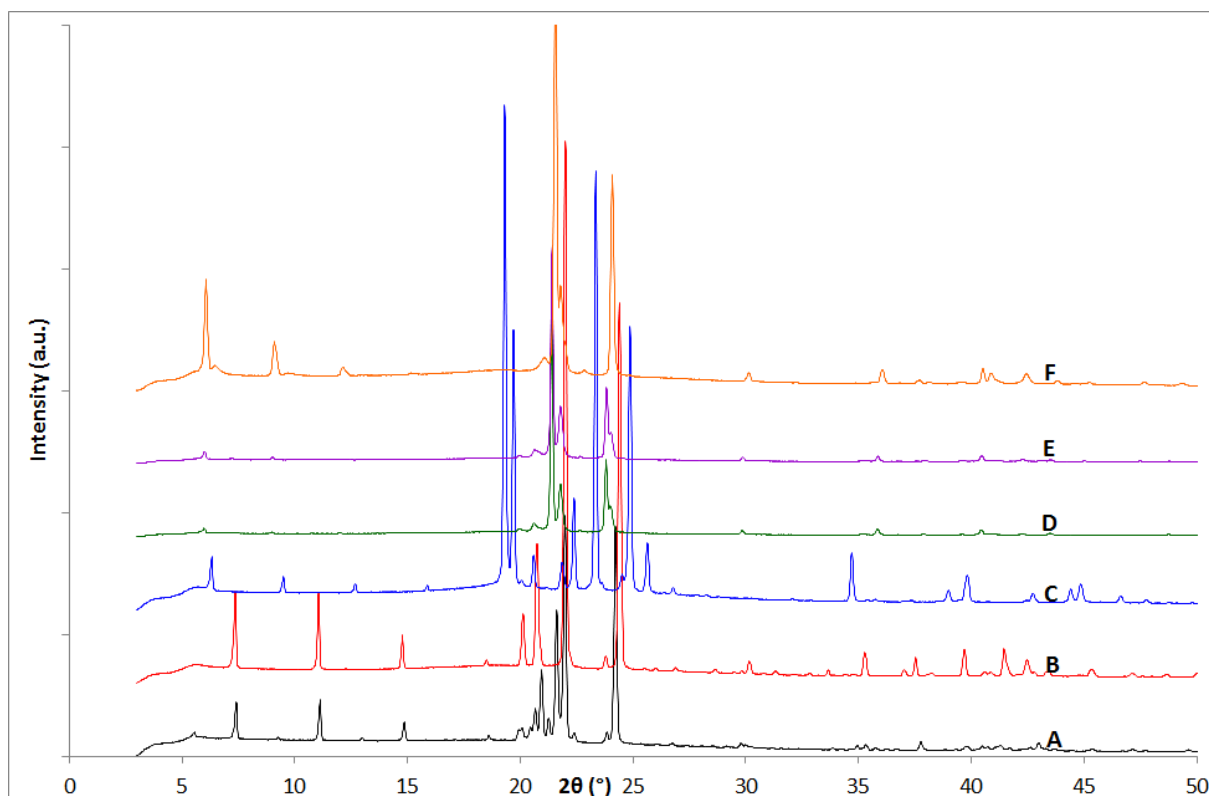
Figure 5.40 PXRD patterns of (A) MS-*Pnab* (ro*om* temperature), (B) MS-*C*2 (233 K), (C) docosane as bought (room temperature K), (D) the product from experimental method 5, (E) the product from experimental method 6, (F) the product from experimental method 7. *λ* = 1.54056 Å

All from the melt cocrystallisation experiments with no solvent present produced the same unknown phase, as shown in Figure 5.40; however the low angle peaks are relatively more intense in pattern F than D and E. This new phase is very similar to that of the rotator phase published of eicosane, and the unknown potential rotator phase produced by the methyl stearate : octadecane experiments. It therefore could be a docosane rotator phase with the methyl stearate either evaporating or remaining amorphous within the crystallised material.
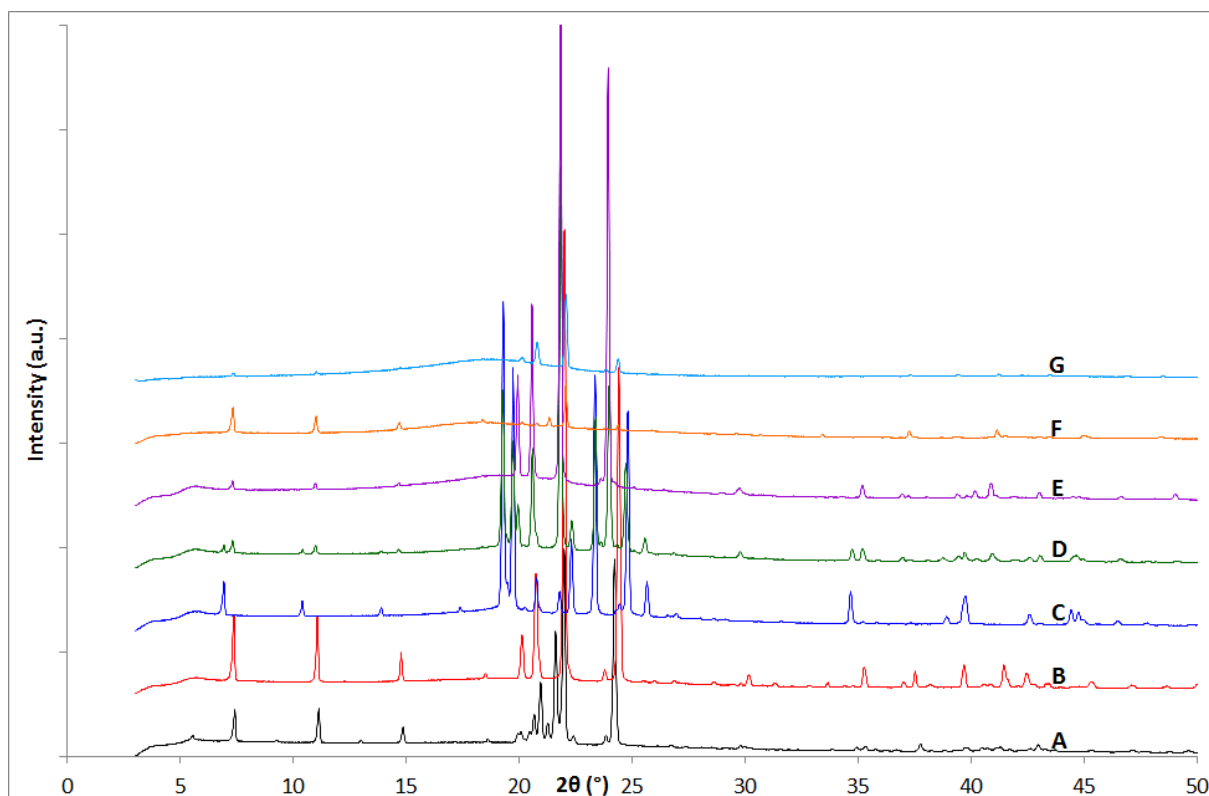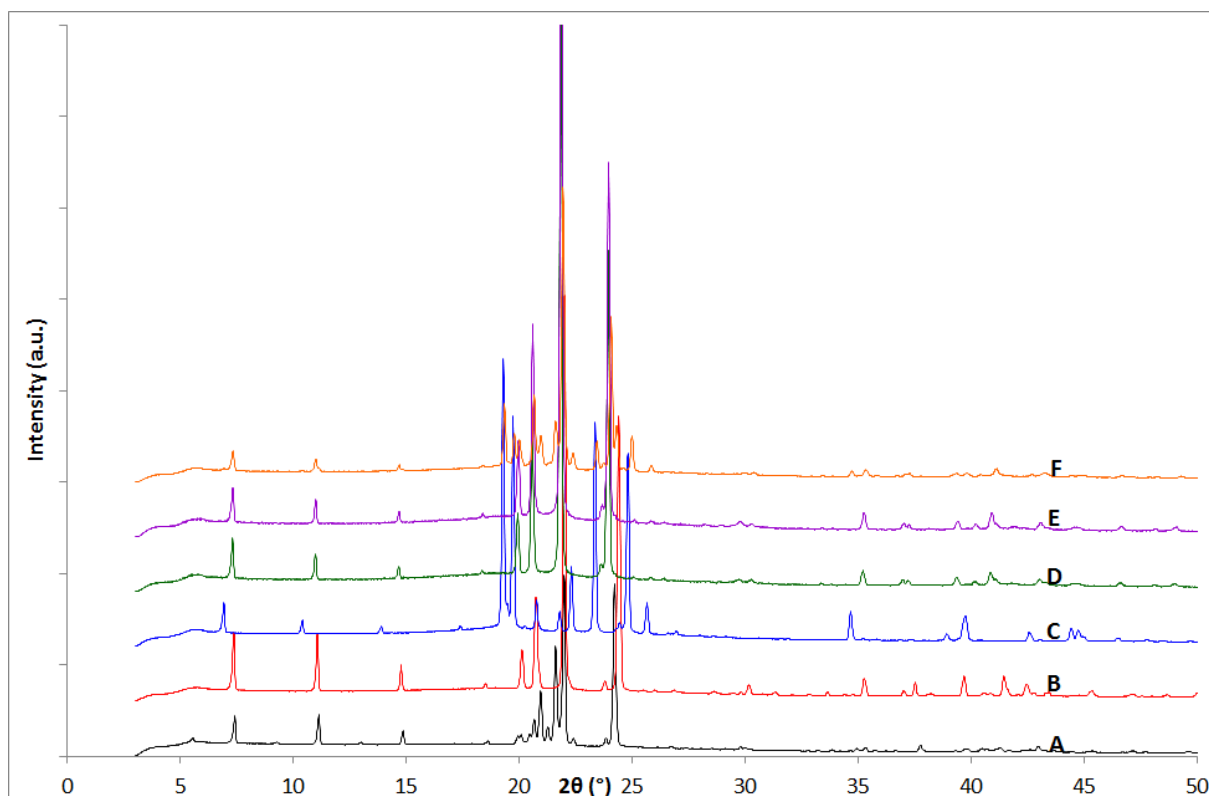
Figure 5.41 PXRD patterns of (A) MS-*Pnab* (ro*om* temperature), (B) MS-*C*2 (233 K), (C) docosane as bought (room temperature K), (D) the product from experimental method 8, (E) the product from experimental method 9, (F) the product from experimental method 10, (G) the product from experimental method 11. *λ* = 1.54056 Å

The recrystallisation of the melt material in toluene, pattern D, produced a mix of the MS-*C*2 and docosane phases but with kerosene, pattern E, just the docosane phase crystallises. Both of the variable temperature experiments to 190 K produced a mix of the MS-*C*2 and docosane phases, however both phases contain broad overlapping peaks as with the 233 K scans but this is to be expected due to the high solvent background and the high concentration of peaks at mid-angle.
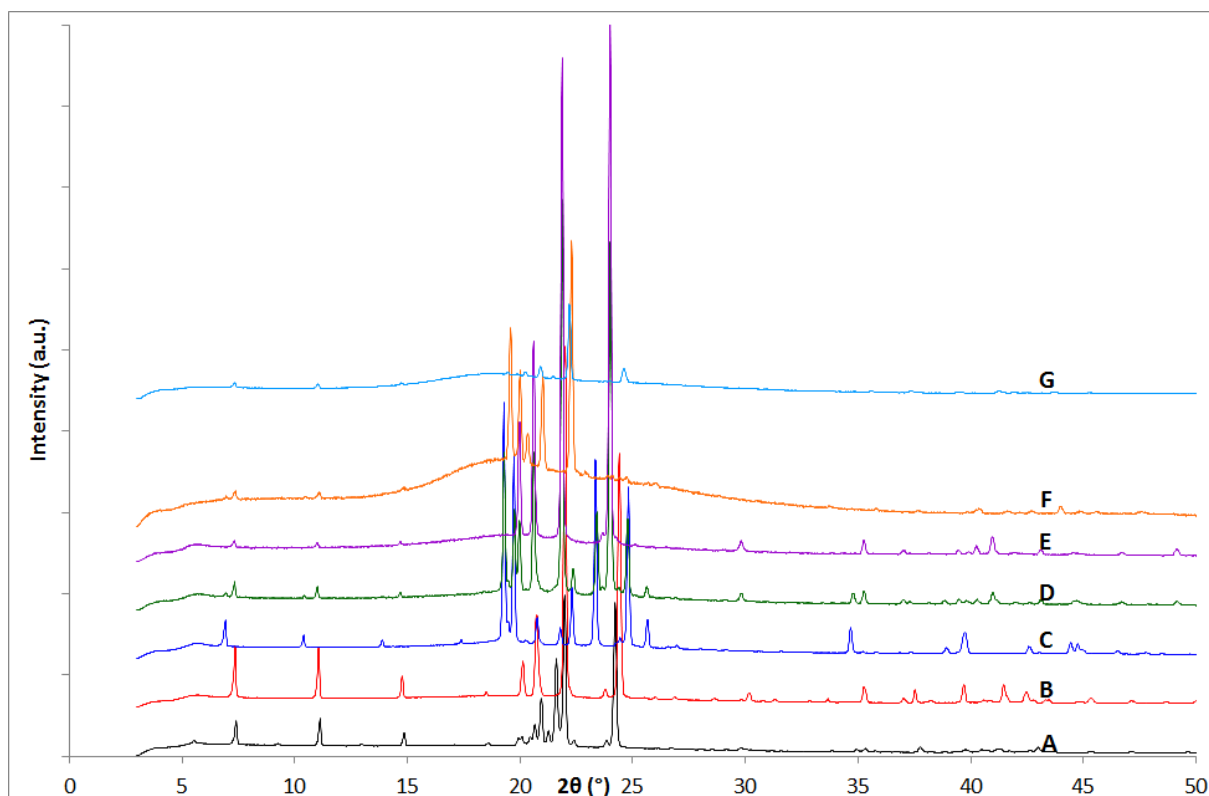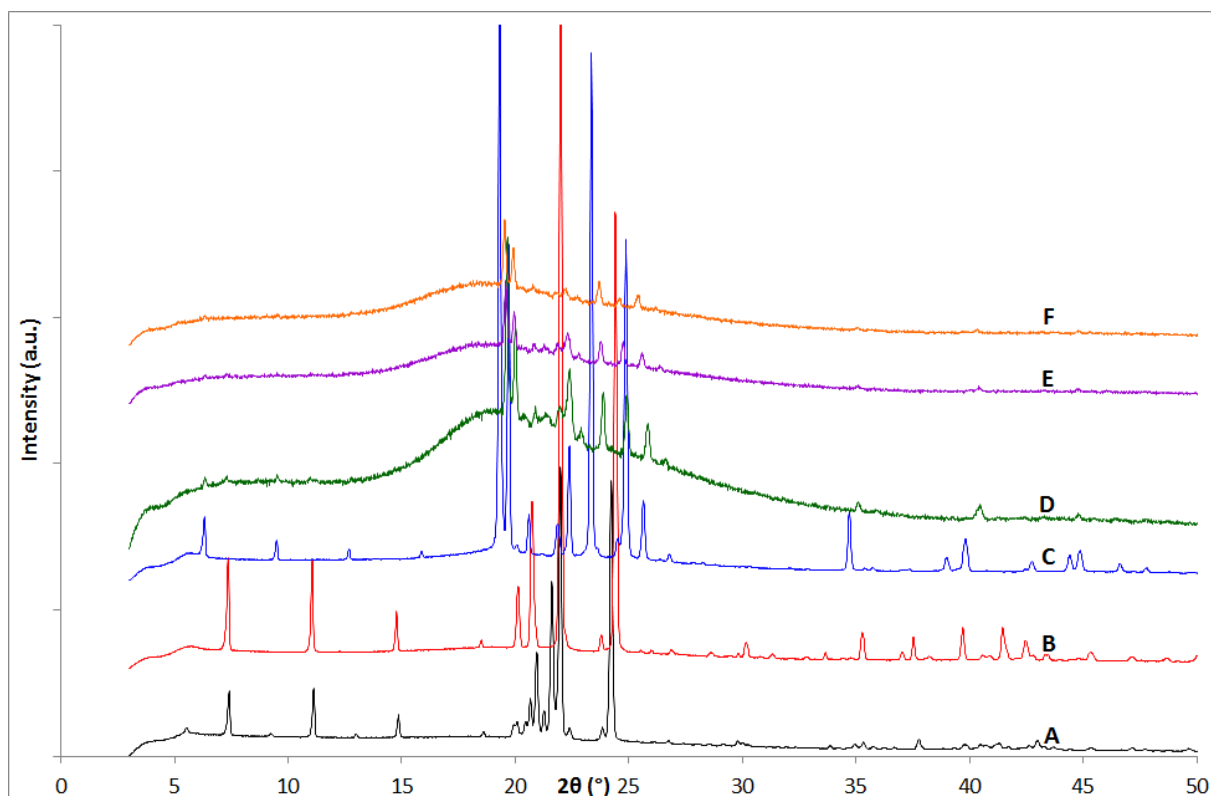
Figure 5.42 PXRD patterns of (A) MS-*Pnab* (ro*om* temperature), (B) MS-*C*2 (233 K), (C) docosane as bought (233 K), (D) the product from experimental method 12 (190 K), (E) the product from experimental method 12 (225 K), (F) the product from experimental method 12 (250 K). *λ* = 1.54056 Å

As with all the stepwise cocrystallisation experiments, crystallinity increases on decreasing temperature and pattern D shows a mixture of MS-*C*2 and docosane phases with broad overlapping mid angle peaks, which was also shown with the two cocrystallisation experiments to 190 K in Figure 5.41.

Rietveld refinements of the products formed between methyl stearate and docosane can be found in appendix 5.9.

5.9 Methyl Palmitate : Dodecane

5.9.1 Characterisation

Experiments of mixtures of methyl palmitate and dodecane were carried out using the experimental methods noted in Table 5.27 and detailed in section 5.3, with the results of these experiments shown in Figures 5.43 and 5.44.

Table 5.27 Conditions of methyl palmitate : dodecane cocrystallisation experiments.

| Pattern / Figure	Material	Experimental Methods
D / 5.43	Methyl Palmitate : Dodecane	3
E / 5.43	Methyl Palmitate : Dodecane	4
F / 5.43	Methyl Palmitate : Dodecane	10
G / 5.43	Methyl Palmitate : Dodecane	11
D / 5.44	Methyl Palmitate : Dodecane	12 at 190 K
E / 5.44	Methyl Palmitate : Dodecane	12 at 225 K
F / 5.44	Methyl Palmitate : Dodecane	12 at 250 K
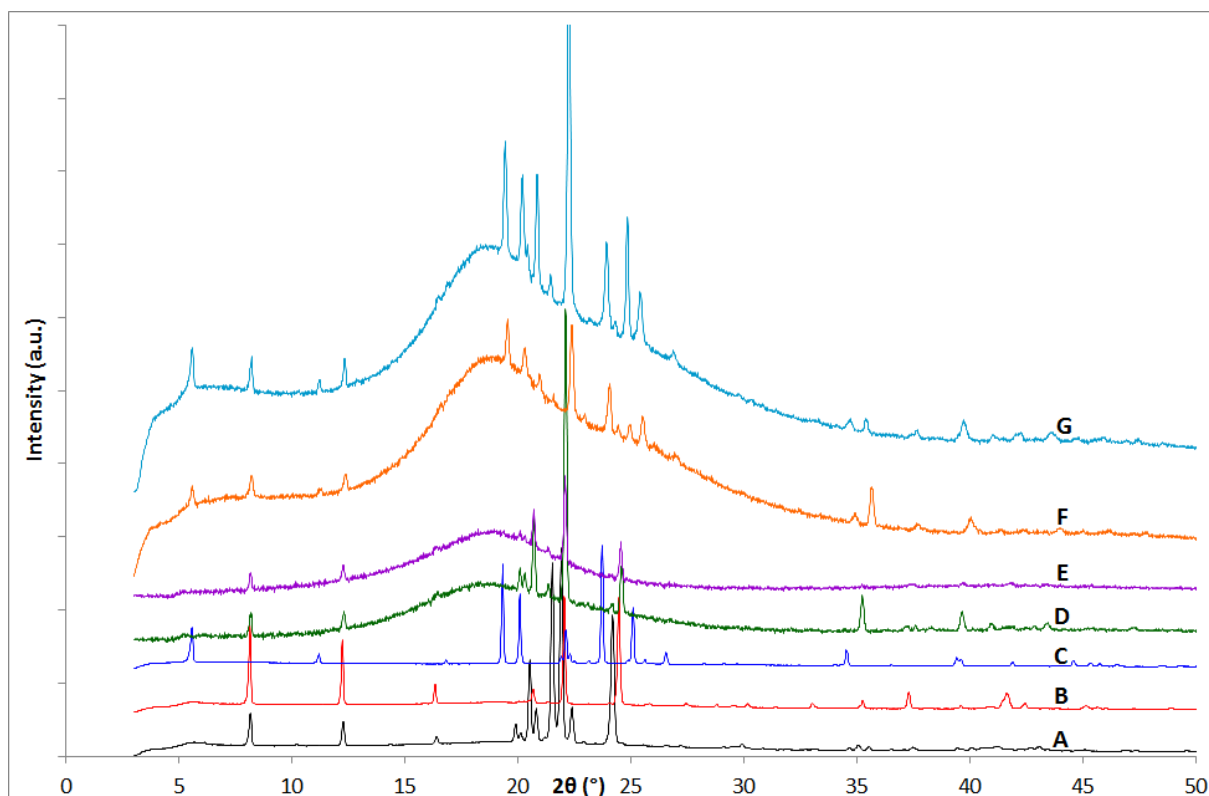
Figure 5.43 PXRD patterns of (A) MP-*Pnab* (ro*om* temperature), (B) MP-*C*2 (233 K), (C) dodecane as bought (233 K), (D) the product from experimental method 3, (E) the product from experimental method 4, (F) the product from experimental method 10, (G) the product from experimental method 11. *λ* = 1.54056 Å

From comparison in Figure 5.43, both solvent variable temperature cocrystallisation experiments to 233 K, patterns D and E, produced only the MP-*C*2 phase but on both experiments to 190 K a mix of the MP-*C*2 and dodecane phases crystallised out. This was the same as with the methyl stearate solutions with dodecane confirming that dodecane only crystallises out at temperatures lower than 233 K with the concentrations used in this project.
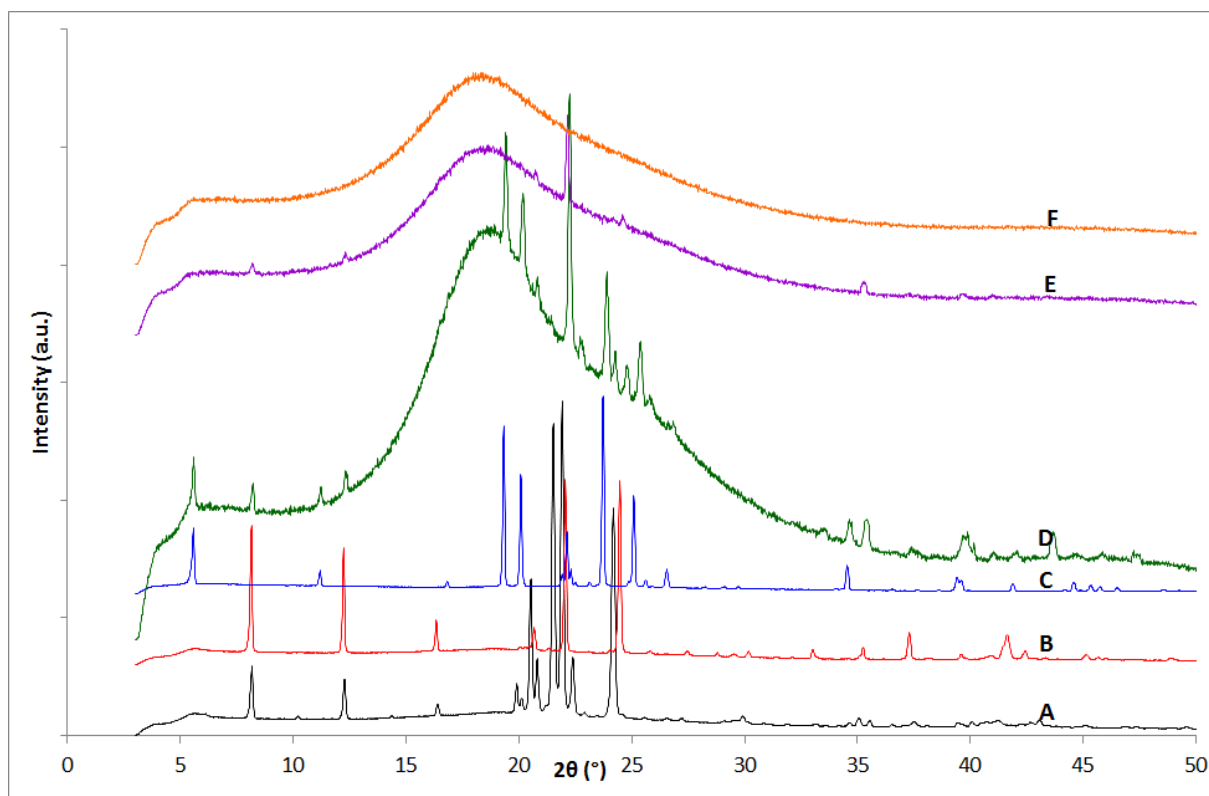
Figure 5.44 PXRD patterns of (A) MP-*Pnab* (ro*om* temperature), (B) MP-*C*2 (233 K), (C) dodecane as bought (233 K), (D) the product from experimental method 12 (190 K), (E) the product from experimental method 12 (225 K), (F) the product from experimental method 12 (250 K). *λ* = 1.54056 Å

As with the methyl stearate : dodecane stepwise variable temperature cocrystallisation, Figure 5.44, show increased crystallisation as temperature decreases and that by the 190 K scan a mixture of the MP-*C*2 and dodecane phases.

Rietveld refinements of the products formed between methyl palmitate and dodecane can be found in appendix 5.10.

5.10 Methyl Palmitate : Tetradecane

5.10.1 Characterisation

Experiments of mixtures of methyl palmitate and tetradecane were carried out using the experimental methods noted in Table 5.28 and detailed in section 5.3, with the results of these experiments shown in Figures 5.45 and 5.46.

Table 5.28 Conditions of methyl palmitate : tetradecane cocrystallisation experiments.

| Pattern / Figure	Material	Experimental Methods
D / 5.45	Methyl Palmitate : Tetradecane	3
E / 5.45	Methyl Palmitate : Tetradecane	4
F / 5.45	Methyl Palmitate : Tetradecane	10
G / 5.45	Methyl Palmitate : Tetradecane	11
D / 5.46	Methyl Palmitate : Tetradecane	12 at 190 K
E / 5.46	Methyl Palmitate : Tetradecane	12 at 225 K
F / 5.46	Methyl Palmitate : Tetradecane	12 at 250 K
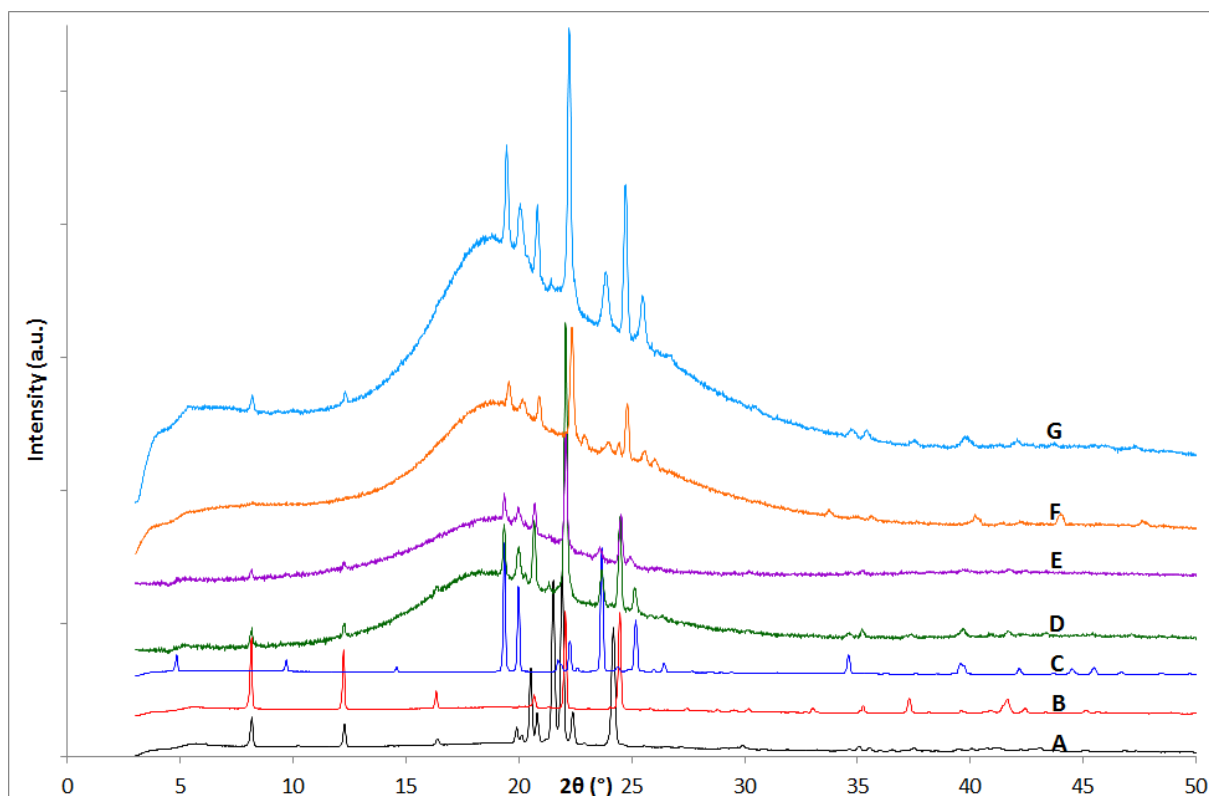
Figure 5.45 PXRD patterns of (A) MP-*Pnab* (ro*om* temperature), (B) MP-*C*2 (233 K), (C) tetradecane as bought (233 K), (D) the product from experimental method 3, (E) the product from experimental method 4, (F) the product from experimental method 10, (G) the product from experimental method 11. *λ* = 1.54056 Å

All methyl palmitate : tetradecane cocrystallisation experiments in both toluene and kerosene at both 233 K and 190 K scans produced a mix of the MP-*C*2 and tetradecane phases. However there are no low angle tetradecane peaks present which could be due to preferred orientation and the methods of crystallisation. This is in contrast to only the single MS-*C*2 phase crystallising out at 233 K with tetradecane.
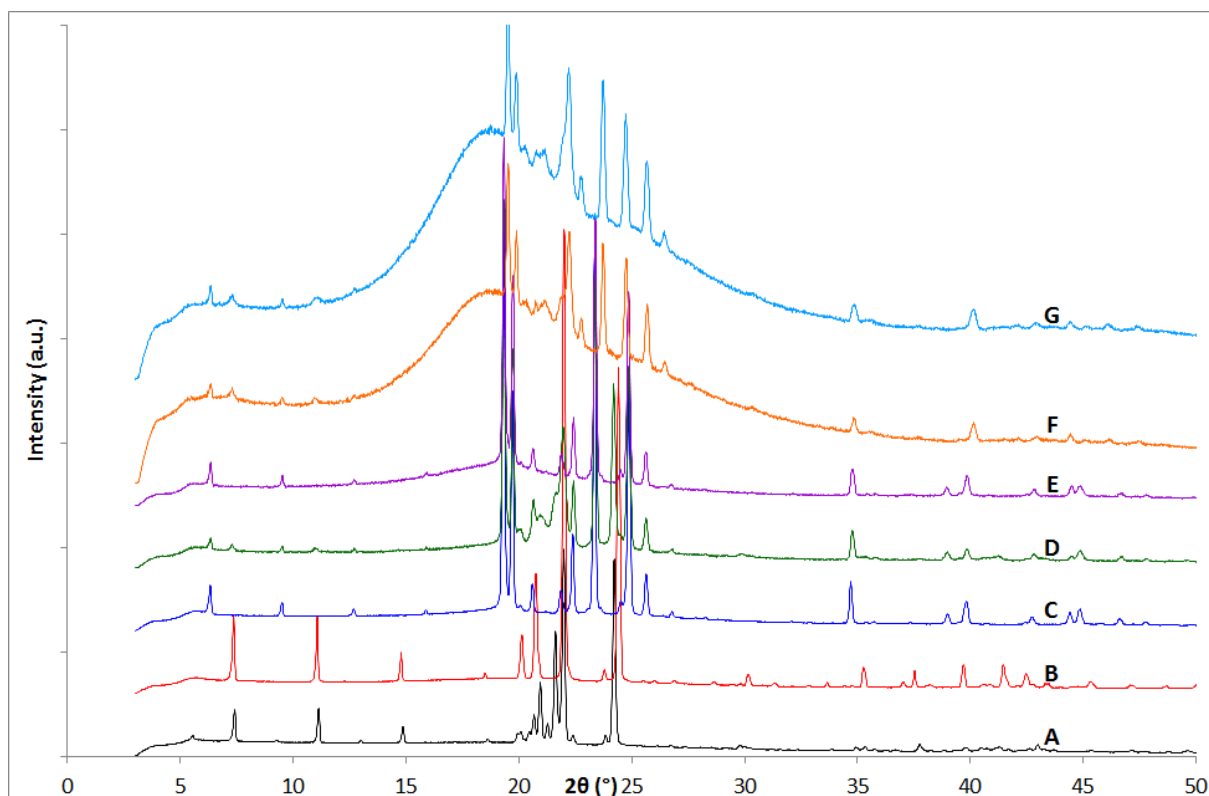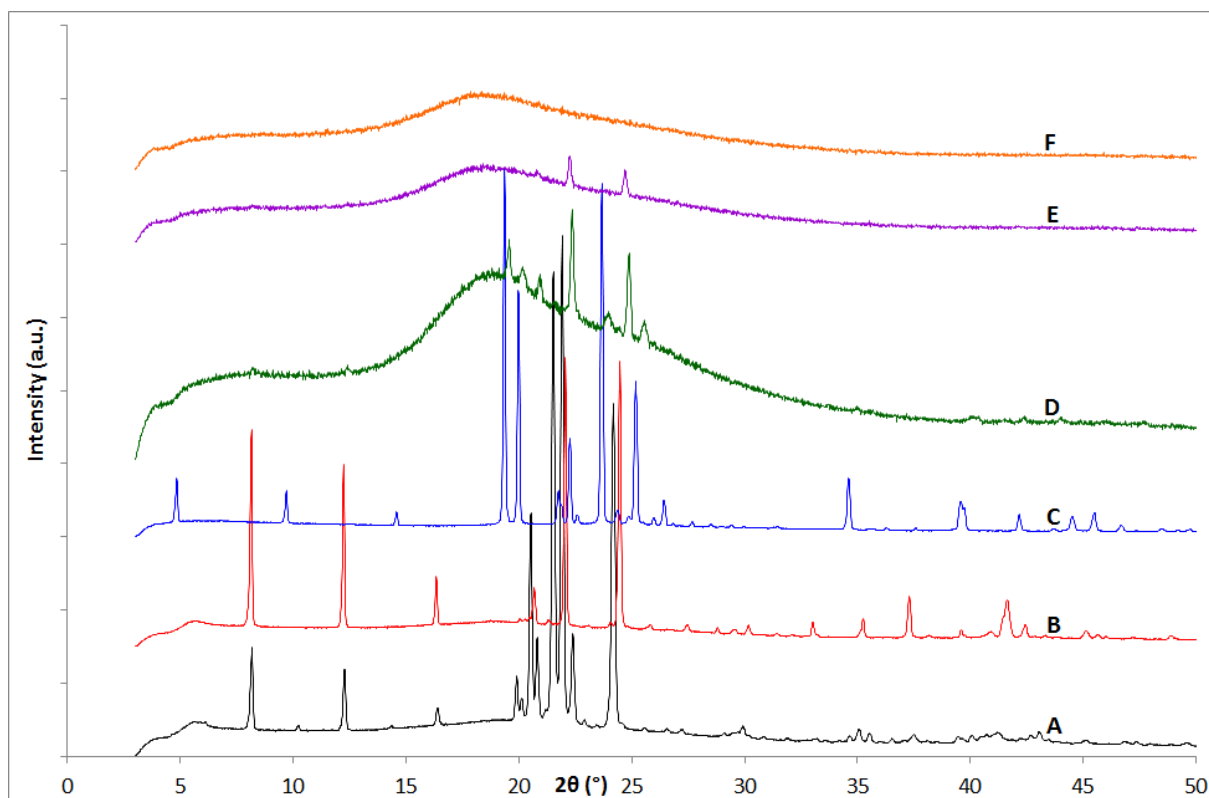
Figure 5.46 PXRD patterns of (A) MP-*Pnab* (ro*om* temperature), (B) MP-*C*2 (233 K), (C) tetradecane as bought (233 K), (D) the product from experimental method 12 (190 K), (E) the product from experimental method 12 (225 K), (F) the product from experimental method 12 (250 K). *λ* = 1.54056 Å

The stepwise crystallisation shown in Figure 5.46 shows consistency in a mixed phase crystallising out at 190 K, and as with Figure 5.45, there are no tetradecane low angle peaks present, and the methyl palmitate low angle peaks have low intensity.

Rietveld refinements of the products formed between methyl palmitate and tetradecane can be found in appendix 5.11.

5.11 Methyl Palmitate : Octadecane

5.11.1 Characterisation

Experiments of mixtures of methyl palmitate and octadecane were carried out using the experimental methods noted in Table 5.29 and detailed in section 5.3, with the results of these experiments shown in Figures 5.47, 5.48, 5.49 and 5.50.

Table 5.29 Conditions of methyl palmitate : octadecane cocrystallisation experiments.

Pattern / Figure	Material	Experimental Methods
D / 5.47	Methyl Palmitate : Octadecane	1
E / 5.47	Methyl Palmitate : Octadecane	3
F / 5.47	Methyl Palmitate : Octadecane	4
D / 5.48	Methyl Palmitate : Octadecane	5
E / 5.48	Methyl Palmitate : Octadecane	6
F / 5.48	Methyl Palmitate : Octadecane	7
D / 5.49	Methyl Palmitate : Octadecane	8
E / 5.49	Methyl Palmitate : Octadecane	10
F / 5.49	Methyl Palmitate : Octadecane	11
D / 5.50	Methyl Palmitate : Octadecane	12 at 190 K
E / 5.50	Methyl Palmitate : Octadecane	12 at 225 K
F / 5.50	Methyl Palmitate : Octadecane	12 at 250 K

Figure 5.47 PXRD patterns of (A) MP-*Pnab* (ro*om* temperature), (B) MP-*C*2 (233 K), (C) octadecane as bought (room temperature K), (D) the product from experimental method 1, (E) the product from experimental method 3, (F) the product from experimental method 4. *λ* = 1.54056 Å

From comparison in Figure 5.47 pattern D, cocrystallisation in toluene without heat showed a single phase of octadecane with no methyl palmitate present. The variable temperature cocrystallisations to 233 K show a MP-*C*2 and octadecane mixed phase with toluene, pattern E, and a single phase of MP-*C*2 with kerosene, pattern F.

Figure 5.48 PXRD patterns of (A) MP-*Pnab* (ro*om* temperature), (B) MP-*C*2 (233 K), (C) octadecane as bought (room temperature K), (D) the product from experimental method 5, (E) the product from experimental method 6, (F) the product from experimental method 7. *λ* = 1.54056 Å

All the melt experiments with no solvent shown in Figure 5.48 have produced a single phase of MP-*C*2. The lack of octadecane in the scans indicated that it remained either amorphous or evaporated in crystallisation.

Figure 5.49 PXRD patterns of (A) MP-*Pnab* (ro*om* temperature), (B) MP-*C*2 (233 K), (C) octadecane as bought (room temperature K), (D) the product from experimental method 8, (E) the product from experimental method 10, (F) the product from experimental method 11. *λ* = 1.54056 Å

Both the recrystallisation of the melted compounds in toluene and both variable temperature cocrystallisations to 190 K produced a mixed phase of MP-*C*2 and octadecane.
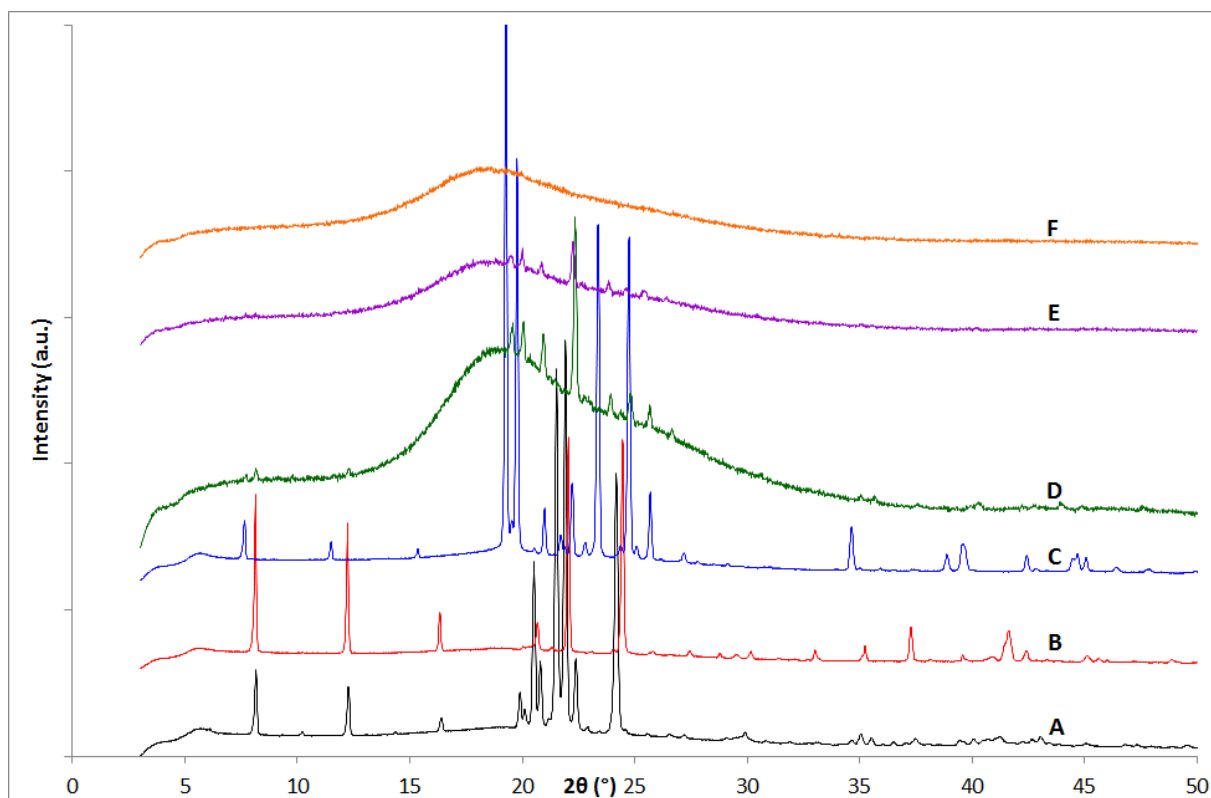
Figure 5.50 PXRD patterns of (A) MP-*Pnab* (ro*om* temperature), (B) MP-*C*2 (233 K), (C) octadecane as bought (room temperature K), (D) the product from experimental method 12 (190 K), (E) the product from experimental method 12 (225 K), (F) the product from experimental method 12 (250 K). λ = 1.54056 Å

The stepwise variable temperature cocrystallisation in Figure 5.50 shows that by the 190 K scan, and consistent with the results in Figure 5.49, a mixture of MP-*C*2 and octadecane crystallised out.

Rietveld refinements of the products formed between methyl palmitate and octadecane can be found in appendix 5.12.

5.12 Methyl Palmitate : Eicosane

5.12.1 Characterisation

Experiments of mixtures of methyl palmitate and eicosane were carried out using the experimental methods noted in Table 5.30 and detailed in section 5.3, with the results of these experiments shown in Figures 5.51, 5.52, 5.53 and 5.54.

Table 5.30 Conditions of methyl palmitate : eicosane cocrystallisation experiments.

Pattern / Figure	Material	Experimental Methods
D / 5.51	Methyl Palmitate : Eicosane	1
E / 5.51	Methyl Palmitate : Eicosane	2
F / 5.51	Methyl Palmitate : Eicosane	3
G / 5.51	Methyl Palmitate : Eicosane	4
D / 5.52	Methyl Palmitate : Eicosane	5
E / 5.52	Methyl Palmitate : Eicosane	6
F / 5.52	Methyl Palmitate : Eicosane	7
D / 5.53	Methyl Palmitate : Eicosane	8
E / 5.53	Methyl Palmitate : Eicosane	9
F / 5.53	Methyl Palmitate : Eicosane	10
G / 5.53	Methyl Palmitate : Eicosane	11
D / 5.54	Methyl Palmitate : Eicosane	12 at 190 K
E / 5.54	Methyl Palmitate : Eicosane	12 at 225 K
F / 5.54	Methyl Palmitate : Eicosane	12 at 250 K

Figure 5.51 PXRD patterns of (A) MP-*Pnab* (ro*om* temperature), (B) MP-*C*2 (233 K), (C) eicosane as bought (room temperature K), (D) the product from experimental method 1, (E) the product from experimental method 2, (F) the product from experimental method 3, (G) the product from experimental method 4. *λ* = 1.54056 Å

From the comparison in Figure 5.51, the solvent cocrystallisations with toluene and kerosene, patterns D and E, produced a single phase of eicosane, with the methyl palmitate remaining dissolved in the solution. The variable temperature solvent cocrystallisation experiments with toluene and kerosene to 233 K, patterns F and G, however, produced a mixed phase of MP-*C*2 and eicosane but several mid angle peaks are broad and overlapped at mid angle where there is a high concentration of peaks. There are also a couple of peaks which have low relative intensity which could be due to preferred orientation.

Figure 5.52 PXRD patterns of (A) MP-*Pnab* (room temperature), (B) MP-*C*2 (233 K), (C) eicosane as bought (room temperature K), (D) the product from experimental method 5, (E) the product from experimental method 6, (F) the product from experimental method 7. *λ* = 1.54056 Å

All three from the melt cocrystallisations shown in Figure 5.52 are very similar to the potential new rotator phases shown previously with methyl stearate cocrystallisations with octadecane and docosane, therefore the products of these experiments are most likely a mix of MP-*C*2 and the eicosane rotator phase.
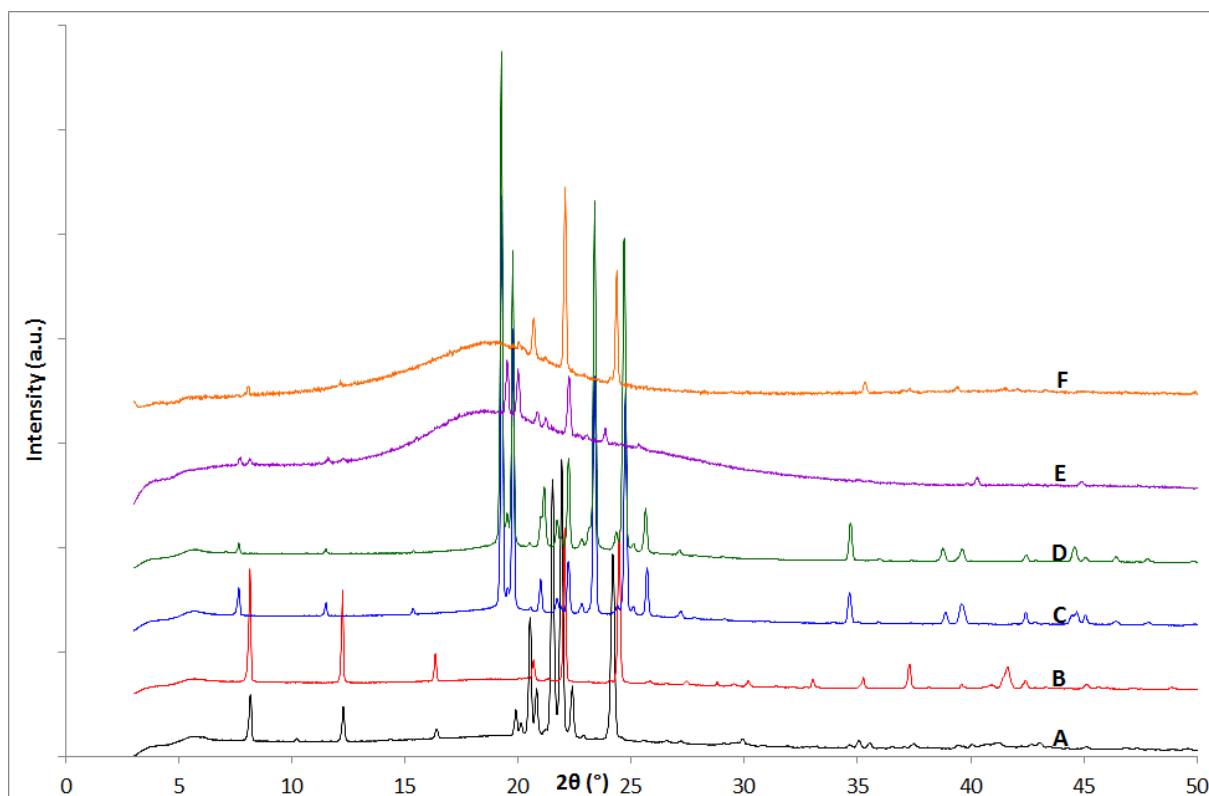
Figure 5.53 PXRD patterns of (A) MP-*Pnab* (room temperature), (B) MP-*C*2 (233 K), (C) eicosane as bought (room temperature K), (D) the product from experimental method 8, (E) the product from experimental method 9, (F) the product from experimental method 10, (G) the product from experimental method 11. *λ* = 1.54056 Å

The solvent recrystallisation of the melted product with toluene, pattern D, produced a mix of the MP-*C*2 and eicosane phases but with kerosene, pattern E, only a single phase of eicosane forms. Both slow and quick cooling to 190 K patterns F and G, produced mixed phases of MP-*C*2 and eicosane however there are a few overlapping mid angle peaks.
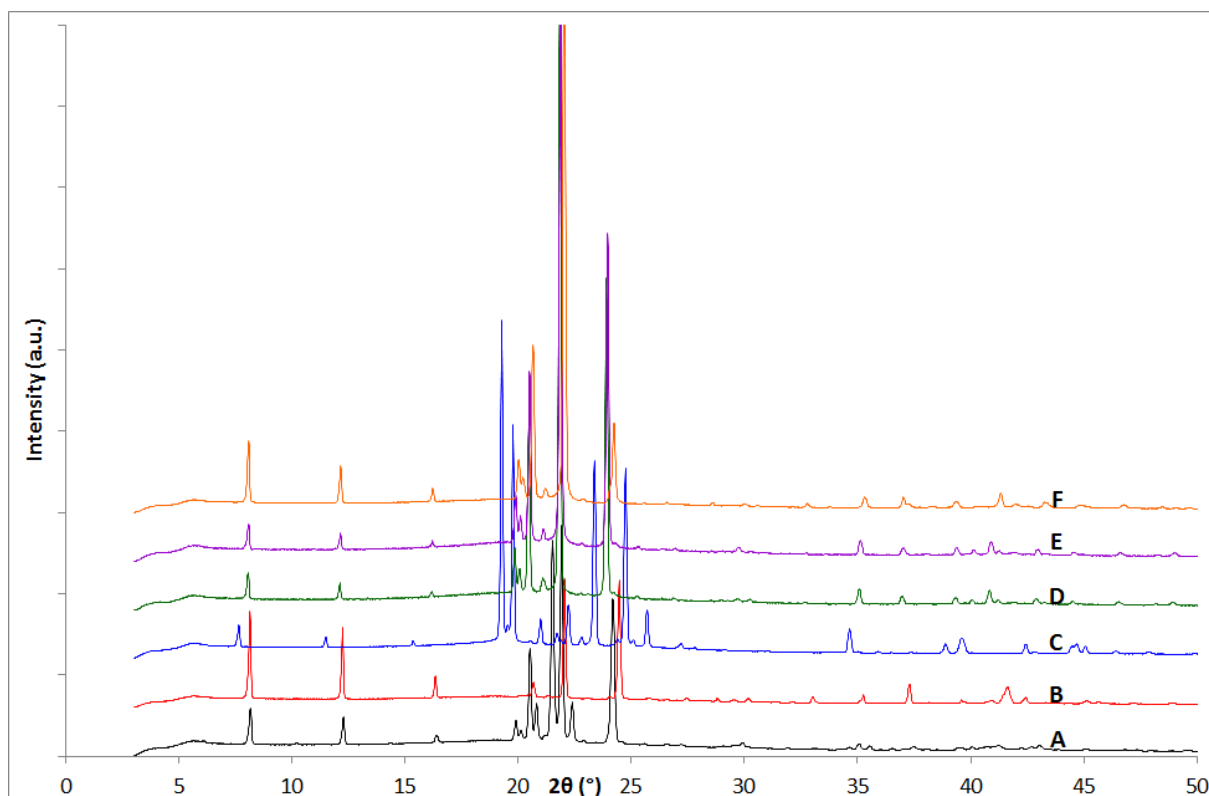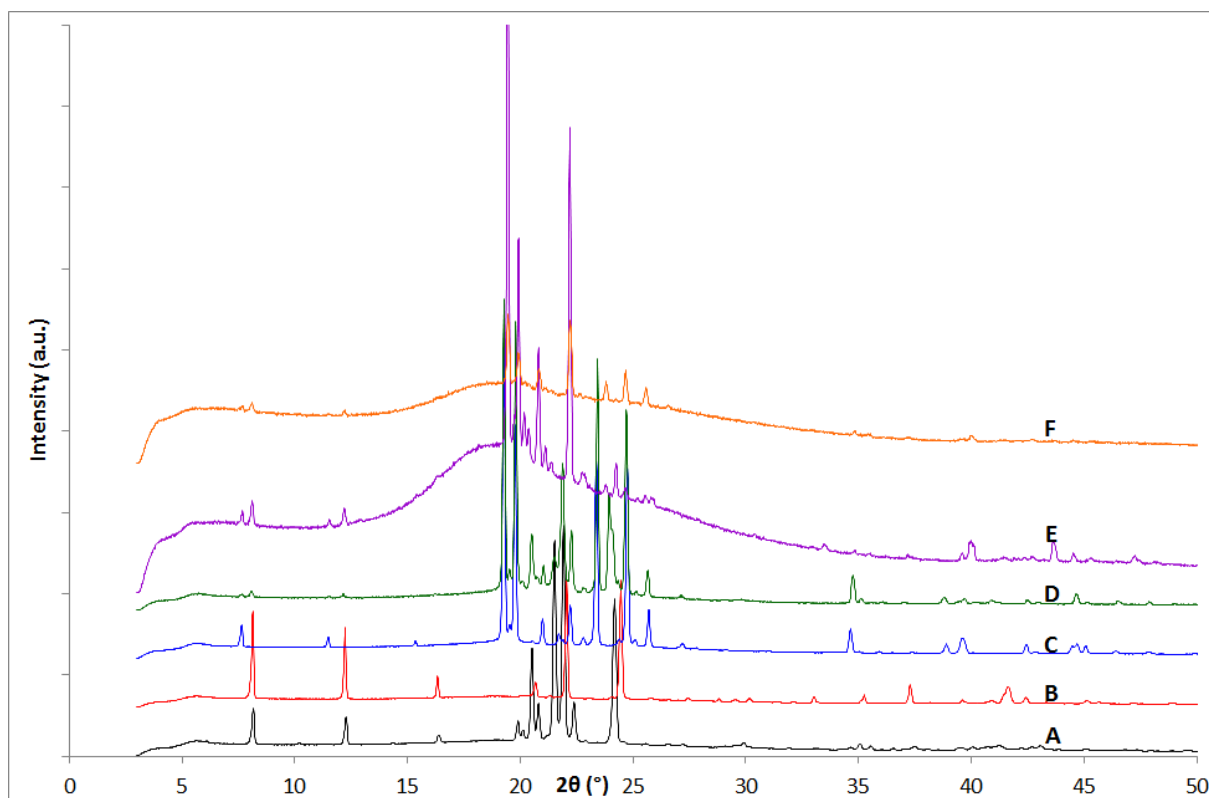
Figure 5.54 PXRD patterns of (A) MP-*Pnab* (ro*om* temperature), (B) MP-*C*2 (233 K), (C) eicosane as bought (room temperature K), (D) the product from experimental method 12 (190 K), (E) the product from experimental method 12 (225 K), (F) the product from experimental method 12 (250 K). *λ* = 1.54056 Å

As with the two scans at 190 K in Figure 5.53, Figure 5.54 shows a mixed phase of MP-*C*2 and eicosane forms at 190 K with an increase in the amount of crystalline material formed on cooling after the melt.

Rietveld refinements of the products formed between methyl palmitate and eicosane can be found in appendix 5.13.

5.13 Methyl Palmitate : Docosane

5.13.1 Characterisation

Experiments of mixtures of methyl palmitate and docosane were carried out using the experimental methods noted in Table 5.31 and detailed in section 5.3, with the results of these experiments shown in Figures 5.55, 5.56, 5.57 and 5.58.

Table 5.31 Conditions of methyl palmitate : docosane cocrystallisation experiments.

| Pattern / Figure	Material	Experimental Methods
D / 5.55	Methyl Palmitate : Docosane	1
E / 5.55	Methyl Palmitate : Docosane	2
F / 5.55	Methyl Palmitate : Docosane	3
G / 5.55	Methyl Palmitate : Docosane	4
D / 5.56	Methyl Palmitate : Docosane	5
E / 5.56	Methyl Palmitate : Docosane	6
F / 5.56	Methyl Palmitate : Docosane	7
D / 5.57	Methyl Palmitate : Docosane	8
E / 5.57	Methyl Palmitate : Docosane	9
F / 5.57	Methyl Palmitate : Docosane	10
G / 5.57	Methyl Palmitate : Docosane	11
D / 5.58	Methyl Palmitate : Docosane	12 at 190 K
E / 5.58	Methyl Palmitate : Docosane	12 at 225 K
F / 5.58	Methyl Palmitate : Docosane	12 at 250 K
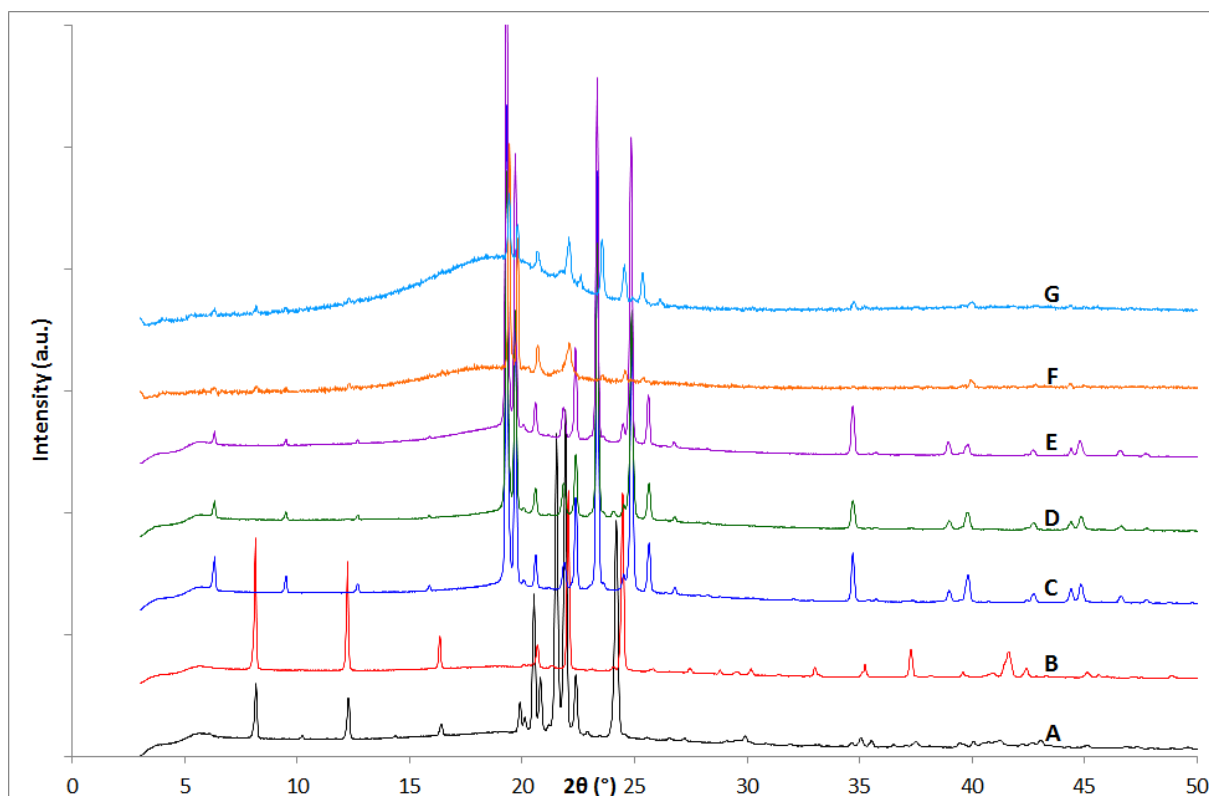
Figure 5.55 PXRD patterns of (A) MP-*Pnab* (ro*om* temperature), (B) MP-*C*2 (233 K), (C) docosane as bought (room temperature K), (D) the product from experimental method 1, (E) the product from experimental method 2, (F) the product from experimental method 3, (G) the product from experimental method 4. λ = 1.54056 Å

Both solvent cocrystallisations with toluene and kerosene, patterns D and E, with the same conditions as with eicosane, produced a single phase of the hydrocarbon docosane, with the methyl palmitate again remaining dissolved in solution. Both variable temperature solvent cocrystallisations, patterns F and G, produced a mixed phase of MP-*C*2 and docosane; however there are a few overlapping mid angle peaks.
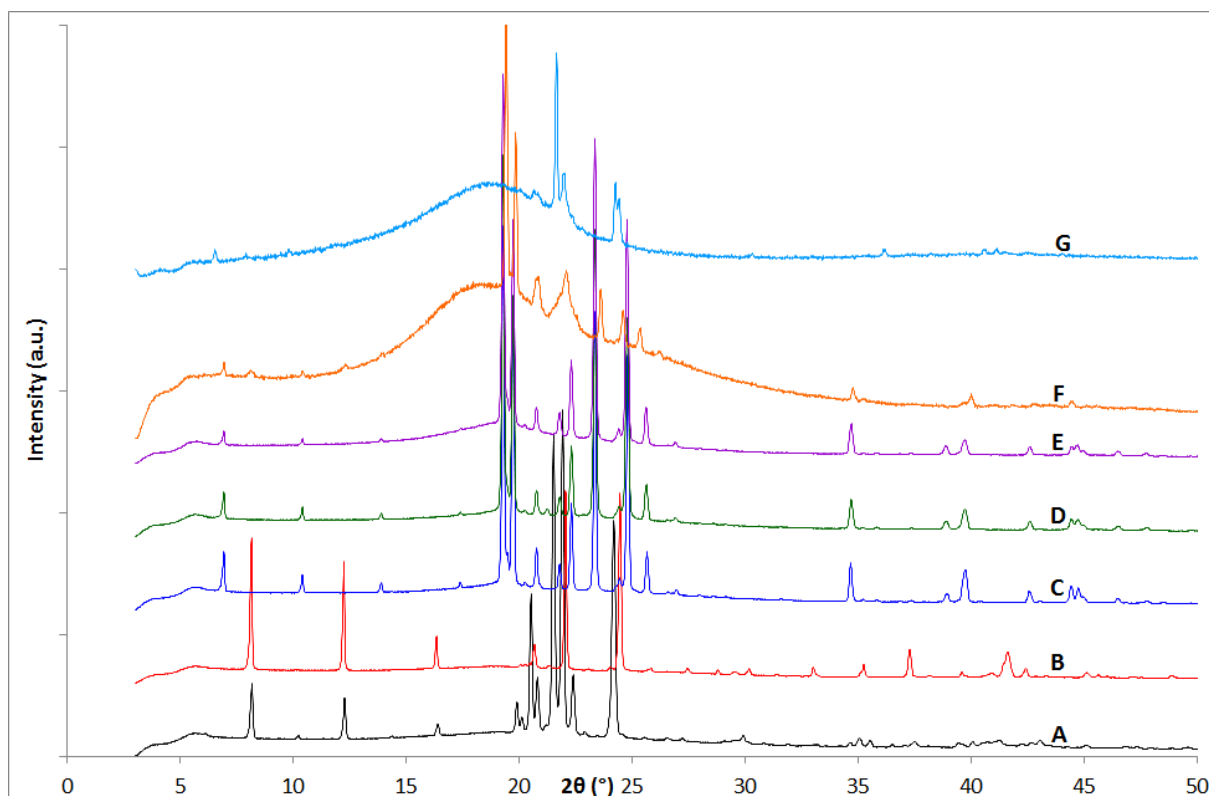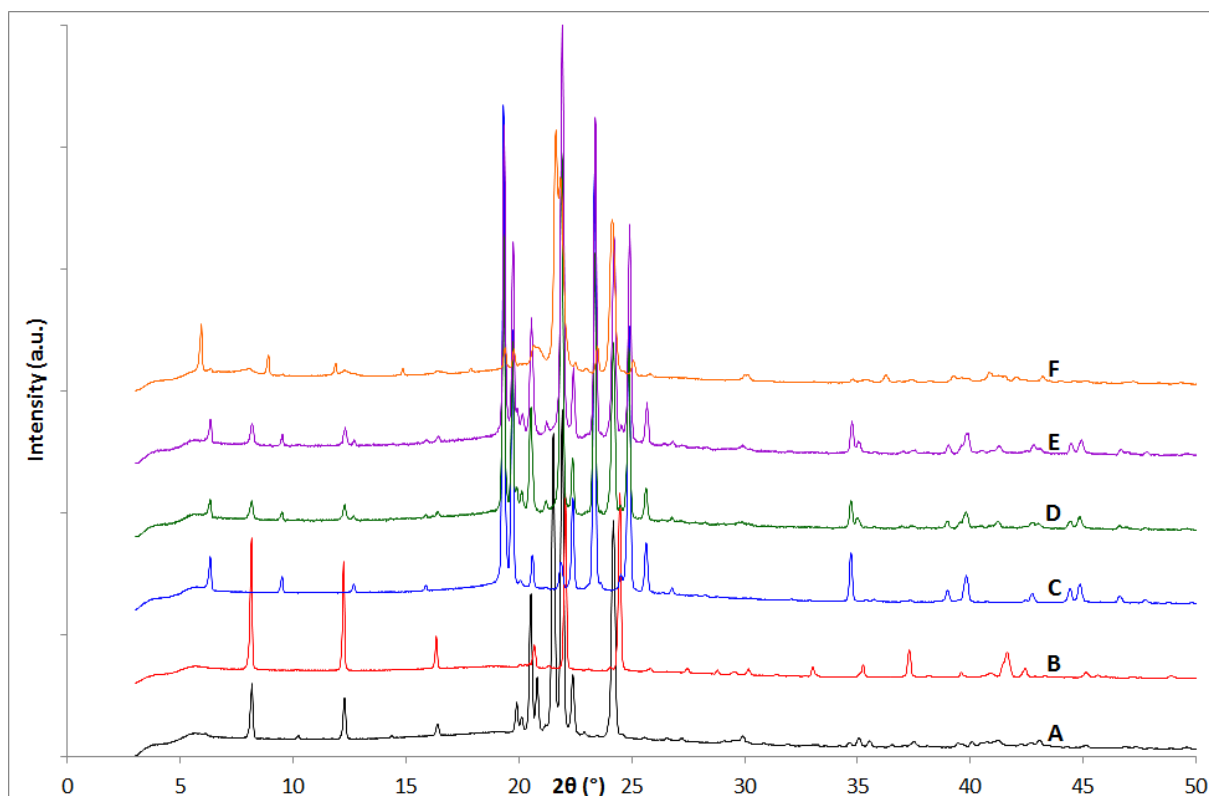
Figure 5.56 PXRD patterns of (A) MP-*Pnab* (room temperature), (B) MP-*C*2 (233 K), (C) docosane as bought (room temperature K), (D) the product from experimental method 5, (E) the product from experimental method 6, (F) the product from experimental method 7. λ = 1.54056 Å

Unlike from the melt, no solvent cocrystallisations between methyl stearate and docosane produced a potential rotator phase; the cocrystallisation between methyl palmitate and docosane all produced mixed phases of MP-*C*2 and docosane. Whilst the two cocrystallisation experiments carried out in Teflon pots produced clear mixed phases in the experiment carried out in situ in a capillary, the MP-*C*2 low angle peaks are quite broad and the mid angle peaks of both methyl palmitate and docosane are broad and overlapped with a few low intensity peaks due to preferred orientation.
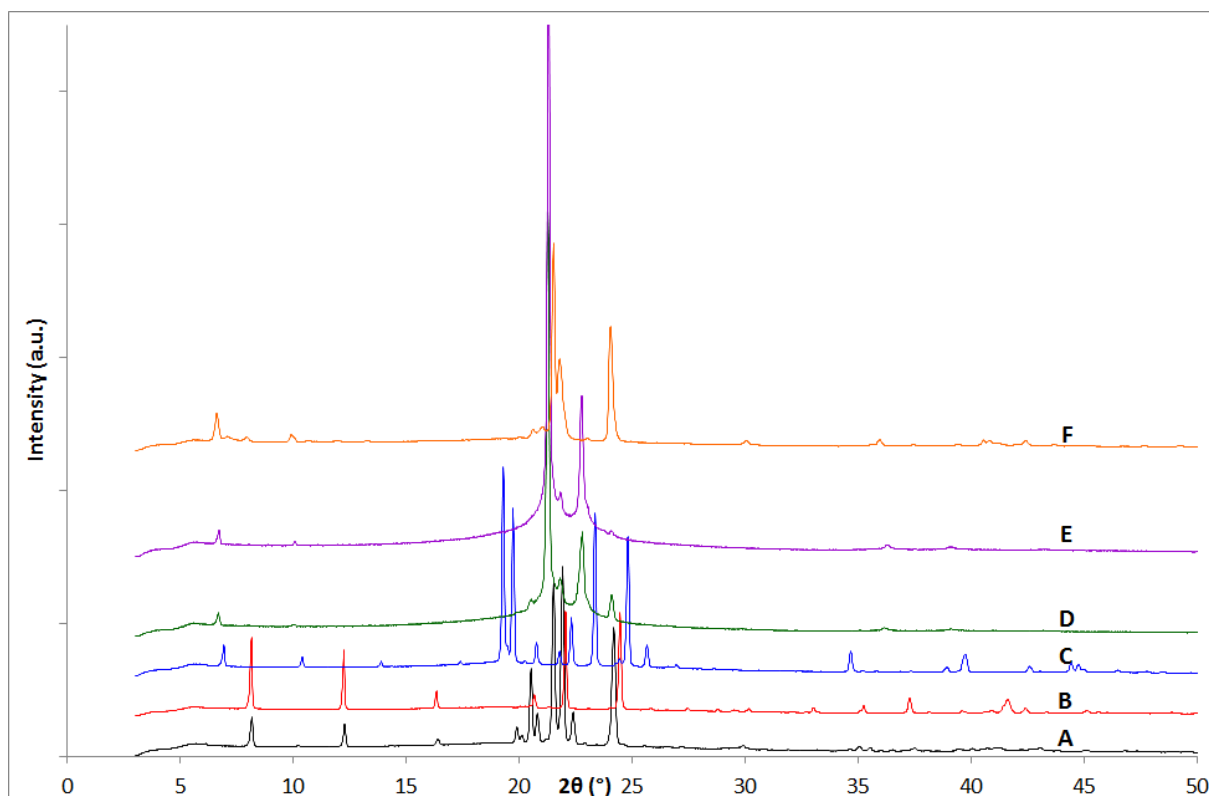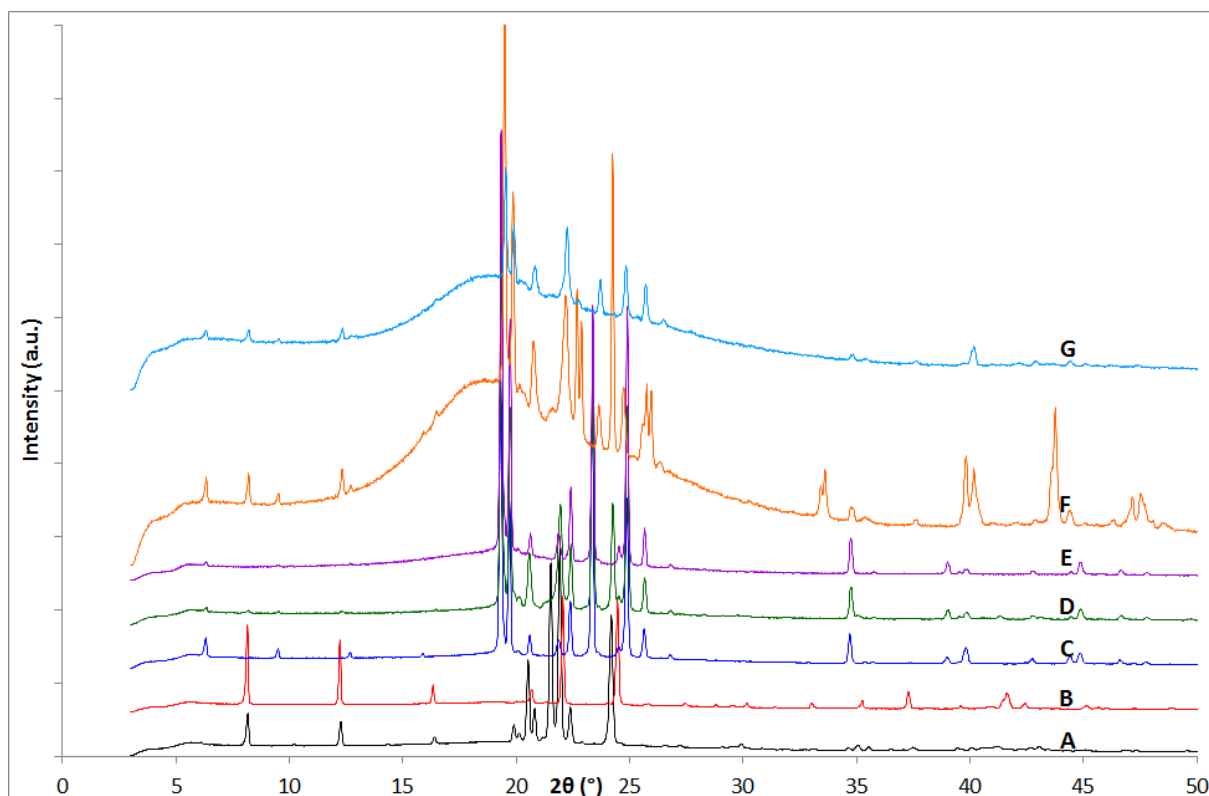
Figure 5.57 PXRD patterns of (A) MP-*Pnab* (ro*om* temperature), (B) MP-*C*2 (233 K), (C) docosane as bought (room temperature K), (D) the product from experimental method 8, (E) the product from experimental method 9, (F) the product from experimental method 10, (G) the product from experimental method 11. *λ* = 1.54056 Å

From comparison in Figure 5.57 the recrystallisation of cocrystallised melt material with toluene, pattern D produced a mixed MP-*C*2 and docosane phase but with kerosene, pattern E, a single phase of docosane is produced with methyl palmitate remaining dissolved in solution. Both variable temperature solvent cocrystallisations with slow and quick cooling rates, patterns F and G, produced mixed phases of MP-*C*2 and docosane.
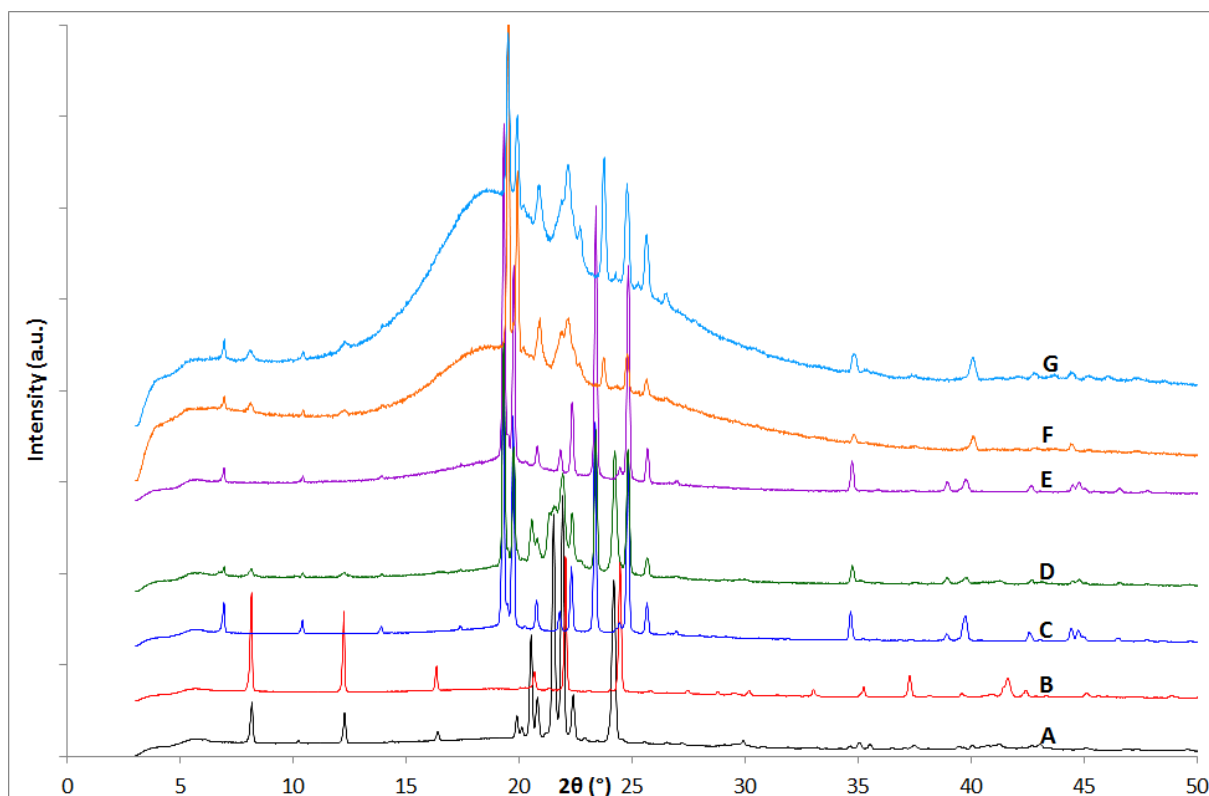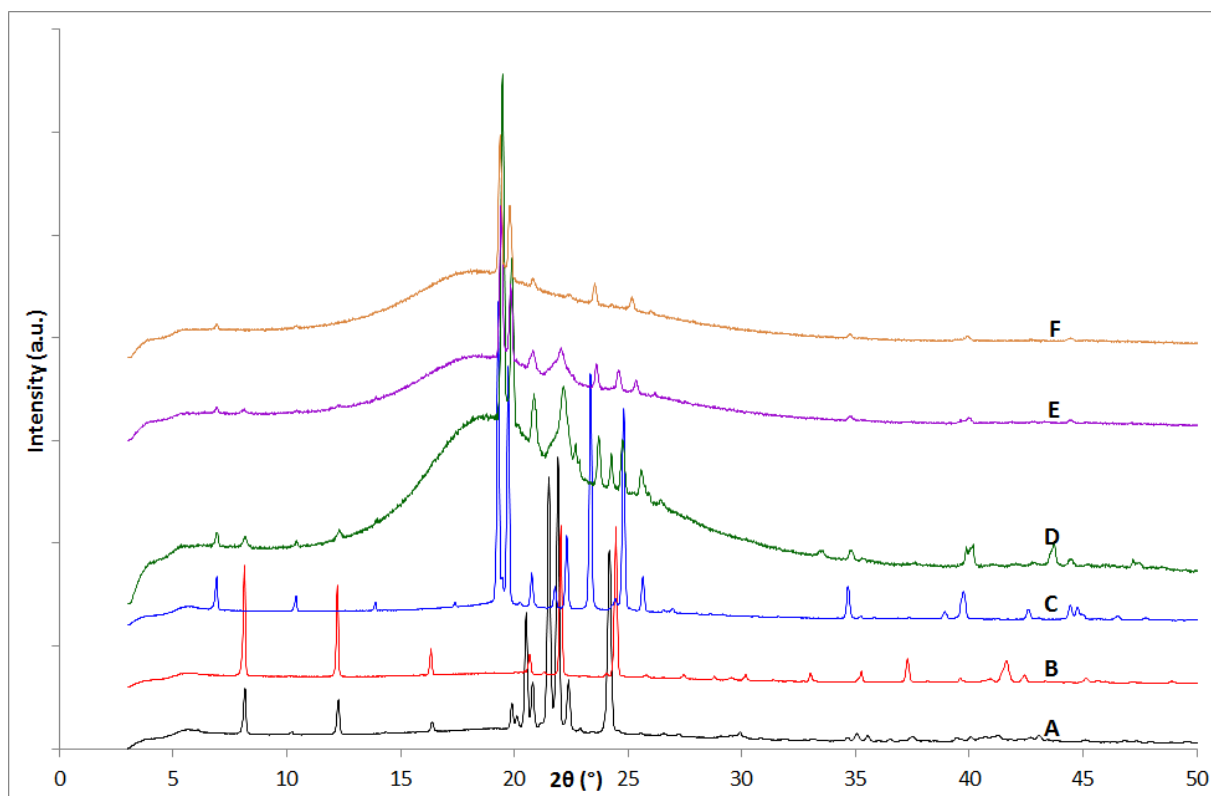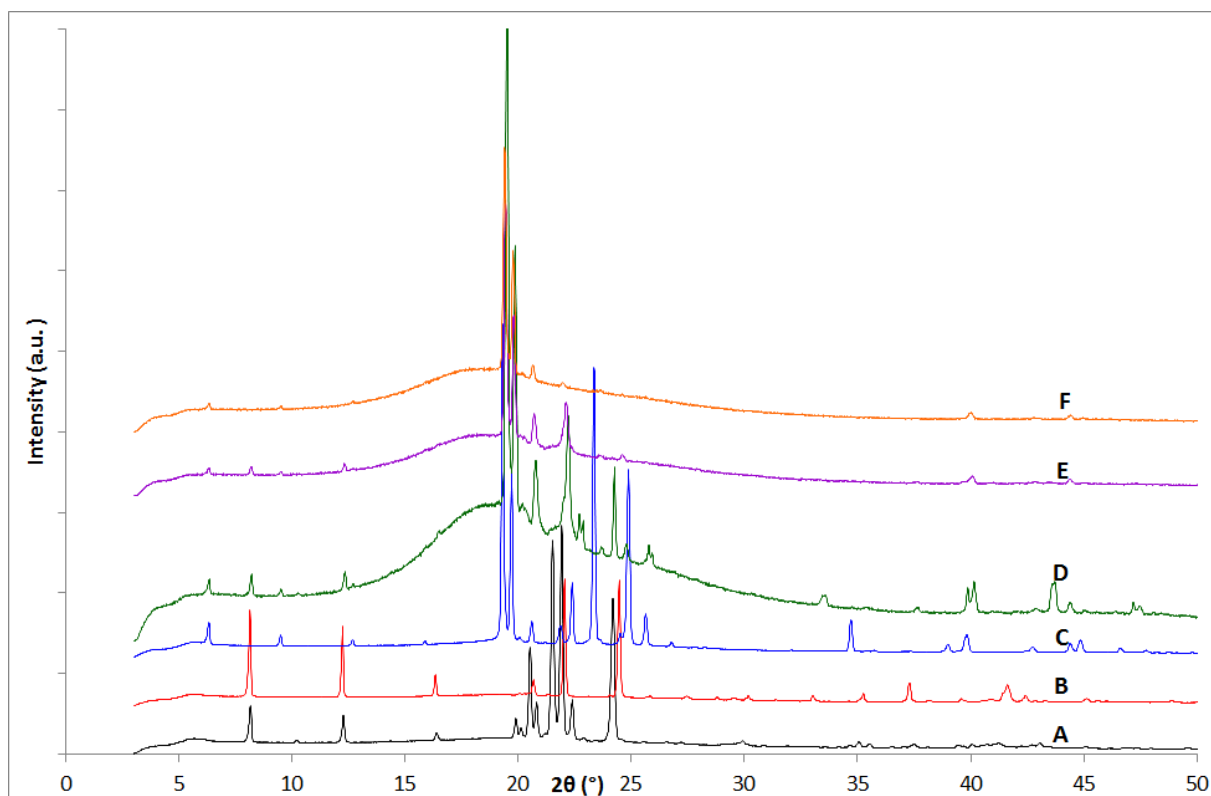
Figure 5.58 PXRD patterns of (A) MP-*Pnab* (ro*om* temperature), (B) MP-*C*2 (233 K), (C) docosane as bought (room temperature K), (D) the product from experimental method 12 (190 K), (E) the product from experimental method 12 (225 K), (F) the product from experimental method 12 (250 K). *λ* = 1.54056 Å

Remaining consistent with the two scans to 190 K in Figure 5.57, the stepwise cocrystallisation in Figure 5.58 increases in crystallinity on cooling and the final scan at 190 K shows a mixed phase of MP-*C*2 and docosane formed.

Rietveld refinements of the products formed between methyl palmitate and docosane can be found in appendix 5.14.

5.14 Methyl Palmitate : Methyl Stearate

5.14.1 Characterisation

Experiments of mixtures of methyl palmitate and methyl stearate were carried out using the experimental methods noted in Table 5.32 and detailed in section 5.3, with the results of these experiments shown in Figures 5.59, 5.60, 5.61 and 5.62.

Table 5.32 Conditions of methyl palmitate : methyl stearate cocrystallisation experiments.

Pattern / Figure	Material	Experimental Methods
E / 5.59	Methyl Palmitate : Methyl Stearate	3
F / 5.59	Methyl Palmitate : Methyl Stearate	4
E / 5.60	Methyl Palmitate : Methyl Stearate	5
F / 5.60	Methyl Palmitate : Methyl Stearate	6
G / 5.60	Methyl Palmitate : Methyl Stearate	7
E / 5.61	Methyl Palmitate : Methyl Stearate	8
F / 5.61	Methyl Palmitate : Methyl Stearate	10
G / 5.61	Methyl Palmitate : Methyl Stearate	11
E / 5.62	Methyl Palmitate : Methyl Stearate	12 at 190 K
F / 5.62	Methyl Palmitate : Methyl Stearate	12 at 225 K
G / 5.62	Methyl Palmitate : Methyl Stearate	12 at 250 K
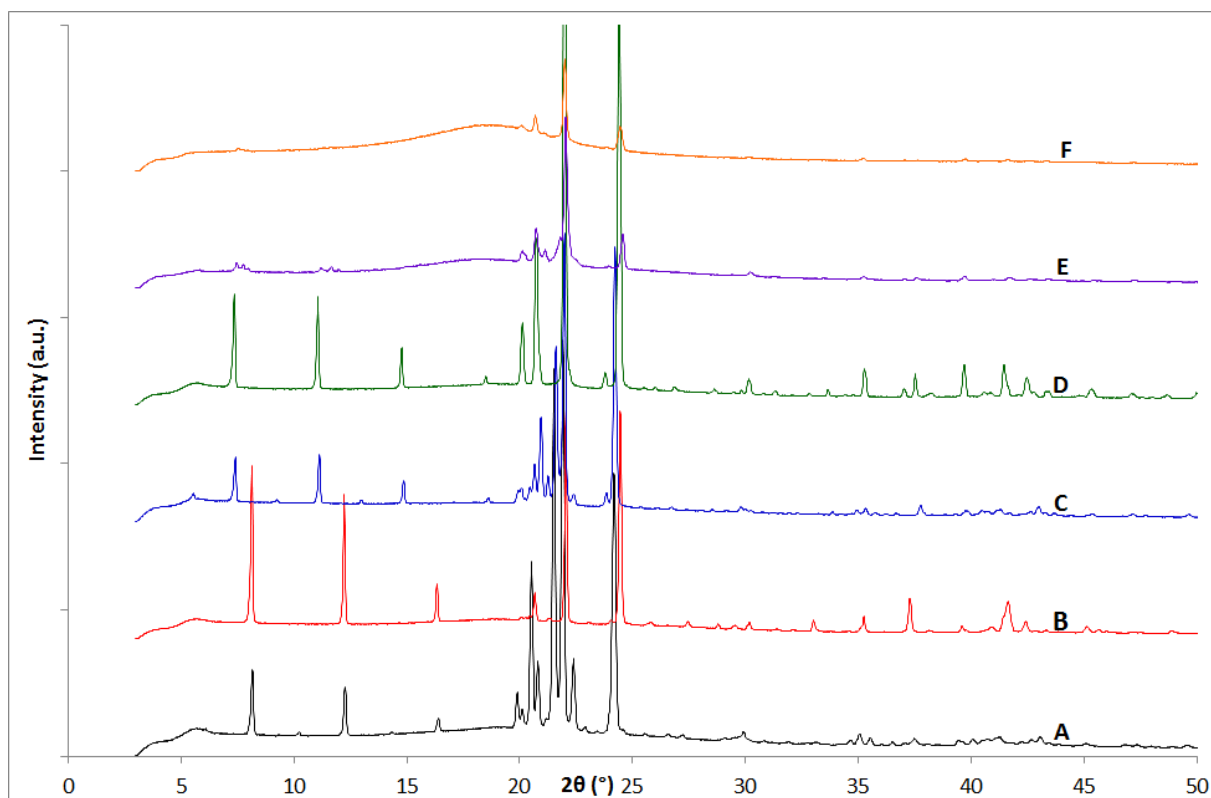
Figure 5.59 PXRD patterns of (A) MP-*Pnab* (ro*om* temperature), (B) MP-*C*2 (233 K), (C) MS-*Pnab* (ro*om* temperature), (D) MS-*C*2 (233 K), (E) the product from experimental method 3, (F) the product from experimental method 4. λ = 1.54056 Å

From comparison in Figure 5.59, the variable temperature solvent cocrystallisation to 233 K with toluene, pattern E, produced a MP-*C*2 and MS-*C*2 mixed phase but with kerosene, pattern F, only the MS-*C*2 phase is formed.
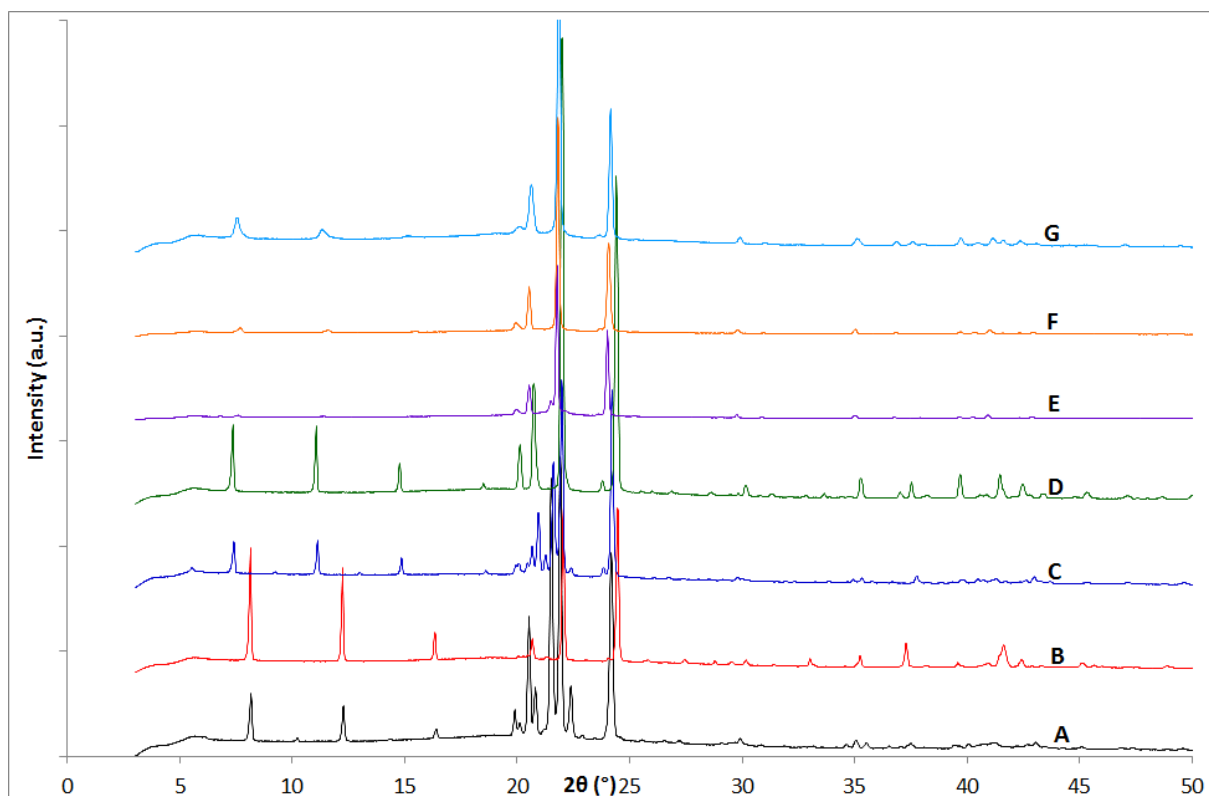
Figure 5.60 PXRD patterns of (A) MP-*Pnab* (ro*om* temperature), (B) MP-*C*2 (233 K), (C) MS-*Pnab* (ro*om* temperature), (D) MS-*C*2 (233 K), (E) the product from experimental method 5, (F) the product from experimental method 6, (G) the product from experimental method 7. *λ* = 1.54056 Å

All three from the melt experiments produced a single phase of MS-*C*2 with no methyl palmitate present. The methyl palmitate must have produced an amorphous phase to account for the absence of crystalline peaks from this phase in the scans.
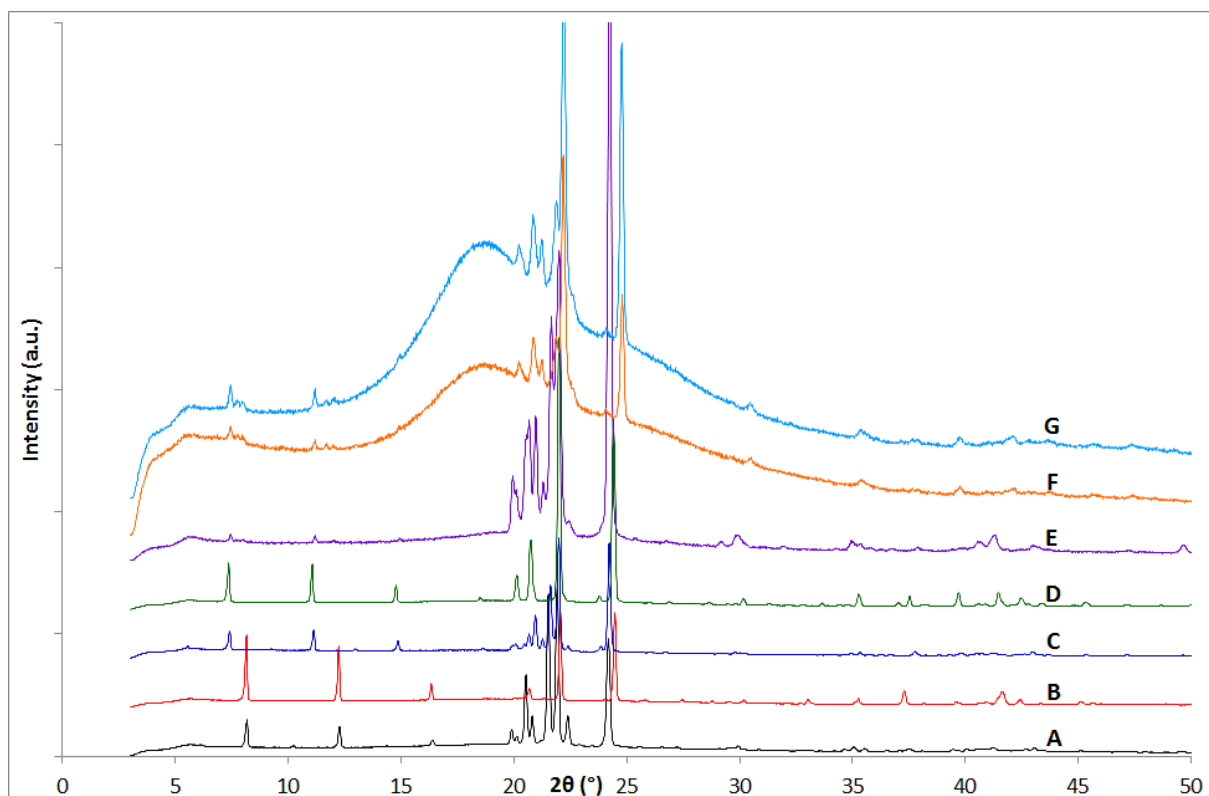
Figure 5.61 PXRD patterns of (A) MP-*Pnab* (ro*om* temperature), (B) MP-*C*2 (233 K), (C) MS-*Pnab* (ro*om* temperature), (D) MS-*C*2 (233 K), (E) the product from experimental method 8, (F) the product from experimental method 10, (G) the product from experimental method 11. *λ* = 1.54056 Å

Whilst the from the melt experiments seemed to produce only a single phase the recrystallisation of the melt phase in toluene produced a mixed melt phase of both of the esters and both variable temperature experiments to 190 K shown in Figure 5.61 also produced the same mixed melt phase.
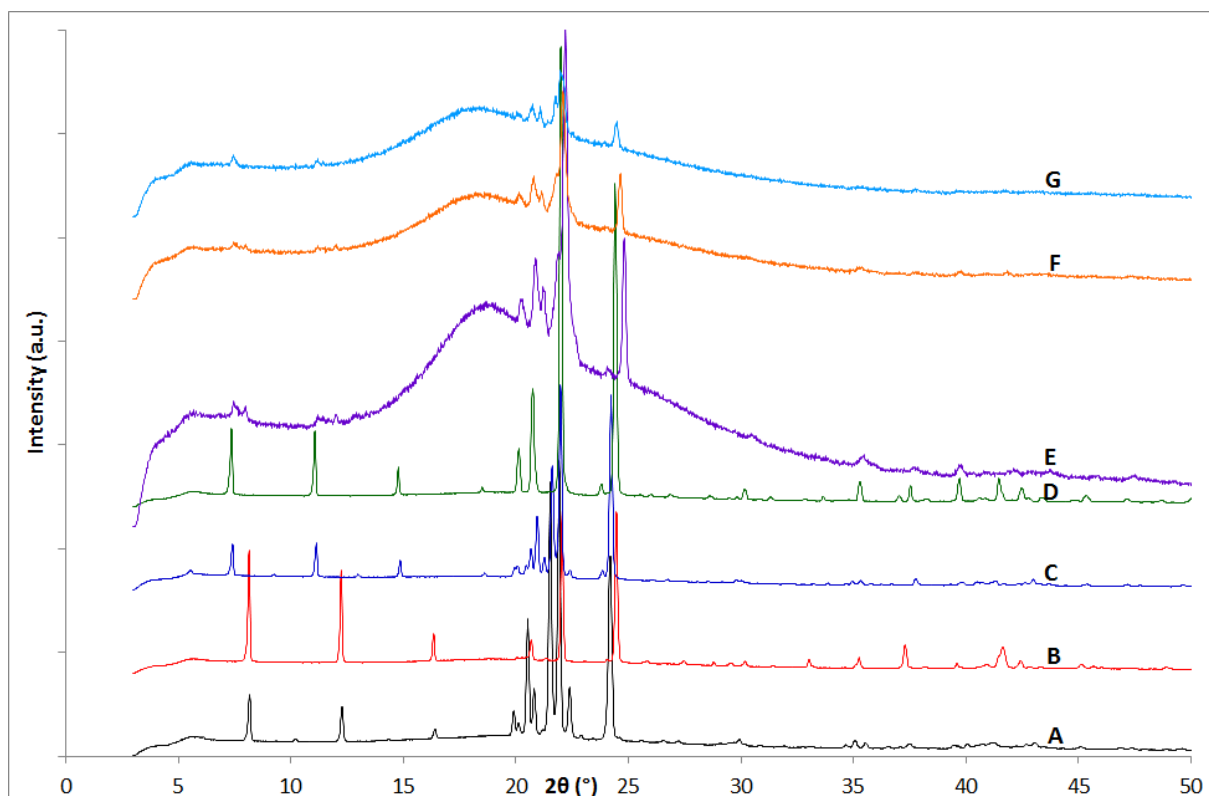
Figure 5.62 PXRD patterns of (A) MP-*Pnab* (ro*om* temperature), (B) MP-*C*2 (233 K), (C) MS-*Pnab* (ro*om* temperature), (D) MS-*C*2 (233 K), (E) the product from experimental method 12 (190 K), (F) the product from experimental method 12 (225 K), (G) the product from experimental method 12 (250 K). λ = 1.54056 Å

As with the cocrystallisation experiments to 190 K shown in Figure 5.61, the low temperature scan in Figure 5.62 also shows a mixed phase of the two melt phases.

Rietveld refinements of the products formed between methyl palmitate and methyl stearate can be found in appendix 5.15.

5.15 Conclusions

In this chapter the structures for three straight chain hydrocarbons (dodecane, tetradecane and docosane) have been successfully solved from PXRD lab data with strong correlation to previously published structures. The five hydrocarbons in this project have also been shown not to recrystallise into a different phase under the conditions tested.

An extensive set of crystallisation conditions and combinations of the two methyl esters (methyl palmitate and methyl stearate) with the five hydrocarbons has been studied in this project. When the solution of a mixture is heated above the melting point of the methyl esters, then the $C2$ melt phases crystallise out preferentially over the $Pnab$ phases.

Most often a mixed phase of the ester and hydrocarbon forms, however sometimes only a single phase forms, often at higher crystallisation temperatures. However, whenever a single phase forms it is always the compound with the highest melting point and largest relative molecular mass. Solvent doesn't appear to make a difference as to which phase or mixture of phases is formed, however, it could influence the temperature at which crystalline material begins to form.

Whilst most PXRD patterns were clear to determine the products, most scans where crystallisation took place in the presence of a solvent have a high amorphous background due to the solvent, and sometimes with peak overlap often at mid-angle due to the high concentration of peaks. Also due to the method of crystallisation and due to the shape of crystals that form, the relative intensities of several peaks are not the same as the as standard known phase simulated patterns, due to preferred orientation.

Potential new rotator phases formed from cocrystallisations of both methyl palmitate and methyl stearate with octadecane, eicosane and docosane hydrocarbons, these have patterns which are very similar to that of the PXRD pattern for the rotator phase of eicosane reported by Di Giambatti[83]. As there hasn't been much published PXRD data for rotator phases of which there are up to five, and are often only accessed in a few degrees below their melting point, it is impossible to confirm whether these new phases are in fact a rotator phase. The data quality is poor with too few peaks for successful indexing to be possible and the potential presence of methyl ester peaks. As rotator phases are often identified by other methods to PXRD, and often during their transitions from the liquid or stable crystalline states or at quasi-equilibrium low temperature states, further investigation would be needed to characterise these new phases. Experimental techniques that could be useful in characterising these phases include infrared and raman spectroscopy, differential scanning calorimetry, optical microscopy and differential thermal analysis.

6.   Chapter 6 – Summary

The aims of this project were to confirm the structures of the two major components of biodiesel that cause cold flow properties, methyl stearate and methyl palmitate, and solve the structures of any new polymorphs that may be formed. Crystallisations by various routes and combinations of the methyl esters and similar sized hydrocarbons were investigated to see whether the biodiesel compounds are likely to interact with the petroleum diesel when blended together and form any new phases. If any new phases were to form a greater number of structures would need to be considered, when designing additives to prevent or limit cold flow problems.

6.1 Methyl Stearate

Five known methyl stearate structures were discussed in this chapter, however only three of them were observed during this work. In the recrystallisations covered in this work the MS-*Pnab* phase is the principal phase, but if the material has been melted then either of two melt phases will form depending on the cooling rates.

Thermal expansion coefficients were determined for all three of the polymorphs that were observed, with larger coefficients calculated than those reported in the literature for rigid inorganic structures. This is plausible due to less rigidity in the organic ester structures, and unit cells with greater room for expansion and contraction.

Gaussian dipole calculations show a net zero dipole for the three single crystal structures of methyl stearate, but a small dipole for the two melt phase unit cells.

Whilst it is expected that solid crystal structures would have a zero dipole, published single crystal structures of ethyl and propyl stearate also have significant dipoles, due to the same molecular orientation as the MS-*Cc* phase.

Ethyl stearate recrystallisations were carried out under the same conditions used for methyl stearate, showing that only the polymorph first reported in 1968 forms. Diamond beamline I11 powder diffraction data was collected to see whether thermal expansion coefficients could also be obtained for this phase, however due to either poor data quality or a subtle phase change on cooling the material, these could not be calculated.

6.2 Methyl Palmitate

The first two methyl palmitate structures were solved from I11 PXRD data; one using as-bought material and one phase formed from the melt. These two structures are very similar to their counterpart methyl stearate phases, the MS-*Pnab* phase and the MS-*C*2 phase.

Thermal expansion coefficients were calculated for the MP-*Pnab* with similar values as those calculated for the three methyl stearate phases, further proving that compounds of this type have more flexibility in expansion and contraction of their unit cells.

Gaussian results for the two methyl palmitate phases are fairly similar to the two methyl stearate related structures. The MP-*Pnab* phase has a net zero dipole for the unit cell, but the MP-*C*2 phase has a small net dipole like the MS-*C*2 structure.

6.3 Structures of *n*-alkanes and crystallisations of Methyl Stearate or Methyl Palmitate with hydrocarbons

Three straight chain *n*-alkane structures were solved from lab PXRD data (dodecane, tetradecane and docosane) to aid in phase refinements. Recrystallisations with these compounds along with two more alkanes of similar size, showed that under the conditions used throughout this project the phases which are likely to crystallise out are the as-bought phases, as no other phases were discovered.

Various crystallisation experiments were carried out with mixtures of methyl palmitate or methyl stearate with the 5 hydrocarbons. These results conclude that generally a phase mixture of the materials will form, but occasionally only a single phase will form. If a phase mixture forms it will be of the *Pnab* phases if the materials have not been above their melting points, but if they have then the as-bought phase of the hydrocarbon, and the *C*2 melt phases of the ester will form. However if just a single phase forms and the other phase remains dissolved in solution, then the compound with the highest relative molecular mass will preferentially crystallise out. This could be a combination of solubility and concentration of the compounds with one compound crashing out, and the temperature of the PXRD scan not being low enough for crystals to form in the concentrations used.

Whilst most of the crystallisation experiments produced mixtures of known phases, a couple of PXRD patterns showed potentially new phases which look very similar to those of rotator phases of alkanes. These new phases were found with three of the longer chain hydrocarbons, showing that it may be a more common occurrence that should be investigated further.

The original aims of this project to determine the phases of methyl stearate and methyl palmitate were successful, with the first two structures of methyl palmitate solved. Through various experiments it has been shown that methyl esters and hydrocarbons don't interact with one another, to form new phases under the conditions used in this work; however further work should be carried out in more realistic mixtures and environments, to get a true understanding of the systems that would be experienced in a fuel tank.

6.4 Further work

There are other areas of work which could be expanded on, to gain a better understanding on the crystal structures discussed in this work, and how they may behave in a more realistic environment.

Due to the inconsistency of some crystal structures in when they may form, and two crystal structures of MS-$A2/a$ and MS-$C2/c$ phases which have not been observed; lattice energy calculations would be useful in determining the stability of all the crystal phases discussed in this work, and why some phases may preferentially form over others.

Further neutron powder diffraction data of the MS-$C2$ phase should be done, to confirm the existence of both melt phases which cannot categorically be determined from PXRD data. Neutron powder diffraction data would also be useful for the two methyl palmitate phases to confirm their structures which were solved from PXRD data.

The inconsistency as to when the methyl palmitate melt phase will form should also be investigated with different crystallisation conditions which are more realistic to a fuel tank; however lattice energies may also shed light as to the stability of the structures.

As it wasn't possible to get uniform thermal contraction with the ethyl stearate data, further cooling data should be collected to determine whether it was just poor data quality that prevented obtaining the thermal expansion coefficients or whether there is a phase change on cooling. If there is a phase change structural solution should be attempted.

In chapter 5 several PXRD patterns showed phases which looked potentially like rotator phases, which can be found in hydrocarbons. These phases, of which there are five currently reported, are distortions of the hexagonal lattice if it is assumed the molecules are arranged normally, as hexagonally close packed rods. These phases are usually found in the few degrees below the melting point of the compound. Due to lack of rotational order in these types of molecules PXRD diffraction is not a suitable method of observation, and initially DSC or other calorimetry techniques would be useful to determine any phase changes. These phases also could be a mixture due to the methyl ester also being present during crystallisation, which needs to be taken into account.

Whilst many different crystallisation conditions were used throughout this project, some of them are not very realistic with respect to those that are likely to be experienced in a fuel tank. Lab conditions in this project only take into account binary mixtures, and do not take into account the bulk solution of the many different compounds that make up both petroleum diesel and biodiesel, and many additives

which are added to the fuel, not just cold flow improvers. The fuel tank surfaces should also be taken into account, as they may influence the structures which form. Whilst new crystallisation conditions should be investigated, due to the similarity in peak positions of many compounds used in this project, PXRD is unlikely to be a suitable method of identifying the compounds that crystallise out, due to the potential for overlapping peaks.

7.   Chapter 7 – Appendicies

See attached CD

8. References

(1)   Knothe, G. *Fuel Processing Technology* **2005**, *86*, 1059.

(2)   Misra, R. D.; Murthy, M. S. *Renewable & Sustainable Energy Reviews* **2011**, *15*, 2413.

(3)   Hoekman, S. K.; Broch, A.; Robbins, C.; Ceniceros, E.; Natarajan, M. *Renewable & Sustainable Energy Reviews* **2012**, *16*, 143.

(4)   Dunn, R. O. *Journal of the American Oil Chemists Society* **2008**, *85*, 961.

(5)   Perez, A.; Casas, A.; Fernandez, C. M.; Ramos, M. J.; Rodriguez, L. *Bioresource Technology* **2010**, *101*, 7375.

(6)   Graboski, M. S.; McCormick, R. L. *Progress in Energy and Combustion Science* **1998**, *24*, 125.

(7)   Dunn, R. O. *Energy & Fuels* **2009**, *23*, 4082.

(8)   Knothe, G. *Energy & Fuels* **2008**, *22*, 1358.

(9)   Dunn, R. O.; Knothe, G. *Journal of Oleo Science* **2001**, *50*, 415.

(10)   Fukuda, H.; Kondo, A.; Noda, H. *Journal of Bioscience and Bioengineering* **2001**, *92*, 405.

(11)   Demirbas, A. *Energy Conversion and Management* **2009**, *50*, 14.

(12)   Demirbas, A. H.; Demirbas, I. *Energy Conversion and Management* **2007**, *48*, 2386.

(13)   Smith, P. C.; Ngothai, Y.; Nguyen, Q. D.; O'Neill, B. K. *Renewable Energy* **2010**, *35*, 1145.

(14)   Westbrook, C. K.; Pitz, W. J.; Sarathy, S. M.; Mehl, M. *Proceedings of the Combustion Institute* **2013**, *34*, 3049.

(15)   Naik, C. V.; Westbrook, C. K.; Herbinet, O.; Pitz, W. J.; Mehl, M. *Proceedings of the Combustion Institute* **2011**, *33*, 383.

(16)   Lin, B.-F.; Huang, J.-H.; Huang, D.-Y. *Fuel* **2009**, *88*, 1779.

(17)   Hu, J. B.; Du, Z. X.; Li, C. X.; Min, E. *Fuel* **2005**, *84*, 1601.

(18)   JW., P. Automobile, truck and speciality vehicle market research statistics, trends & leading companies. [Online Early Access]. Published Online: 2008.

(19)   Development, W. B. C. f. S. Mobility 2030: meeting the challenges to sustainability. *The sustainable mobility project* [Online Early Access]. Published Online: 2004.

(20)   Bharathiraja, B.; Chakravarthy, M.; Kumar, R. R.; Yogendran, D.; Yuvaraj, D.; Jayamuthunagai, J.; Kumar, R. P.; Palani, S. *Renewable & Sustainable Energy Reviews* **2015**, *47*, 634.

(21)   Su, Y.; Zhang, P.; Su, Y. *Renewable & Sustainable Energy Reviews* **2015**, *50*, 991.

(22)   Gui, M. M.; Lee, K. T.; Bhatia, S. *Energy* **2008**, *33*, 1646.

(23)   Rawat, I.; Kumar, R. R.; Mutanda, T.; Bux, F. *Applied Energy* **2013**, *103*, 444.

(24)   Rashid, N.; Rehman, M. S. U.; Sadiq, M.; Mahmood, T.; Han, J.-I. *Renewable & Sustainable Energy Reviews* **2014**, *40*, 760.

(25)   Speranza, L. G.; Ingram, A.; Leeke, G. A. *Renewable Energy* **2015**, *78*, 406.

(26) Beal, C. M.; Gerber, L. N.; Sills, D. L.; Huntley, M. E.; Machesky, S. C.; Walsh, M. J.; Tester, J. W.; Archibald, I.; Granados, J.; Greene, C. H. *Algal Research-Biomass Biofuels and Bioproducts* **2015**, *10*, 266.

(27) Chisti, Y. *Biotechnology Advances* **2007**, *25*, 294.

(28) Knothe, G.; Van Gerpen, J.; Krahl, J. *The Biodiesel Handbook*; AOCS Press, 2005.

(29) Knothe, G.; Matheaus, A. C.; Ryan, T. W. *Fuel* **2003**, *82*, 971.

(30) Imahara, H.; Minami, E.; Saka, S. *Fuel* **2006**, *85*, 1666.

(31) Knothe, G. *Energy & Environmental Science* **2009**, *2*, 759.

(32) Garside, J.; Davey, R. J.; Jones, A. G. *Advances in Industrial Crystallization*; Butterworth-Heinemann Ltd: Oxford, 1991.

(33) Dunn, R. O.; Bagby, M. O. *Journal of the American Oil Chemists Society* **1995**, *72*, 895.

(34) Craig, S. R.; Hastie, G. P.; Roberts, K. J.; Sherwood, J. N. *Journal of Materials Chemistry* **1994**, *4*, 977.

(35) Dunn, R. O.; Shockley, M. W.; Bagby, M. O. *Journal of the American Oil Chemists Society* **1996**, *73*, 1719.

(36) Yang, F.; Zhao, Y.; Sjoblom, J.; Li, C.; Paso, K. G. *Journal of Dispersion Science and Technology* **2015**, *36*, 213.

(37) Jin, W. B.; Jing, J. Q.; Wu, H. F.; Yang, L.; Li, Y.; Shu, X. B.; Wang, Y. L. *Journal of Dispersion Science and Technology* **2014**, *35*, 1434.

(38) El-Gamal, I. M.; Khidr, T. T.; Ghuiba, F. M. *Fuel* **1998**, *77*, 375.

(39) *CRC Handbook of Chemistry and Physics*; 92nd ed.; CRC Press, Boca Raton, Fl United States of America, 2011.

(40) Wang, P. S.; Tat, M. E.; Van Gerpen, J. *Journal of the American Oil Chemists Society* **2005**, *82*, 845.

(41) Foglia, T. A.; Nelson, L. A.; Dunn, R. O.; Marmer, W. N. *Journal of the American Oil Chemists Society* **1997**, *74*, 951.

(42) Dogan, T. H.; Temur, H. *Fuel* **2013**, *108*, 793.

(43) *Introduction to fats and oils technology*; 2nd ed.; AOCS Press, Champaign, IL, 2000.

(44) Aleby, S. *Acta Chemica Scandinavica* **1968**, *22*, 811.

(45) Aleby, S.; Vonsydow, E. *Acta Crystallographica* **1960**, *13*, 487.

(46) Macgilla.Ch; Wolthuis.M *Acta Crystallographica Section B-Structural Crystallography and Crystal Chemistry* **1970**, *B 26*, 645.

(47) Mathieso.Am; Welsh, H. K. *Acta Crystallographica* **1965**, *18*, 953.

(48) Aleby, S. *Acta Chemica Scandinavica* **1968**, *22*, 3146.

(49) Aleby, S. *Acta Crystallographica* **1962**, *15*, 1248.

(50) Dorset, D. L. *Crystallography of the Polymethylene Chain: An inquiry into the structure of waxes*; Oxford University Press: Oxford, 2005.

(51) Norman, N.; Mathisen, H. *Acta Chemica Scandinavica* **1972**, *26*, 3913.

(52) Nyburg, S. C.; Gerson, A. R. *Acta Crystallographica Section B-Structural Science* **1992**, *48*, 103.

(53) Nyburg, S. C.; Luth, H. *Acta Crystallographica Section B-Structural Crystallography and Crystal Chemistry* **1972**, *B 28*, 2992.

(54) *The Lipid Handbook*; Chapman and Hall: London, 1986.

(55) King, H. E.; Sirota, E. B.; Shao, H.; Singer, D. M. *Journal of Physics D-Applied Physics* **1993**, *26*, B133.

(56)   Mukherjee, P. K. *Physics Reports-Review Section of Physics Letters* **2015**, *588*, 1.

(57)   Sirota, E. B.; King, H. E.; Singer, D. M.; Shao, H. H. *Journal of Chemical Physics* **1993**, *98*, 5809.

(58)   Ungar, G.; Masic, N. *Journal of Physical Chemistry* **1985**, *89*, 1036.

(59)   Ungar, G. *Journal of Physical Chemistry* **1983**, *87*, 689.

(60)   Jenkins, R.; Snyder, R. L. *Introduction to X-Ray Powder Diffractometry*; John Wiley & Sons, Inc.: New York, 1996; Vol. 138.

(61)   Dinnebier, R. E.; Billinge, S. J. L. *Powder Diffraction Theory and Practice*; The Royal Society of Chemistry: Cambridge, UK, 2008.

(62)   http://www.isis.rl.ac.uk/crystallography/hrpd.

(63)   Shirley, R. A. University of Surrey, England, 2000.

(64)   Altomare, A.; Cuocci, C.; Giacovazzo, C.; Moliterni, A.; Rizzi, R.; Corriero, N.; Falcicchio, A. *Journal of Applied Crystallography* **2013**, *46*, 1231.

(65)   Coelho, A.; TOPAS Academic V4.1 ed.; Coelho Software: Brisbane, 2007.

(66)   Oszlanyi, G.; Suto, A. *Acta Crystallographica Section A* **2004**, *60*, 134.

(67)   Oszlanyi, G.; Suto, A. *Acta Crystallographica Section A* **2008**, *64*, 123.

(68)   Coelho, A. A. *Journal of Applied Crystallography* **2000**, *33*, 899.

(69)   McCusker, L. B.; Von Dreele, R. B.; Cox, D. E.; Louer, D.; Scardi, P. *Journal of Applied Crystallography* **1999**, *32*, 36.

(70)   Rietveld, H. M. *Journal of Applied Crystallography* **1969**, *2*, 65.

(71)   Young, R. A. *The Rietveld Method*; Oxford University Press: New York, USA, 1993.

(72)   Frisch, M. J.; Trucks, G. W.; Schlegel, H. B.; Scuseria, G. E.; Robb, M. A.; Cheeseman, J. R.; Scalmani, G.; Barone, V.; Mennucci, B.; Petersson, G. A.; Nakatsuji, H.; Caricato, M.; Li, X.; Hratchian, H. P.; Izmaylov, A. F.; Bloino, J.; Zheng, G.; Sonnenberg, J. L.; Hada, M.; Ehara, M.; Toyota, K.; Fukuda, R.; Hasegawa, J.; Ishida, M.; Nakajima, T.; Honda, Y.; Kitao, O.; Nakai, H.; Vreven, T.; Montgomery, J. A., Jr.; Peralta, J. E.; Ogliaro, F.; Bearpark, M.; Heyd, J. J.; Brothers, E.; Kudin, K. N.; Staroverov, V. N.; Kobayashi, R.; Normand, J.; Raghavachari, K.; Rendell, A.; Burant, J. C.; Iyengar, S. S.; Tomasi, J.; Cossi, M.; Rega, N.; Millam, J. M.; Klene, M.; Knox, J. E.; Cross, J. B.; Bakken, V.; Adamo, C.; Jaramillo, J.; Gomperts, R.; Stratmann, R. E.; Yazyev, O.; Austin, A. J.; Cammi, R.; Pomelli, C.; Ochterski, J. W.; Martin, R. L.; Morokuma, K.; Zakrzewski, V. G.; Voth, G. A.; Salvador, P.; Dannenberg, J. J.; Dapprich, S.; Daniels, A. D.; Farkas, Ö.; Foresman, J. B.; Ortiz, J. V.; Cioslowski, J.; Fox, D. J.; Revision D.01 ed.; Gaussian Inc: Wallingford, CT, 2009.

(73)   Jensen, F. *Introduction to Computational Chemistry*; John Wiley & Sons Inc.: England, 2007; Vol. 2nd.

(74)   Lewtas, K.; Hutchins, P.; Shotton, E.; Barnett, S., Methyl Stearate *C*2/*c* single crystal structure.

(75)   Chen, T.-Y.; Hriljac, J. A.; Tang, C., Methyl Stearate structure formed from the melt by slow cooling to 233 K.

(76)   Liu, X.; Tang, C., Methyl stearate structure formed from the melt by quenching to 193 K.

(77)   Sears, V. F. *Neutron News* **1992**, *3*, 26.

(78)   Dolomanov, O. V. B., L.J.; Gildea, R.J.; Howard, J.A.K.; Puschmann, H. *J. Appl. Cryst.* **2009**, *42*, 339.

(79)   Mathisen, H.; Norman, N.; Pedersen, B. F. *Acta Chemica Scandinavica* **1967**, *21*, 127.

(80)   Boese, R.; Weiss, H. C.; Blaser, D. *Angew. Chem.-Int. Edit.* **1999**, *38*, 988.

(81)   Bond, A. D.; Davies, J. E. *Acta Crystallographica Section E-Structure Reports Online* **2002**, *58*, o196.

(82)   Gerson, A. R.; Nyburg, S. C. *Acta Crystallographica Section B-Structural Science* **1992**, *48*, 737.

(83)   Di Giambattista, C.; Sanctuary, R.; Perigo, E.; Baller, J. *Journal of Chemical Physics* **2015**, *143*.